fluids

Special Issue Reprint

Boundary Layer Processes in Geophysical/ Environmental Flows

Edited by
Joseph Kuehl, Pengfei Xue and Fabrice Veron

mdpi.com/journal/fluids

MDPI

Boundary Layer Processes in Geophysical/Environmental Flows

Boundary Layer Processes in Geophysical/Environmental Flows

Editors

Joseph Kuehl
Pengfei Xue
Fabrice Veron

MDPI

Basel • Beijing • Wuhan • Barcelona • Belgrade • Novi Sad • Cluj • Manchester

Editors

Joseph Kuehl
University of Delaware
Delaware
USA

Pengfei Xue
Michigan Technological
University
Houghton
USA

Fabrice Veron
University of Delaware
Newark
USA

Editorial Office
MDPI AG
Grosspeteranlage 5
4052 Basel, Switzerland

This is a reprint of articles from the Special Issue published online in the open access journal *Fluids* (ISSN 2311-5521) (available at: https://www.mdpi.com/journal/fluids/special_issues/geophysical_environmental_flows).

For citation purposes, cite each article independently as indicated on the article page online and as indicated below:

Lastname, A.A.; Lastname, B.B. Article Title. *Journal Name* **Year**, *Volume Number*, Page Range.

ISBN 978-3-7258-1355-1 (Hbk)
ISBN 978-3-7258-1356-8 (PDF)
doi.org/10.3390/books978-3-7258-1356-8

Contents

fluids

MDPI

Editorial

Editorial Summary: Boundary Layer Processes in Geophysical/Environmental Flows

Joseph Kuehl †

Department of Mechanical Engineering, University of Delaware, Newark, DE 19716, USA; jkuehl@udel.edu; Tel.: +1-302-831-2150

† Current address: 130 Academy Street, Spencer Lab Room 210, Newark, DE 19716, USA.

Boundary layer processes play a crucial role in establishing the circulation patterns of the oceans and atmosphere, significantly affecting both regional and global climate, as well as the distributions of heat, nutrients, species, pollutants and more. This Special Issue of *Fluids* is dedicated to recent advances in the theoretical, numerical, observational, and experimental investigation of geophysical/environmental boundary layer processes, and how those process may influence regional and global circulation. While traditional geophysical boundary layers, such as the major eastern and western boundary currents [1–3], or those associated with the air–sea interface [4], have enjoyed over a decade of intense study, our understanding of their dynamics continues to evolve.

Lyu et al. [5] advance the understanding of momentum exchanges across the air–sea boundary. Such exchanges are an integral component of the earth system, and their parametrization is essential for climate and weather models. This study focuses on the impact of gustiness on the momentum flux, using three months of direct flux observations from a moored surface buoy. Gustiness, which quantifies the fluctuations of wind speed and direction, is shown to impact air–sea momentum fluxes. It is shown that, during runs classified as gusty, the aerodynamic drag coefficient [6] is increased up to 57% when compared to their non-gusty counterparts. This is caused by a correlated increase in vertical fluctuations during gusty conditions, and explains variability in the drag coefficient for wind speeds of up to 20 m/s.

Quintana et al. [7] advance the understanding of the seasonality of surface-balanced motions in eastern boundary currents. Balanced motions and internal gravity waves account for most of the kinetic energy budget, and capture most of the vertical velocity in the ocean. However, estimating the contributions of balanced motions to both issues at time scales of less than a day is a challenge, because balanced motions are obscured by internal gravity waves. To remove this obscurity, a dynamic filtering protocol that separates these motions is developed. The feasibility of such a filter is confirmed, which opens new possibilities for more accurate estimation of the vertical exchanges of any tracers at any vertical level in the water column.

Kuehl and Sheremet [8] advance the understanding of so-called gap leaping boundary currents [9–12] by considering the effects of coastline geometry. For traditional straight, parallel gaps, such systems are known to exhibit two dominant states (gap penetrating and leaping), with the transitional dynamics between states displaying hysteresis [13,14]. However, for more complex geometries, such as angled or offset gap configurations, the question of multiple states and hysteresis was unresolved. It is shown that the presence of multiple states with hysteresis for gap-leaping western boundary current systems is robust to both angled and offset gap geometries. This result contributes to larger discussions about how basin geometry, and how the distribution of both side and bottom boundary dissipation throughout the basin in particular, influence the basin scale circulation patterns [15–17].

While such traditional geophysical boundary layers have enjoyed over a decade of intense study, the inaccessibility of the deep ocean and the need for large spatial arrays to resolve scale dependent processes has limited our understanding of the ocean bottom

Citation: Kuehl, J. Editorial Summary: Boundary Layer Processes in Geophysical/Environmental Flows. *Fluids* **2023**, *8*, 279. https://doi.org/10.3390/fluids8100279

Received: 4 October 2023
Accepted: 10 October 2023
Published: 19 October 2023

boundary layer. Indeed, this is an emerging field of study, and the need to revise classical works [18,19] is recognized. The remaining manuscripts in this Special Issue, in one way or another, advance the understanding of how steep and complex topography influences ocean circulation. At the present time, this open question is at the forefront of climate science (IWG-NOPP [20]).

Polzin et al. [21] report a novel attempt to utilize a turbulence flux current meter on a conventional mooring. The physical situation is a downwelling Ekman layer supported by sub-inertial flow in excess of 0.2 m s^{-1}, slope Burger number of 0.7, and moderate stratification with $N/f = 40$. Importantly, the mooring was placed immediately in the lee of a ridge superimposed on the continental slope, and flow speeds were within a transitional regime for non-rotating hydraulics. The observations are at odds with conventional wisdom concerning the arrested Ekman paradigm [22] and one-dimensional models of boundary layers associated with mixing over sloping topography (see [23] for a review). The moored data document a well-mixed region smaller than the stratified Ekman layer [24] and significantly smaller than Ekman arrest metrics. The limited height of the well-mixed region occurs in conjunction with buoyancy and momentum fluxes in an internal wave band regime, with internal waveband vertical momentum fluxes directed directly upslope. The observations also document a near-boundary downslope turning of the velocity vector in the boundary layer that is antiparallel to the turbulent stress vector and larger than standard Ekman theory. The internal waveband fluxes are relatively broadly distributed in the frequency domain, rather than appearing at the frequency associated with internal wave rays paralleling the slope (e.g., [25]). The author's opinion is that the limited extent of the well-mixed layer and internal wave band fluxes are casually related, i.e., the internal waveband process represents a rapid ventilation of the boundary layer. If the observations are a round hole, concepts of boundary layer ventilation accomplished by modifying the internal waveguide to support submesoscale instabilities [26] or near-inertial wave trapping [27] represent a square peg. A key issue is that such theoretical concepts are developed for planar sloping boundaries rather than complex topography.

Ruan [28] also advances the understanding of the ocean bottom boundary layer by considering bulk dissipation estimates. Large-scale ocean currents are primarily powered by atmospheric winds and astronomical tidal forces, which have been well quantified through satellite observations. However, there is a significant disagreement regarding where the kinetic energy (KE) is lost, and one of the major uncertainties lies in the bottom drag, which converts the KE from mean flows to heat loss through irreversible molecular mixing in the oceanic bottom boundary layer (BBL). Typically, the contribution from bottom drag is quantified using a formula proposed by G.I. Taylor [29], which relates the integrated BBL dissipation rate to a drag coefficient and a flow magnitude outside of the BBL. Building upon Taylor's formula, the study by Ruan [30] offers a theoretical basis for better estimating BBL dissipation, given measured mean flows outside of the BBL. It shows that Taylor's formula only provides an upper bound estimate for the BBL dissipation, and should be applied with caution since the performance of the bulk formula depends on the distribution of velocity and shear stress near the seafloor, which can be disrupted by bottom roughness in the real ocean.

Nagano et al. [31] advance the understand of the ocean bottom boundary layer through observations performed around Japan under a unique cooperative project among oceanographers and seismologists, which has unveiled the ocean variabilities near the bottom [32–36]. In this Special Issue, a bottom-intensified current was found on the continental slope off the southeast coast of Hokkaido, Japan. The thickness varies, being affected by the El Niño and the southern oscillation (ENSO). The ENSO-timescale thickening of the oceanic bottom boundary layer is represented by superposed coastal-trapped wave modes excited on the slope by ENSO-related Rossby wave disturbances.

Kozelkov et al. [37] further advance the understanding of bottom boundary layer dissipation by considers turbulence effects on tsunami runup. The turbulence effects on tsunami propagation and runup are studied using the Reynolds-averaged Navier–Stokes

shear stress transport (RAN SST) over a nonuniform-bottom pool and collapsing with a barrier. While turbulence is found to have little effect on wave shape and propagation, turbulence effects during the runup and collapse became noticeable and could boost the flow (increasing the pressure force and the total force) by up to 25 percent.

Gundersen et al. [38] advance the understanding of complex topography by experimental investigation of the flow produced by mound-bearing impact craters. Both an idealized crater and a scaled model of a real Martian craters are investigated using high-resolution planar particle image velocimetry (PIV) in a refractive-index matching (RIM) flow environment [39]. The experimental investigation revealed significant structural differences between a simple crater with or without a mound, and a Gale Crater model showed both similarities with and differences from the primary flow features found for the idealized model. These results have implications for intra- to extra-crater mass and momentum exchange, and for sediment transport processes.

Hu et al. [40] also advance the understanding of the complex interactions between turbulent flow and sediment transport utilizing a lattice Boltzmann method [41,42]. It is found that the presence of heavy particles substantially reduces the maximum fluid streamwise velocity fluctuations, and that particles suppress the generation of the large-scale coherent vortices and simultaneously create numerous small-scale vortices in the near-wall region. Moreover, several typical transport modes of the sediment particles, such as resuspension, saltation, and rolling, are captured by tracking the trajectories of particles.

Finally, Burmasheva et al. [43] advance the understanding of how bottom conditions affect flow structure by considering exact solutions for flows of a viscous incompressible fluid with unknown free boundaries. Exact solutions are extremely insightful for understanding fundamental dynamics [44,45], and there is a known procedure for taking into account the boundary conditions for a free boundary by adding a new force to the equations of fluid motion. Fluid flows with the Rayleigh friction force are considered. Accounting for this force makes it possible to consider large-scale currents of the world's oceans with an unknown function for the bottom and for the boundary of water with the atmosphere. The class of exact solutions announced in this Special Issue will be useful for modeling and simulating fluid flows in the ocean and thin layers with unknown boundaries.

Ultimately, geophysical boundary layer interactions are at the cutting edge of environmental science. It is my hope that this Special Issue both advances the knowledge pool and offers new avenues of research for the larger scientific community.

Conflicts of Interest: The author declares no conflict of interest.

References

1. Charney, J.G. The gulf stream as an inertial boundary layer. *Proc. Natl. Acad. Sci. USA* **1955**, *41*, 731–740. [CrossRef] [PubMed]
2. Stommel, H. *The Gulf Stream: A Physical and Dynamical Description*; Cambridge University Press: Cambridge, UK, 1965.
3. Stommel, H.; Yoshida, A. *Kuroshio, Its Physical Aspects*; University of Tokyo Press: Tokyo, Japan, 1972.
4. Hidy, G.M. A view of recent air-sea interaction research. *Bull. Am. Meteorol. Soc.* **1972**, *53*, 1083–1102. [CrossRef]
5. Lyu, M.; Potter, H.; Collins, C.O. The Impacts of Gustiness on Air–Sea Momentum Flux. *Fluids* **2021**, *6*, 336. [CrossRef]
6. Potter, H. Swell and drag coefficient. *Ocean. Dyn.* **2015**, *65*, 375–384. [CrossRef]
7. Quintana, A.; Torres, H.S.; Gomez-Valdes, J. Dynamical Filtering Highlights the Seasonality of Surface-Balanced Motions at Diurnal Scales in the Eastern Boundary Currents. *Fluids* **2022**, *7*, 271. [CrossRef]
8. Kuehl, J.; Sheremet, V.A. Effect of the Coastline Geometry on the Boundary Currents Intruding through the Gap. *Fluids* **2022**, *7*, 71. [CrossRef]
9. Sheremet, V.A. Hysteresis of a Western Boundary Current Leaping across a Gap. *J. Phys. Oceanogr.* **2001**, *31*, 1247–1259. [CrossRef]
10. Sheremet, V.A.; Kuehl, J. Gap-Leaping Western Boundary Current in a Circular Tank Model. *J. Phys. Oceanogr.* **2007**, *37*, 1488–1495. [CrossRef]
11. Song, C.; Yuan, D.; Wang, Z. Hysteresis of a periodic or leaking western boundary current flowing by a gap. *Acta Oceanol. Sin.* **2019**, *38*, 90–96. [CrossRef]
12. McMahon, C.W.; Kuehl, J.J.; Sheremet, V.A. A viscous, two-layer western boundary current structure function. *Fluids* **2020**, *5*, 63. [CrossRef]
13. McMahon, C.W.; Kuehl, J.J.; Sheremet, V.A. Dynamics of Gap-leaping Western Boundary Currents with Throughflow Forcing. *J. Phys. Oceanogr.* **2021**, *51*, 2243–2256. [CrossRef]

14. Mei, H.; Qi, Y.; Qiu, B.; Cheng, X.; Wu, X. Influence of an Island on Hysteresis of a Western Boundary Current Flowing across a Gap. *J. Phys. Oceanogr.* **2019**, *49*, 1353–1366. [CrossRef]
15. National Academies of Sciences, Engineering, and Medicine; Gulf Research Program; Committee on Advancing Understanding of Gulf of Mexico Loop Current Dynamics. *Understanding and Predicting the Gulf of Mexico Loop Current: Critical Gaps and Recommendations*; National Academies Press: Washington, DC, USA, 2018.
16. Yuan, D.; Song, X.; Yang, Y.; Dewar, W.K. Dynamics of Mesoscale Eddies Interacting with a Western Boundary Current Flowing by a Gap. *J. Geophys. Res. Ocean.* **2019**, 014949. [CrossRef]
17. Sheremet, V.A.; Kan, A.A.; Kuehl, J. Multiple Equilibrium States of the Gulf of Mexico Loop Current. *Ocean. Dyn.* **2022**, *72*, 731–740. [CrossRef]
18. Stommel, H.; Arons, A.B.; Faller, A.J. Some examples of stationary flow patterns in bounded basins. *Tellus* **1958**, *10*, 179–187. [CrossRef]
19. Stommel, H.; Arons, A.B. On the abyssal circulation of the world ocean-l. Stationary planetary flow patterns on a sphere. *Deep Sea Res.* **1959**, *6*, 140–154. [CrossRef]
20. National Ocean Partnership Program. Available online: https://nopp.org/projects/nopp-project-table/ (accessed on 9 October 2023).
21. Polzin, K.L.; Wang, B.; Wang, Z.; Thwaites, F.; Williams, A.J. Moored Flux and Dissipation Estimates from the Northern Deepwater Gulf of Mexico. *Fluids* **2021**, *6*, 237. [CrossRef]
22. Garret, C.; MacCready, P.; Rhines, P. Boundary mixing and arrested Ekman layers: Rotating stratified flow near a sloping boundary. *Annu. Rev. Fluid Mech.* **1993**, *25*, 291–323. [CrossRef]
23. Polzin, K.L.; McDougall, T.J. Mixing at the ocean's bottom boundary. In *Ocean Mixing*; Elsevier: Amsterdam, The Netherlands, 2022.
24. Pollard, R.T.; Rhines, P.B.; Thompson, T. The deepening of the wind-mixed layer. *Geophys. Fluid Dyn.* **1973**, *4*, 381–404. [CrossRef]
25. Brink, K.H.; Lentz, S.J. Buoyancy arrest and bottom Ekman transport. Part I: Steady flow. *J. Phys. Oceanogr.* **2010**, *40*, 621–635. [CrossRef]
26. Thomas, L.N.; Taylor, J.R.; Ferrari, R.; Joyce, T.M. Symmetric instability in the Gulf Stream. *Deep Sea Res. Part Top. Stud. Oceanogr.* **2013**, *91*, 96–110. [CrossRef]
27. Qu, L.; Thomas, L.N.; Hetland, R.D.; Kobashi, D. Mixing Driven by Critical Reflection of Near-Inertial Waves over the Texas–Louisiana Shelf. *J. Phys. Oceanogr.* **2022**, *52*, 2891–2906. [CrossRef]
28. Ruan, X. Note on the Bulk Estimate of the Energy Dissipation Rate in the Oceanic Bottom Boundary Layer. *Fluids* **2022**, *7*, 82. [CrossRef]
29. Taylor, G.I. Tidal friction in the Irish Sea. *Philos. Trans. R. Soc. Lond. Ser. Contain. Pap. Math. Phys. Character* **1920**, *220*, 1–33.
30. Ruan, X.; Thompson, A.F.; Taylor, J.R. The evolution and arrest of a turbulent stratified oceanic bottom boundary layer over a slope: Upslope regime and PV dynamics. *J. Phys. Oceanogr.* **2021**, *51*, 1077–1089. [CrossRef]
31. Nagano, A.; Hasegawa, T.; Ariyoshi, K.; Matsumoto, H. Interannual Bottom-Intensified Current Thickening Observed on the Continental Slope Off the Southeastern Coast of Hokkaido, Japan. *Fluids* **2022**, *7*, 84. [CrossRef]
32. Nagano, A.; Ichikawa, K.; Ichikawa, H.; Yoshikawa, Y.; Murakami, K. Large ageostrophic currents in the abyssal layer southeast of Kyushu, Japan, by direct measurement of LADCP. *J. Oceanogr.* **2013**, *69*, 259–268. [CrossRef]
33. Nagano, A.; Wakita, M. Wind-driven decadal sea surface height and main pycnocline depth changes in the western subarctic North Pacific. *Prog. Earth Planet* **2019**, *6*, 59. [CrossRef]
34. Nagano, A.; Wakita, M.; Fujiki, T.; Uchida, H. El Niño Vertical Mixing Enhancement under the Winter Mixed Layer at Western Subarctic North Pacific Station K2. *J. Geophys. Res.* **2021**, *126*, e2020JC016913. [CrossRef]
35. Hasegawa, T.; Nagano, A.; Matsumoto, H.; Ariyoshi, K.; Wakita, M. El Niño-related sea surface elevation and ocean bottom pressure enhancement associated with the retreat of the Oyashio southeast of Hokkaido, Japan. *Mar. Geophys. Res.* **2019**, *40*, 505–512. [CrossRef]
36. Hasegawa, T.; Nagano, A.; Ariyoshi, K.; Miyama, T.; Matsumoto, H.; Iwase, R.; Wakita, M. Effect of Ocean Fluid Changes on Pressure on the Seafloor: Ocean Assimilation Data Analysis on Warm-core Rings off the Southeastern Coast of Hokkaido, Japan on an Interannual Timescale. *Front. Earth Sci.* **2021**, *9*, 600930. [CrossRef]
37. Kozelkov, A.; Tyatyushkina, E.; Kurulin, V.; Kurkin, A. Influence of Turbulence Effects on the Runup of Tsunami Waves on the Shore within the Framework of the Navier–Stokes Equations. *Fluids* **2022**, *7*, 117. [CrossRef]
38. Gundersen, D.; Blois, G.; Christensen, K.T. Flow past mound-bearing impact craters: An experimental study. *Fluids* **2021**, *6*, 216. [CrossRef]
39. Blois, G.; Bristow, N.; Kim, T.; Best, J.; Christensen, K. Novel Environment Enables PIV Measurements of Turbulent Flow around and within Complex Topographies. *J. Hydraul. Eng.* **2020**, *146*, 04020033. [CrossRef]
40. Hu, L.; Dong, Z.; Peng, C.; Wang, L.P. Direct Numerical Simulation of Sediment Transport in Turbulent Open Channel Flow Using the Lattice Boltzmann Method. *Fluids* **2021**, *6*, 217. [CrossRef]
41. Gao, H.; Li, H.; Wang, L.P. Lattice Boltzmann simulation of turbulent flow laden with finite-size particle. *Comput. Math. Appl.* **2013**, *65*, 194–210. [CrossRef]
42. Peng, C. Study of Turbulence Modulation by Finite-Size Solid Particles with the Lattice Boltzmann Method. Ph.D. Thesis, University of Delaware, Newark, DE, USA, 2018.

43. Burmasheva, N.; Ershkov, S.; Prosviryakov, E.; Leshchenko, D. Exact Solutions of Navier–Stokes Equations for Quasi-Two-Dimensional Flows with Rayleigh Friction. *Fluids* **2023**, *8*, 123. [CrossRef]
44. Csanady, G.T. The arrested topographic wave. *J. Phys. Oceanogr.* **1978**, *8*, 47–62. [CrossRef]
45. Kuehl, J.J. An analytic solution for barotropic flow along a variable slope topography. *Geophys. Res. Lett.* **2014**, *41*, 7591–7594. [CrossRef]

fluids

MDPI

Article

The Impacts of Gustiness on Air–Sea Momentum Flux

Meng Lyu [1,*], Henry Potter [1] and Clarence O. Collins [2]

[1] Department of Oceanography, Texas A&M University, College Station, TX 77843, USA; hpotter@tamu.edu
[2] Coastal and Hydraulics Laboratory, U.S. Army Engineering Research and Development Center, Duck, NC 27949, USA; Clarence.O.Collins@usace.army.mil
* Correspondence: meng@tamu.edu

Abstract: The exchange of momentum across the air–sea boundary is an integral component of the earth system and its parametrization is essential for climate and weather models. This study focuses on the impact of gustiness on the momentum flux using three months of direct flux observations from a moored surface buoy. Gustiness, which quantifies the fluctuations of wind speed and direction, is shown to impact air–sea momentum fluxes. First, we put forward a new gustiness formula that simultaneously evaluates the impact of fluctuations in wind direction and speed. A critical threshold is established using a cumulative density function to classify runs as either gusty or non-gusty. We find that, during runs classified as gusty, the aerodynamic drag coefficient is increased up to 57% when compared to their non-gusty counterparts. This is caused by a correlated increase in vertical fluctuations during gusty conditions and explains variability in the drag coefficient for wind speeds up to 20 m/s. This increase in energy is connected with horizontal fluctuations through turbulent interactions between peaks in the turbulent spectra coincident with peaks in the wave spectra. We discus two potential mechanistic explanations. The results of this study will help improve the representation of gustiness in momentum flux parameterizations leading to more accurate ocean models.

Keywords: gustiness; momentum flux; drag coefficient; air–sea interaction; marine boundary layer

Citation: Lyu, M.; Potter, H.; Collins, C.O. The Impacts of Gustiness on Air–Sea Momentum Flux. *Fluids* **2021**, *6*, 336. https://doi.org/10.3390/fluids6100336

Academic Editors: Pavel S. Berloff, Joseph J. Kuehl, Pengfei Xue and Fabrice Veron

Received: 1 May 2021
Accepted: 16 September 2021
Published: 22 September 2021

1. Introduction

In the marine boundary layer, the ocean is tightly coupled to the atmosphere through the wind stress τ. The wind stress is a quantification of the momentum flux across the air–sea interface which is important for many processes such as wave growth and breaking [1–3], aerosol production [4], atmospheric and oceanic circulation (e.g., [5–7]), global climate [8], and upper ocean mixing (e.g., [9,10]). The momentum flux is also a key component of tropical cyclone intensity [11].

In the constant-flux layer the total wind stress can be decomposed into three parts:

$$\tau = \tau_t + \tau_w + \tau_v \quad (1)$$

Here, τ_t is the turbulent stress, τ_w the wave-induced stress, and τ_v the viscous stress [12]. τ_v is caused by the differential of wind and sea surface current speed within the viscous sub-layer which has a thickness on the order of 10^{-5} m, much thinner than the wave-induced boundary layer [12,13], and is negligible away from the sea surface. τ_w occurs in the wave-boundary layer, within which air flow is influenced by waves [14]. The wave-boundary layer height has been shown to depend on wind speed [15,16] and sea state [17], and is predicted to be order 1 m for pure wind sea conditions in [18]. It has also been demonstrated that the wave induced stress is less than 5% of the total stress at the height of 1 m, and less than 1% at 3 m. Previous experiments have established the practice of making measurements 3–4 m above the sea surface e.g., [19,20] where viscous

and wave-induced stress were deemed negligible. (i.e., $\tau \approx \tau_t \gg \tau_w \gg \tau_v$). Under such conditions, turbulent fluxes approximate the total momentum flux, e.g., [21]:

$$\tau_t \approx \tau_t = -\rho\overline{u'w'} - \rho\overline{v'w'} \tag{2}$$

Here $u', v',$ and w', are velocity in the along, cross, and downwind directions, respectively, with primes denoting the fluctuating component and overbar representing time average (O~30 min). Air–sea coupling within the marine boundary layer is widely parameterized by the wind stress equation:

$$\tau = \rho * u_*^2 = \rho C_d U_{10}^2 \tag{3}$$

where u_* is the shear or friction velocity of the wind at the sea surface, ρ is the air density, C_d is the drag coefficient, and U_{10} is the wind speed at a reference height of 10 m. Combining Equations (2) and (3), we arrive at C_d, calculated from direct measurements

$$C_d = \frac{\sqrt{\overline{(-u'w')}^2 + \overline{(-v'w')}^2}}{U_{10}^2} \quad . \tag{4}$$

Because of the isolation and harsh environmental conditions, measuring fluxes at sea is very challenging and expensive, especially at high wind speeds. As such, it is common for the momentum flux to be determined instead by using the nondimensional drag coefficient as a function of the mean wind speed. Since the drag coefficient is widely adopted and used in lieu of direct flux measurements when quantifying air–sea momentum exchange (e.g., [22,23]), we focus on the impact of gustiness on the drag coefficient such that results have direct implications for Earth system models.

Many studies have shown that C_d increases approximately linearly with wind speed [21,24,25]. However there remains substantial variability in C_d. Several secondary variables have been shown to affect C_d, including sea state [19,26–29], currents [6], air–sea temperature difference and stability [3,30], and gustiness [30,31].

Many studies have quantified the influence of sea state on C_d. Results show that wave age C_p/U_{10}, where C_p is the phase speed of the peak wave frequency, is well correlated to C_d [24,27,32,33], and C_d tends to be higher in young seas, $C_p/U_{10} < 1.5$. The association between wave age and C_d is not surprising given that young waves are steeper and rougher than old waves [29,34,35]. Also based on the association between wave age and drag, Oost et al. [36] found a reliable relationship between for C_p and ocean roughness.

The impacts of swell on C_d have also been extensively investigated with mixed results. For example, Dobson et al. [37] found no evidence that swell influences C_d, but Drennan et al. [38] observed reduced wind stress in the presence of swell. This finding was supported by the finds of Potter [39], who determined that swell can reduce C_d up to 37% due to the reduced turbulent energy around the swell frequency. In contrast, Drennan et al. [40] found that both crossing- and opposing-swell significantly increase C_d, and Vincent et al. [41] showed an increase in drag due to increased energy in the high-frequency waves relative to pure wind seas, consistent with their previous work [42]. Increased drag coefficient in the left-rear of a tropical cyclone where conditions are thought to be predominantly crossing and opposing-swell, has also been shown [28].

Surface currents have been shown to reduce C_d, especially when the current is aligned with the wind [30]. Kara, Metzger, and Bourassa [7] reported that C_d can be reduced over 10% in the tropical Pacific Ocean due to currents being in line with the prevailing winds. Furthermore, a numerical modelling study of an idealized typhon showed that surface current can reduce the momentum fluxes in the right-rear typhoon quadrant about 6% in [5]. In contrast, Wüest and Lorke [43] found that currents in the Kuroshio Extension have very little influence on C_d. Currents can also affect the momentum fluxes in indirectly; Kenyon and Sheres [44] found that strong current gradients impact the surface gravity wave field which can then affect air–sea momentum fluxes.

The stability of atmosphere influences C_d according to Monin–Obukhov similarity theory [45–49]. Monin and Obukhov [50] put forward the Obukhov length to describe the air–sea fluxes processes.

$$L = -\frac{v_*^3}{k * \left(\frac{g}{T_0}\right)\left(\frac{q}{C_t \rho}\right)} \tag{5}$$

where k is the von Karman constant, T_0 is surface temperature, g is gravity acceleration, v_* is friction velocity, q is kinematic heat flux, C_t is specific heat, and ρ is air density. The Obukhov length accounts for the relationship between sea surface temperature, specific heat, air density, heat flux, and friction velocity. In light winds, the momentum fluxes are sensitive to the stability of the atmosphere, with increased flux for unstable conditions [51].

While much attention has been given to sea state, currents, and atmospheric stability, there are few studies that directly address the effect of gustiness on C_d. The importance of accounting for gustiness when estimating momentum fluxes was first addressed by Janssen [52], who believed that the friction velocity should be related to both the mean and standard deviation of wind speed. Miles and Ierley [53], using a theoretical model, found that, under some circumstances, 20–30% more energy is transferred to the ocean during gusty conditions but that a reduction in the stress is also possible. Abdalla and Cavaleri [54] used a model to compare the wave field under normal and gusty winds and found that wave height is increased under gusty conditions, implying increased momentum flux. Ponce and Ocampo–Torres [55] also showed that wind speed variability increases wave height while Pleskachevsky et al. [56] remotely observed higher wave height under the influences of gustiness. Annenkov and Shrira [57] studied wave responses to different gustiness regimes using an idealized numerical model. They found that gustiness can impact growth rate during wave development but had little impact as waves approached full development. Uz et al. [58] found that decreasing winds had higher wind stress than the increasing winds for any given wind speed, which is mainly caused by the delayed response of short wind waves to the modulated wind forcing.

Previous research notwithstanding, it is very difficult to account for the impact of gustiness on momentum flux because typical wind speed data, whether extracted from satellite remote sensing, collected in situ, or model derived, are produced as an average over space and/or time and so high frequency fluctuations are unknown. As such, it is difficult to incorporate gustiness information into C_d parameterizations. Babanin and Makin [31] addressed this by developing a method to estimate maximum gustiness using U_{10}, which can be then used to estimate the contribution of gustiness to C_d for any given wind speed. In their study, gustiness was quantified using the mean and standard deviation of wind speed calculated over 30 min:

$$G = std(U_{10})/\overline{U_{10}} \tag{6}$$

Following Babanin and Makin [59], Ting et al. [60] found that gustiness can increase scatter in C_d, and used a scale analysis based on the equation of motion to determine that wind stress was proportional to gustiness. They speculated that the variability in the drag coefficient was caused by gustiness through distortion of the air–sea boundary layer structure. The Coupled Ocean-Atmosphere Response Experiment (COARE) algorithm [30] represents gustiness as boundary layer–scale eddies and is more akin to vertical thermal stability rather than horizontal wind fluctuations.

In this study, we focus on the influence of gustiness on the momentum flux. We introduce a gustiness formula that is sensitive to the fluctuations of both wind speed and direction. The metric captures variation within scales of 0.01–1 Hz. We apply the new formula to data from the Impact of Typhoons on the Ocean in the Pacific (ITOP) experiment [61]. Our results indicate that gusty periods exhibit higher C_d than predicted by the linear wind speed parameterization [25]. We also used a scaled Miyake-Cospectrum [62] to explore the momentum fluxes transferred into the ocean. This Miyake-Cospectrum is normalized by wind speed, which is helpful for comparing the gustiness influences under

different mean wind speeds. We ultimately conclude that gustiness is important to C_d, accounting for about 57% of the variability in C_d. We also find that the cospectra of the momentum flux is proportional to the gustiness. When winds are gusty, we find an associated increase in energy in the cospectra.

2. Data and Methods

2.1. Data

Data used in this study were collected during the Impact of Typhoons on the Ocean in the Pacific (ITOP) experiment [61]. Data were collected between August and December 2010, from an instrumented Extreme Air–Sea Interaction (EASI) buoy (Drennan et al. [63]) deployed in the Philippine Sea approximately 750 km east of Taiwan. Direct fluxes were measured onboard with simultaneous mean parameters including air and ocean temperature, humidity, and atmospheric pressure. The EASI buoy, which was based on the hull of a 6-m Navy Oceanographic Meteorological Automatic Device (NOMAD), also measured directional wave spectra that were produced over 30 min, as was wind speed [64]. Several studies have previously used data collected by EASI during ITOP (e.g., [9,27,39,63,65]) and provide extensive information about the experiment, instrumentation, and data processing and quality. Here, we only reproduce information about the wind sensors and associated processing methods.

The EASI buoy was equipped with two Gill R2A sonic anemometers. However, due to severe weather, only one R2A anemometer collected reliable data. The sampling frequency of the wind anemometer was 20 Hz with runs of 30 min, which was found suitable for collecting all turbulent scales [66]. The anemometer was positioned 5.45 m above mean sea level and away from the buoy structure such that flow distortion was negligible. Two motion packages in the buoy measured six degrees of freedom of motion along with the compass bearing. The motion of the platform was accounted for when calculating the wind velocity in accordance with the methods by [67]. Following motion-correction, a quality control procedure removed spikes in the 20 Hz u, v, and w time series [66]. Ogives were calculated and it was revealed that the scales of 0.01–1.0 Hz were adequate to fully characterize momentum flux, as expected from universal curves [62]. Next, u, v, and w were rotated according to the mean wind vector so that the w' was around 0 and u pointed towards the mean wind direction, thereby $mean(v) = 0$. These data were then used to calculate C_d following Equation 4. Log layer theory was used to adjust the value of C_d to the equivalent measured at 10 m in neutral conditions, which is referred to as C_{d10N}.

2.2. Gustiness Formulation

The Babanin and Makin [31] equation for gustiness (Equation (5)) quantifies the fluctuation of wind speed but does not consider wind direction variability. We show that directional variability can also increase variance in both u and v, and therefore must be part of the gustiness formulation in order to more fully characterize wind variability. For example, if wind speed is constant, the runs with unstable direction will contain more turbulent energy than runs with stable direction. As such, we put forward a new gustiness formula, G_A, (Equation (7)), to account for fluctuations in both wind speed and direction.

$$G_A = std\left(u' + v'\right)/U_{10} \tag{7}$$

Equation (7) can be expanded as below:

$$std\left(u' + v'\right)/U_{10} = \sqrt{var(u') + var(v') + 2cov(u', v')}/U_{10} \tag{8}$$

The $cov(u', v')$ term represents the influence of changing wind direction, and it reduces to 0 when the wind direction is stable. Supposing at one moment that the mean wind direction has turned about x degrees, it will add an extra fluctuation $(u', v') \sim U{\cdot}(1 - cosx, sinx)$ to the original wind vector. A change in wind direction projects an extra velocity onto the (u', v'). It can be seen that the added fluctuation $(U - Ucosx, Usinx)$

is correlated, which is one source of the covariance term. One thing to note, $cov(u', v')$ can be underestimated to some extent given that some portions of (u', v') are still independent, similar to Brownian motion [68], when the wind direction is changing. When $cov(u', v') \neq 0$, observation samples of (u', v') are distributed symmetrically but the main axis is not along the x or y axis. Graphical representations of $cov(u', v') = 0$ and $cov(u', v') \neq 0$ are shown in Figure 1.

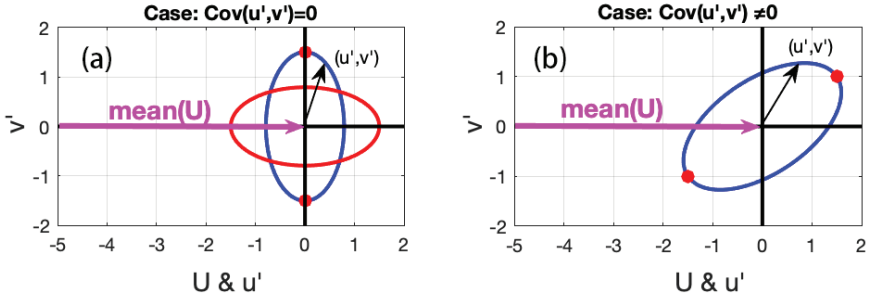

Figure 1. Graphical representation of two cases: $cov(u', v') = 0$. (**a**) and $cov(u', v') \neq 0$. (**b**). The pink vector represents the mean wind speed (along x). The red or blue ellipse represents how the observations of u', v' can be distributed. The black arrows represent possible individual observations of wind fluctuation. The red dots mark the ends of the long axis of the ellipse.

To better characterize G_A, sensitivity to sampling frequency was explored. Figure 2 shows the standard deviation of $u' + v'$ for an arbitrary run as a function of sampling frequency. When the frequency reaches approximately 1 Hz, $std(u' + v')$ converges upon a constant value, in this case 1.83. This is a typical result (though other runs converge upon different values), indicating that our sampling frequency of 20 Hz is more than adequate to obtain a stable standard deviation of u' and v'.

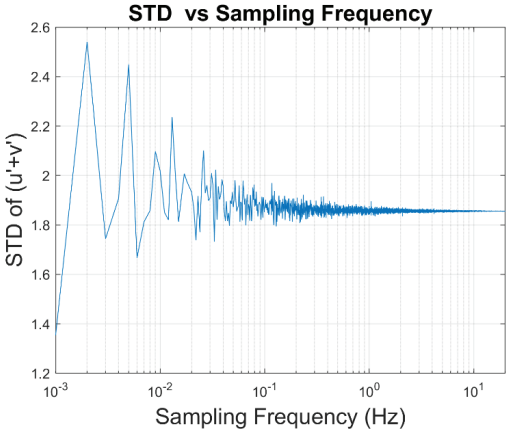

Figure 2. Stand deviation of $(u' + v')$, as a function of sampling frequency for an arbitrary 30-min run.

Our definition of gustiness is sensitive to run length because of the increased potential for wind direction change with time. Thirty-minute run-time is a compromise between a length adequate to capture all turbulent length scales (e.g., [19,37,63]) and short enough such that stationarity is not violated. This record length was used in many previous studies focused on C_d (e.g., [19,21,24,38,66,69]), and, furthermore, 30 min is a typical time domain used by air–sea coupled climate or hurricane models (e.g., [70,71]). Hence, by

adopting a 30 min sampling period, we seek to maximize the applicability of the results to future research.

3. Results

Figure 3 shows the times series of wind speed (U_{10N}) and gustiness G_A. High G_A can be attributed to the fluctuation of wind speed and direction or low U_{10N}, which increases G_A in Equation (7).

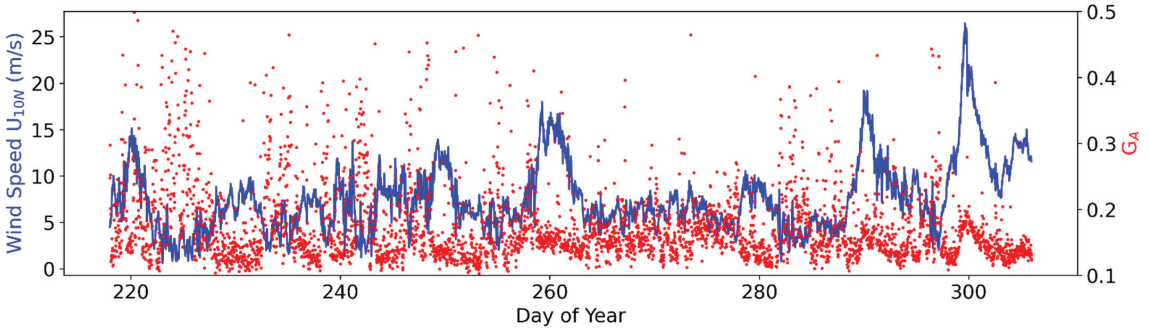

Figure 3. U_{10N} (blue) and G_A (red) during the experiment.

Figure 4 shows the cumulative probability function of G_A for all the runs to help define a limit above which the wind is gusty. G_A of gusty and not-gusty runs is calculated via Equation (6). A value of 0.165 was chosen for selecting gusty runs and represents the time when the CPF is 50%.

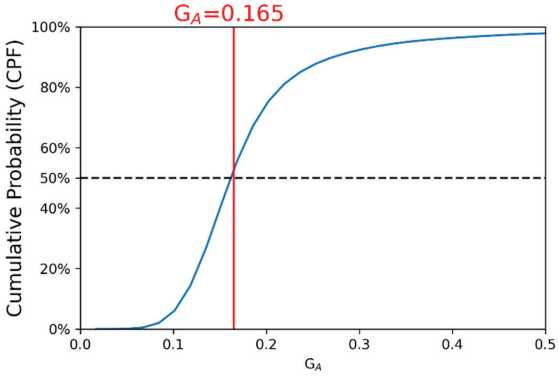

Figure 4. Cumulative probability function of G_A for entire data set. $G_A > 0.165$ means the wind is gusty. Otherwise, the wind is not gusty. The value 0.165 is chosen for best performance. The red line is $G_A = 0.165$. The black dash line is $CPF = 50\%$.

Based on the formula for G_A, Figure 5 shows C_{d10N} as a function of U_{10N}. Each data point is color coded by gustiness, with dark green indicating $G_A \leq 0.165$. When the winds are not gusty, a clear linear relationship between C_{d10N} & U_{10N} emerges. This relationship is similar to the linear empirical equation proposed by [25,30]. This suggests that these widely used linear equations were established based on data collected during relatively wind speed stable conditions. Most gusty points are over this linear relationship, suggesting that gusty conditions are generally associated with an increase in momentum flux. From the error bar plot, for moderate winds (5–12 m/s), we find that the variation in C_{d10N} of winds can be reduced by as much as 57% by removing the gusty runs.

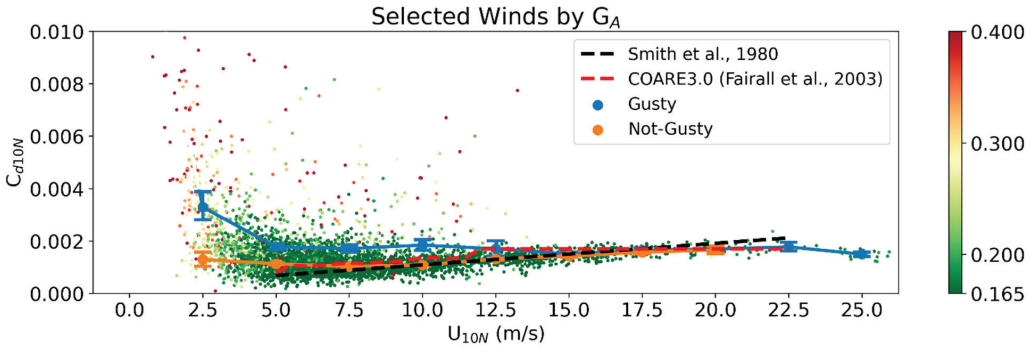

Figure 5. C_d of gusty winds (red & yellow points) and not-gusty winds (green points) selected by G_A. Non-gusty winds are selected by the condition $G_A \leq 0.165$ and marked as green. The blue line is the averaged C_d for $G_A \leq 0.165$ with error bars denoting 95% confidence interval binned every 2.5 m/s. The orange line is the averaged C_d for $G_A > 0.165$ with error bars also denoting 95% confidence interval binned every 2.5 m/s. The black dash line is the C_{d10N} predicted by [25]. The red line is C_{d10N} predicted by COARE 3.0 algorithm [30].

Figure 6 shows C_{d10N} vs. U_{10N}. Points are colored by the covariance term, $\sqrt{|cov(u',v')|}/U_{10}$. This term can be attributed to the changing wind direction, since a change in direction (θ) will add extra correlated oscillation $u' \sim U_{10} \cdot (1 - cos\theta)$, $v' \sim U_{10} \cdot sin\theta$ to the fluctuation. The covariance term will be increased when the direction is turning. Therefore, Figure 6 indicates that changing wind direction could play an important role in contributing to the gustiness, and thus C_d. In another words, some scatter in C_d, or increased gustiness, can be explained by changes in direction. To parallel this viewpoint, the data are plotted again (Figure 7), but are now identified based on the stability of their wind speed and direction. Here, we used $std(u) > 1$m/s and $std(\theta) > 7^\circ$ to identify runs that were considered either wind speed unstable or wind direction unstable. Using these values results in 25% and 31% of data characterized as gusty due to variability in speed and direction, respectively. For comparison, if we set the threshold to 0.5, 2, or 3 m/s, the percentage of gusty data would be 78%, 4%, 0.7%, respectively. Setting the threshold to 3, 5, or 10° would result in 100%, 82%, and 11%, respectively, classed as gusty. Most importantly, Figure 7 shows that deviations in both speed and direction are important considerations when quantifying gustiness. Notably, directional deviations identify much of the scatter in the $U_{10N} - C_{d10N}$ relationship at low to moderate wind speeds that cannot be captured when considering fluctuations in wind speed alone. Furthermore, we avoid another issue with identifying gustiness based on wind speed, which is that all data above ~15 m s^{-1} are classified as gusty because, inherently, $std(u)$ increases with U.

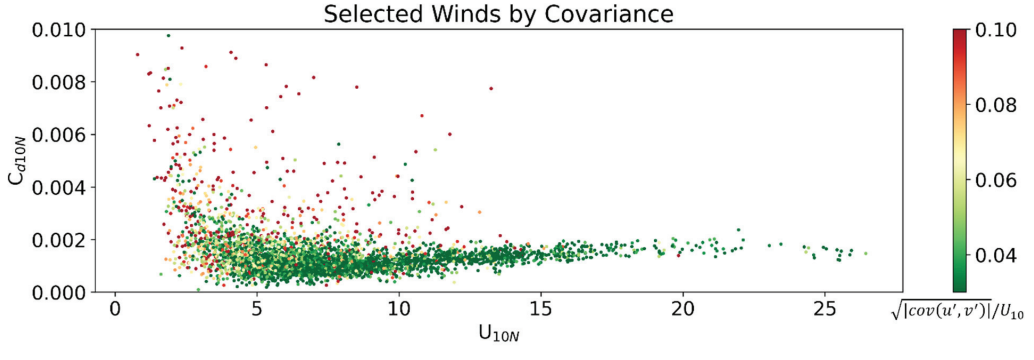

Figure 6. C_d of gusty winds selected by the covariance term $\sqrt{|cov(u',v')|}/U_{10}$.

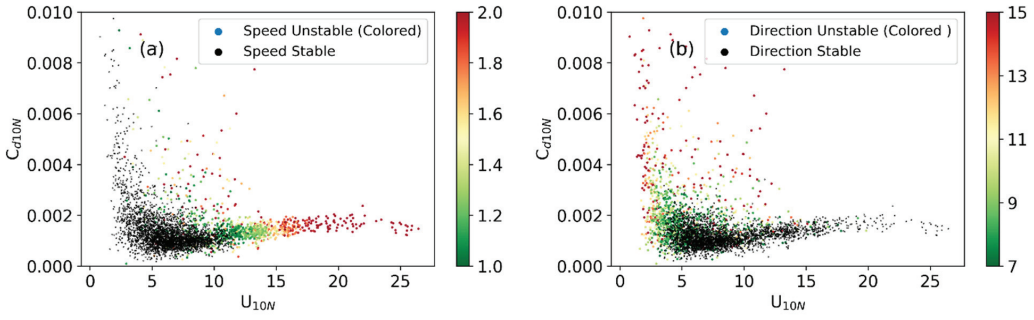

Figure 7. C_{d10N} as a function of U_{10N}. Left panel (**a**): Runs with $std(u) \leq 1$ m/s are marked as black, runs with $std(u) > 1$ m/s are colored by $std(u)$. Right panel (**b**): Runs with $std(\theta) \leq 7^{\circ}$) are marked as black, runs with $std(\theta) > 7^{\circ}$ are colored by $std(\theta)$.

We find that variations in both wind speed and direction can have significant influences on C_d. In fact, the stability of wind direction is potentially a better metric than the stability of wind speed (Figure 7). When wind direction is stable, a linear relationship suggested by previous studies (e.g., [21,24,66]) between C_{d10N} and U_{10N} emerges. In contrast to $cov(u', v')$, speed stability does not correlate with variation in C_{d10N} at moderate wind speeds (5–12 m/s). This implies that direction is more effective in explaining the variation in C_{d10N}.

4. Discussion

4.1. Gustiness and Vertical Oscillation

Next, we examine in detail the difference between a gusty run and a not-gusty run. Figure 8 shows a histogram of the distribution of u'& v' over 30 min for two different runs. These runs are controlled for wind speed, i.e., both have $U_{10N} = 10$ m/s. For Figure 8a, $G_A = 0.12$ (low gustiness), and for Figure 8b, $G_A = 0.21$ (high gustiness). In each panel there are 36,000 data points (i.e., 30 min * 60 s * 20 Hz) of (u', v') that distribute around (0,0) in a cloud of points. In Figure 8a, the data are distributed symmetrically, forming a circle, and the histogram is symmetric, which indicates the wind direction remained relatively stable. In Figure 8b, the data are asymmetrically distributed over a larger area in u', v' space, skewed towards the lower-left. In this case, the distribution is an ellipse and the major axis is rotated away from the wind direction, indicating that the direction was changing over the duration of the run. In Figure 8c, the directions of the gusty and non-gusty runs are shown. We can see that the direction of the run in Figure 8b has changed about 20 degrees over 30 min, while the direction of the not-gusty run in Figure 8a has a negligible trend.

Note that the mean of $|w'|$ in Figure 8a,b is larger during the gusty run than the non-gusty. This suggests a stronger vertical oscillation in the gusty runs which may account for the observed higher C_d. To explore this further, we plot the mean of $|w'|$ in Figure 9 as a function of wind speed for all our data. This shows that gusty periods tend to have higher $|w'|$ compared to periods when the wind speed and direction remain more stable, as determined using $G_A = 0.165$. This indicates a stronger oscillation in the vertical direction during gusty conditions which, when correlated with the u', v', increases C_d. For moderate winds speeds, $|w'|$ is 30~50% larger for gusty than non-gusty periods. Hence, higher gustiness can inspire a stronger vertical oscillation, which transports the extra energy across the air–sea interface.

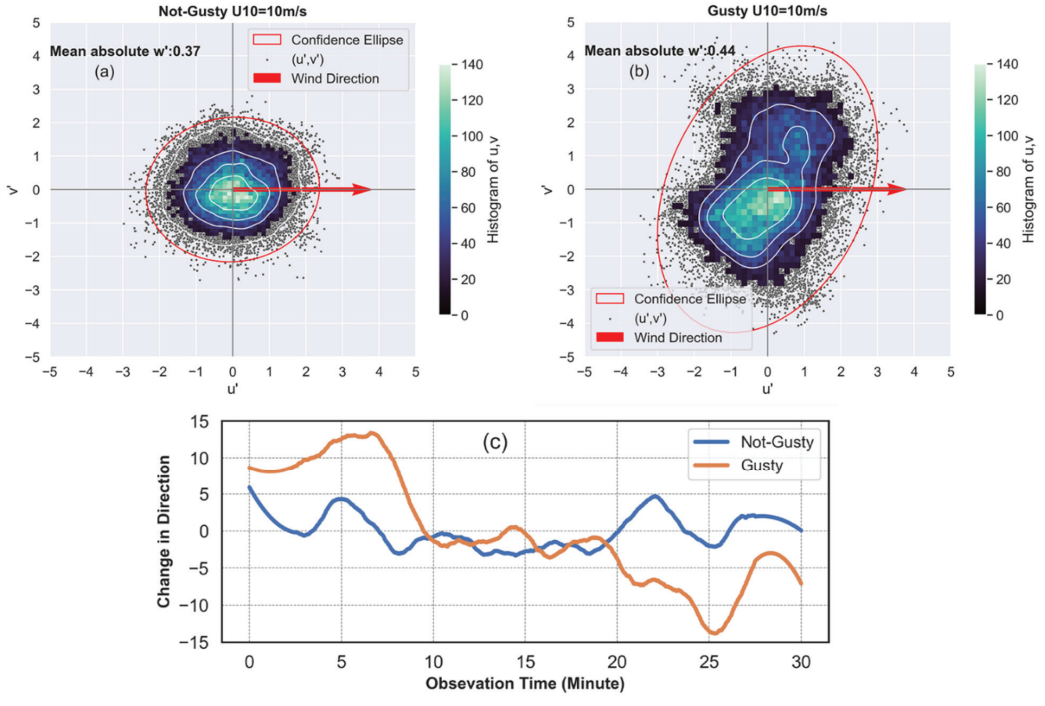

Figure 8. (**a**,**b**) are (u', v') scatter plots of gusty (**a**) and not-gusty (**b**) runs (30 min). The (u', v') points are the measured fluctuation velocity. The red circle is the 95% confidence ellipse for these points. The color is the histogram, which means how many points are located within the colored area. Wind direction is overlaid on these two scatterplots as the red quivers. (**c**) Wind direction deviation from the mean as a function of time for the selected not-gusty and gusty runs shown in panels (**a**,**b**). Data are smoothed by 5 min with a Savitzky–Golay filter.

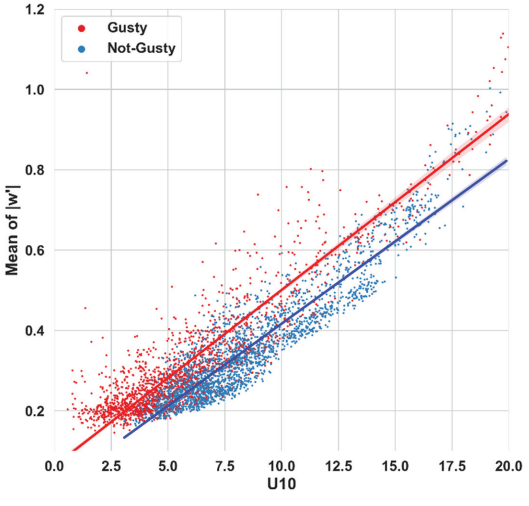

Figure 9. Mean of $|w'|$ as a function of U_{10}, red points are the gusty winds ($G_A > 0.165$), blue points are the not-gusty winds ($G_A < 0.165$). The red and blue line are best fit linear regressions with shaded area marking the 95% confidence intervals.

We now offer two potential explanations for the source $cov(u', v')$ term. The first source is that the wind direction is changing while the other is that the waves may be intermittently coupling with the gustiness. When the wind stress is between wave and wind directions, waves can explain some gustiness. These two sources may function simultaneously. We inspected many cases finding that, for a few runs, the stress direction was in between the wave direction and wind direction.

4.2. Possible Reason and Evidence for the Increased Momentum Fluxes

Figure 10 shows the mean power spectra of w' for the entire data set. Each subplot represents a different wind speed range, data are further subdivided based on gusty and non-gusty conditions. Concurrent mean wave spectra are overlaid on the turbulence spectra. Turbulent power spectra can be seen to increase with wind speed, as expected; however, in each case, the gusty conditions are always more energetic than the non-gusty runs. For the lowest wind speeds, the gusty case has 20% higher energy, increasing to over 50% at the highest wind speeds. The increases are concentrated around the peak frequency. The peak frequencies of the wave spectra are located around the peaks in the w' spectra, which shows some coupled or at least correlated behavior between turbulence and waves. This is true whether or not conditions are gusty. This analysis is repeated for u' spectra (Figure 11) and no difference is found between the u' power spectrum of gusty and not-gusty runs ($p < 0.05$). The same is true of v' (not shown), i.e., there is no marked increase in energy in horizontal velocity at ocean wave scales. This suggests that the increased C_d during gusty conditions is due to increased energy in the vertical oscillation.

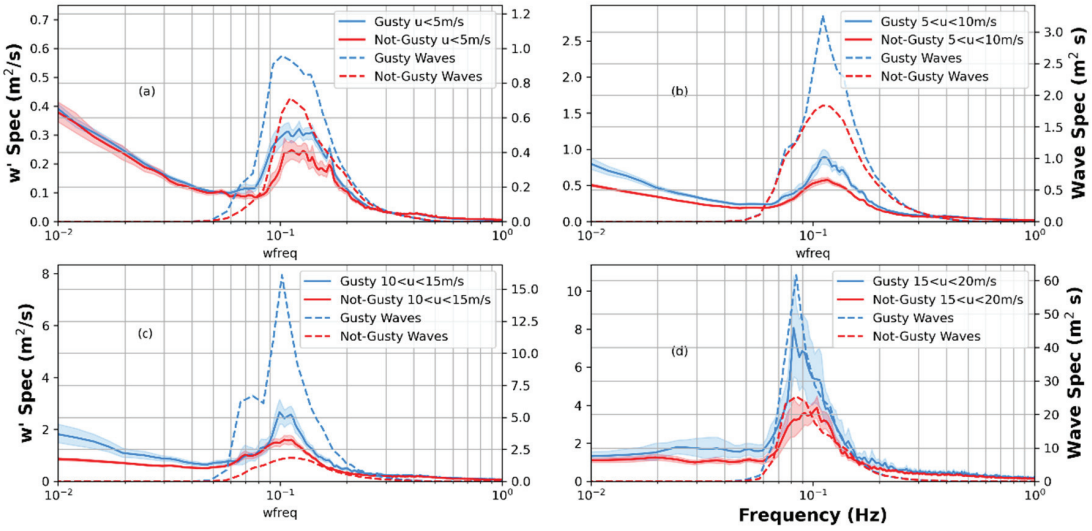

Figure 10. Mean power spectra of w' combined with wave spectra for (**a**) $0 < U < 5$ m/s, (**b**) $5 < U < 10$ m/s, (**c**) $10 < U < 15$ m/s, and (**d**) $15 < U < 20$ m/s wind speeds. The solid lines are the w' spectra (left y-axis), the dashed lines are wave spectra (right y-axis). In each panel, blue represents the gusty runs and the red represents non-gusty. Note that the limits of the y-axis in each subplot are not the same. Shaded area is 95% confidence interval for the w' spec.

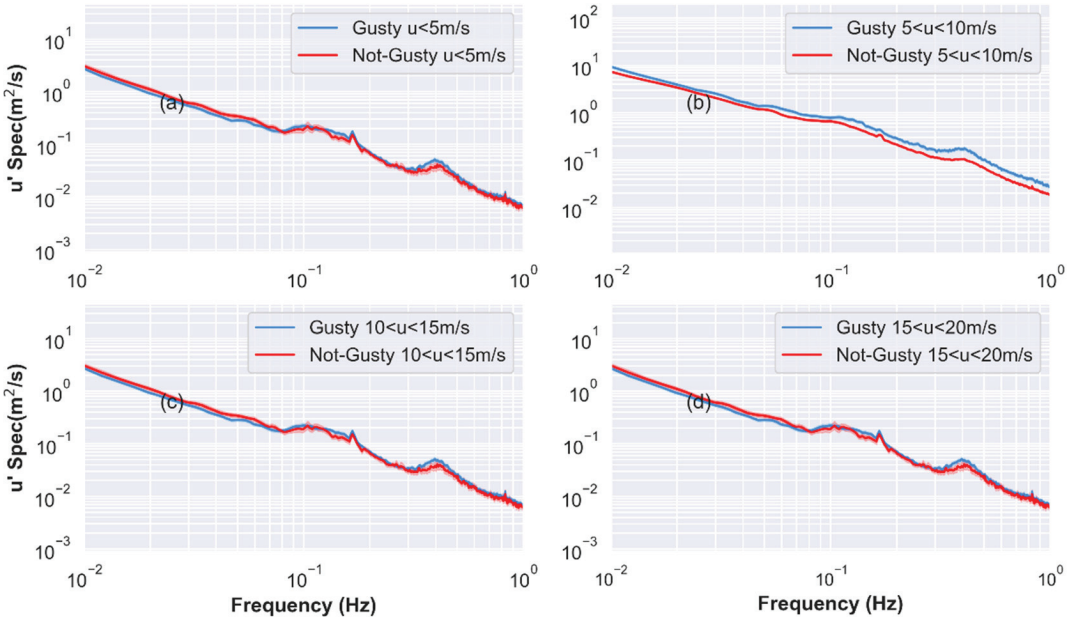

Figure 11. Power spectrum of u' under the same wind conditions. (**a**) $0 < U < 5$ m/s, (**b**) $5 < U < 10$ m/s, (**c**) $10 < U < 15$ m/s, and (**d**) $15 < U < 20$ m/s. The blue represents the gusty runs, and the red represents the not-gusty runs. The positive means the downward momentum fluxes, and the negative means the upward momentum fluxes. Shaded area is 95% confidence interval for the u' spec.

Figure 10 shows that gusty runs coincided with more energetic w' spectra. When more energetic w' is correlated with u', gustiness translates directly to increased momentum flux. Figure 11 shows the u' spectra, in which there are less changes in the spectra. To investigate whether this extra energy is correlated with u', we examine a probability density function (PDF) of normalized momentum flux in Figure 12. The momentum flux is normalized by friction velocity ($-uw/u_*^2$) where u_*^2 is estimated using [25] and the data are binned by G_A. Positive values represent momentum transferred into the ocean and negative values are momentum transferred into the atmosphere. The PDFs have asymmetric shapes skewed towards positive values. This means downward momentum fluxes exceed the upward fluxes. As G_A increases, the PDFs flatten and the probability of high and low $-u'w'/u_*^2$ increases, while the probability of $-u'w'/u_*^2$ around zero decreases. This shows that more energetic w' do indeed increase momentum flux to the ocean.

To show how much the net momentum fluxes increased as a result of gustiness, we introduce the $u'w'$ dimensionless cospectrum, which is scaled using the Miyake formula [62]. This spectrum can contain valuable information about momentum fluxes [30,38,72]. To quantify the net momentum flux, we integrate the $u'w'$ cospectra along the frequency domain.

$$\overline{u'w'} = \int_0^\infty S_{uw} df \tag{9}$$

Here, S_{uw} is the real part of the cross spectrum of u and w. Figure 13 exhibits the cospectra scaled by mean wind speed U, the measurement height z, and u_*. Cospectra are shown for different gusty conditions along with the Miyake universal curve, which is widely used in similar studies [38,39,41].

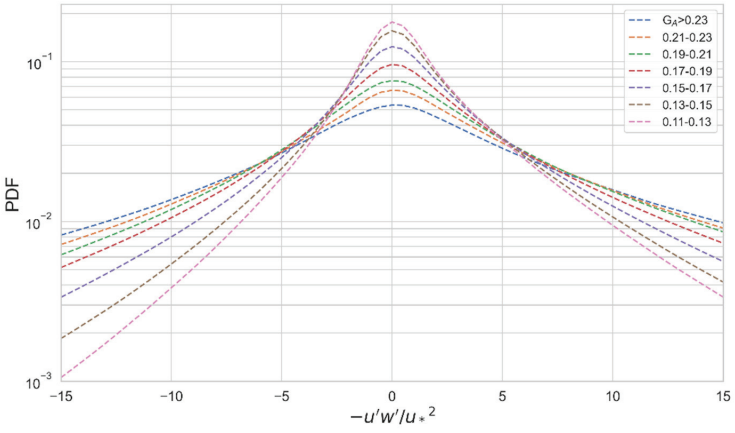

Figure 12. Probability density functions of $-u'w'/u_*^2$ as a function of wind gustiness, G_A.

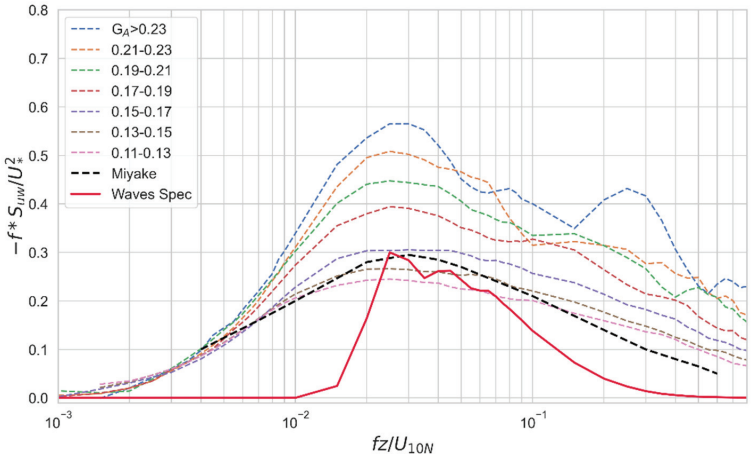

Figure 13. Observed $u'w'$ cospectra S_{uw} normalized using the universal scaling of Miyake, Stewart, and Burling [62] and averaged according to the wind gustiness, shown in multiple colored dash lines. The black dashed line is the Miyake universal curve with values taken from [72]. The red is the averaged wave spectrum of all runs, also normalized using scaling of Miyake, and standardized to a maximum value of 0.3.

In Figure 13, the magnitude of each spectrum increases with increasing gustiness. The cospectra therefore present further evidence that gustier winds have higher momentum fluxes. The energy containing region of the wave spectrum is aligned with that of the cospectra. This overlapping of energetic scales suggests some connection or coupling between the surface waves and the winds. The energy of the vertical turbulence spectra is strengthened in the presence of high gustiness. Although gustiness is characterized by horizontal wind variance, it is clear that when it is gusty there is a coincident increase in the vertical wind variance and at a similar turbulent scale-around 0.10 Hz. The vertical wind variance is connected with the horizontal wind variance due to the turbulent interactions and cascade of energy, which is isotropic. We know that, close to the sea surface, some of the vertical wind variance is coherent with the surface waves, however, direct physical connection remains unclear.

Among the possible explanations, we propose two potential mechanisms for how gustiness can cause the stronger w'. First, when the wind direction is rotating, it will cause extra horizontal turbulence and produce additional positive vorticity in the z-direction. Additionally, the ocean surface has a frictional force which can consume this vorticity, which is to say a negative vorticity in the z-direction induced by friction. For example, in a cylinder, extra positive vorticity in the upper layer will be balanced by the negative vorticity held in the bottom layer. In this case, this mechanism causes friction upon the sea surface and may explain the increased w' during gusty conditions. Another potential mechanism is that, when the wind speed is increasing, the vertical shear will be strengthened, in turn inspiring a lateral vorticity. For example, when U is increasing, it can create a positive vorticity in the mean wind direction. The only way to consume this extra vorticity is by bottom friction. In this case, small-scale lateral circulation will be produced which can connect the bottom wave surface layer with the upper layer. Ultimately, stronger vertical mixing occurs. However, proof of these two potential mechanisms requires more detailed observations to understand energy pathways and how the extra vorticity is balanced. For example, it is advisable to use the Particle Image Velocity method to take snapshots of the vertical profiles of the winds near the air–sea interface in a laboratory water tank or over the ocean. Measurements made at multiple levels may also help to understand the processes when the gustiness becomes increased.

5. Summary and Conclusions

A new gustiness formula [Equation (8)] is put forward which quantifies the fluctuations of wind speed and direction. We find that it is important to account for wind direction in explaining variability in the drag coefficient. We find that gustiness can increase C_d independent of mean wind speed. The nominal linear relationship between C_d and U_{10} put forward by previous studies (e.g., [19,24,30], etc.) is found to emerge under non-gusty (or less gusty) conditions. From examining spectra, more energetic vertical turbulence is correlated with gustiness and is perhaps induced by some of the same mechanisms that produce gustiness. The wind cospectra and wave spectra share a peak frequency, suggesting a coupling between the two. From investigation of the cospectra and PDFs, the gusty winds have a clear increase in the normalized momentum fluxes, proving that gustiness results in extra momentum flux under the same wind speed. Overall, gustiness is an important factor for understanding momentum fluxes into the ocean and should be considered in an effective parameterization.

Author Contributions: Conceptualization, M.L. and H.P; methodology, M.L. and H.P.; software, M.L.; validation, M.L.; formal analysis, M.L., H.P. and C.O.C.; investigation, M.L.; resources, H.P. and C.O.C.; data curation, M.L., H.P. and C.O.C.; writing—original draft preparation, M.L.; writing—editing, H.P. and C.O.C.; visualization, M.L.; supervision, H.P. All authors have read and agreed to the published version of the manuscript.

Funding: ITOP was funded by the Office of Naval Research under Grant N0014-09-1-0392 with additional support from the National Science Foundation under Grant OCE-0526442.

Data Availability Statement: ITOP data are freely available from EOL data archives at https://data.eol.ucar.edu/ (accessed on 1 January 2019).

Acknowledgments: We would like to acknowledge and thank many people at the University of Miami who were involved in collection of the data we used here, especially Hans Graber and William Drennan, and their team, Neil Williams, Mike Rebozo, Rafael Ramos, and many graduate students. We are also thankful to the Woods Hole Oceanographic Institution mooring team, Environment Canada, and the Captain and Crew of the R/V Roger Revelle who contributed to the project success. COC was supported by the USACE civil works under the CODS program managed by Spicer Bak. We thank the Chinese Scholarship Council who helps support Meng Lyu's graduate studies. Finally, we thank the five anonymous reviewers and the editors.

Conflicts of Interest: The authors declare no conflict of interest.

References

1. Miles, J.W. On the generation of surface waves by shear flows. *J. Fluid Mech.* **1957**, *3*, 185–204. [CrossRef]
2. Melville, W.; Romero, L.; Kleiss, J.; Swift, R. Extreme wave events in the Gulf of Tehuantepec. In Proceedings of the Rogue Waves: Proceedings 14th 'Aha Huliko 'a Hawaiian Winter Workshop, Manoa, HI, USA, 24–28 January 2005; pp. 23–28.
3. Young, I.R.; Banner, M.L.; Donelan, M.A.; McCormick, C.; Babanin, A.V.; Melville, W.K.; Veron, F. An integrated system for the study of wind-wave source terms in finite-depth water. *J. Atmos. Ocean. Technol.* **2005**, *22*, 814–831. [CrossRef]
4. Zavarsky, A.; Booge, D.; Fiehn, A.; Krüger, K.; Atlas, E.; Marandino, C. The influence of air-sea fluxes on atmospheric aerosols during the summer monsoon over the tropical Indian Ocean. *Geophys. Res. Lett.* **2018**, *45*, 418–426. [CrossRef]
5. Fan, Y.; Ginis, I.; Hara, T. The effect of wind–wave–current interaction on air–sea momentum fluxes and ocean response in tropical cyclones. *J. Phys. Oceanogr.* **2009**, *39*, 1019–1034. [CrossRef]
6. Kara, A.B.; Metzger, E.J.; Bourassa, M.A. Ocean current and wave effects on wind stress drag coefficient over the global ocean. *Geophys. Res. Lett.* **2007**, *34*, L01604. [CrossRef]
7. Kara, B.; Metzger, J.; Bourassa, M. *Impacts of Ocean Currents and Waves on the Wind Stress Drag Coefficient: Relevance to Hycom*; Naval Research Lab Stennis Detachment Stennis Space Center MS: Stennis Space Center, Kiln, MS, USA, 2006.
8. Roberts, M.J.; Camp, J.; Seddon, J.; Vidale, P.L.; Hodges, K.; Vannière, B.; Mecking, J.; Haarsma, R.; Bellucci, A.; Scoccimarro, E. Projected future changes in tropical cyclones using the Cmip6 Highresmip multimodel ensemble. *Geophys. Res. Lett.* **2020**, *47*, e2020GL088662. [CrossRef]
9. Potter, H.; Drennan, W.M.; Graber, H.C. Upper ocean cooling and air-sea fluxes under typhoons: A case study. *J. Geophys. Res. Ocean.* **2017**, *122*, 7237–7252. [CrossRef]
10. Moum, J.; Smyth, W. Upper ocean mixing processes. *Encycl. Ocean Sci.* **2001**, *6*, 3093–3100.
11. Rogers, R.; Aberson, S.; Black, M.; Black, P.; Cione, J.; Dodge, P.; Dunion, J.; Gamache, J.; Kaplan, J.; Powell, M. The Intensity Forecasting Experiment: A NOAA multiyear field program for improving tropical cyclone intensity forecasts. *Bull. Am. Meteorol. Soc.* **2006**, *87*, 1523–1538. [CrossRef]
12. Chalikov, D.; Rainchik, S. Coupled numerical modelling of wind and waves and the theory of the wave boundary layer. *Bound.-Layer Meteorol.* **2011**, *138*, 1–41. [CrossRef]
13. Monin, A.; Iaglom, A.; Lumley, J. *Statistical Fluid Mechanics: Mechanics of Turbulence*; Revised and Enlarged Edition; MIT Press: Cambridge, MA, USA, 1975; Volume 2.
14. Buckley, M.P.; Veron, F. Structure of the airflow above surface waves. *J. Phys. Oceanogr.* **2016**, *46*, 1377–1397. [CrossRef]
15. Benilov, A.; Gumbatov, A.; Zaslavsky, M.; Kitaigorodskii, S. Non-Steady Model of Development of Turbulent Boundary Layer Above Sea under Generating of Surface Waves. *Izv. Acad. Sci. USSR Atmos. Ocean Phys.* **1978**, *14*, 1177.
16. Chalikov, D.; Belevich, M.Y. One-dimensional theory of the wave boundary layer. *Bound.-Layer Meteorol.* **1993**, *63*, 65–96. [CrossRef]
17. Chalikov, D. The parameterization of the wave boundary layer. *J. Phys. Oceanogr.* **1995**, *25*, 1333–1349. [CrossRef]
18. Makin, V.; Mastenbroek, C. Impact of waves on air-sea exchange of sensible heat and momentum. *Bound.-Layer Meteorol.* **1996**, *79*, 279–300. [CrossRef]
19. Donelan, M.A.; Drennan, W.M.; Katsaros, K.B. The air–sea momentum flux in conditions of wind sea and swell. *J. Phys. Oceanogr.* **1997**, *27*, 2087–2099. [CrossRef]
20. Thomson, J.; D'Asaro, E.; Cronin, M.; Rogers, W.; Harcourt, R.; Shcherbina, A. Waves and the equilibrium range at Ocean Weather Station P. *J. Geophys. Res. Ocean.* **2013**, *118*, 5951–5962. [CrossRef]
21. Large, W.; Pond, S. Open ocean momentum flux measurements in moderate to strong winds. *J. Phys. Oceanogr.* **1981**, *11*, 324–336. [CrossRef]
22. Potter, H.; Rudzin, J.E. Upper Ocean Temperature Variability in the Gulf of Mexico with Implications for Hurricane Intensity. *J. Phys. Oceanogr.* **2021**. [CrossRef]
23. Zedler, S.E.; Kanschat, G.; Korty, R.; Hoteit, I. A new approach for the determination of the drag coefficient from the upper ocean response to a tropical cyclone: A feasibility study. *J. Oceanogr.* **2012**, *68*, 227–241. [CrossRef]
24. Smith, S.D.; Anderson, R.J.; Oost, W.A.; Kraan, C.; Maat, N.; De Cosmo, J.; Katsaros, K.B.; Davidson, K.L.; Bumke, K.; Hasse, L. Sea surface wind stress and drag coefficients: The HEXOS results. *Bound.-Layer Meteorol.* **1992**, *60*, 109–142. [CrossRef]
25. Smith, S.D. Wind stress and heat flux over the ocean in gale force winds. *J. Phys. Oceanogr.* **1980**, *10*, 709–726. [CrossRef]
26. Smedman, A.; Högström, U.; Bergström, H.; Rutgersson, A.; Kahma, K.; Pettersson, H. A case study of air-sea interaction during swell conditions. *J. Geophys. Res. Ocean.* **1999**, *104*, 25833–25851. [CrossRef]
27. Collins, C.O.; Potter, H.; Lund, B.; Tamura, H.; Graber, H.C. Directional wave spectra observed during intense tropical cyclones. *J. Geophys. Res. Ocean.* **2018**, *123*, 773–793. [CrossRef]
28. Holthuijsen, L.H.; Powell, M.D.; Pietrzak, J.D. Wind and waves in extreme hurricanes. *J. Geophys. Res. Ocean.* **2012**, *117*. [CrossRef]
29. Lin, S.; Sheng, J. Revisiting dependences of the drag coefficient at the sea surface on wind speed and sea state. *Cont. Shelf Res.* **2020**, *207*, 104188. [CrossRef]
30. Fairall, C.W.; Bradley, E.F.; Hare, J.; Grachev, A.A.; Edson, J.B. Bulk parameterization of air–sea fluxes: Updates and verification for the COARE algorithm. *J. Clim.* **2003**, *16*, 571–591. [CrossRef]
31. Babanin, A.V.; Makin, V.K. Effects of wind trend and gustiness on the sea drag: Lake George study. *J. Geophys. Res. Ocean.* **2008**, *113*. [CrossRef]

32. Stewart, R. The air-sea momentum exchange. *Bound.-Layer Meteorol.* **1974**, *6*, 151–167. [CrossRef]
33. Drennan, W.M.; Graber, H.C.; Hauser, D.; Quentin, C. On the wave age dependence of wind stress over pure wind seas. *J. Geophys. Res. Ocean.* **2003**, *108*. [CrossRef]
34. Yelland, M.; Moat, B.; Taylor, P.; Pascal, R.; Hutchings, J.; Cornell, V. Wind stress measurements from the open ocean corrected for airflow distortion by the ship. *J. Phys. Oceanogr.* **1998**, *28*, 1511–1526. [CrossRef]
35. Gao, Z.; Wang, Q.; Wang, S. An alternative approach to sea surface aerodynamic roughness. *J. Geophys. Res. Atmos.* **2006**, *111*. [CrossRef]
36. Oost, W.A.; Komen, G.J.; Jacobs, C.M.; van Oort, C.; Bonekamp, H. Indications for a wave dependent Charnock parameter from measurements during ASGAMAGE. *Geophys. Res. Lett.* **2001**, *28*, 2795–2797. [CrossRef]
37. Dobson, F.W.; Smith, S.D.; Anderson, R.J. Measuring the relationship between wind stress and sea state in the open ocean in the presence of swell. *Atmos.-Ocean* **1994**, *32*, 237–256. [CrossRef]
38. Drennan, W.M.; Kahma, K.K.; Donelan, M.A. On momentum flux and velocity spectra over waves. *Bound.-Layer Meteorol.* **1999**, *92*, 489–515. [CrossRef]
39. Potter, H. Swell and the drag coefficient. *Ocean Dyn.* **2015**, *65*, 375–384. [CrossRef]
40. Drennan, W.M.; Graber, H.C.; Donelan, M.A. Evidence for the effects of swell and unsteady winds on marine wind stress. *J. Phys. Oceanogr.* **1999**, *29*, 1853–1864. [CrossRef]
41. Vincent, C.L.; Thomson, J.; Graber, H.C.; Collins, C.O., III. Impact of swell on the wind-sea and resulting modulation of stress. *Prog. Oceanogr.* **2019**, *178*, 102164. [CrossRef]
42. Vincent, C.L.; Graber, H.C.; Collins, C.O., III. Effect of Swell on Wind Stress for Light to Moderate Winds. *J. Atmos. Sci.* **2020**, *77*, 3759–3768. [CrossRef]
43. Wüest, A.; Lorke, A. Small-scale hydrodynamics in lakes. *Annu. Rev. Fluid Mech.* **2003**, *35*, 373–412. [CrossRef]
44. Kenyon, K.E.; Sheres, D. Wave force on an ocean current. *J. Phys. Oceanogr.* **2006**, *36*, 212–221. [CrossRef]
45. Kader, B.; Yaglom, A. Mean fields and fluctuation moments in unstably stratified turbulent boundary layers. *J. Fluid Mech.* **1990**, *212*, 637–662. [CrossRef]
46. Foken, T. 50 years of the Monin–Obukhov similarity theory. *Bound.-Layer Meteorol.* **2006**, *119*, 431–447. [CrossRef]
47. Zeng, X.; Zhao, M.; Dickinson, R.E. Intercomparison of bulk aerodynamic algorithms for the computation of sea surface fluxes using TOGA COARE and TAO data. *J. Clim.* **1998**, *11*, 2628–2644. [CrossRef]
48. Obukhov, A. Charakteristiki mikrostruktury vetra v prizemnom sloje atmosfery (Characteristics of the micro-structure of the wind in the surface layer of the atmosphere). *Izv. AN SSSR Ser. Geofiz.* **1951**, *3*, 49–68.
49. Obukhov, A. Turbulentnost'v temperaturnoj-neodnorodnoj atmosfere. *Tr. Inst. Theor. Geofiz. AN SSSR* **1946**, *1*, 95–115.
50. Monin, A.S.; Obukhov, A.M. Basic laws of turbulent mixing in the surface layer of the atmosphere. *Contrib. Geophys. Inst. Acad. Sci. USSR* **1954**, *151*, e187.
51. Vignon, E.; Genthon, C.; Barral, H.; Amory, C.; Picard, G.; Gallée, H.; Casasanta, G.; Argentini, S. Momentum-and heat-flux parametrization at Dome C, Antarctica: A sensitivity study. *Bound.-Layer Meteorol.* **2017**, *162*, 341–367. [CrossRef]
52. Janssen, P. On the effects of gustiness on wave growth. In *KNMI Afdeling Oceanografisch Onderzoek Memo*; Koninklijk Nederlands Meteorologisch Instituut: De Bilt, The Netherlands, 1986.
53. Miles, J.; Ierley, G. Surface-wave generation by gusty wind. *J. Fluid Mech.* **1998**, *357*, 21–28. [CrossRef]
54. Abdalla, S.; Cavaleri, L. Effect of wind variability and variable air density on wave modeling. *J. Geophys. Res. Ocean.* **2002**, *107*, 17-1–17-17. [CrossRef]
55. Ponce, S.; Ocampo-Torres, F.J. Sensitivity of a wave model to wind variability. *J. Geophys. Res. Ocean.* **1998**, *103*, 3179–3201. [CrossRef]
56. Pleskachevsky, A.L.; Lehner, S.; Rosenthal, W. Storm observations by remote sensing and influences of gustiness on ocean waves and on generation of rogue waves. *Ocean Dyn.* **2012**, *62*, 1335–1351. [CrossRef]
57. Annenkov, S.; Shrira, V. Evolution of wave turbulence under "gusty" forcing. *Phys. Rev. Lett.* **2011**, *107*, 114502. [CrossRef]
58. Uz, B.M.; Donelan, M.A.; Hara, T.; Bock, E.J. Laboratory studies of wind stress over surface waves. *Bound.-Layer Meteorol.* **2002**, *102*, 301–331. [CrossRef]
59. Babanin, A.V.; McConochie, J. Wind measurements near the surface of waves. In Proceedings of the International Conference on Offshore Mechanics and Arctic Engineering, Nantes, France, 9–14 June 2013.
60. Ting, C.H.; Babanin, A.V.; Chalikov, D.; Hsu, T.W. Dependence of drag coefficient on the directional spreading of ocean waves. *J. Geophys. Res. Ocean.* **2012**, *117*, C00J14. [CrossRef]
61. D'Asaro, E.; Black, P.; Centurioni, L.; Chang, Y.-T.; Chen, S.; Foster, R.; Graber, H.; Harr, P.; Hormann, V.; Lien, R.-C. Impact of typhoons on the ocean in the Pacific. *Bull. Am. Meteorol. Soc.* **2014**, *95*, 1405–1418. [CrossRef]
62. Miyake, M.; Stewart, R.; Burling, R. Spectra and cospectra of turbulence over water. *Q. J. R. Meteorol. Soc.* **1970**, *96*, 138–143. [CrossRef]
63. Drennan, W.M.; Graber, H.C.; Collins, C., III; Herrera, A.; Potter, H.; Ramos, R.; Williams, N. EASI: An air–sea interaction buoy for high winds. *J. Atmos. Ocean. Technol.* **2014**, *31*, 1397–1409. [CrossRef]
64. Collins, C.O.; Lund, B.; Ramos, R.J.; Drennan, W.M.; Graber, H.C. Wave measurement intercomparison and platform evaluation during the ITOP (2010) experiment. *J. Atmos. Ocean. Technol.* **2014**, *31*, 2309–2329. [CrossRef]
65. Potter, H. The cold wake of typhoon Chaba (2010). *Deep Sea Res. Part I Oceanogr. Res. Pap.* **2018**, *140*, 136–141. [CrossRef]

66. Potter, H.; Graber, H.C.; Williams, N.J.; Collins, C.O., III; Ramos, R.J.; Drennan, W.M. In situ measurements of momentum fluxes in typhoons. *J. Atmos. Sci.* **2015**, *72*, 104–118. [CrossRef]
67. Anctil, F.; Donelan, M.A.; Drennan, W.M.; Graber, H.C. Eddy-correlation measurements of air-sea fluxes from a discus buoy. *J. Atmos. Ocean. Technol.* **1994**, *11*, 1144–1150. [CrossRef]
68. Mörters, P.; Peres, Y. *Brownian Motion*; Cambridge University Press: Cambridge, UK, 2010; Volume 30.
69. Drennan, W. On parameterisations of air-sea fluxes. *Atmos.-Ocean Interact.* **2006**, *2*, 1–34.
70. Hersbach, H.; Janssen, P. Improvement of the short-fetch behavior in the Wave Ocean Model (WAM). *J. Atmos. Ocean. Technol.* **1999**, *16*, 884–892. [CrossRef]
71. Haines, K. Ocean data assimilation. In *Data Assimilation*; Springer: Berlin/Heidelberg, Germany, 2010; pp. 517–547.
72. Tamura, H.; Drennan, W.M.; Collins, C.O.; Graber, H.C. Turbulent airflow and wave-induced stress over the ocean. *Bound.-Layer Meteorol.* **2018**, *169*, 47–66. [CrossRef]

fluids

MDPI

Article

Dynamical Filtering Highlights the Seasonality of Surface-Balanced Motions at Diurnal Scales in the Eastern Boundary Currents

Antonio Quintana [1,*,†], Hector S. Torres [2,†] and Jose Gomez-Valdes [1,†]

[1] Physical Oceanography Department, Center for Scientific Research and Higher Education at Ensenada, Baja California, Ensenada 22860, Mexico
[2] Jet Propulsion Laboratory, California Institute of Technology, Pasadena, CA 91109, USA
* Correspondence: cesarperez@cicese.edu.mx
† These authors contributed equally to this work.

Abstract: Balanced motions (BM) and internal gravity waves (IGW) account for most of the kinetic energy budget and capture most of the vertical velocity in the ocean. However, estimating the contribution of BM to both issues at time scales of less than a day is a challenge because BM are obscured by IGW. To study the BM regime, we outlined the implementation of a dynamical filter that separates both classes of motion. This study used a high-resolution global simulation to analyze the Eastern Boundary Currents during the winter and summer months. Our results confirm the feasibility of recovering BM dynamics at short time scales, emphasizing the diurnal cycle in winter and its dampening in summer due to local stratification that prevents large vertical excursion of the surface boundary layer. Our filter opens up new possibilities for more accurate estimation of the vertical exchanges of any tracers at any vertical level in the water column. Moreover, it could be a valuable tool for studies focused on wave–turbulence interactions in ocean simulations.

Keywords: eastern boundary currents; submesoscale; internal gravity waves; balanced motions; dynamical filtering; spectral analysis; global numerical model

Citation: Quintana, A.; Torres, H.S.; Gomez-Valdes, J. Dynamical Filtering Highlights the Seasonality of Surface-Balanced Motions at Diurnal Scales in the Eastern Boundary Currents. *Fluids* **2022**, *7*, 271. https://doi.org/10.3390/fluids7080271

Academic Editors: Joseph J. Kueh, Pengfei Xue and Fabrice Veron

Received: 14 May 2022
Accepted: 14 June 2022
Published: 8 August 2022

1. Introduction

Eastern Boundary Currents (from now on EBC) have been of interest since they house large areas of net primary production [1]. Since wind runs equatorward alongshore on the EBC, Ekman dynamics transport rich-nutrient water to the mixed layer [2,3], feeding the trophic chain base [4], which explains why a large portion of the world fishery takes place within these regions. On the other hand, internal gravity waves (IGW) account for a higher portion of the total kinetic energy in EBC [5], unlike Western Boundary Currents [5] where balanced motions (BM) do. In addition, low-frequency relaxation of alongshore winds creates an undercurrent that flows poleward, following the continental slope [6].

In the present work, we analyze the four major Eastern Boundary Currents, namely the California, Canary, Peru-Benguela, and Benguela currents, as they can be studied as a whole, at least to a first approximation, and we discard other regions such as the Australian or Indian Eastern boundary currents since their size and geographical features make them not that similar to the four EBC mentioned above [7]. However, most differences can be found by comparing the Benguela current near 26° S and Canary current around 28° N: whereas bathymetric settings such the Walvis ridge on the former lead to the generation of strong internal waves regardless of the season, the latter experiments a high disturbance that is located near the Canary Island Archipielago, and therefore induces prominent mesoscale phenomena such as multi-scale, energetic eddies [8]. Despite these differences in the large-to-medium scale, the question remains open on which submesoscale characteristics behave similarly across the four current systems.

Balanced motions and internal gravity waves impact the ocean kinetic energy (KE) budget differently [9]. BM mostly experience an inverse KE cascade, with KE fluxing from sources toward larger scales. This cascade helps to sustain mesoscale eddy turbulence [10]. IGW, on the other hand, and in particular, the IGW continuum, experience a direct KE cascade with KE fluxing toward smaller scales, ultimately leading to irreversible mixing [11].

Within the BM regime, submesoscale oceanic currents ($Ro \sim 1$) play a crucial role in the vertical transport of tracers and heat in the upper ocean [12]. These motions occur predominantly within the mixed layer, where secondary circulations arise from lateral density gradients induced by larger-scale flows. Modeling studies have further emphasized that submesoscale BM can evolve over time scales of shorter than 1 day, contributing to the doubling of the amplitude of vertical heat flux [13]. A critical issue when assessing these fast-evolving submesoscale currents in the presence of an internal gravity field is that BM and IGW share similar temporal and spatial scales. Moreover, each has unique dynamical features [5,13–15].

Our motivation for this study was based on two intensive experiments that NASA is carrying out in the California Current System, the S-MODE (Sub-Mesoscale Ocean Dynamics Experiment, https://espo.nasa.gov/s-mode/content/S-MODE accessed on 5 May 2022) and the SWOT Cal/Val experiment (calibration and validation of the Surface and Water Ocean Topography mission) [16], in which in situ and airborne observations are being collected and high-resolution, submesoscale, and tidal resolving ocean numerical simulations are being run. The former experiment is testing the hypothesis that submesoscale-balanced motions (from now on SBM) make essential contributions to the vertical exchange of physical variables in the upper ocean. The latter is dedicated to calibrating and validating SWOT sea surface height (SSH) measurements at a high spatial resolution [16]. In anticipation of these experiments, using numerical simulations, the present study aims to further document the spatial and temporal characteristics of BM and IGW in the Eastern Boundary Currents (EBC).

The aim of this research work is to study the temporal variability of BM in the submesoscale regime (i.e., $Ro \sim 1$) in the EBC. However, the EBC pose an additional challenge to the analysis of submesoscales, since, compared to other more energetic regions in the ocean, kinetic energy from IGW dominates and tends to obscure other dynamical regimes, particularly in summer when higher stratification enhances the presence of internal waves [17].

There have been attempts to separate BM and IGW. Most recently, Qui et al [18] and Chereskin et al. [19] applied different strategies to find a transition scale in such a way motions smaller than it are labeled as submesoscale, and larger motions are considered on the regime of mesoscale or larger scale. Such approaches are more suitable for cases when only data from instruments with a low temporal resolution (e.g., satellite altimeters) are available. As it turns out, the main drawback of methods that go along the same line is that filtering submesoscale BM with a single horizontal scale will inevitably include internal gravity waves, regardless of the refinement of the considerations to calculate a *transition scale*. Additionally, there are cases where it is not always possible to determine a transition scale uniquely because, depending on the phenomenon being researched, IGW may be a high source of noise, particularly in regions such as the EBC, where IGW dominate [5,18].

Due to the need to separate BM and IWG more efficiently, we implemented a dynamical filter in the frequency–wavenumber domain based on the tenth baroclinic normal mode IGW dispersion relation and the permissible tides, following Qiu et al. [18]. After successfully separating BM and IGW, we analyzed the temporal variability of the intensity of the vertical vorticity, ζ, and the divergence, δ, fields within the EBC for both the BM and IGW regimes.

The methodology proposed here allowed us to recover BM at short time scales as well as recovering the vital properties of submesoscale BM in terms of intense ζ and δ. Our findings include a lag between the intensities of the divergence and vorticity fields at

around 2 to 3.5 h, in perfect agreement with the transient turbulent thermal wind balance (TTTW) system outlined by [20] for both the summer and winter seasons.

Furthermore, we report, for the first time, the seasonal dependency on these fields' intensity, which is mainly induced by *KPP* diagnostics. During the winter time, the diurnal cycle of ζ and δ exhibits marked changes between day and night, following the vertical excursion of the surface boundary layer, whereas in summer, the diurnal cycle is almost negligible, emphasizing the impact of the local stratification on the diurnal excursion of the surface boundary layer that modulates the diurnal cycle of ζ and δ.

Our dynamical filter described here opens up the possibility of separating BM and IGW at any vertical level in the water column and estimating the contribution of deep-reaching submesoscale motions [21] on vertical transport of heat and any tracer. Moreover, it could be a valuable tool for use in studies focused on wave–turbulence interactions in realistic ocean simulations, an active topic nowadays.

2. Data and Methods

In this study, we characterized submesoscale relative vorticity (RV or ζ) and divergence (DIV or δ) fields in $6^\circ \times 6^\circ$ ($\sim$500 km side at mid-latitudes) areas within the four major EBC: California, Peru, Canary, and Benguela currents (as displayed in Figure 1). We examined the time–space (x, y, t) and frequency–wavenumber (ω, k, l) domains for the summer and winter months in 2012. Our starting point was the collection of ω-k_h (k_h stands for the horizontal wavenumber, i.e., $k_h^2 = k^2 + l^2$) spectra from Torres et al. [5] to represent surface KE, along with its vortical (ζ) and divergent (δ) parts. As for the spatio-temporal data, we employed the output of a realistic high-resolution ocean simulation (LLC4320) based on the Massachusetts Institute of Technology general circulation model (MITgcm).

Figure 1. Study areas within each of the Eastern Boundary Currents: California (North Pacific, from 24.17 N to 50.26 N), Canary (North Atlantic, from 13.8 N to 33.76 N), Peru–Chile (South Pacific, from 42.55 S to 13.7 S), and Benguela (South Atlantic, from 29.1 S to 8.32 S). Each tile in the map represents a quasi-quadrangular area of $\sim$6° side. Specific (latitude, longitude) locations of each quadrangular area can be found on Table 1.

Table 1. Phase difference Δt (in hours) between normalized divergence (δ) and vorticity (ζ) by current, center (latitude, longitude), and season for each quadrangular area examined. The phase difference is the angle of the complex power spectral density, calculated with a 10-day window using Welch's method [22]. All phase differences correspond to the diurnal (24 h) component. Positive values indicate that divergence occurs first and is then *followed* by the relative vorticity. Rows in bold mark the study areas compared in this paper. Values with an asterisk (*) correspond to cases when the coherence did not pass the F-test for the 90% confidence interval.

			Summer		Winter	
Current	**Latitude**	**Longitude**	**Δt [h]**	**$C_{\zeta\delta}$**	**Δt [h]**	**$C_{\zeta\delta}$**
California	48.4° N	137° W	2.41	0.6	3.86	0.97
California	44.5° N	131° W	3.14	0.88	3.81	0.97
California	40.4° N	131° W	3.57	0.88	3.55	0.95
California	36.05° N	131° W	3.22	0.93	3.21	0.97
California	31.46° N	125° W	2.95	0.95	3.02	0.97
California	**26.64° N**	**125° W**	**2.75**	**0.99**	**3.02**	**0.99**
Canary	31.46° N	23° W	3.61	0.95	3.83	0.99
Canary	**26.64° N**	**23° W**	**3.33**	**0.96**	**3.57**	**0.99**
Canary	21.61° N	23° W	3.35	0.98	3.33	0.99
Canary	16.40° N	29° W	2.75	0.97	3.13	0.99
Peru	16.39° S	83° W	2.16	0.67	3.09	0.99
Peru	**21.61° S**	**77° W**	**3.42**	**0.65**	**3.17**	**0.99**
Peru	40.41° S	83° W	3.15	0.94	2.66	0.97
Benguela	11.03° S	7° E	2.96	0.76	2.79	0.99
Benguela	16.39° S	7° E	2.98	0.63	3.19	0.99
Benguela	**26.64° S**	**7° E**	**8.5**	**0.19** *	**3.13**	**0.99**

2.1. LLC4320

The primary data source is the LLC4320 global ocean simulation output, which uses the MITgcm. LLC4320 is a realistic, high-resolution simulation (24 s steps, $1/48°$ horizontal grid spacing, 90 vertical levels with $\mathcal{O}$(1 m) resolution for the top 100 m) that spans 14 months from September 2011 to November 2012, for which hourly snapshots are available. The model is forced with 16 tidal constituents and high-frequency atmospheric boundary conditions. The interaction between wind and ocean occurs at the ocean surface, where energy and momentum are exchanged. Roughly speaking, surface wind stress is commonly parameterized as

$$\tau_s = \rho_{air} C_D |U_{wind} - U_{ocean}| (U_{wind} - U_{ocean}), \quad (1)$$

where ρ_{air} is the density of the air, C_D is known as the drag coefficient, U_{wind} is the wind speed field, and U_{ocean} is the surface ocean speed [23]. On the other hand, the ocean net heat flux is parameterized as

$$Q_{net} = Q_{rad} + Q_{lat} + Q_{sen}, \quad (2)$$

where Q_{rad}, Q_{lat}, and Q_{sen} are the radiation, latent, and sensible heat fluxes, respectively [24]. As we will see later in this paper, both wind stress and net heat flux modulate the mesoscale and submesoscale regimes. Therefore, evaluating the impact of atmospheric forcing on our observed variables is crucial.

Since $1/48°$ horizontal spacing is equivalent to $\sim$2 km at mid-latitudes, numerical diffusion yields an effective resolution of about four times the grid size ($\sim$8 km) [17,25], so LLC4320 allows us to observe and study submesoscale features. In this study, as we aimed to compare the dynamics of EBC during the winter (January, February, March) and summer (August, September, October) months, we used hourly snapshots of LLC4320 for these months to examine the vorticity features of the EBC, resulting in about 2200 snapshots for each variable (e.g., U, V, θ) as well as the season and depth. Data can be accessed by

either directly downloading them from the ECCO Data Portal (see: https://data.nas.nasa.gov/ecco/data.php?dir=/eccodata/llc_4320, accessed on 10 November 2021) or by reading them using the xmitgcm Python package (see: https://github.com/MITgcm/xmitgcm, accessed on 3 March 2022).

2.2. Software for Data Processing

After we downloaded all the variables for our study, it was necessary to merge them into data collections that hold the information for each study area and season. Since managing and performing calculations over each of such collection would not be scalable, we used Python package https://www.dask.org/Dask (accessed on 5 May 2022) along with https://xarray.pydata.org/ (accessed on 5 May 2022); the former is a library that facilitates the creation of parallel calculations, with array functions similar to what https://numpy.org/ (accessed on 5 May 2022) offers, while the latter takes Dask variables and gathers them into data structures that are netCDF-friendly, while taking advantage of its *lazy evalation scheme* (i.e., it only reads data when it is required). In short, our workflow is as follows:

1. Download hourly snapshots for each variable, area and season.
2. Combine hourly data into time series for each variable and season, and the merge all variables into a single dataset per season and area.
3. Calculate dynamical filter in 3D ω-k_h spectral space.
4. Apply dynamical filter to each variable of interest, namely horizontal components of the ocean surface speed, from which one will obtain the low-pass (balanced motions) and high-pass (internal gravity waves) components.
5. Compute derived quantities (i.e.,ζ and δ) for further analyses.

In addition to this succinct summary, specific implementation details have been already shared in our sample Jupyter notebook (https://github.com/antonimmo/ebc-wk-spectral-analysis/blob/master/wk_3dfilter_.ipynb, accessed on 5 May 2022) [26].

2.3. ω-k_h Spectrum

For a given variable $\phi(x, y, t)$ (e.g., kinetic energy, sea surface height), season (summer or winter), area (tiles in Figure 1), or vertical level, by performing a Fast Fourier Transform, we obtained the 3D spectral density in the wavenumber (k, l) and frequency (ω) domains, $\Phi(k, l, \omega)$. A close examination of $\Phi(k, l, \omega)$ on the k–l plane confirmed that they are mostly azimuthally symmetric for all frequencies, so we were able to map the k–l plane into a horizontal wavenumber k_h; hence, the azimuthally averaged spectrum $\Phi(k_h, \omega)$ was produced. An example of such isotropic 2D spectra in the ω-k_h space is shown in Figure 2, and the temporal and spatial reference scales are also displayed. An estimation of the average local buoyancy frequency N was used to calculate the dispersion relation curves corresponding to the first four and the tenth vertical modes of the IGW. The dispersion relation of IGW is:

$$\omega_n^2(k_h) = \frac{N^2 + f^2(n\pi/k_h H)^2}{1 + (n\pi/k_h H)^2}, \tag{3}$$

where H is the average depth at the area being studied, k_h is the horizontal wavenumber, and n ($n = 1, 2, 3 \ldots$) is the IGW mode.

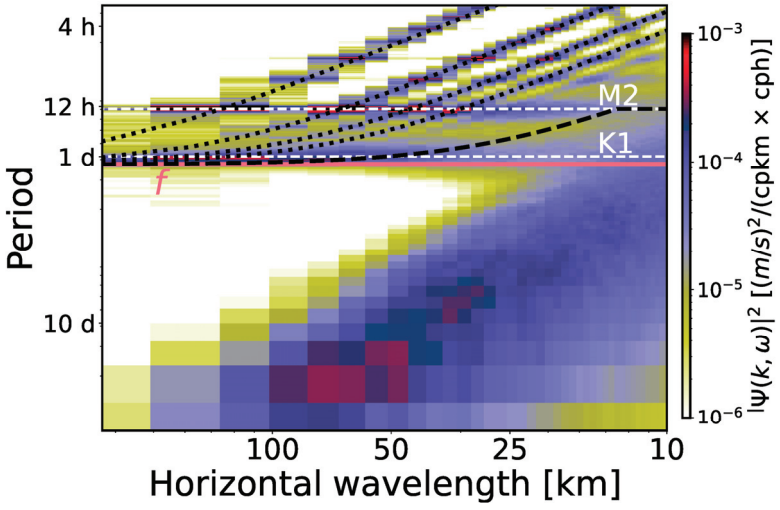

Figure 2. Power spectral density of the surface kinetic energy (KE) in the frequency–horizontal wavenumber (ω-k_h) domain for the area centered at 26.64° N within the Canary current during the winter (January, February, March) of 2012. The black dotted lines represent dispersion relations for modes 1, 2, 3, and 10 of the internal gravity waves. The black dashed line denotes the minimum frequency between the internal gravity waves (IGW) at mode 10 and the M_2 tide, whereas the white dashed lines mark the M_2 and K_1 tide frequencies for reference purposes. The solid dark pink line corresponds to the average Coriolis frequency f in that area.

2.4. Temporal Variability of the Vorticity and Divergence Fields

In this work, we analyzed the rotational, ζ, and divergent ,δ, components of horizontal motions, with ζ and δ being defined as $\zeta = v_x - u_y$, $\delta = u_x + v_y$, where u and v are the horizontal velocity components in Cartesian coordinates x and y. The relative vorticity ζ is related to the spin of horizontal motions, and the horizontal divergence δ is related to the vertical derivative of the vertical velocity via the 3D incompressibilty condition. Both ζ and δ are normalized by f, which corresponds to the local inertial period. We describe the analysis of the fields of ζ/f and δ/f in the following sections. Since both divergence (δ) and vorticity (ζ) have a spatial mean of almost zero in the ocean [27], the standard deviation of these quantities (S can be either ζ or δ) $\sigma[S](t)$ can be approximated by

$$\sigma[S](t) \simeq \sqrt{\frac{1}{NM}\sum_{n=0,m=0}^{N,M}(S_{n,m}(t))^2} = RMS[S](t), \tag{4}$$

thus serving as a measure of the instantaneous average intensity of these fields. If one calculates the standard deviation of these variables for each hourly snapshot, a time series that shows the evolution of such fields' intensity can be obtained.

2.5. A Dynamical Filter to Discriminate BM from IGW

Chereskin et al. [19] reported a significant contribution of IGW to ζ and δ in the California Current System, and Torres et al. [5] reported IGW dominance in the EBC, where both studies were based on an LLC4320 simulation. In order to filter out IGW, we made use of a dynamical filter based on the dispersion relation of IGW in the frequency–wavenumber (ω-k_h) space. The main feature of this filter is that it does not have a fixed cutoff frequency or horizontal wavenumber, k_h, but we designed it to filter as many internal waves and tides as possible. We achieved this by using a function in the ω-k_h spectral space to obtain a cutoff frequency for each k_h, $\omega_{cutoff}(k_h)$.

Our candidate function was the dispersion relation for the tenth vertical normal mode given by Equation (3) (i.e., ω_{10}). Qiu et al. [18] and Torres et al. [5] used this tenth vertical normal to quantify the relative contributions of IGW and BM to the kinetic energy. As we can see in Figure 2, this criterion does not manage to filter out semidiurnal or diurnal tides at scales below 30 km. Hence, we included an additional constraint to discard them by considering the dominant tidal band below the ω_{10} (see Equation (3)) dispersion curve (M2 in the cases we examined). The resulting filter is a function in the ω-k_h spectral space that obtains a cutoff frequency that depends on k_h in the form

$$\omega_{cutoff}(k_h) = min[\omega_{10}, \omega_{tide}(k_h)], \tag{5}$$

where ω_{tide} corresponds to the frequency of the additional tidal band that needs to be discarded. The dispersion relation curve modified to discriminate BM from IGW (including M2 tides in this example) is represented by the black dashed line in Figure 2.

BM and IGW are known to be present in a wide and similar range of horizontal scales, whereas IGW are, in general, faster than BM. Large BM are, in general, slow and can mostly be described by geostrophic dynamics, such as eddies. However, near the submesoscale ($Ro \sim 1$) regime, we found submesoscale BM (SMB) with horizontal scales of up to a couple of dozen kilometers, frequencies near the local Coriolis parameter, and enclosed motions, such as fronts, gradient wind (cyclostrophic) balance, and filaments. Since SBM tend to have frequencies and scales similar to the IGW domain, we needed to set a sensible threshold to allow us to study most SBM without interference from tides or higher IGW modes. This is the reason behind all choices made thus far in the design of the dynamical filter.

Figure 3 better illustrates how the filter separates IGW and tides from BM in the spectral space. The actual filtering should be performed in the three-dimensional spectral space (k, l, ω) (Figure 3, left panel), which allows the inverse FFT to be applied to the filtered signal and then go back to the physical (x, y, t) space. Therefore, BM (IGW) are found below (above) the dispersion relation curve (Figure 3, right panel) or outside (inside) the cone shape (Figure 3, left panel).

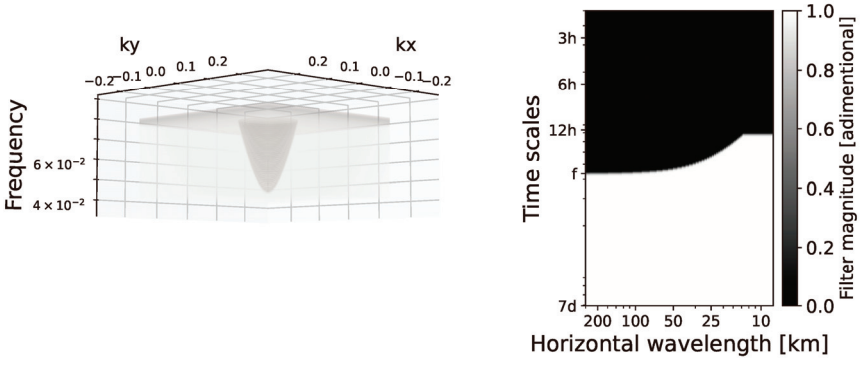

Figure 3. Dynamical filter in the k-l-ω space (**left panel**) and in the ω-k_h space (**right panel**). Internal gravity waves (balanced motions) are located inside (outside) the cone shape in the left panel and in the black (white) region in the right panel.

Coherence and Phase Difference between Average Intensities of Divergence and Vorticity

Close inspection of both time series shows a temporal phase shift between them for the diurnal frequency component. As this shift might not be evident for time series with several frequency components, we calculated the cross power spectral density $P_{\zeta\delta}(\omega)$ [22], from which we obtained phase differences between both signals as a function of frequency. A positive shift implies that δ precedes ζ, and the converse is true when the shift is negative. We then used Welch's method to obtain the spectral coherence between δ and ζ, $C_{\zeta\delta}(\omega)$ in the form

$$C_{\zeta\delta}(\omega) = \frac{\left|P_{\zeta\delta}(\omega)\right|^2}{P_{\zeta\zeta}(\omega)P_{\delta\delta}(\omega)}, \tag{6}$$

where $P_{AB}(\omega) = |P_{AB}(\omega)|e^{i\theta(\omega)}$ is the cross spectral density between variables A and B. Spectral coherence is the frequency-domain analogue of the correlation coefficient [28], so values near 1 indicate a high correlation at a given frequency or, in other terms, such frequencies have major contributions to the total covariance. This methodology allowed us to confirm that diurnal divergence drives submesoscale vorticity in winter, but this result does not hold in summer.

3. Results

This section presents most of our results and provides comparisons between areas centered at the same latitude whenever possible. We compared areas at 26.64°(north or south) for the California, Canary, and Benguela currents and at 21.61° S for the Peru current. Our results and conclusions were proved to be valid for all areas and seasons, except when we state otherwise.

3.1. Comparing ζ and δ at Seasonal and Diurnal Time Frames

Snapshots of vorticity and divergence in summer and winter are presented in Figure 4 as the first comparison between these two seasons. In winter, elongated positive and negative filaments with magnitudes of order 1 for ζ/f and 0.5 for δ/f dominated the vorticity and divergence fields, respectively. Additionally, small-scale cyclonic eddies were all over the space, reaching magnitudes of order 1 for ζ/f. On the other hand, internal gravity waves overshadowed balanced motions in the δ map in the summer season, whereas submesoscale BM features were weak but observable in the ζ map, compared to their winter counterpart.

To compare the diurnal variations in δ and ζ, maps of vorticity and divergence can be visualized in Figure 5, which shows snapshots at times during the same day that are near the maximum and minimum δ and ζ values. In most cases, in all EBC, the maximum divergence occurred at around 5:00 p.m. local time (end of daytime), and the minimum divergence occurred at around 5:00 a.m. local time (end of night-time), with the only differences being the intensity of these fields and the exact time at which their minima and maxima occurred. Submesoscale structures strongly emerged during the afternoon with positive skewness for vorticity ($Ro > 1$) and negative skewness for divergence. As revealed by comparing the 5:00 a.m. and 5:00 p.m. PDFs side by side, the skewness indicates that frontogenesis was more significant during the afternoon than late at night. This implies a change in the kinetic energy transfer, since small-scale motions intensified during the night.

Another point of dynamical comparison was the ζ-δ joint probability distribution of both the divergence and vorticity fields for each season and area. Figures 4 and 5, in addition to the comparison in the physical space, display their corresponding joint probability distribution functions (joint PDFs, or JPDFs). Each of these instantaneous JPDFs shows how one can translate dynamical differences in physical space into a JPDF that allows such differences to be described. Additionally, each of these four quadrants corresponds to different motion regimes. In particular, the higher probability densities found in the fourth quadrant (positive ζ, negative δ) and Rossby numbers ζ/f close to

an order of 1 give us evidence of intense frontal activity, which is directly associated with submesoscale instabilities, such as fronts or filaments.

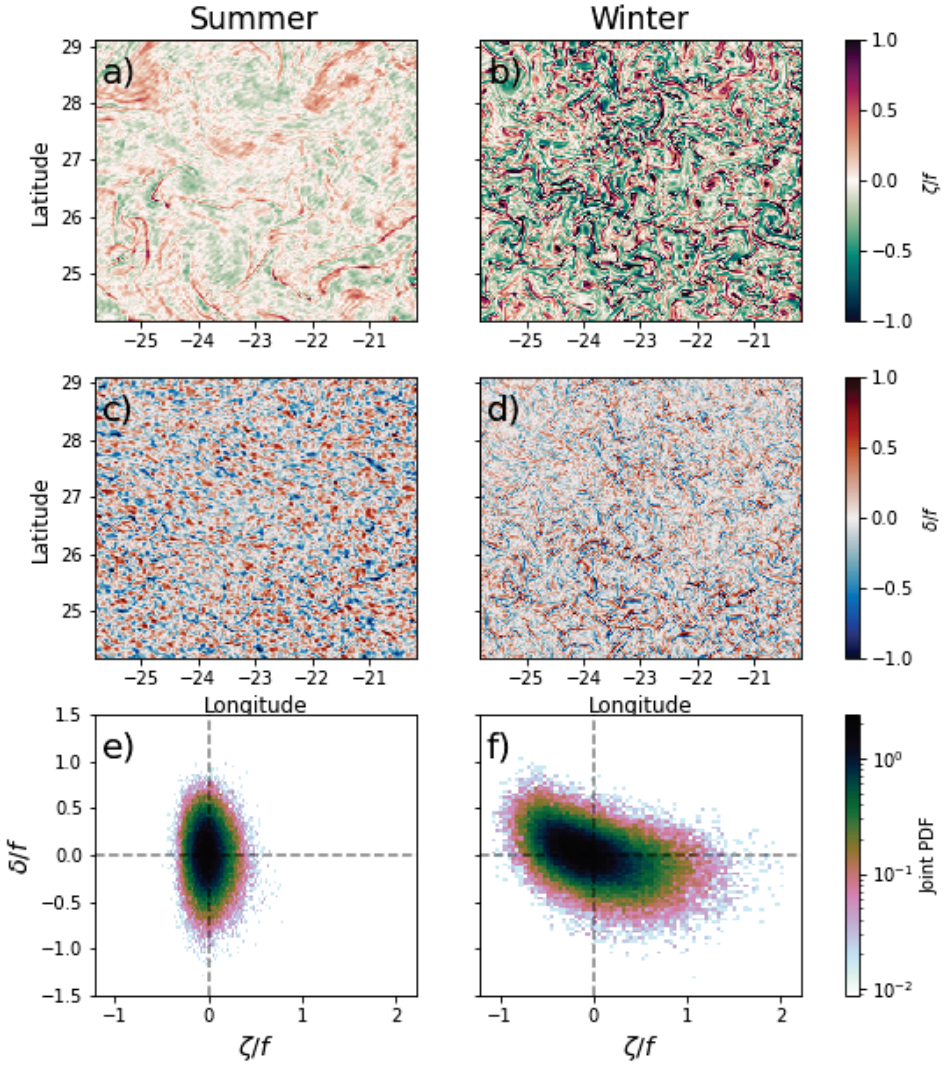

Figure 4. Snapshots of the total (unfiltered normalized) relative vorticity (ζ/f: (**a**,**b**)) and divergence (δ/f: (**c**,**d**)) fields, along with their corresponding ζ-δ joint probability distributions (**e**,**f**) at Canary (26.64 N) for summer (**a**,**c**,**e**) and winter (**b**,**d**,**f**) at times when the sea surface temperature was maximal (at around 5:00 p.m. local time). ζ and δ were then normalized by their Coriolis frequencies f. Joint PDF colors are presented on a logarithmic scale.

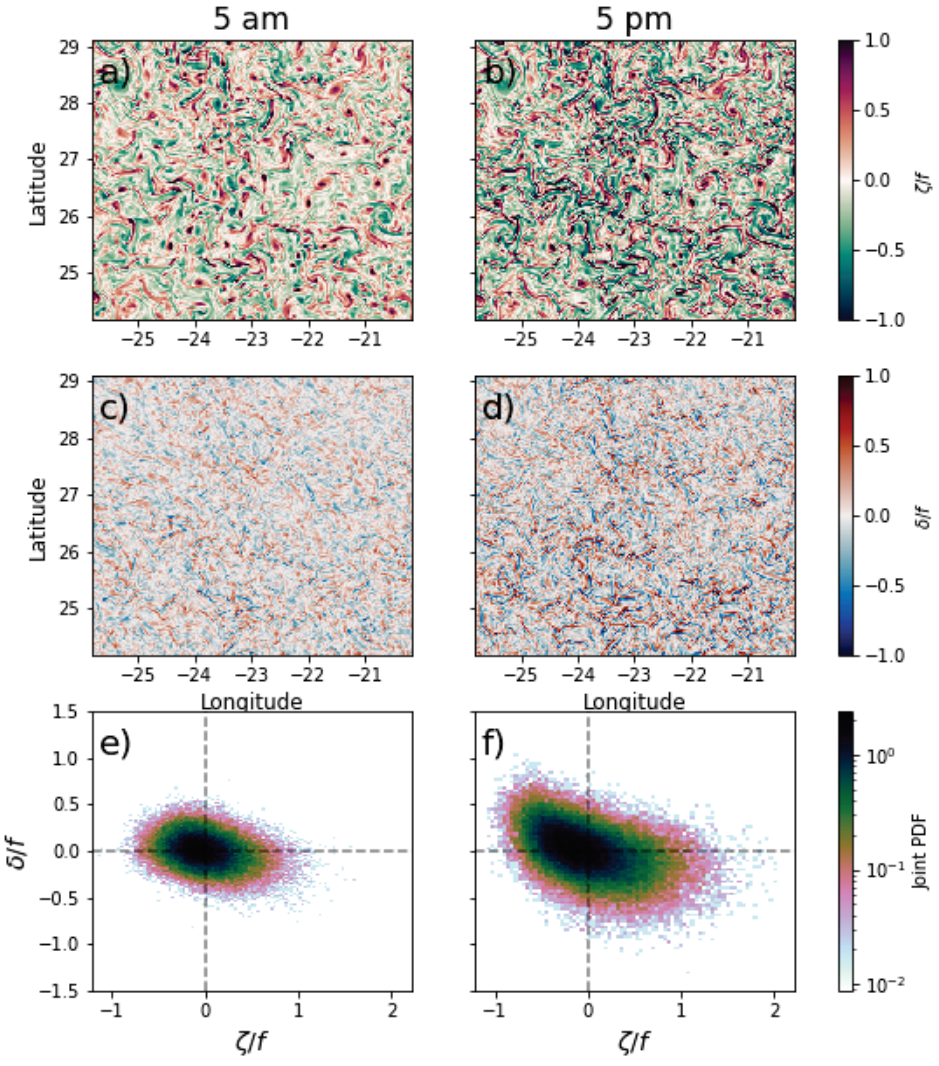

Figure 5. Snapshots of the relative vorticity (ζ: (**a**,**b**)), divergence (δ: (**c**,**d**)), and instantaneous ζ-δ joint probability distributions (**e**,**f**) at Canary (26.64° N) for times where the sea surface temperature was maximal (at around 5:00 p.m. local time, left) and minimal (at around 5:00 a.m. local time, right) on an arbitrary day in winter (1 March 2012). Joint PDF colors are presented on a logarithmic scale.

3.2. Rotational-Divergent Ratio in the Frequency–Wavenumber Space

We also calculated the corresponding ω-k_h kinetic energy spectral densities $KE_\zeta = \left|\hat{\zeta}\right|^2/k_h^2$ and $KE_\delta = \left|\hat{\delta}\right|^2/k_h^2$, where $\hat{\zeta}$ and $\hat{\delta}$ denote the Fourier transform of the relative vorticity and divergence fields. Figure 6 shows how the quotient of spectral densities KE_ζ/KE_δ varies by current and season, making it evident that vorticity fields dominate over a broader range of frequencies in winter than they do in summer.

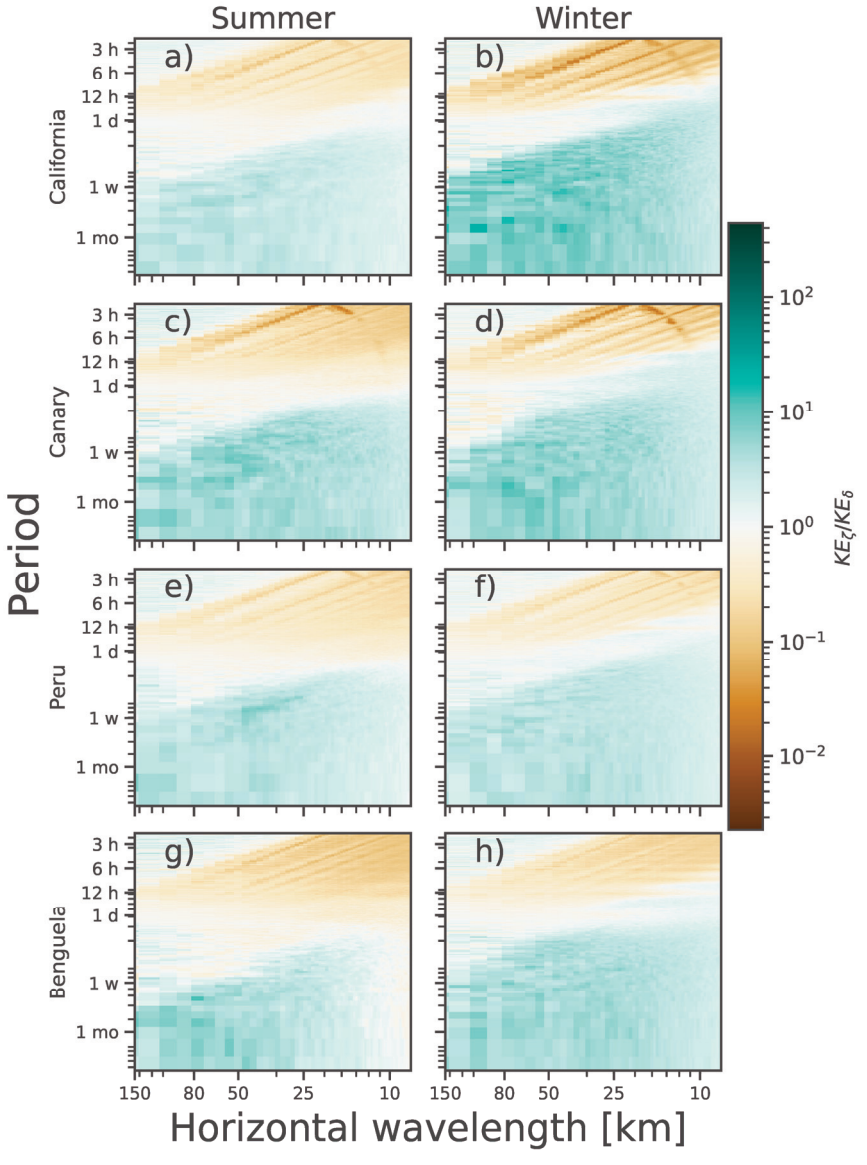

Figure 6. The quotient of spectral densities KE_ζ/KE_δ in the frequency–horizontal wavenumber domain by current and season at selected areas within the California (26.64° N: (**a**,**b**)), Canary (26.64° N: (**c**,**d**)), Peru (21.61° S: (**e**,**f**)), and Benguela (26.64° S: (**g**,**h**)) current systems. Green and orange highlight scales where either KE_ζ or KE_δ dominate, respectively.

By inspecting Figure 6, we determined which temporal and spatial scales are dominant in each regime from these spectra. During summer, at periods of one day, both divergence and vorticity have roughly the same kinetic energy, where the ratio $KE_\zeta/KE_\delta \approx 1$. The kinetic energy for motions with periods longer than one day can be explained, mainly, by the divergent component (IGW); hence, in this case, $KE_\zeta/KE_\delta >> 1$ (brown color). For motions with periods longer than one day, the vorticity component explains most of the variance (green color). During winter, the vorticity component tends to extend towards periods shorter than one day, particularly motions with horizontal wavelengths smaller than $\sim$50 km. This is consistent with our findings in Section 3.1, where Figure 4 provides evidence of which field dominates during each season.

From these spectra, one can argue that a temporal filter with a cut-off period of 1 day (or, in a more general case, the inertial period) is sufficient to discriminate BM from IGW. This procedure might work in summer, but not in winter due to the presence of submesoscale BM with periods of shorter than 1 day. It is precisely in winter that the scientific community has focused its efforts to discriminate both classes of motion. On the other hand, the implementation of a filter in the horizontal wavenumber space would rely on the definition of a *transition scale* (see, e.g., [18]), which cannot always be uniquely determined by area of study and season and also poses the challenge of choosing a dynamical criterion that suits all cases and does not depend on measurements of KE in the spectral space (which are, by themselves, sensitive to the selected timeframe or method). Here, we present a dynamical filter that intends to achieve such BM–IGW separation, whose performance is assessed in the next section.

3.3. Separating IGW and BM

The findings for the ratio of rotational to divergent components in the preceding section show that IGW and BM share the same small horizontal wavelengths and time scales as submesoscale BM, making their separation by applying a temporal or spatial filter difficult. In Section 2.4, we propose a dynamical filter that takes advantage of the dispersion relation of the tenth vertical normal mode limited to its maximum frequency at M2 (1/12.42 h) (Figure 3). The fields presented before applying the filter are hereinafter referred to as unfiltered fields. After applying the filter, we follow the convention described in Section 2.4: BM (IGW) for motions below (above) the dispersion relation of the aforementioned vertical normal mode.

Figure 7 serves as a visual evaluation of how the dynamical filter works. The first row shows both ζ and δ unfiltered fields for a snapshot in summer, whereas the second and third rows showcase the (ζ, δ)-BM and (ζ, δ)-IGW components, respectively. By inspecting the unfiltered fields, it is noticeable that, on one hand, ζ partially filters out IGW. Blurry elongated cyclonic filaments can be identified visually. However, eddy-like structures are unclear. Torres et al. [5] and Torres et al. [15] reported that the signature of internal tides and their subharmonics is non-negligible. On the other hand, the impact of IGW is overwhelming in the unfiltered δ field. The typical dipole associated with elongated filaments [29] is visually undetectable. The IGW dominance over BM is well known during the summer season [18,30]: δ/f is characterized by having higher values than ζ/f. This description is emphasized in the joint PDF (JPDF) by following a vertical distribution, with δ/f values from -1 to 1, whereas ζ/f is limited from -0.5 to 0.5.

This scenario changes after applying the dynamical filter. The second and third columns of Figure 7 demonstrate that the filter manages to separate BM and IGW regimes and preserve their respective relevant dynamical features in the ζ-BM and δ-BM fields, such as mesoscale cyclonic and anticyclonic eddies and elongated fronts and filaments, with their respective dipoles in δ-BM. Additionally, the JPDF is slightly yet noticeably skewed towards the fourth quadrant, following a diagonal distribution. It is also noteworthy that the separation of BM is not sensitive to the intensity of the IGW component once the maximum cutoff frequency of the filter has been defined. As shown in Figure 8, the JPDF of the four EBC areas for the whole summer and winter seasons matches the distribution in Figure 7,

regardless of the intensity of the IGW field. As expected, we found a stronger vorticity field in winter (yielding a diagonal distribution in the JPDF), whereas divergence (primarily associated with IGW) was more dominant in summer (yielding a vertical the distribution in the JPDF). Particularly in winter, the filter allows the leakage of information from the BM to the IGW component, as revealed by the gentile diagonal component in the JPDF of IGW (fourth column in Figure 8). This is explained by submesoscale motions with frequencies higher than the M2 internal tides, since the dispersion relation used is limited at M2. However, the JPDF associated with this leakage in the IGW component is three orders of magnitude smaller than the JPDF of BM.

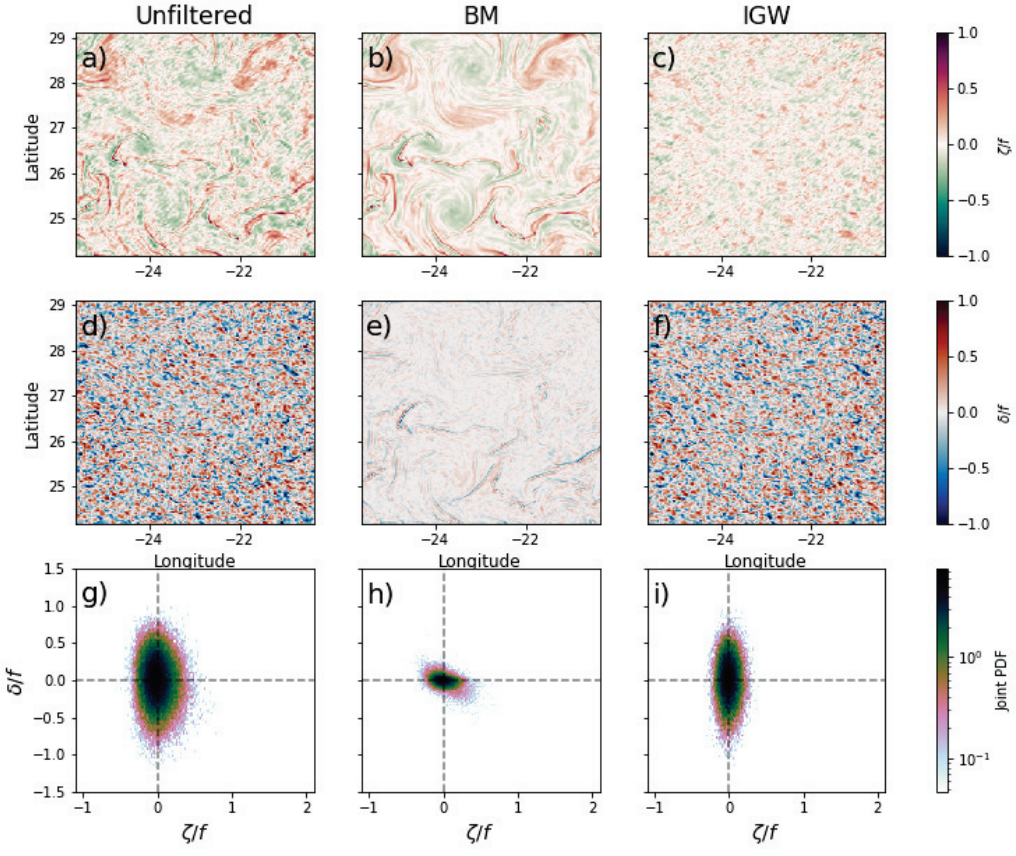

Figure 7. Snapshots of the normalized relative vorticity (ζ/f: (**a**–**c**)), divergence (δ/f: (**d**–**f**)), and joint ζ-δ PDF (**g**–**i**) for a snapshot on 30 September 2012 at Canary (26.64° N). Fields are shown in an unfiltered state (**a**,**d**,**g**) as well as for the BM (**b**,**d**,**h**) and IGW (**c**,**e**,**i**) regimes. JPDF bin colors are presented on a logarithmic scale.

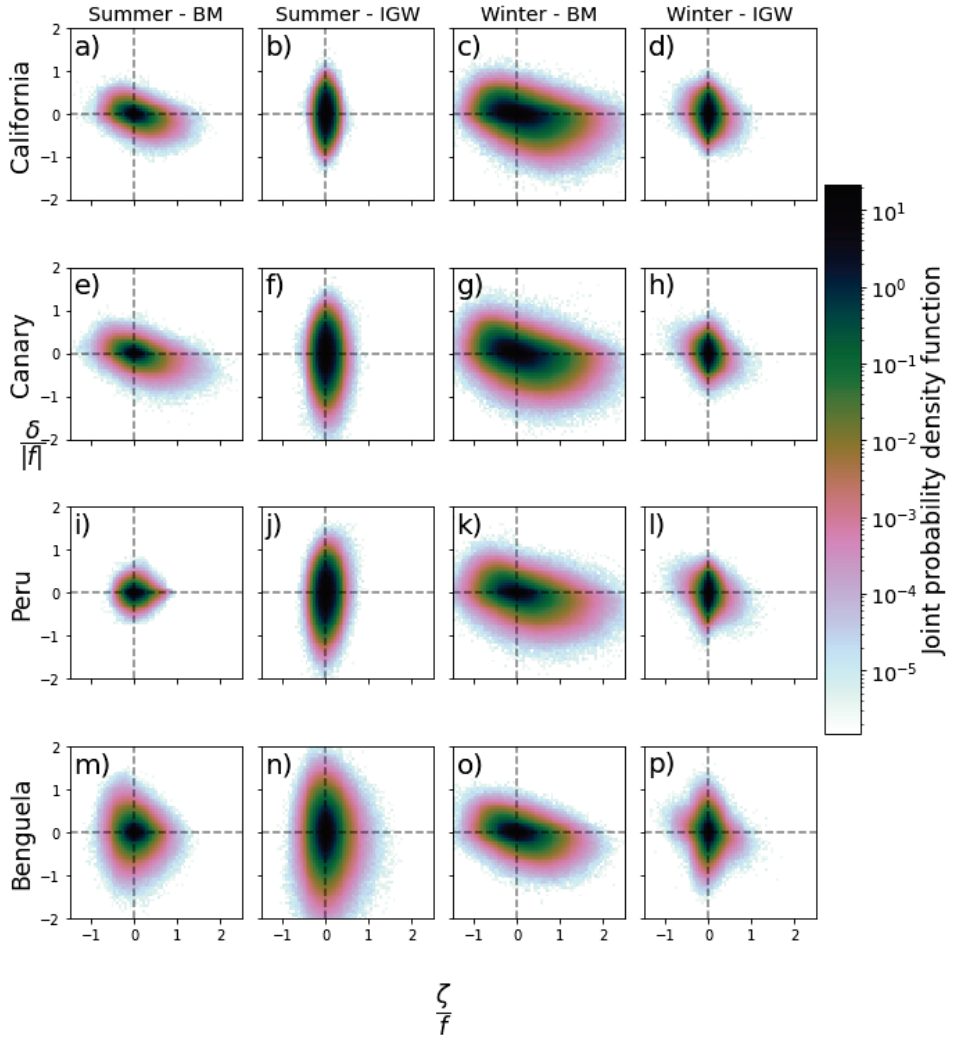

Figure 8. Joint probability distribution of ζ (x-axis) and δ (y-axis) at selected study areas within the California (26.64° N: (**a**–**d**)), Canary (26.64° N: (**e**–**h**)), Peru (21.61° S: (**i**–**l**)), and Benguela (26.64° S: (**m**–**p**)) current systems for both the balanced motion (BM) and internal gravity wave (IGW) regimes. Both vorticity (ζ) and divergence (δ) are normalized by f. Bin colors are presented on a logarithmic scale.

3.4. Seasonal and Diurnal Variability of BM and IGW

We now examine the evolution of the RMS values of both ζ and δ, as per Equation (4), for the BM and IGW regimes. These calculations are plotted along with the corresponding surface sea temperature (SST), surface net heat flux, magnitude of wind stress, and depth of the KPP boundary layer depth (KPP_{hbl}), since atmospheric forcing is known to impact the frontal dynamics through the vertical viscosity [31,32]. We show the findings for the Canary (Figure 9) and Benguela (Figure 10) currents, considering that these two currents have less common features, especially in winter. Canary has high temperature (and density) gradients and is located near a source of energetic eddies that are ejected towards the West Atlantic. The Benguela current around 26.64° S, on the other hand, has a weaker vorticity

field and is mostly dominated by internal tides generated over topographic features at the Walvis Ridge.

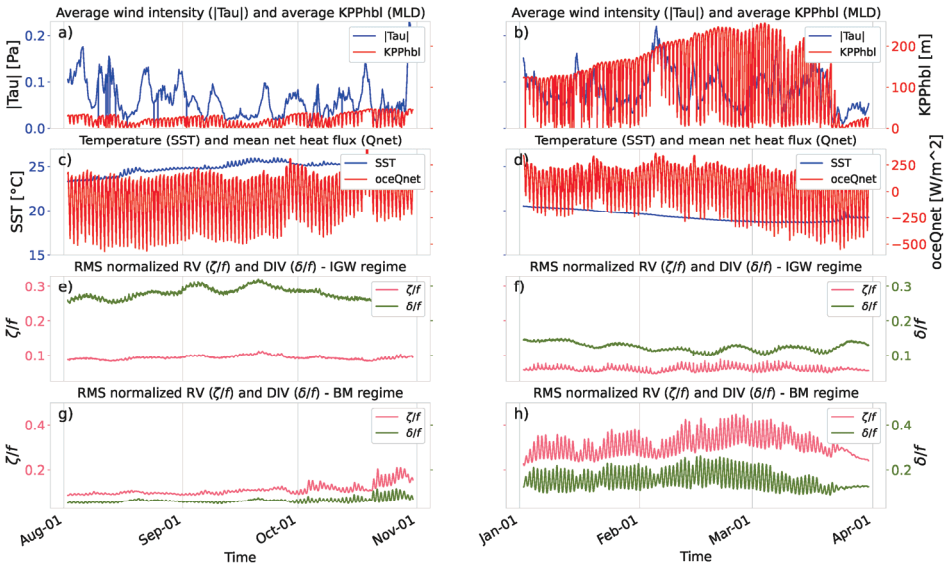

Figure 9. Time series of dynamical variables for the study area centered at 26.6° N within the Canary current from 2 August to 30 October 2012 (**a**,**c**,**e**,**g**) and from 2 January to 30 March 2012 (**b**,**d**,**f**,**h**) seasons. First row (**a**,**b**): mean values for the wind stress ($|\tau|$, blue) and the KPP turbulent boundary layer depth (KPP_{hbl}, red). Second row (**c**,**d**): mean values for the sea surface temperature (T, blue) and ocean net heat flux (oceQnet, red). Third row (**e**,**f**): standard deviation of the normalized vorticity (ζ/f, magenta) and divergence (δ/f, green) fields in the internal gravity wave (IGW) regime. Fourth row (**g**,**h**): standard deviation of the normalized vorticity (ζ/f, magenta) and divergence (δ/f, green) fields in the balanced motion (BM) regime.

The time series of RMS values of BM-ζ/f and BM-δ/f exhibits intermittency at daily to weekly time scales as well as strong seasonality (third and fourth panels in Figures 9 and 10). In addition to the well-known seasonal variability in the KPP_{hbl} (deeper in winter and shallower in summer), high-frequency variability can be detected in Figures 9 and 10 (top panels red line). Simultaneously, KPP_{hbl} displays a strong phase relationship with the ocean net heat flux (red line in the second row). The daily vertical excursion of KPP_{hbl} in winter can be around $\sim$100 m, while in summer, this excursion gets weaker since the stratification increases during this season. The intensity of the δ and ζ fields in the BM regime follows the seasonal and diurnal variability of KPP_{hbl}. During winter, when KPP_{hbl} reaches its maximum depth (around 250 m in the Canary Current and 150 m in the Benguela Current), the overall RMS values of ζ and δ increase and the high-frequency variability is intense, such that the RMS values of both BM-δ and BM-ζ increase and decrease drastically at diurnal time scales. From early spring to late summer, the diurnal pattern weakens (even vanishes), as revealed by a reduction in the amplitude of the diurnal variability (see panel g and the final part of panel h in Figures 9 and 10). This dampening of the diurnal cycle follows the shallowness of KPP_{hbl}. The diurnal excursion of KPP_{hbl} in summer is from 5 m to $\sim$50 m.

Regarding the IGW-ζ and IGW-δ time series, it is remarkable that the diurnal cycle is negligible, in both summer and winter. However, we should remark that dynamical filter is not 100% accurate. A comparison of panels f and h in both Figures 9 and 10 indicated that there is leakage of high frequency BM onto the IGW component, which is more noticeable during the winter when the RMS values of BM-ζ (pink lines) are large. This is consistent

with the IGW-ζ-δ JPDFs in Figure 8, which shows a slight tendency towards the BM regime (fourth quadrant: positive ζ and negative δ) near $Ro{\sim}1$, although their JPDFs are three orders of magnitude smaller than those of their BM counterpart.

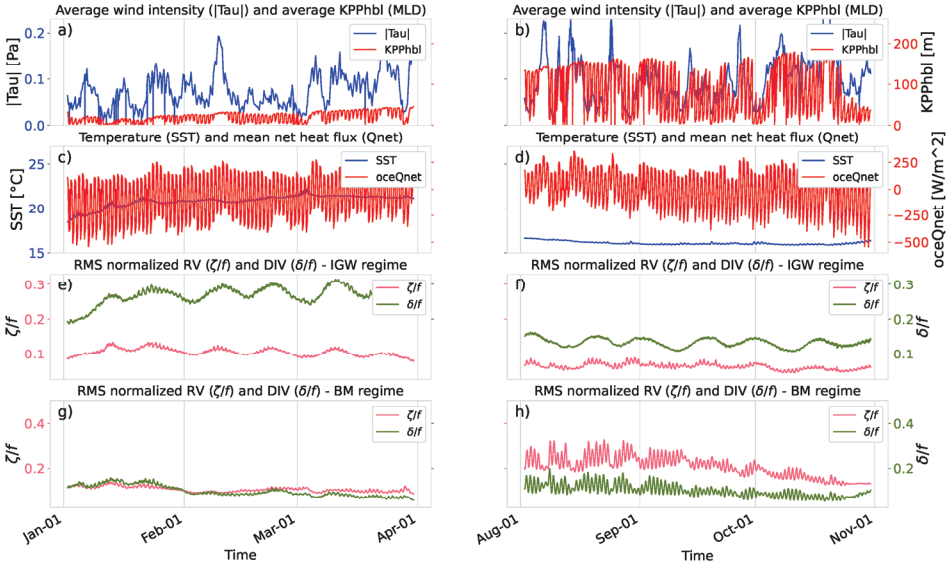

Figure 10. Time series of dynamical variables for the study area centered at 26.6° S within the Benguela current from 2 January to 30 March 2012 (**a**,**c**,**e**,**g**) and from 2 August to 30 October 2012 (**b**,**d**,**f**,**h**) seasons. First row (**a**,**b**): mean values for the wind stress ($|\tau|$, blue) and the KPP turbulent boundary layer depth (KPP_{hbl}, red). Second row (**c**,**d**): mean values for the sea surface temperature (T, blue) and the ocean net heat flux (oceQnet, red). Third row (**e**,**f**): standard deviation of the normalized vorticity (ζ/f, magenta) and divergence (δ/f, green) fields in the internal gravity wave (IGW) regime. Fourth row (**g**,**h**): standard deviation of the normalized vorticity (ζ/f, magenta) and divergence (δ/f, green) fields in the balanced motion (BM) regime.

Figures 9 and 10 illustrate the synchronization of the RMS values of BM-ζ and BM-δ with KPP_{hbl} and the ocean net heat flux. Garrett and Loder [31] described that vertical viscosity forces are an effective divergent flow, δ_κ that further stimulates frontogenesis. A simple scaling analysis was conducted, following [31] and assuming that the vertical viscosity κ was constant in space, which led to

$$\delta_\kappa \approx \frac{\kappa}{f}\zeta_{zz} \approx \frac{\kappa}{f^2}\Delta b_{zz} \tag{7}$$

with Δ representing the horizontal Laplacian operator and b representing the buoyancy. This equation means that, through the modulation of the vertical viscosity, the wind intermittency and the diurnal cycle of surface heat fluxes impact the divergence and relative vorticity of BM. In our case, we did not have access to κ, but we show the time series of KPP_{hbl}, which was directly estimated from the vertical viscosity coefficient κ under the KPP parameterization scheme [33]. One can infer that, when the net heat flux is maximal during the day, κ is small because of heating (oceQnet < 0); therefore, KPP_{hbl} is shallow, and ζ and δ increase. On the contrary, κ increases during the night because of cooling (oceQnet > 0); therefore, KPP_{hbl} is deeper, and ζ and δ decrease. This diurnal variation modifies the frontogenetic tendency. Torres et al. [15] reported that the frontogenesis tendency [34]

exhibits a clear relationship with the net heat flux, with frontogenesis emphasized during the day and frontolysis emphasized during the night.

The time series of ζ and δ emphasizes the efficiency of the dynamical filter for separating BM and IGW and its ability to recover the BM dynamics on short time scales. Furthermore, the filtering highlights the seasonal variability of the diurnal cycle and its dependence on the seasonality of KPP_{hbl}. In the next section, we focus on the diurnal cycle of the filtered fields and its latitudinal dependence.

3.5. Diurnal Lag between Divergence and Vorticity

In addition to the seasonal differences in the diurnal cycle that were discussed in Section 3.4, we found a time lag between the δ and ζ instantaneous intensities in the BM regime. This lag became instantly noticeable in the BM regime by closely inspecting the time series of vorticity and divergence for arbitrary 8-day periods, as per Figure 11h. This pattern was observed for all EBC time series at diurnal scales, particularly in winter. In Figure 11, δ peaks first at around midday and ζ peaks later with a lag of $\sim$3 h. This behavior is consistent with previous studies based on numerical simulations with a higher horizontal resolution [15,20,32].

Figure 11. Time series of dynamical variables for the study area centered at 26.6° N within the Canary current from 17 September to 24 September 2012 (**a**,**c**,**e**,**g**) and from 17 February to 24 February 2012 (**b**,**d**,**f**,**h**). First row (**a**,**b**): mean values for the wind stress ($|\tau|$, blue) and the KPP turbulent boundary layer depth (KPP_{hbl}, red). Second row (**c**,**d**): mean values for the sea surface temperature (T, blue) and ocean net heat flux (oceQnet, red). Third row (**e**,**f**): standard deviations of the normalized vorticity (ζ/f, magenta) and divergence (δ/f, green) fields in the internal gravity wave (IGW) regime. Fourth row (**g**,**h**): standard deviation of the normalized vorticity (ζ/f, magenta) and divergence (δ/f, green) fields in the balanced motion (BM) regime.

To provide a more quantitative perspective, Table 1 shows the phase separation and coherence between ζ and δ calculated by season and area for the diurnal component. The first thing noted is that the coherence between δ and ζ is consistently high in winter with values above 0.95 in all cases, while phase separation shows a trend towards larger values (around 3.5 h) as we approach high latitudes and lower values (around 2.5 h) as we get closer to the tropics. In summer, the picture is not that different, although the trend in

the ζ-δ lag is not as evident as in winter, along with the fact that coherence is considerably smaller in certain study areas, particularly in northern California and southern Benguela.

A complement to Table 1 is Figure 12, which illustrates the trend that the ζ-δ lag follows as a function of latitude in the winter and summer seasons. These delays match what Dauhajre and McWilliams [20] found using their transient turbulent thermal wind balance (TTTW) model, which takes into consideration the difference between the maximum (κ_{max}) and minimum (κ_{min}) RMS values of the vertical viscosity ($\Delta K = \kappa_{max} - \kappa_{min}$), the period in which this varies (T_κ), and the mixed layer depth (H), described in its 1D formulation by a system of nondimensional equations:

$$\begin{pmatrix} u \\ v \end{pmatrix}_t + \Omega \begin{pmatrix} -v \\ u \end{pmatrix} - \Gamma[\mathcal{K}(t) + k] \begin{pmatrix} u \\ v \end{pmatrix}_{zz} = \mathcal{K}(t)(1 - \Gamma) \begin{pmatrix} \overline{u} \\ \overline{v} \end{pmatrix}, \tag{8}$$

where subscripts indicate partial derivatives, $\overline{\mathbf{u}} = (\overline{u}, \overline{v})$ is the steady solution, $\Omega = T_\kappa f_0$, $\mathcal{K}(t) = \cos(2\pi t/T_\kappa)$, $k = 2K_0/\Delta K$, and $\Omega = T_\kappa \Delta K/2H^2$, where Γ represents the ratio of the inertial frequency f_o to the diurnal period, and Γ represents the ratio of the range of mixed time scales ($\Delta K/2H^2$) relative to the diurnal period. These 1D Ekman layer dynamics are strongly determined by atmospheric forcings as well as by their impacts on the amplitude (ΔK) and frequency (or period T_κ) of the variability of the vertical viscosity. Equation (8) expresses that the amplitude and phase separation between ζ and δ are primarily controlled by inertial (Ω) and diffusive (Γ) mechanisms. If the phase separation is zero, the diffusive mechanism is the main driver (δ and ζ evolve in phase with each other). As long as the phase separation is nonzero, there is competition between both mechanisms. Additionally, if the difference between κ_{min} and κ_{max} tends to zero, the amplitude of the diurnal cycle tends to zero as well. The above-mentioned scenario applies when the wind stress is weak and the surface net heat flux is the main atmospheric forcing. Table 1 indicates that both mechanisms play crucial roles in dictating the diurnal cycle. The variation between high latitudes and the lower latitude is about 1 h, indicating that the diffusive mechanism becomes slightly more relevant. In summer, the diurnal excursion of KPP_{hbl} is not as dramatic as in winter. This indicates that the difference between κ_{min} and κ_{max} is small compared to in the winter season. This explains the weak signal of the diurnal cycle in ζ and δ for the summer season.

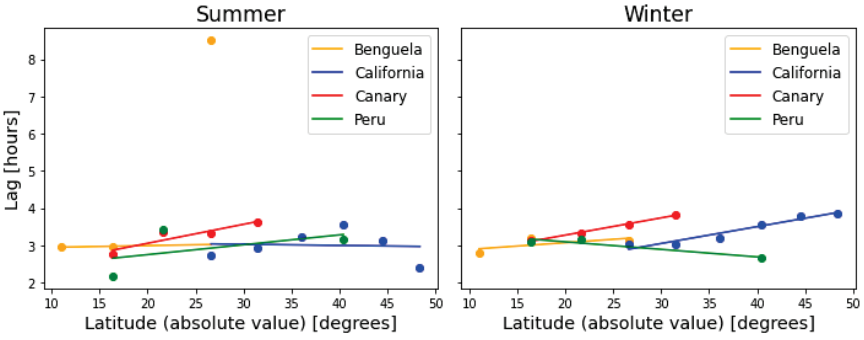

Figure 12. Lag between the divergence and vorticity fields for the four EBC in summer (**left**) and winter (**right**) as a function of the latitude (absolute value). Data points were taken from Table 1, and solid lines correspond to a first-order linear regression for each current, calculated by first excluding data points with a coherence below the 90% confidence interval (as per Table 1).

4. Discussion

BM and IGW are the two main classes of oceanic motion, since they encompass most of the different phenomena observed there and, consequently, account for most of the kinetic energy [9]. Although different in nature, there have been found to be interactions between

these two dynamical regimes, so the interest in studying and understanding BM and IGW has increased in recent years [5,9,18,19].

BM explains most of the advective horizontal and vertical transport of heat and any tracers in the ocean [9,35]. However, diagnosing such transport in the presence of IGW requires, first, the partitioning of both classes of motion. Using low-pass temporal filters to remove IGW contributions also removes the high-frequency part of frontal dynamics [36]. A spatial filter that removes large horizontal scales results in incomplete removal of IGW (see supporting information in Torres et al. [15]). The challenge is that IGW and submesoscale BM share the same short time scale and small horizontal scale ranges. The application of dynamical filters is an alternative to accurately partition BM and IGW. In this research, we aimed to make improvements in two areas: (a) isolating IGW from BM regimes and (b) studying them separately within the four major EBC.

The dynamical filter presented in this study relies on the dispersion relation of IGW of the local tenth baroclinic normal mode. Qiu et al. [18] and Torres et al. [5] applied this approach in the spectral space. However, they did not recover BM in the physical space. Here, we tested the performance of this dynamical filter by recovering BM and IGW in the physical space in four EBC, where IGW showed a kinetic energy level close to the submesoscale BM [5,18,30]. Preliminary analyses (not shown) demonstrated that the correct way to use the dispersion relation of the tenth baroclinic is to combine it with the permissible tide as a cut-off wavenumber-dependent frequency [18].

Recently, Torres et al. [15] developed a simple approach to separate small-scale frontal dynamics from energetic internal gravity waves. Their method relies on two assumptions: IGW are mostly captured by low baroclinic normal modes and, therefore, by vertical scales larger than the mixed-layer depth. Second, small-scale frontal dynamics are trapped within the mixed-layer depth and, therefore, are explained by smaller vertical scales. The disadvantage of the method described by Torres et al (2022) is that BM and IGW cannot be separated below the mixed-layer depth. The method proposed here circumvents this constraint by relying on the local dispersion relation of IGW. The workflow used to apply our method to the ocean numerical simulation was as follows: (1) compute the frequency–wavenumber spectrum of KE; (2) compute the n-*th* local baroclinic normal modes as long as the spacing interval allows it; (3) identify the dispersion relation of the n-*th* baroclinic mode that best separates IGW and B; (4) use this dispersion relation as a criterion to separate BM and IGW in the Fourier space (3D spectral space (k,l,ω)), and (5) compute the inverse Fourier transform to get back to the physical space (x,y,t). This workflow can be applied at any vertical level in the water column and to any component of the speed vector and tracer. Calculations over the filtered variables can be performed, always considering that there will be some noise as the complexity of such calculations grows, since handling slightly unevenly spaced, discrete, windowed data leads to some sort of spectral leakage.

The BM and IGW separation during winter poses a challenge due to the small-scale motions with frequencies larger than M2 internal tides. In this paper, we used the model output of the LLC4320 simulation with a nominal horizontal resolution of $\sim$2 km (1/48°). Our method mitigates the leakage of information from BM to IGW during winter. Nevertheless, the horizontal and vertical resolutions of the LLC4320 prevent the proliferation of small-scale motions with frequencies larger than M2 internal tides. Nelson et al. [37] demonstrated the strengthening of the kinetic energy frequency spectrum at frequencies greater than M2 internal tides when the horizontal and vertical resolutions increase. However, this scenario needs to be tested by analyzing the Joint-PDF of ζ and δ, as we did in this study.

Recovering high-frequency ($>f$) submesoscale motions in the presence of IGW is a critical issue for diagnosing vertical heat transport in the ocean. Su et al. [13] and Siegelman et al. [21] reported the impact of high-frequency motions on vertical heat fluxes using LLC4320, and Richards et al. [38] reported the impact using ROMS simulations, further confirming the contribution of such high-frequency motions as a doubling of the amplitude of the vertical heat flux when compared with low-frequency estimates (<1/36-h).

The performance of our dynamical filter when recovering BM at short time scales was tested in four EBC and in two seasons. The Joint-PDF of ζ-δ in the BM regime revealed ζ/f values close to or larger than one during winter, which reflects the presence of ageostrophic motions [39]. The time series of the same variables displays diurnal variability, which is a distinctive characteristic of submesoscale motions [15,20,40]. Previous studies have described the dependency of the diurnal cycle on the vertical eddy viscosity κ [41]. Here, we reveal, for the first time, the seasonal variability of the diurnal cycle of ζ and δ, which is mainly modulated by *KPP* diagnostics. The model output of LLC4320 does not provide κ, but one can use KPP_{hbl} as a proxy for the seasonal and diurnal variability of the strength of κ.

5. Conclusions and Perspectives

This work contributes to an improvement in the understanding of the Eastern Boundary Currents in the BM regime. The temporal evolution of BM within these currents was characterized. To achieve our objective, we developed a criterion based on dynamical filtering to separate IGW from BM, even in the presence of high-frequency submesoscale BM. Additionally, we identified the air–sea coupling factors with the most impact on short time scale motions—namely, diurnal changes in the eddy viscosity induced by ocean surface heat flux.

The main lesson from our work is twofold. First, within relative low-energy regions such as the EBC, IGW overshadows strong, quasi diurnal submesoscale activity, mainly driven by atmospheric and seasonal forcings. Second, when high resolution tidal-resolving and submesoscale-resolving ocean numerical simulations are available, it is possible to isolate IGW from BM by means of the *dynamical filtering* we propose in this paper.

Currently, highly realistic ocean numerical simulations are continuously running, both regionally and globally. Simulations are capable of resolving submesoscale dynamics and the internal gravity wave continuum. It is critical to separate BM from IGW to achieve accurate vertical heat flux estimates induced by BM at low and high frequencies. The method proposed here can be applied at any vertical level in the water column, opening up the possibility of separating IGW and deep-reaching submesoscale balanced motions [21,42] (whose vertical scale is larger than the mixed-layer depth) and quantifying their respective contributions to vertical heat fluxes. Additional concerns may exist regarding the interaction between IGW and BM motions, such as inertial (or near-inertial) waves that are trapped by eddies. These interactions, however, would not have any impact on the filter. Conversely, analyses in the physical or spectral spaces of BM–IGW interactions could benefit from the separation of the dynamical regimes achieved by our method.

Author Contributions: Conceptualization, H.S.T. and J.G.-V.; Data curation, A.Q.; Formal analysis, A.Q. and H.S.T.; Investigation, A.Q.; Methodology, A.Q. and J.G.-V.; Resources, J.G.-V.; Supervision, H.S.T. and J.G.-V.; Writing—original draft, A.Q.; Writing—review and editing, H.S.T. and J.G.-V. All authors have read and agreed to the published version of the manuscript.

Funding: This research was supported by the Center for Scientific Research and Higher Education at Ensenada (CICESE). The first author received a grant from Consejo Nacional de Ciencia y Tecnología (CONACyT). H.S.T. received support from the S-MODE project, an EVS-3 Investigation awarded under NASA Research Announcement NNH17ZDA001N-EVS3 and the NASA prime contract 80NM0018D0004 with the Jet Propulsion Laboratory, California Institute of Technology.

Data Availability Statement: The LLC4320 model data output used in this study are available as binary files at the ECCO Data Portal (https://data.nas.nasa.gov/ecco/data.php?dir=/eccodata/llc_4320, accessed on 10 November 2021). Version 0.5.1 of the xmitgcm package used for reading LLC4320 data files from the ECCO Data Portal is preserved at https://doi.org/10.5281/zenodo.4574204 (accessed on 5 May 2022) via https://github.com/MITgcm/xmitgcm (accessed on 15 March 2020) [43]. Version 1.2.0 of the code we developed to perform further analyses (e.g., calculation of time series or the frequency–wavenumber spectra of physical variables) is preserved at https://doi.org/10.5281/zenodo.6510574 (accessed on 5 May 2022) via https://github.com/antonimmo/ocean-wk-spectral-analysis (accessed on 5 May 2022) [26].

Acknowledgments: We want to express our thanks to the ECCO Data Portal (https://data.nas.nasa.gov/ecco/data.php?dir=/eccodata/llc_4320, accessed on 10 November 2021) and PO.DAAC (https://podaac.jpl.nasa.gov, accessed on 10 November 2021) service offices for their support in getting access to the necessary LLC4320 data and addressing the issues we encountered during this research.

Conflicts of Interest: The authors declare no conflict of interest.

Abbreviations

The following abbreviations are used in this manuscript:

EBC	Eastern Boundary Current
BM	Balanced motions (regime)
SBM	Submesoscale balanced motions (regime)
IGW	Internal gravity waves (regime)
KE	Kinetic energy
SSH	Surface sea height
FFT	Fast Fourier Transform
LLC4320	MITgcm general circulation model (MITgcm) on a 1/48° nominal Lat/Lon-Cap (LLC) numerical grid
MITgcm	Massachusetts Institute of Technology 55 general circulation model
RV	Vertical component of the relative vorticity (also ζ)
DIV	Horizontal divergence (also δ)
ASO	August–September–October months
JFM	January–February–March months
NASA	National Aeronautics and Space Administration
SWOT	Surface Water and Ocean Topography (satellite mission)
S-MODE	Sub-Mesoscale Ocean Dynamics Experiment
TTTW	Transient turbulent thermal wind balance

References

1. Cubillos, L.; Núñez, S.; Arcos, D. Producción primaria requerida para sustentar el desembarque de peces pelágicos en Chile. *Investig. Mar.* **1998**, *26*, 83–96. [CrossRef]
2. Checkley, D.M.; Barth, J.A. Patterns and processes in the California Current System. *Prog. Oceanogr.* **2009**, *83*, 49–64. Eastern Boundary Upwelling Ecosystems: Integrative and Comparative Approaches. [CrossRef]
3. Chereskin, T.K.; Price, J.F. Ekman Transport and Pumping. In *Encyclopedia of Ocean Sciences*, 2nd ed.; Academic Press: Cambridge, MA, USA, 2008; pp. 222–227. [CrossRef]
4. Thomas, A.C.; Strub, P.T.; Carr, M.E.; Weatherbee, R. Comparisons of chlorophyll variability between the four major global eastern boundary currents. *Int. J. Remote Sens.* **2004**, *25*, 1443–1447. [CrossRef]
5. Torres, H.S.; Klein, P.; Menemenlis, D.; Qiu, B.; Su, Z.; Wang, J.; Chen, S.; Fu, L.L. Partitioning Ocean Motions Into Balanced Motions and Internal Gravity Waves: A Modeling Study in Anticipation of Future Space Missions. *J. Geophys. Res. Ocean.* **2018**, *123*, 8084–8105. [CrossRef]
6. Samelson, R.M. Time-Dependent Linear Theory for the Generation of Poleward Undercurrents on Eastern Boundaries. *J. Phys. Oceanogr.* **2017**, *47*, 3037–3059. [CrossRef]
7. Hill, A.E.; Hickey, B.M.; Shillington, F.A.; Strub, P.T.; Brink, K.H.; Barton, E.D.; Thomas, A.C. Eastern Ocean Boundaries, Coastal Segment (E). In *The Sea: The Global Coastal Ocean: Regional Studies and Syntheses*; Robinson, A.R., Brink, K.H., Eds.; Harvard University Press: Boston, MA, USA, 1998; Volume 11, pp. 29–67.
8. Barton, E.; Arístegui, J.; Tett, P.; Cantón, M.; García-Braun, J.; Hernández-León, S.; Nykjaer, L.; Almeida, C.; Almunia, J.; Ballesteros, S.; et al. The transition zone of the Canary Current upwelling region. *Prog. Oceanogr.* **1998**, *41*, 455–504. [CrossRef]
9. Klein, P.; Lapeyre, G.; Siegelman, L.; Qiu, B.; Fu, L.L.; Torres, H.; Su, Z.; Menemenlis, D.; Le Gentil, S. Ocean-Scale Interactions from Space. *Earth Space Sci.* **2019**, *6*, 795–817. [CrossRef]
10. Arbic, B.K.; Scott, R.B.; Flierl, G.R.; Morten, A.J.; Richman, J.G.; Shriver, J.F. Nonlinear cascades of surface oceanic geostrophic kinetic energy in the frequency domain. *J. Phys. Oceanogr.* **2012**, *42*, 1577–1600. [CrossRef]
11. Polzin, K.L. Mesoscale Eddy-Internal Wave Coupling. Part II: Energetics and Results from PolyMode. *J. Phys. Oceanogr.* **2010**, *40*, 789–801. [CrossRef]
12. Thomas, L.N.; Ferrari, R. Friction, Frontogenesis, and the Stratification of the Surface Mixed Layer. *J. Phys. Oceanogr.* **2008**, *38*, 2501–2518. [CrossRef]

13. Su, Z.; Torres, H.; Klein, P.; Thompson, A.F.; Siegelman, L.; Wang, J.; Menemenlis, D.; Hill, C. High-Frequency Submesoscale Motions Enhance the Upward Vertical Heat Transport in the Global Ocean. *J. Geophys. Res. Ocean.* **2020**, *125*, e2020JC016544. [CrossRef]
14. Balwada, D.; Smith, K.S.; Abernathey, R. Submesoscale Vertical Velocities Enhance Tracer Subduction in an Idealized Antarctic Circumpolar Current. *Geophys. Res. Lett.* **2018**, *45*, 9790–9802. [CrossRef]
15. Torres, H.S.; Klein, P.; D'Asaro, E.; Wang, J.; Thompson, A.F.; Siegelman, L.; Menemenlis, D.; Rodriguez, E.; Wineteer, A.; Perkovic-Martin, D. Separating Energetic Internal Gravity Waves and Small-Scale Frontal Dynamics. *Geophys. Res. Lett.* **2022**, *49*, e2021GL096249. [CrossRef]
16. Wang, J.; Fu, L.L.; Torres, H.S.; Chen, S.; Qiu, B.; Menemenlis, D. On the Spatial Scales to be Resolved by the Surface Water and Ocean Topography Ka-Band Radar Interferometer. *J. Atmos. Ocean. Technol.* **2019**, *36*, 87–99. [CrossRef]
17. Rocha, C.B.; Gille, S.T.; Chereskin, T.K.; Menemenlis, D. Seasonality of Submesoscale Dynamics in the Kuroshio Extension. *Geophys. Res. Lett.* **2016**, *43*, 11304–11311. [CrossRef]
18. Qiu, B.; Chen, S.; Klein, P.; Wang, J.; Torres, H.; Fu, L.L.; Menemenlis, D.; Qiu, B.; Chen, S.; Klein, P.; et al. Seasonality in Transition Scale from Balanced to Unbalanced Motions in the World Ocean. *J. Phys. Oceanogr.* **2018**, *48*, 591–605. [CrossRef]
19. Chereskin, T.K.; Rocha, C.B.; Gille, S.T.; Menemenlis, D.; Passaro, M. Characterizing the Transition From Balanced to Unbalanced Motions in the Southern California Current. *J. Geophys. Res. Ocean.* **2019**, *124*, 2088–2109. 2018JC014583. [CrossRef]
20. Dauhajre, D.P.; McWilliams, J.C. Diurnal Evolution of Submesoscale Front and Filament Circulations. *J. Phys. Oceanogr.* **2018**, *48*, 2343–2361. [CrossRef]
21. Siegelman, L.; Klein, P.; Rivière, P.; Thompson, A.F.; Torres, H.; Flexas, M.; Menemenlis, D. Enhanced upward heat transport at deep submesoscale ocean fronts. *Nat. Geosci.* **2020**, *13*, 50–55. [CrossRef]
22. Welch, P.D. The Use of Fast Fourier Transform for the Estimation of Power Spectra: A Method Based on Time Averaging Over Short, Modified Periodograms. *IEEE Trans. Audio Electroacoust.* **1967**, *15*, 70–73. TAU.1967.1161901. [CrossRef]
23. Flexas, M.M.; Thompson, A.F.; Torres, H.S.; Klein, P.; Farrar, J.T.; Zhang, H.; Menemenlis, D. Global Estimates of the Energy Transfer From the Wind to the Ocean, with Emphasis on Near-Inertial Oscillations. *J. Geophys. Res. Ocean.* **2019**, *124*, 5723–5746. [CrossRef] [PubMed]
24. Pinker, R.T.; Bentamy, A.; Katsaros, K.B.; Ma, Y.; Li, C. Estimates of Net Heat Fluxes over the Atlantic Ocean. *J. Geophys. Res. Ocean.* **2014**, *119*, 410–427. [CrossRef]
25. Erickson, Z.K.; Thompson, A.F.; Callies, J.; Yu, X.; Garabato, A.N.; Klein, P. The Vertical Structure of Open-Ocean Submesoscale Variability during a Full Seasonal Cycle. *J. Phys. Oceanogr.* **2020**, *50*, 145–160. [CrossRef]
26. Quintana, A. Antonimmo/ebc-wk-Spectral-Analysis: V1.2.0, 2022. Available online: https://github.com/antonimmo/ebc-wk-spectral-analysis/tree/1.2.0 (accessed on 5 May 2022).
27. Shcherbina, A.Y.; D'Asaro, E.A.; Lee, C.M.; Klymak, J.M.; Molemaker, M.J.; McWilliams, J.C. Statistics of Vertical Vorticity, Divergence, and Strain in a Developed Submesoscale Turbulence Field. *Geophys. Res. Lett.* **2013**, *40*, 4706–4711. [CrossRef]
28. Biltoft, C.A.; Pardyjak, E.R. Spectral Coherence and the Statistical Significance of Turbulent Flux Computations. *J. Atmos. Ocean. Technol.* **2009**, *26*, 403–410. [CrossRef]
29. Capet, X.; McWilliams, J.C.; Molemaker, M.J.; Shchepetkin, A.F. Mesoscale to submesoscale transition in the California Current system. Part II: Frontal processes. *J. Phys. Oceanogr.* **2008**, *38*, 44–64. [CrossRef]
30. Savage, A.C.; Arbic, B.K.; Alford, M.H.; Ansong, J.K.; Farrar, J.T.; Menemenlis, D.; O'Rourke, A.K.; Richman, J.G.; Shriver, J.F.; Voet, G.; et al. Spectral decomposition of internal gravity wave sea surface height in global models. *J. Geophys. Res. Ocean.* **2017**, *122*, 7803–7821. [CrossRef]
31. Garrett, C.J.R.; Loder, J.W. Dynamical aspects of shallow sea fronts. *Philos. Trans. R. Soc. Lond. Ser. A Math. Phys. Sci.* **1981**, *302*, 563–581. [CrossRef]
32. Dauhajre, D.P.; McWilliams, J.C.; Uchiyama, Y.; Dauhajre, D.P.; McWilliams, J.C.; Uchiyama, Y. Submesoscale Coherent Structures on the Continental Shelf. *J. Phys. Oceanogr.* **2017**, *47*, 2949–2976. [CrossRef]
33. Large, W.G.; McWilliams, J.C.; Doney, S.C. Oceanic vertical mixing: A review and a model with a nonlocal boundary layer parameterization. *Rev. Geophys.* **1994**, *32*, 363–403. [CrossRef]
34. Hoskins, B.J.; Bretherton, F.P. Atmospheric Frontogenesis Models: Mathematical Formulation and Solution. *J. Atmos. Sci.* **1972**, *29*, 11–37. [CrossRef]
35. Ferrari, R.; Wunsch, C. Ocean Circulation Kinetic Energy: Reservoirs, Sources, and Sinks. *Annu. Rev. Fluid Mech.* **2009**, *41*, 253–282. [CrossRef]
36. Feliks, Y.; Tziperman, E.; Farrell, B. Nonnormal Frontal Dynamics. *J. Atmos. Sci.* **2010**, *7*, 1218–1231. [CrossRef]
37. Nelson, A.D.; Arbic, B.K.; Zaron, E.D.; Savage, A.C.; Richman, J.G.; Buijsman, M.C.; Shriver, J.F. Toward realistic nonstationarity of semidiurnal baroclinic tides in a hydrodynamic model. *J. Geophys. Res. Ocean.* **2019**, *104*, 6632–6642. [CrossRef]
38. Richards, K.J.; Whitt, D.B.; Brett, G.; Bryan, F.O.; Feloy, K.; Long, M.C. The Impact of Climate Change on Ocean Submesoscale Activity. *J. Geophys. Res. Ocean.* **2021**, *126*, e2020JC016750. [CrossRef]
39. McWilliams, J.C. A Perspective on the Legacy of Edward Lorenz. *Earth Space Sci.* **2019**, *6*, 336–350. [CrossRef]

40. Sun, D.; Bracco, A.; Barkan, R.; Berta, M.; Dauhajre, D.; Molemaker, M.J.; Choi, J.; Liu, G.; Griffa, A.; McWilliams, J.C. Diurnal Cycling of Submesoscale Dynamics: Lagrangian Implications in Drifter Observations and Model Simulations of the Northern Gulf of Mexico. *J. Phys. Oceanogr.* **2020**, *50*, 1605–1623. [CrossRef]
41. Wenegrat, J.O.; McPhaden, M.J.; Wind, Waves, and Fronts: Frictional Effects in a Generalized Ekman Model. *J. Phys. Oceanogr.* **2016**, *46*, 371–394. [CrossRef]
42. Yu, X.; Garabato, A.C.N.; Martin, A.P.; Buckingham, C.E.; Brannigan, L.; Su, Z. An Annual Cycle of Submesoscale Vertical Flow and Restratification in the Upper Ocean. *J. Phys. Oceanogr.* **2019**, *49*, 1439–1461. [CrossRef]
43. Abernathey, R.; Dussin, R.; Smith, T.; Fenty, I.; Bourgault, P.; Bot, S.; Doddridge, E.; Goldsworth, F.; Losch, M.; Almansi, M.; et al. MITgcm/xmitgcm: V0.5.1, 2021. Available online: https://github.com/MITgcm/xmitgcm (accessed on 5 May 2022).

fluids

MDPI

Article

Effect of the Coastline Geometry on the Boundary Currents Intruding through the Gap

Joseph Kuehl [1,*,†] and Vitalii A. Sheremet [2,†]

[1] Spencer Lab Room 210, Mechanical Engineering, University of Delaware, 130 Academy Street, Newark, DE 19716, USA
[2] Graduate School of Oceanography, University of Rhode Island, Kingston, RI 02881, USA; vsheremet@uri.edu
* Correspondence: jkuehl@udel.edu; Tel.: +1-302-831-2150
† These authors contributed equally to this work.

Abstract: The problem of a geophysical western boundary current negotiating a gap in its supporting boundary is considered. For traditional straight, parallel gaps, such systems are known to exhibit two dominant states, gap penetrating and leaping, with the transitional dynamics between states displaying hysteresis. However, for more complex geometries, such as angled or offset gap configurations, the question of multiple states and hysteresis is unresolved. In such cases, the inertia of the western boundary current is oriented into the gap, hence the assumption that increased inertia promotes gap penetrating loop current states. Here we address the problem numerically in an idealized setting. It is found that despite the inertia of the current being directed into the gap, for large western boundary current transport values, leaping states will be present. That is, we show here that the presence of multiple states with hysteresis for gap-leaping western boundary current systems is robust to both angled and offset gap geometries.

Keywords: western boundary current; loop current; hysteresis; geophysical fluid dynamics

Citation: Kuehl, J.; Sheremet, V.A. Effect of the Coastline Geometry on the Boundary Currents Intruding through the Gap. *Fluids* **2022**, *7*, 71. https://doi.org/10.3390/fluids7020071

Academic Editor: Pavel S. Berloff

Received: 6 January 2022
Accepted: 28 January 2022
Published: 8 February 2022

Publisher's Note: MDPI stays neutral with regard to jurisdictional claims in published maps and institutional affiliations.

1. Introduction

Loop current systems, like the Loop Current in the Gulf of Mexico, which flows between the Yucatan Peninsula and Florida, or the Kuroshio current near the Luzon Strait, between the islands of Luzon and Taiwan, are known to admit at least two fundamental states: gap penetrating and leaping (Figure 1). Which state the system assumes and when the system will transition between states is a major factor influencing hurricane intensity, offshore energy applications, local fisheries, and regional climate [1]. Despite decades of scientific inquiry and major field program initiatives, the fundamental question of loop current predictability remains [1]. Several theories have been proposed to address the underlying physical mechanisms governing transitions between penetrating and leaping states: Farris and Wimbush [2] related the accumulation of local wind stress exceeding a critical value with transitions from leaping to penetrating states for the Kuroshio. Wind forcing has also been shown to affect the seasonal variation of the Kuroshio Intrusion [3,4] including the inertia of the Kuroshio Current upstream of the Luzon Strait [5–7]. Metzger and Hurlburt [8] proposed that mesoscale instabilities cause the Kuroshio penetration to be nondeterministic on long timescales, which is consistent with Yuan et al. [9] who showed how perturbation from mesoscale eddies influence Kuroshio intrusion variability. Sheremet [10] considered changes in the inertia of the western boundary current as a major controlling influence on state transitions and was the first to point out the existence of hysteresis in such systems.

This manuscript seeks to extend the original work of Sheremet, who considered an idealized model for a gap-leaping western boundary current. Transitions between penetrating and leaping states were studied as the gap width was varied in a quasi-geostrophic numerical model. When the gap width is sufficiently large, the western

boundary current inertia competes with the β-effect in the gap, resulting in leaping and penetrating states with hysteresis. Penetrating-to-leaping transitions occur when the width of the zonal jet flowing into the gap becomes comparable with the gap halfwidth. Leaping-to-penetrating transitions occur when meridional advection balances the β-effect. For sufficiently narrow gaps, there are only direct transitions between leaping and penetrating states (no hysteresis). Sheremet's results suggest that when analyzing observational data, it is important to take into account the history of parameters in order to interpret loop current state transitions (and not just parameters describing the current state). It should be noted that this is supported qualitatively by the authors of [2], who related transitions to penetrating states to if local wind stress accumulation exceeded a critical value.

These idealized numerical results have been verified via single-layer model rotating table experiments by Sheremet and Kuehl [11]. This early confirmation was important as it showed that hysteresis in gap-traversing systems is not a numerical artifact. Kuehl and Sheremet [12] continued work on the same laboratory model by considering an expanded parameter space. The ranges of flow rates that exhibited hysteresis were studied for different table rotation rates, Ω, which controls the β-effect in the model. The width of the hysteresis region increased as the rotation rate was increased. The state of the system (penetrating or leaping) was formulated in a two-dimensional phase space as the western boundary current inertia and planetary vorticity varied, which resulted in a mathematical cusp catastrophe surface [13]. Because of the bifurcation of this surface, it is noted that in such systems transitions from one state to another are a result of the disappearance or turning of a particular solution branch, and not necessarily due to an instability to small-scale perturbations as emphasized by [14]. Kuehl and Sheremet [15] further examined hysteresis for a two-layer system to better model more realistic western boundary currents [16]. The bifurcation set for hysteresis was studied for variable Ω. Periodic eddy shedding states were studied as well, and it was noted that eddies shed from a periodic state are fundamentally different from eddies shed during a transition event. For strong penetrating flows, Ekman dissipation can no longer balance the vorticity advection and vorticity must be dissipated from the current as westward-traveling eddies, which is consistent with the momentum imbalance paradox of Pichevin and Nof [17]. Most recently McMahon et al. have extended both the experimental and numerical investigations to include the effects of mean flow through the gap [18,19] and applied a Newton iteration solution method to the numerical model which enables identification of unstable loop current states [20].

Despite the demonstrated resilience of hysteresis to stratification, multiple parameter variations, and mean flow through the gap in the idealized setting, as well as for realistic ocean parameters [21] including the presence of islands in the gap [22], eddy forcing [23–25], and western boundary current variability [18], the hypothesis has not widely been adopted by the Gulf of Mexico Loop current community. The likely reason for this is the unique geometry of the Gulf of Mexico (Figure 2). Notice that the Yucatan Peninsula has a zonal "offset" from the southern tip of Florida by about 2.5°. Further, the orientation of the boundary current forming along the Yucatan is not parallel to the southern coast of Florida. Instead, the inflowing current makes an approximately 120° degree angle with the outflowing current (180° being straight gap with parallel flow). The goal of this manuscript is to show that hysteresis in such gap-leaping western boundary current systems is robust both to gap angle and gap offset.

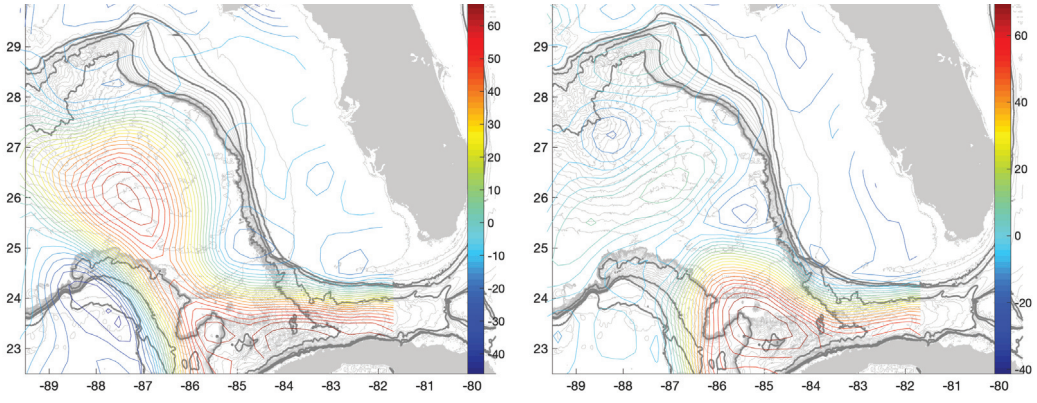

Figure 1. Gulf of Mexico topography with light grey indicating isobaths 5:100:3500 m and dark grey indicating isobaths 250, 500, 1000, and 2000 m. Grey mask indicates land. Superimposed are sea surface height contours for: (**Left**) on and around the 193rd day of 2015. (**Right**) on and around the 57th day of 2017.

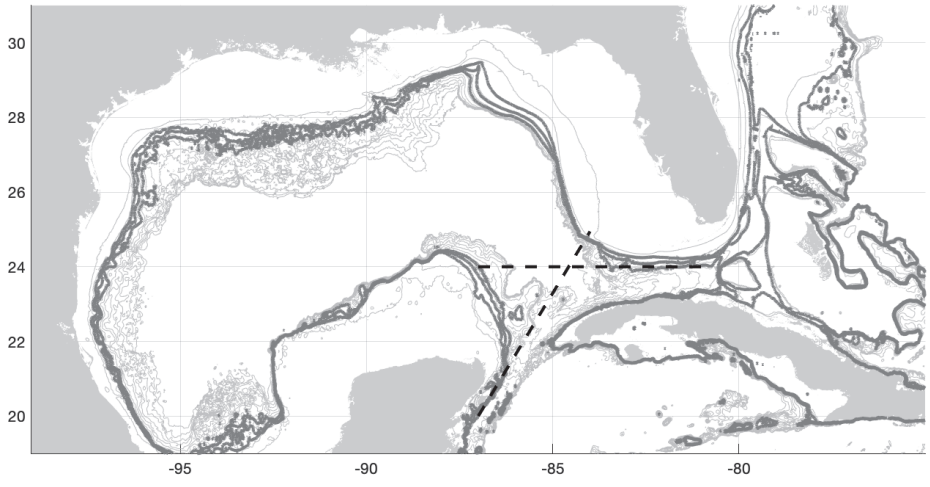

Figure 2. Gulf of Mexico topography with light grey indicating isobaths and dark grey contours indicating the slope. Grey mask indicates land. Dashed lines extend regions of slope against which boundary currents flow. Notice that the Yucatan Peninsula has a zonal "offset" from the southern tip of Florida by about 2.5°. Further, the orientation of the boundary current forming along the Yucatan is not parallel to the southern coast of Florida. Instead, the inflowing current makes an approximately 120° degree angle with the outflowing current (180° being a straight gap with parallel flow).

2. Numerical Model

The numerical model utilized in this study is a barotropic version of the baroclinic model developed and validated in [16,26]. The numerical model was developed to support a series of rotating table laboratory experiments (referenced above). Both the experimental setup and validation of the numerical model have been well-established in the literature, so only a brief summary is provided here. The idealized setup consists of a square tank of width $2L = 1$ m with a sloping bottom to induce a topographic β-effect. In Figure 3, north corresponds to up and east corresponds to right. The flow is driven by a broad Sverdrup interior circulation from the east, which impinges on a north–south oriented vertical ridge,

which extends to the surface, where a predominantly inertial western boundary current forms. Note, in the lab and also in the present model study, it is more convenient to consider a southward flowing western boundary current (flowing from top to bottom in the figures), but, due to the north–south invariance of the quasi-geostrophic barotropic equations, this does not present an issue when interpreting our results in the context of northward-flowing oceanic western boundary currents. The ridge is interrupted at its center by a gap with halfwidth $L_g = 6$ cm, which the western boundary current must negotiate. In the gap region, the western boundary current will either follow geostrophic contours (in this case, constant depth contours) turning into the western basin and forming a loop current or leap directly across the gap. The computations correspond to a mean water depth of $H_0 = 20$ cm, topographic slope of $S = 0.2$ (where $\beta = Sf/H_0$), and a table rotation rate of $\Omega = 0.65$ rad/sec (where $f = 2\Omega$).

The nondimensional problem is formulated as the potential vorticity advection–diffusion equation, as in the quasi-geostrophic approximation

$$\begin{aligned} J(\psi, q) + \lambda_S \tfrac{1}{h}\omega - \lambda_M^3 \nabla^2 \omega = 0 \\ -\nabla(\tfrac{1}{h}\nabla\psi) - \omega = 0, \end{aligned} \tag{1}$$

where ψ is the transport function (defined through the Helmholtz decomposition $h\mathbf{u} = \hat{\mathbf{k}} \times \nabla\psi + \nabla\phi$ with $\nabla^2\phi = \frac{1}{2}h_E\omega$ representing Ekman divergence), $\omega = \nabla \times \vec{u}$ is the relative vorticity, and $q = (1/\hat{\beta} + \lambda_I^2\omega)/h$, $h = 1 - \hat{\beta}y$ and $h_E = (\frac{\nu}{\Omega})^{\frac{1}{2}}$ is the Ekman depth. The nondimensional parameter $\hat{\beta} = \beta L/f = SL/H_0$ is the relative meridional variation of depth over the basin due to the sloping bottom, and h is the fluid depth. Our laboratory experiments and numerical model allow for small but finite values of $\hat{\beta}$, while the quasi-geostrophic approximation is the limit of infinitely small $\hat{\beta}$. The domain is $-1 < x < 1$, $-1 < y < 1$, with north corresponding to positive y and east corresponding to positive x. The kinematic conditions for solving the elliptic equation are $\psi = 0$ along all boundaries, except at the eastern boundary $x = 1$ where inflow/outflow is prescribed $\psi = \Psi_B(y)$, with Ψ_B varying between 0 and 1. The dynamical conditions are no-slip: $v = 0$ at the western $x = -1$, eastern $x = 1$ boundaries and along the ridge, and no-stress $\omega = 0$ at the southern $y = -1$ and northern $y = 1$ boundaries. The "no-slip" is a natural condition of vanishing velocity at a solid boundary. The northern and southern boundaries correspond to the fluid gyre boundaries in the ocean where vorticity and stress are vanishing. In our numerical method, we were restricted by the ridge to be oriented either north–south or diagonally in such a way that the boundary passes through rectangular grid nodes. The values of vorticity at the solid boundaries were calculated assuming the antisymmetry of the tangential velocity component as it was extended outside the fluid domain, which reduces to the formula by Thom [27] for a straight wall. The vorticity values were different on the different sides of the ridge. The arising parameters $\lambda_I = \sqrt{\frac{U_0}{\beta L^2}}$, $\lambda_S = \frac{k_0}{\beta L}$ with $k_0 = f(h_E/H_0)$ and $\lambda_M = \left(\frac{\nu}{\beta L^3}\right)^{\frac{1}{3}}$ are the nondimensional inertial, Stommel, and Munk boundary layer thicknesses as in the standard theory. Where $U_0 = Q/(HL)$ is the Sverdrup interior velocity scale, L is the basin length scale, ν is the kinematic viscosity, and Q is the volume flux. With the viscosity of water $\nu = 0.01$ cm^2/s, for the cases considered here $\lambda_M = 0.0183252$, $\lambda_S = 0.0124034$, and λ_I is varied (typically, $\lambda_I = 0.0392232$ for $Q = 50$ cm^3/s). The corresponding dimensional values (obtained by multiplication by L) were $L_M = 0.92$ cm, $L_S = 0.62$ cm, and $L_I = 1.96$ cm, respectively.

The numerical problem is solved using standard finite differences on a rectangular grid dividing the domain into $N_x \times N_y$ cells. The parameters λ_S and λ_M represent the dissipative effects, while λ_I characterizes the nonlinearity, the strength of the flow. For small boundary layer Reynolds numbers $R = (\lambda_I/\lambda_M)^3$, simple explicit iterations with treating the nonlinear terms as perturbations work well, but for the moderate R the iterations fail to converge [14]. In this case, Newton's method has be to employed for finding steady solutions. We consider a state vector $X = (\omega, \psi)$ consisting of values at all grid nodes

including the boundaries, the size of this vector is $M = (N_x + 1) * (N_y + 1) * 2$. In a symbolic form, the set of Equation (1) is represented by $F(X) = 0$. Substituting an initial guess X_0 into Equation (1) results in the vector of residuals $F(X_0)$ at each grid node of the same size M. In order to find the next iteration X_1 that brings residual closer to vanishing $F(X) = 0$, we need to calculate the Jacobian matrix $J_F[X_0]$ (of size $M \times M$ which depends on X_0) of all first-order partial derivatives of F with respect to X and then solve the linear system

$$J_F[X_0](X_1 - X_0) = -F(X_0) \tag{2}$$

The iterations then continue until the residual (standard deviation and pointwise error) vanishes to the machine accuracy, $O(10^{-11})$. It usually took about seven or fewer iteration steps to reach such convergence. The elements of the Jacobian matrix can be calculated analytically by considering the variational problem corresponding to Equation (1).

$$\begin{aligned} J(\delta\psi, q) + J(\psi, \delta q) + \lambda_S \frac{1}{h}\delta\omega - \lambda_M^3 \nabla^2 \delta\omega = 0 \\ -\nabla(\frac{1}{h}\nabla\delta\psi) - \delta\omega = 0, \end{aligned} \tag{3}$$

where $\delta q = \lambda_I^2 \delta\omega / h$. The variations of the boundary conditions are trivial. It should be noted that the elements of the Jacobian matrix do not have to be calculated exactly. As long as the iterations converge and the residual $F(X)$ vanishes, we get an exact solution to the original problem (1). However, in this idealized problem, we do perform exact analytic calculation of the matrix elements. Finite difference approximations result in a sparse banded type of J_F, and the grids of size up to 1000×1000 can be solved on a computer with 24 GiB of operational memory.

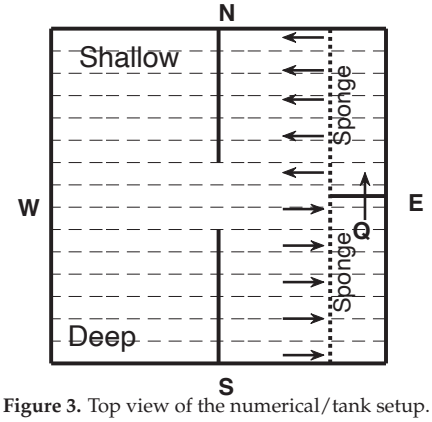

Figure 3. Top view of the numerical/tank setup. Constant depth contours are indicated by dashed lines. The transport, Q, drives the interior circulation.

3. Results

3.1. Angled Gap

We begin by considering the effect of the gap configuration angle. As noted above, the Gulf of Mexico Loop Current encounters an approximately 120° gap angle. Here, we will consider the more extreme configuration of a 90° angle between the ridges forming a gap. This is mainly due to ease of computation. For a 90° configuration, the ridge walls align diagonally with the computational nodes, which facilitates the boundary condition specifications. We note that the existence of hysteresis for a 90° angled gap certainly guarantees the existence of lower gap angle geometries. The resulting hysteresis trace for a $L_g = 5$ cm gap halfwidth at 90° gap angle configuration is shown in Figure 4 in the top two rows.

Starting with lower flow rates and increasing towards higher values (upper panels from left to right in Figure 4A–C), we see the flow is initially in a gap-penetrating flow state with modified β-plumes extending from either gap edge towards the west, roughly following the geostrophic contours [28–32]. As the flow rate increases, the northern β-plume bends further to the south, as the inertia induces the flow to cross isobaths. Eventually, at approximately $Q = 59$ cm^3/s, the penetrating state abruptly transitions to a gap-leaping flow state. The system continues to evolve along the gap-leaping solution branch as the flow rate is decreased (the second row of panels from right to left in Figure 4D–F). Eventually, at approximately $Q = 33$ cm^3/s, the gap leaping flow state abruptly transitions to a gap-penetrating flow state and the hysteresis loop has been fully traced. In presenting the flow patterns we refer to dimensional values of Q relevant for laboratory experiments. The nondimensional boundary-layer Reynolds number $R \propto Q^{3/2}$ is also shown in figure panels. The advection dominates the viscous effects when $R > 1$.

The configuration with 180° gap configuration angle (essentially a straight ridge) also exhibits multiple states and hysteresis, but the range is smaller between Q = 18–21 cm^3/s. The extreme gap-penetrating flow at $Q = 21$ cm^3/s and gap-leaping flow pattern at $Q = 18$ cm^3/s are shown in Figure 4 (third row, two left panels: G, H).

An opposite configuration, when the angle between ridges is 270°, is illustrated in Figure 4 (third row, last two panels). For a weak flow $Q = 10$ cm^3/s the β-plume penetrates into the gap. However, as the flow rate increases the pattern soon smoothly changes into a gap leaping state $Q = 13$ cm^3/s, and remains such for higher Q. No hysteresis is observed in this smooth transition.

In the 90° angle configuration the upstream current points into the gap, which promotes the penetrating flow pattern: the current only needs to turn 45° in order to enter the gap and become a zonal current in the β-plume region. In the 180° case the upstream current needs to make a sharper turn of 90° in order to enter the gap; therefore, the conditions are less favorable for penetration and the range of hysteresis is smaller. Furthermore, in the 270° angle configuration, the upstream boundary current has to turn 315° in order to enter the gap; therefore, the penetrating flow pattern is not favorable and is easily switched to a gap-leaping pattern as the inertia is increased.

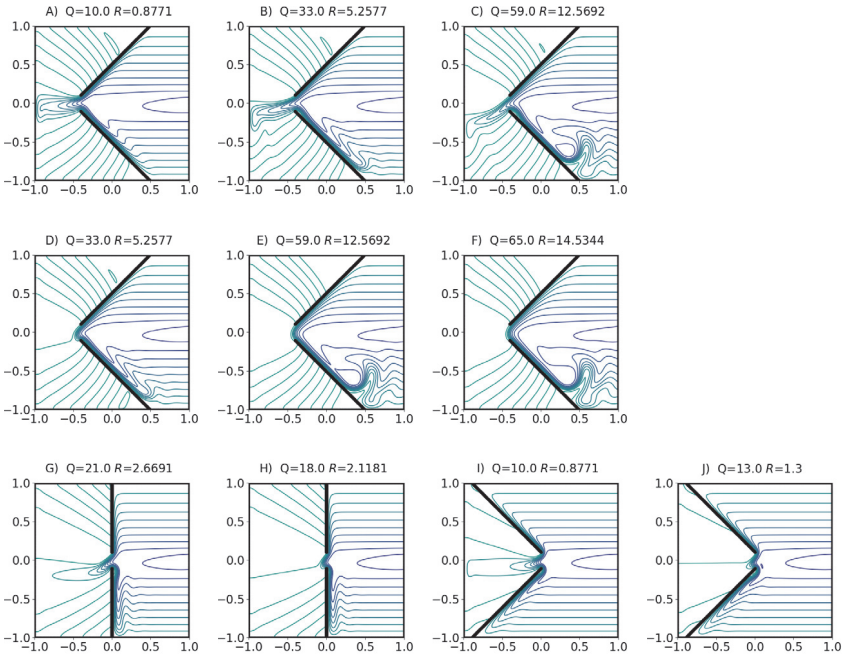

Figure 4. Hysteresis trace for various angled gap configurations of western boundary current, gap halfwidth $L_g = 5$ cm. Shown are the transport functions with contour interval 0.1. Two upper rows are for 90° configuration: from left to right, the top row (panels **A**–**C**) shows the transport function for gap-penetrating states for increasing transport, Q; from right to left, the second row (panels **D**–**F**) shows the transport function in leaping states for decreasing transport. Note the presence of multiple steady flow states between $Q = 33 - 59$ cm^3/s (panels **B**–**E**). The third lowest row shows (first two panels: **G**,**H**) 180° configuration (straight ridge) $Q = 21$ cm^3/s gap-penetrating and $Q = 18$ cm^3/s gap-penetrating state, with multiple states possible between Q = 18–21 cm^3/s. The last two panels in the third row (**I**,**J**) illustrate smooth (without hysteresis) flow pattern transition for 270° gap configuration as the flow rate varies.

3.2. Offset Gap

Similar to the process described above, a series of hysteresis trace studies were performed for a gap that is formed by two meridional ridges that have not only the meridional separation (halfwidth of $L_g = 6$ cm) but also have a zonal offset, L_z, which was varied.

In each case, again, lower flow rates result in penetrating flow states which abruptly transition to leaping flow states as the strength of the western boundary current is increased. Once the system has transitioned to the leaping solution branch, it remains in the leaping states as the strength of the western boundary current is decreased until an abrupt transition back to the penetrating solution branch. The critical flow states can be seen in Figure 5 for a $L_z = -6$ cm negative offset (left panels: A, D); zero-gap offset (middle panels: B, E); a $L_z = 6$ cm positive-gap offset (right panels: C, F). The trend for critical transition states can be seen in Figure 6 with the width of the hysteresis range increasing for positive gap offset and decreasing with negative gap offset. The positive offset corresponds to a configuration that is more favorable for the upstream boundary current to enter the gap if it continued straight forward.

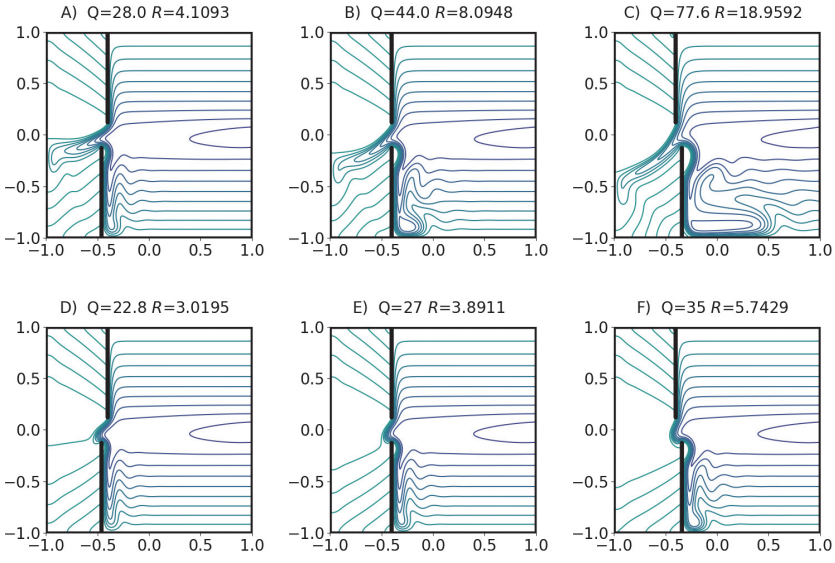

Figure 5. Shown are the critical flow states (transport function) for: (left panels: **A**,**D**) −6 cm gap offset; (middle panels: **B**,**E**) zero gap offset; (right panels: **C**,**F**) 6 cm gap offset. Contour interval is 0.1. Upper panels show increasing flow rates, while lower panels show decreasing flow rates.

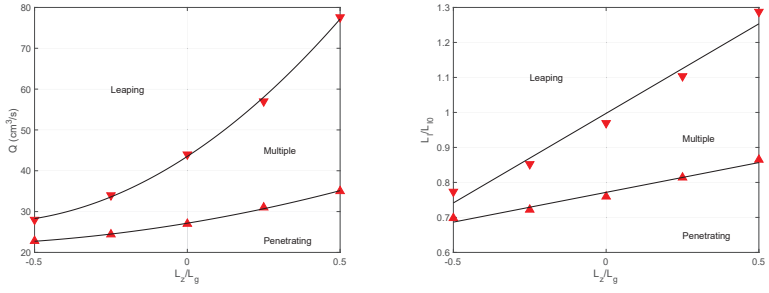

Figure 6. Critical transition transport values as a function of gap offset. Downward triangles indicate the penetrating to leaping transition. Upward triangles indicate the leaping to penetrating transition. Left Panel: Dimensional transport with black curves representing quadratic fits. Right panel: L_I/L_{I0} with black curves representing linear fits.

4. Discussion

For the meridional, north–south oriented, ridges without an offset, the mechanism producing the multiple states is intuitively clear: on one hand, the beta-effect (via a potential vorticity gradient across the gap) promotes the boundary current to drift westward and to penetrate through the gap; on the other hand, the meridional advection promotes the current to jump across. Balancing meridional advection and zonal advection against the β-effect lead to two different scaling: $Q \simeq L_g^3$ and $Q \simeq L_g$ (see details in [10]). Hence, two different sets of critical parameter values at which transitions between penetrating and leaping states occur. This is essentially the root cause of hysteresis in such systems. Furthermore, a cusp bifurcation occurs in the parameter space where the two branches coalesce. The cusp is an invariant feature. If instead of varying the gap width as in [10], we vary another parameter that promotes the current penetration (in the present case it is the configuration angle or gap offset), we will recover a similar behavior: the range of hysteresis will vary and disappear when the penetration is sufficiently obstructed. In the

angled and offset ridges cases, the upstream boundary current may be directed inside the gap thus promoting the intrusion (gap penetration). So the question is, if we increase the inertia (or transport of the boundary current), will it always promote intrusion?

Our previous results (cited above), which are consistent with the findings presented in Figures 4 and 5, have shown that as the width scale of the boundary current, which is a combination of L_M, L_S, and dominantly L_I, exceeds the gap halfwidth, L_g, the current ultimately switches to the gap-leaping regime. This apparent contradiction is most easily explained by considering the offset gap results (Figure 5). Increasing the gap offset, L_z, with the jet pointing inside the gap (positive offset) will delay this transition compared to the zero offset case, but not prohibit a leaping state. Once the boundary current length scale exceeds the gap halfwidth, a transition occurs. Essentially, as the inertia of the current increases, the boundary layer length scale grows to a point where the current will not be able to squeeze through the gap, and a leaping state will result.

Note the quadratic trend of the leaping to penetrating transitions (Figure 6 upward facing triangles, quadratic trend given by solid curve). The transition condition for a straight gap ($L_z = 0$) scales as the boundary layer length scale becoming comparable to L_g. In the case of offset gaps, it is not just the gap halfwidth but also the gap offset must also be accounted. The boundary layers considered are primarily inertial with $L_I \propto \sqrt{Q}$. Thus, relative to the straight gap case, we would expect to see a quadratic dependence of critical boundary current transport as a function of L_z. This is emphasized by the right panel which shows a near-linear dependence of L_I/L_{I0}, where L_{I0} is the inertial length scale at transition for $L_z = 0$. Interestingly, the trend for the penetrating to leaping transition behaves similarly.

This also emphasizes the importance of the parameter L_I/L_g to the penetrating to leaping transition. Or more completely, the ratio of the boundary layer length scale to the gap halfwidth, which is a combination of the Stommel, Munk, and inertial length scale. For typical Gulf of Mexico parameters, the inertial length scale is about 60 km, the Munk length scale is about 30 km, and the Stommel length scale is smaller yet. Thus, typical boundary current length scales would be on the order of 90–100 km. It is also observed that the effective gap halfwidth, between Yucatan and the west Florida shelf, is approximately 150 km. As expected, this puts the Gulf of Mexico Loop Current into a boundary length scale to gap halfwidth ratio parameter regime of around 0.6–0.7, which is consistent with our numerical parameter space. Further, recent results from consideration of realistic Gulf of Mexico topography [20], suggest the Gulf typically operates in an R = 5–15 parameter space, also in agreement with our findings.

The results presented in this manuscript are intended to break the stigma that hysteresis in gap-leaping western boundary current systems only occurs for special geometries (straight gaps with zero offset). Indeed, we have explicitly shown that both angled and offset gap geometries exhibit multiple states and hysteresis. The key insight emphasized in this work is that the more the upstream current is directed into the gap due to geometrical configuration (angled or offset gaps), the more distinct the penetrating and leaping flow patterns are, and the bigger the range of hysteresis in the system is. It should also be noted that the methods utilized in this manuscript have recently been applied to the full-scale Gulf of Mexico [20]. It was found that a barotropic approximation to the upper-layer circulation in the Gulf of Mexico (at full-scale, with a realistic oceanic parameter regime, and for realistic topography similar to Figure 2) displays hysteresis and multiple steady states. Which, given the above results, should be expected.

Author Contributions: J.K. and V.A.S. contributed equally to the analysis, interpretation, and generation of this manuscript. V.A.S. developed the code used in this study. All authors have read and agreed to the published version of the manuscript.

Funding: This research was funded by the National Science Foundation, USA via grant number 1823452 and the National Academies of Sciences, Engineering and Medicine (NASEM) UGOS-1 via grant number 2000009918 and UGOS-2 via grant number 200011071.

Institutional Review Board Statement: Not applicable.

Informed Consent Statement: Not applicable.

Data Availability Statement: The numerical code used in this work can be found at http://sites.udel.edu/kuehl-group/software/ (accessed on 1 January 2022) .

Acknowledgments: The authors are thankful to the National Science Foundation, USA for funding this research via grant number 1823452, and to the National Academies of Sciences, Engineering and Medicine (NASEM) UGOS-1 via grant number 2000009918 and UGOS-2 via grant number 200011071.

Conflicts of Interest: The authors declare no conflict of interest. The founding sponsors had no role in the design of the study; in the collection, analyses, or interpretation of data; in the writing of the manuscript, and in the decision to publish the results.

Sample Availability: Not applicable.

References

1. Committee on Advancing Understanding of Gulf of Mexico Loop Current Dynamics; Gulf Research Program; National Academies of Sciences, Engineering, and Medicine. *Understanding and Predicting the Gulf of Mexico Loop Current: Critical Gaps and Recommendations*; National Academies Press: Washington, DC, USA, 2018; p. 24823. [CrossRef]
2. Farris, A.; Wimbush, M. Wind-induced Kuroshio intrusion into the South China Sea. *J. Oceanogr.* **1996**, *52*, 771–784. [CrossRef]
3. Qiu, B.; Lukas, R. Seasonal and interannual variability of the North Equatorial Current, the Mindanao Current and the Kuroshio along the Pacific western boundary. *J. Geophys. Res.* **1996**, *101*, 12315–12330. [CrossRef]
4. Nan, F.; Xue, H.; Xiu, P.; Chai, F.; Shi, M.; Guo, P. Oceanic eddy formation and propagation southwest of Taiwan. *J. Geophys. Res.* **2011**, *116*, C12045. [CrossRef]
5. Centurioni, L.R.; Niiler, P.P.; Lee, D. Observations of Inflow of Philippine Sea Surface Water into the South China Sea through the Luzon Strait. *J. Phys. Oceanogr.* **2004**, *34*, 113–121. [CrossRef]
6. Wu, C.R.; Hsin, Y.C. The forcing mechanism leading to the Kuroshio intrusion into the South China Sea: Wind-Driven Kuroshio Intrusion. *J. Geophys. Res. Oceans* **2012**, *117*, C7. [CrossRef]
7. Hsin, Y.C.; Wu, C.R.; Chao, S.Y. An updated examination of the Luzon Strait transport: Luzon Strait Transport. *J. Geophys. Res. Oceans* **2012**, *117*, C3. [CrossRef]
8. Metzger, E.; Hurlburt, H. The nondeterministic nature of the Kuroshio penetration and eddy shedding in the South China Sea. *J. Phys. Oceanogr.* **2001**, *31*, 1712–1732. [CrossRef]
9. Yuan, D.; Han, W.; Hu, D. Surface Kuroshio path in the Luzon Strait area derived from satellite remote sensing data. *J. Geophys. Res.* **2006**, *111*, C11007. [CrossRef]
10. Sheremet, V.A. Hysteresis of a Western Boundary Current Leaping across a Gap. *J. Phys. Oceanogr.* **2001**, *31*, 1247–1259. [CrossRef]
11. Sheremet, V.A.; Kuehl, J. Gap-Leaping Western Boundary Current in a Circular Tank Model. *J. Phys. Oceanogr.* **2007**, *37*, 1488–1495. [CrossRef]
12. Kuehl, J.J.; Sheremet, V.A. Identification of a cusp catastrophe in a gap-leaping western boundary current. *J. Mar. Res.* **2009**, *67*, 25–42. [CrossRef]
13. Gilmore, R. *Catastrophe Theory for Scientist and Engineers*; John Wiley and Sons Inc.: Hoboken, NJ, USA, 1981.
14. Sheremet, V.A. A method for finding unstable steady solutions by forward time integration: relaxation to the running mean. *Ocean Model.* **2002**, *5*, 77–89. [CrossRef]
15. Kuehl, J.J.; Sheremet, V.A. Two-layer gap-leaping oceanic boundary currents: experimental investigation. *J. Fluid Mech.* **2014**, *740*, 97–113. [CrossRef]
16. McMahon, C.W.; Kuehl, J.J.; Sheremet, V.A. A Viscous, Two-Layer Western Boundary Current Structure Function. *Fluids* **2020**, *5*, 63. [CrossRef]
17. Pichevin, T.; Nof, D. The momentum imbalance paradox. *Tellus A* **1997**, *49*, 298–319. [CrossRef]
18. Song, X.; Yuan, D.; Wang, Z. Hysteresis of a periodic or leaking western boundary current flowing by a gap. *Acta Oceanol. Sin.* **2019**, *38*, 90–96. [CrossRef]
19. McMahon, C.W.; Kuehl, J.J.; Sheremet, V.A. Dynamics of Gap-leaping Western Boundary Currents with Throughflow Forcing. *J. Phys. Oceanogr.* **2021**, *accepted*. [CrossRef]
20. Sheremet, V.A.; Kan, A.A.; Kuehl, J. Multiple Equilibrium States of the Loop Current in the Gulf of Mexico. *arXiv* **2022**, arXiv:2111.13810.
21. Wang, Z.; Yuan, D.; Hou, Y. Effect of meridional wind on gap-leaping western boundary current. *Chin. J. Oceanol. Limnol.* **2010**, *28*, 354–358. [CrossRef]
22. Mei, H.; Qi, Y.; Qiu, B.; Cheng, X.; Wu, X. Influence of an Island on Hysteresis of a Western Boundary Current Flowing across a Gap. *J. Phys. Oceanogr.* **2019**, *49*, 1353–1366. [CrossRef]
23. Yuan, D.; Wang, Z. Hysteresis and Dynamics of a Western Boundary Current Flowing by a Gap Forced by Impingement of Mesoscale Eddies. *J. Phys. Oceanogr.* **2011**, *41*, 878–888. [CrossRef]

24. Lien, R.C.; Ma, B.; Cheng, Y.H.; Ho, C.R.; Qiu, Q.; Lee, C.M.; Chang, M.H. Modulation of the Kuroshio transport by mesoscale eddies at the Luzon Strait entrance. *J. Geophys. Res. Oceans* **2014**, *119*, 2129-2142. [CrossRef]
25. Yuan, D.; Song, X.; Yang, Y.; Dewar, W.K. Dynamics of Mesoscale Eddies Interacting with a Western Boundary Current Flowing by a Gap. *J. Geophys. Res. Oceans* **2019**, *124*, 4117–4132. [CrossRef]
26. McMahon, C.W.; Kuehl, J.J.; Sheremet, V.A. On the Dynamics of Gap-Traversing Western Boundary Currents with Throughflow Forcing. *J. Phys. Oceanogr.* **2020**, *accepted*.
27. Thom, A. The flow past circular cylinders at low speeds. *Proc. R. Soc. Lond. A* **1933**, *141*, 651–669.
28. Gill, A.E.; Smith, R.K. On similarity solutions of the differential equation $\Psi_{zzzz} + \Psi_x = 0$. *Proc. Camb. Philos. Soc.* **1970**, *67*, 163–171. [CrossRef]
29. Cleary, S.P. A Generalized Heat Equation. Ph.D. Thesis, Department of Mathematics, Michigan Technological University, Houghton, MI, USA, 1987; 33p.
30. Ibanez, R.; Kuehl, J.; Shrestha, K.; Anderson, W. Brief communication: A nonlinear self-similar solution to barotropic flow over varying topography. *Nonlinear Process. Geophys.* **2018**, *25*, 1–17. [CrossRef]
31. Kuehl, J.J. An analytic solution for barotropic flow along a variable slope topography. *Geophys. Res. Lett.* **2014**, *41*, 7591–7594. [CrossRef]
32. Kuehl, J.; McMahon, C. An analytic solution for bottom intensified flow along sloping topography. *Eur. J. Mech.- B/Fluids* **2020**, *82*, 156–160. [CrossRef]

fluids

MDPI

Article

Moored Flux and Dissipation Estimates from the Northern Deepwater Gulf of Mexico

Kurt L. Polzin [1,*], Binbin Wang [2,†], Zhankun Wang [3,4], Fred Thwaites [1] and Albert J. Williams III [1]

[1] Woods Hole Oceanographic Institution, Woods Hole, MA 02543, USA; fthwaites@whoi.edu (F.T.); swilliams@whoi.edu (A.J.W.III)
[2] Geochemical and Environmental Research Group, Texas A&M University, College Station, TX 77845, USA; wangbinb@missouri.edu
[3] NOAA's National Centers for Environmental Information, Stennis Space Center, MS 39529, USA; g.zhankunwang@gmail.com
[4] Northern Gulf Institute, Mississippi State University, Stennis Space Center, MS 39529, USA
* Correspondence: kpolzin@whoi.edu
† Current address: Department of Civil and Environmental Engineering, University of Missouri, Columbia, MO 65211, USA.

Abstract: Results from a pilot program to assess boundary mixing processes along the northern continental slope of the Gulf of Mexico are presented. We report a novel attempt to utilize a turbulence flux sensor on a conventional mooring. These data document many of the features expected of a stratified Ekman layer: a buoyancy anomaly over a height less than that of the unstratified Ekman layer and an enhanced turning of the velocity vector with depth. Turbulent stress estimates have an appropriate magnitude and are aligned with the near-bottom velocity vector. However, the Ekman layer is time dependent on inertial-diurnal time scales. Cross slope momentum and temperature fluxes have significant contributions from this frequency band. Collocated turbulent kinetic energy dissipation and temperature variance dissipation estimates imply a dissipation ratio of 0.14 that is not sensibly different from canonical values for shear instability (0.2). This mixing signature is associated with production in the internal wave band rather than frequencies associated with turbulent shear production. Our results reveal that the expectation of a quasi-stationary response to quasi-stationary forcing in the guise of eddy variability is naive and a boundary layer structure that does not support recent theoretical assumptions concerning one-dimensional models of boundary mixing.

Keywords: turbulence; mixing; bottom boundary layers; stratified Ekman layer

Citation: Polzin, K.L.; Wang, B.; Wang, Z.; Thwaites, F.; Williams, A.J., III. Moored Flux and Dissipation Estimates from the Northern Deepwater Gulf of Mexico. *Fluids* **2021**, *6*, 237. https://doi.org/10.3390/fluids6070237

Academic Editors: Joseph J. Kuehl, Pengfei Xue and Fabrice Veron

Received: 20 May 2021
Accepted: 18 June 2021
Published: 30 June 2021

1. Introduction

Direct flux measurements of momentum, temperature, and salinity have been made in boundary layer regimes for decades using stable platforms such as bottom landers [1] or sensors mounted on rigid structures penetrating ice [2]. Such platforms are of limited height in comparison to the oceanic bottom boundary layer, which often exceeds 10 s of meters in height and the imprint of bottom boundary conditions may exceed 100 s of meters if internal wave processes are in play. There is thus a compelling need to extend flux measurements much further from the bottom boundary than is possible with bottom landers.

This can potentially be accomplished by placing flux sensors on conventional moorings —a collection of devices connected to a wire and anchored on the sea floor. A fundamental unknown in so doing is potential contamination of the ocean velocity and flux estimates by package motion and effects related to flow distortion from the mooring elements. Here, we report on our attempts to place an acoustic travel time sensor, the Modular Acoustic Velocity Sensor (MAVS [3], Figure 1), on a conventional mooring deployed as part of a project whose goal is to document and understand mixing associated with flow over complex topography on the continental slope in the northern Gulf of Mexico.

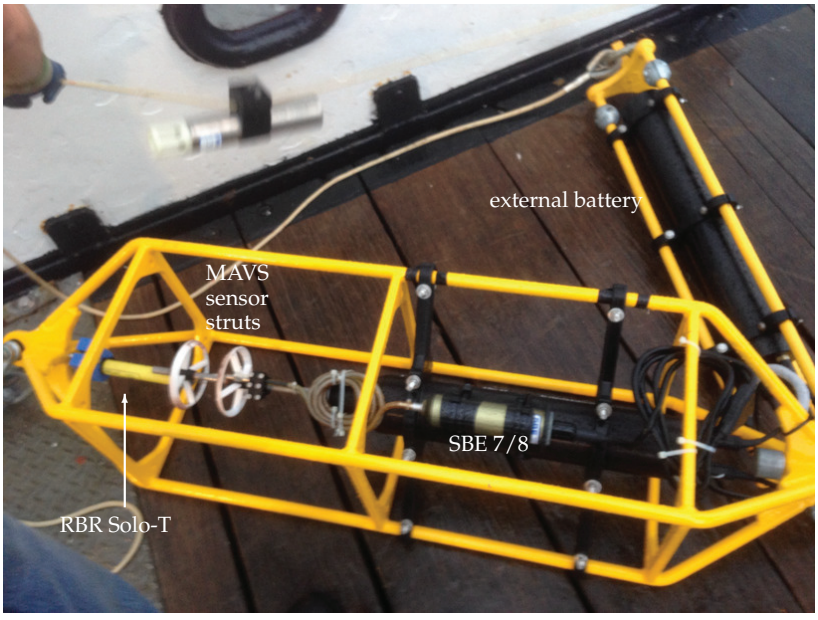

Figure 1. Picture of the enhanced MAVS immediately after recovery. The RBR SoloT temperature sensor is the yellow sensor to the left, the white rings hold the transducer pairs for the MAVS, and the metallic green cylinder is the pressure case for either the SBE-7 or SBE-8 microstructure sensor electronics. An external battery is placed within a second mooring cage in the upper right.

Our experience is that there are no intrinsic limitations to using such enhanced MAVS as flux sensors on conventional moorings relative to their use on bottom landers. This opens up a world of exploration. Caveats, though, abound and further improvements are discussed. This report concerns the geophysical interpretation of data obtained in the first deployment of the prototype, which was tested as part of a boundary mixing experiment along the continental slope of the northern Gulf of Mexico, Figure 2. Moored efforts consisted of short (75 m tall) moorings on the 825 and 600 m isobaths, which we refer to as 'deep' and 'shallow'. The MAVS prototype was placed at 10 m height above bottom (H_{ab}) on the deep mooring, Figure 3, with sensor details contained in Table 1.

Table 1. Table of sensor depths, sampling intervals, mean temperature and dissipation estimates. Turbulent kinetic energy dissipation rate estimates (ϵ) in column 6 are derived from (10) and the temperature variance dissipation rates (χ) are obtained via (11) using those ϵ estimates. In other columns, dissipation rate estimates use (13) and assume a dissipation ratio $\Gamma = 0.2$. The MAVS-RBR $\chi/2$ is a factor of five smaller than the production band estimate, 1.4×10^{-7} C^2 s^{-1}. See text for further details. Estimates are quoted for 2.8 day and 8-day time averages.

Sensor	Variables	H_{ab} [m]	Sampling Interval [s]	$\bar{\theta}$ [C]	ϵ & χ 2.8 Day [m^2 s^{-3}] & [C^2 s^{-1}]	ϵ 2.8 Day [m^2 s^{-3}]	ϵ 8 Day [m^2 s^{-3}]	χ 2.8 Day [C^2 s^{-1}]	χ 8 Day [C^2 s^{-1}]
RDCP	u,v,w	(73)	3600		n/a				
SBE-39	T	60	3	5.696		1.1×10^{-8}	8.9×10^{-9}	1.4×10^{-8}	1.1×10^{-8}
SBE-39	T	47	3	5.631		4.3×10^{-9}	7.9×10^{-9}	5.6×10^{-9}	1.0×10^{-8}
SBE-39	T	34	3	5.565		6.8×10^{-9}	2.3×10^{-8}	7.7×10^{-9}	2.5×10^{-8}
SBE-39	T	13.5	3	5.473		9.2×10^{-8}	5.6×10^{-8}	7.4×10^{-8}	4.4×10^{-8}
MAVS	u,v,w	10	1/6.25		1.4×10^{-7} (u) 1.1×10^{-7} (v) 1.1×10^{-7} (w)				
RBR	T	10	0.5	5.462	5.4×10^{-8}	6.4×10^{-8}	2.9×10^{-8}	4.3×10^{-8}	1.9×10^{-8}
SBE-39	T	8	3	5.459		3.4×10^{-8}	1.8×10^{-8}	1.5×10^{-8}	7.8×10^{-9}

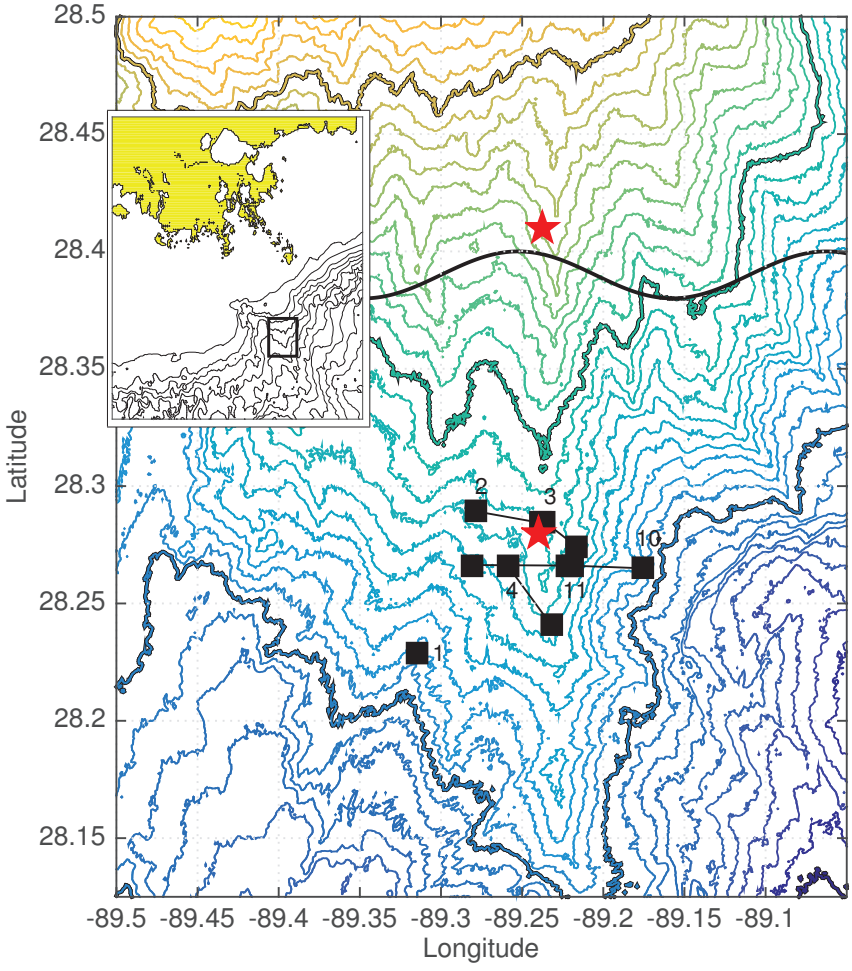

Figure 2. Topography about the deep mooring. Contour intervals are at 25 m with thick lines denoting the 500, 750, and 1000 m isobaths. Mooring locations are depicted with red pentagrams. The locations of CTD casts and tow-yos in the vicinity of the deep mooring are depicted with black squares and connecting lines. Numbers correspond to the initial positions of the respective casts/tow-yos. The inset graphic locates the experimental area on the eastern flank of Mississippi Canyon. The solid black trace at the top depicts the horizontal wavelength $\lambda_h = 2\pi U/f = 18$ km with $U = 0.20$ m s^{-1}.

The need to understand boundary mixing processes in the Gulf of Mexico is placed into perspective by the catastrophic blowout of the Deepwater Horizon oil well, which released about 4 million barrels of oil and 2.5×10^8 standard m^3 of natural gas [4,5]. Nearly half of the discharged oil and most of the low molecular weight gases [4,6] formed a prominent plume about 300 m above the well head [7], which was located at 1522 m water depth. This study follows and was motivated by a deliberate tracer release experiment [8] directed at documenting linkages between small scale processes and large scale effects at the deep plume level.

That tracer release implied that the estimated diapycnal (cross-isopycnal) dispersion was associated with a boundary enhancement, but the process was not revealed in that study: Gulf of Mexico tides are relatively weak [9] and thus near-boundary mixing associ-

ated with internal tide generation and dissipation, e.g., Refs. [10,11] is unlikely. There is a notable near-inertial source associated with sea-breeze forcing at diurnal periods [12,13]. Simple ray tracing kinematics suggests, however, that the response to diurnal forcing over the Texas shelf shoots over the top of the northern Deepwater Gulf. This promotes a hypothesis that low frequency flows over the sloping and rough topography of the northern Gulf are the causal agent. From a phenomenological perspective, low frequency currents along the Northern Gulf are dominated by transient eddies associated with Loop Current Eddies, Topographic Rossby Wave variability, and local atmospheric forcing [14–17] rather than time mean flows. Here, we do not concern ourselves with the episodic nature of such flows or how representative the observations are of an ensemble average. Rather, here we attempt to place our observations into a context of understanding how the bottom boundary layer can couple with the internal wavefield over sloping and rough topography.

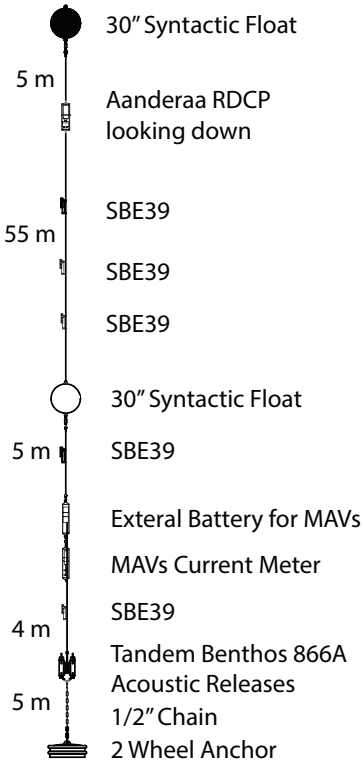

Figure 3. Schematic of the deep mooring.

1.1. Essential Parameters

The moored data resolve the time scales of isotropic 3D turbulence, anisotropic stratified turbulence, and wave-like motions. Given this richness, our initial presentation is necessarily detailed to convey the nuances of the coupling between these timescales on the lower frequency flow. We deliver our interpretation by dynamical regime after noting a few basic external parameters:

- Rotation: The Coriolis parameter f, conveying the time scale at which rotational effects is important, is $f = 6.9 \times 10^{-5}$ s^{-1} at the mooring location. Rotation implies a height scale through Ekman layer dynamics and impacts the aspect ratio along which internal wave crests and troughs are aligned via linear internal wave kinematics.

- Stratification: The buoyancy frequency N represents gravitational forces within a fluid of varying density. Theoretical endeavors refer to an external stratification not influenced by the boundary mixing process. An estimate of this is provided by CTD profiles taken to the south and east of the mooring in slightly deeper water. External to the boundary, stratification at the depth of the MAVS is $N_{ext} \cong 2.8 \times 10^{-3}$ s^{-1}. Stratification at the sensor, positioned at 10 m height above bottom ($H_{\rm ab} = 10$ m), is smaller, $N_{bdy} \cong 2.0 \times 10^{-3}$ s^{-1}.
- Topography provides two non-dimensional parameters by itself: the continental slope is $\alpha \cong 1/70 - 1/50$ if we take the separation between the 600 and 825 m isobaths on which the two moorings are located. Topographic roughness with dominant horizontal wavelengths of $\lambda_h \sim O(20)$ km having a zonal orientation is superimposed upon this slope (Figure 2), with similar aspect ratios (slopes) characterizing the roughness in the vicinity of the mooring.

1.2. Boundary Layers

Turbulent stresses associated with the viscous condition of no-flow at the bottom boundary result in a hierarchy of boundary layers. The one that concerns us most in this geophysical context is the Ekman layer. Stratification is understood to limit the height to which the turbulent stress can penetrate, e.g., Ref. [18]. For a stably stratified bottom boundary layer over a flat bottom, general formulations for the boundary layer height from Weatherly and Martin [19] and Zilitinkevich and Esau [20] are [18]:

$$\begin{aligned} \delta_{\rm WM} &= A\frac{u_*}{f}(1+\frac{N_{ext}^2}{f^2})^{-1/4} \\ \delta_{\rm ZE} &= 0.5\frac{u_*}{f}(1+0.15\frac{N_{ext}}{f})^{-1/2} \end{aligned} \tag{1}$$

in which u_* is the friction velocity. Weatherly and Martin [19] argue for $A = 1.3$ and identify $\delta_{\rm WM}$ as the depth at which the turbulent kinetic energy becomes zero. The 'height' of the Ekman layer is not uniquely defined: one can alternately use the turning of the velocity vector or velocity magnitude relative to the free stream velocity [21,22]. Moreover, the weakly stratified limit of $\delta_{\rm WM}$ can be distinguished from the depth of penetration typically assigned to an unstratified fluid, $\delta_{ekman} = (0.4 \to 0.5)u_*/f$ [23]. The strongly stratified limits both tend to $1.3/\sqrt{fN}$, slightly smaller than the analytic formulation for the ocean's surface layer from Pollard et al [24], $2^{3/4}/\sqrt{fN}$, resulting from a bulk Richardson number closure.

For the intent of interpreting the measurements, we relate u_* to a quadratic drag law with drag coefficient C_d

$$u_* = \sqrt{C_d U^2}\,, \tag{2}$$

where U is the velocity in the farfield of the log-layer underlying the Ekman layer. For scaling purposes, we will use $C_d = 2.5 \times 10^{-3}$, $U = 0.2$ m s^{-1} and $N_{ext}/f = 40$ and refer to these as our 'standard parameters'. In Section 4.5, we review our results and consider the consequences of changes to these standard parameters.

In the absence of stratification, the Ekman layer has a nominal height of

$$\delta_{ekman} = (0.4 \to 0.5)u_*/f \cong 60 \to 70\,\text{m}$$

Using formulae (1), the stratified Ekman scale height clocks in at

$$\delta_{strat} \cong 28\text{–}30\,\text{m}$$

A further caveat is that the height scales δ_{ekman} and δ_{strat} are asymptotic (long time) results for boundary layers over flat topography. Analytics [24] and numerical [25] simulations suggest such states are reached on an e-folding time scale of about half an inertial period. This rapid adjustment is not the case for boundary layers over sloping topography.

When mean flow is oriented in the same direction as Kelvin wave propagation (i.e., with shallower topography to the right in the Northern Hemisphere), this bottom boundary condition is anticipated to trigger a downslope mass and buoyancy transport in the Ekman layer, leading to a reduction in the near-bottom flow and a decrease in drag (a steady-state paradigm known as the arrested Ekman layer [26,27]). In this steady-state paradigm, the Ekman layer is horizontally stratified and in thermal wind balance. Assuming the bottom boundary layer is well mixed, simple geometric considerations return the height of the buoyancy anomaly required to reduce the flow to zero [27]. This scale is

$$\delta_{\text{arrest}} = \frac{Uf}{\alpha N_{ext}^2} \tag{3}$$

in which α is the topographic slope. For our standard parameters, this arrest height scale evaluates as

$$\delta_{\text{arrest}} \cong 100 \text{ m} .$$

This height scale is significantly smaller than more sophisticated approaches to closures for the long-term steady state [25], and the increasing disparity between δ_{arrest} and the nominal penetration depths in a stratified Ekman layer δ_{strat} deserves further inspection.

The underpinning of the arrested Ekman layer state is shear production associated with the along slope geostrophic flow, which then introduces downslope transport of less dense water distributed over the height scale in which the bed stress u_* is deposited. Within this paradigm, the buoyancy flux is supported in association with turbulent production in the along slope direction. The bottom boundary layer height scale grows as approximately $t^{1/2}$, analogous with the behavior of buoyant convection supported by a boundary condition, but metered by the downslope transport of buoyancy distributed within the Ekman layer, for times far longer than the stratified Ekman layer transient phase.

Discarded in this explanation of the arrested state is a fast time scale of approximately f^{-1} [26], which, in a one-dimensional slope normal model of the bottom boundary layer, consists of internal wave motions parallel to the topography [25]. The details of the coupling between the boundary layer processes and the internal wave response are not fully understood [25,28,29], but these oscillatory cross-slope motions play a role in communicating statically unstable conditions associated with downslope buoyancy transport in the Ekman layer to the arrest height scale [25]. This represents a direct coupling of the internal wavefield with the bottom boundary layer.

1.3. Internal Waves

The characterization of the bottom boundary layer in the previous subsection assumes the bottom to either be flat or a planar sloping boundary, leading to a one-dimensional representation. Topographic irregularities represent an intrinsic break in this assumption. Topographic irregularities will impose their horizontal scales on the flow field, introducing a vertical velocity that provides direct coupling with internal waves that potentially leads to significant vertical gradients and mixing. When the amplitude of the topographic variability is small and has length scales permitting the radiation of internal waves, internal lee waves [30] are generated. When the topographic variability is large, however, near-boundary wave breaking, hydraulic like effects, flow separation, and vortex shedding arise and dominate the radiating response, e.g., [31].

In the small amplitude limit of this problem, the internal wave dispersion relation,

$$\frac{\sqrt{\omega^2 - f^2}}{N} = \frac{k_h}{m} \tag{4}$$

links wave frequency ω to wave aspect ratio k_h/m, in which k_h is horizontal wavenumber magnitude and m is vertical wavenumber. The quasi-steady limit of this problem, for which the Eulerian frequency σ is small, i.e., $\omega = \sigma - \mathbf{k} \cdot \mathbf{U} \cong \mathbf{k} \cdot \mathbf{U}$ with horizontal velocity

U and horizontal wavenumber **k**, gives rise to a well defined height scale and vertical wavelength $\lambda_v = 2\pi\delta_{\text{form}}$ of

$$\delta_{form} = U/N_{\text{ext}} \tag{5}$$

in the hydrostatic non-rotating approximation, which evaluates as

$$\delta_{form} \cong 70 \text{ m}$$

As with the Ekman layer on a slope, theory [32] is a bit more complicated with the addition of planar sloping topography. In the quasi-stationary limit, wave crests are aligned with topographic crests, and, if the topographic crests run upslope-downslope, there is a minimum wave aspect ratio and minimum wave frequency[32] at the topographic slope α:

$$\omega(\alpha) \geq (\frac{\alpha^2 N^2}{f^2} + 1)^{1/2} f \tag{6}$$

which evaluates as

$$\omega(\alpha) \geq 1.18 f$$

for our standard parameters.

The distinction between 'large' and 'small' amplitude topography is quantified in this context by a steepness parameter

$$s = N_{ext} h_{rms}/U \tag{7}$$

in which h_{rms} represents the root-mean-squared topographic perturbation and U the impinging flow [31]. The steepness parameter can be cast as a ratio between wave aspect ratio $k/m = kU/N$ and rms topographic slope kh_{rms}. Estimates of the steepness parameter were arrived at by spatial filtering of the topography in Figure 2 using Fourier methods and low-order polynomial fits to isolate horizontal wavelengths $k_h > f/U$. The estimates indicate $1/2 < s < 1$, implying the potential for finite amplitude effects. Evidence for an internal hydraulic transition slightly upslope of the deep mooring is presented in a companion paper. The interpretation of s is qualified by the addition of a large scale slope and possible complications of rotation.

The rotation of the velocity vector with depth is understood to imply the sense of energy propagation [33]: counterclockwise phase rotation of the horizontal velocity vector implies upward energy propagation in the northern hemisphere. This is in the same sense as the rotation of the velocity vector in a downwelling Ekman layer and thus complicates the interpretation of turning angles associated with turbulent stresses.

1.4. Instabilities

A downwelling Ekman layer presents a sink of potential vorticity and the opportunity for anomalously signed potential vorticity at the bottom boundary [34]. In a parallel shear flow without boundaries, such anomalously signed potential vorticity is unconditionally unstable [35] to a class of instabilities that arise in the presence of rotation. It is further understood that the arrested state over uniform sloping topography is unstable to such dynamics [36]. The applicability of potential vorticity dynamics to the observations presented below is speculative. What we see may well arise from forcing related to departures from that planar sloping boundary (i.e., roughness) and external forcing (e.g., by tides) that do not map well onto the boundary conditions assumed for simplified instability calculations.

1.5. Organization

This paper is organized as follows: instrumentation and methods are presented in Section 2. The data are presented as time series in Section 3.1 and the vertical structure is discussed in Section 3.2. Section 3.3 presents the high frequency MAVS and thermistor data as spectra along with inertial subrange interpretations of turbulent dissipation and mixing.

Section 3.4 presents and interprets a co-spectral analysis, largely focused upon the MAVS sensor, in which production regimes and inertial subranges are identified. We discuss our findings in Section 4.

2. Materials and Methods

We deployed two moorings at the work site, one at roughly 825 m and one at 600 m water depth. These moorings both had a downward looking Aanderaa RDCP at about 75 m above bottom and 5 SBE-39s with nominal spacing of about 10–15 m. The deeper mooring additionally had an enhanced MAVS at about 10 m H_{ab} and was outfitted to record analog data being streamed from SBE-7/8 microstructure temperature/conductivity sensors. There was also an RBR-Solo temperature sensor inserted into the sampling volume of the MAVS acoustic travel time sensor. This RBR was internally recording. We will focus on the turbulence measurements from the deep mooring in this study. These moored sensors are discussed in Section 2.1 and methods for their interpretation presented in Section 2.2. Sensor details and statistics are tabulated in Tables 1 and 2.

Table 2. Table of momentum: mean (u, v, w) and $(\overline{u'w'}, \overline{v'w'})$. Turbulent production band estimates utilize $\sigma > 1 \times 10^{-4}$ s^{-1}. Internal swash band fluxes are in parentheses () and employ $\sigma < 1 \times 10^{-4}$ s^{-1}.

Sensor	U [m s^{-1}]	V [m s^{-1}]	W [m s^{-1}]	$u'w'$ [m^2 s^{-2}]	$v'w'$ [m^2 s^{-2}]
RDCP 8.0 day	−0.185	0.009	−0.018	n/a	n/a
RDCP 2.8 day	−0.189	0.003	−0.017	n/a	n/a
MAVS 2.8 day	−0.17	−0.12	−0.019	3.9×10^{-5} (0.2×10^{-5})	2.6×10^{-5} (6×10^{-5})

2.1. Moored Sensors

2.1.1. Modular Acoustic Velocity Sensor (MAVS)

The insight motivating this effort is that the intrinsic resolution of the MAVS is 0.3 mm/s, significantly smaller than the single ping uncertainty associated with Doppler technology with greatly reduced energy costs at that single ping level. Noise sources for the MAVS are understood to be dominated by motion related to strumming of the mooring cable and vortex shedding from the sensor support structures [37]. Both cable and sensor supports have similar dimensions and hence similar Strouhal frequencies, implying contaminations at 6–8 Hz at relative flow speeds of 0.2 m s^{-1}. This implies spatial scales via Taylor's frozen field hypothesis that are similar to, or smaller than, the 10 cm spatial scale of the MAVS sampling volume and, arguably, are well removed from the spatial scales that characterize turbulent production. A model of the sensor response is presented in [38]. Sufficiently rapid sampling will eliminate aliasing of this noise from within the production and inertial subrange regions of interest. Such rapid sampling required increased memory and battery capacity that was (incompletely) implemented here. Issues of package motion, such as contamination of the tilt measurements by horizontal accelerations, were addressed by augmenting the nominal tilt sensor and compass with a VN100 motion package. The instrument is pictured in Figure 1.

The MAVS was set to run as fast as possible by turning off the compass and using the VN-100s magnetometer for heading data. This resulted in a roughly 6.25 Hz sample rate for 4096 samples. The effects of package motion related to mooring strumming were aliased at this sampling rate. Data gaps between files of roughly 3 s were taken care of by linear interpolation. Time base syncing with the other sensors was accomplished by assuming that the MAVS clock drift was negligible and aligning the records during mooring deployment. The MAVS data record is only 2.8 days of the 9-day deployment. The memory filled up because an extra small memory card was unintentionally inserted. Hardware limits at this data density are $O(100)$ days. Additionally, the VN-100 motion package was mounted upside down and backwards. This was corrected by mapping the velocities onto the coordinate system of the motion package, making corrections for package motion, then mapping the velocities back to the nominal instrument coordinate system.

2.1.2. Aanderaa RDCP

An Aanderaa recording Doppler Current Profiler was placed at 73 m H_{ab} on both moorings. Set on low power mode, this sensor was limited to about a 5 m range. Subsequent usage on a high power mode returned a similarly limited range.

2.1.3. RBR Solo-T

A self contained RBR Solo-T temperature logger was mounted such that its sensing element was within the MAVS measurement volume. The protective plastic sensor guard was cut away from the tip to reduce flow obstruction. The manufacturer quotes time constants τ_c of 0.7 s and 0.1 s for their two sensor tips, with five times these metrics representing the time for a response after plunging into a cold bath to be within 99% of the final value. We employed the slower of these and sampled the unit at 2 Hz. This introduces sensor response issues at the highest frequencies that were addressed in the context of a single pole transfer function [39] and simple spectral model for aliasing. The single pole transfer function implies a phase lag of $\pi/4$ radians at $\sigma\tau_c = 1$, where σ is frequency. The associated phase shifts do not extend to low frequencies that would impact our interpretation of temperature–velocity covariance.

2.1.4. SBE-39

Five SBE-39 temperature recorders were placed on the mooring cable at 10–15 m intervals, Table 1. These were early model SBE-39s with limited memory and duration. They were set to sample at 3 s intervals and to exhaust available memory over the 10-day deployment. The manufacturer quotes a 0.5 s time constant in the context of a single pole response function [39]. It was noted that the SBE-39's occasionally pause in their recording of data.

2.1.5. SeaBird 7/8s

The MAVS was modified to log analog output from SeaBird 7 and 8 fast response temperature and dual needle conductivity probes that are more commonly used for microstructure applications. The SBE 7/8 analog capture was a nice idea featuring fast response sensors and the ability to match the sampling rate of the MAVS. This scheme did not return useful data.

2.2. The Turbulent Paradigm

The basic tools for interpreting the moored data are to (1) identify power laws associated with inertial subranges and ratios between variables and (2) quantify production and fluxes in the context of a Reynolds decomposition of the equations of motion. The Reynolds averaged balance for turbulent kinetic energy (TKE) is

$$\partial_t E + N.L. + \mathcal{P} = \mathcal{B} - \epsilon - \nabla \cdot \overline{u'p'} \tag{8}$$

in which $E = (u'^2 + v'^2 + w'^2)/2$ is the turbulent kinetic energy, $N.L.$ are triple correlations and represent nonlinear interactions responsible for transport of energy to smaller scales, production $\mathcal{P}$ corresponds to terms like $\overline{u'w'}\overline{u}_z$, buoyancy flux $\mathcal{B} = -g\rho\overline{w'\rho'}$ represents work done against gravity in a stratified fluid, ϵ is the rate of dissipation of turbulence kinetic energy and $\overline{u'p'}$ represents pressure work. Prime stands for fluctuations and bar is used for the average in our equation notations. Far from boundaries, the expectation [40] is for a production–dissipation balance with buoyancy flux (mixing) being a small (15%) residual. The situation is not so clear in the presence of a boundary for several reasons. First, flow over non-uniform topography can result in significant flow accelerations and turbulent forcing (Section 1.3) in association with pressure work (form drag). Second, the nonlinear terms $N.L.$ can be cast as the divergence of a spatial flux, and integration over a volume leads to the understanding of the potential transport of turbulent energy E

within the boundary layer. The Reynolds averaged balance for a scalar such as temperature θ is:

$$\frac{1}{2}\frac{\partial\overline{\theta'^2}}{\partial t} + \nabla\cdot\overline{u'\theta'^2} + \overline{u'\theta'}\cdot\nabla\overline{\theta} = -\frac{\chi}{2} \tag{9}$$

in which $\nabla\cdot\overline{u'\theta'^2}$ are nonlinear terms responsible for downscale transport of temperature variance, $\overline{u'\theta'}\cdot\nabla\overline{\theta}$ are production terms that are similar to the buoyancy flux in the turbulent kinetic energy equation, and χ is the rate of dissipation of temperature variance. The nominal paradigm is a production–dissipation balance with the vertical production of buoyancy being balanced by dissipation [41]. As with the turbulent kinetic energy equation, the situation is not so clear in the presence of a boundary. A no flux bottom boundary condition requires mean isopycnals to be normal to topography and the boundary region can host significant lateral production in combination with vertical production [42]. As before, a production–dissipation balance can be disrupted by the turbulent transport of temperature variance in the guise of triple correlations [38].

2.2.1. Inertial Subrange Methods

In the case of steady spatially local balances, dimensional analysis provides for inertial subranges in which variance is handed over from large spatial scales to smaller spatial scales in a self-similar way that results in spectral power laws in which energy density scales as $\epsilon^{2/3}k^{-5/3}$, where k is the 3D wavenumber magnitude [43]. Time series recorded by the MAVS do not document 3D wavenumber, but assuming that the small scale turbulence is wafted past the sensor as a frozen field (Taylor's hypothesis), the sensor documents a one-dimensional frequency σ spectrum in which $\sigma = k_1 U$ and k_1 is the wavenumber in the direction of the low frequency velocity U. A more detailed accounting [38,44] returns

$$\Phi_i = \alpha_i \varepsilon^{2/3} k_1^{-5/3} \tag{10}$$

where i refers to the direction of the flow, ε is the turbulent energy dissipation rate, and α_i are the one-dimensional Kolmogorov constants. For streamwise direction ($i = 1$), $\alpha_1 = 1.56 \times 18/55$, and $\alpha_2 = \alpha_3 = 4\alpha_1/3$ for spanwise ($i = 2$) and vertical ($i = 3$) directions. The factor of 1.56 is an empirically defined prefactor for a three-dimensional wavenumber spectrum, 18/55 accounts for the conversion from a three-dimensional into a one-dimensional wavenumber. The condition of local isotropy [45] distinguishes the spectral levels in streamwise and spanwise directions.

Similarly, the temperature spectrum also has a universal format in the inertial subrange:

$$\Phi_\theta = C_\theta \chi \varepsilon^{-1/3} k_1^{-5/3} \tag{11}$$

in which $C_\theta = 0.4$ [38,46].

Turbulent dissipation rates ϵ and χ can be calculated by fitting the measured spectrum from the MAVS and from the various temperature sensors using (10) and (11). Our method consists of multiplying observed spectra by $(k_1 U)^{5/3}$ and fitting models that include sensor response, aliasing, and noise discussed in the previous section. Quoted uncertainty estimates are standard errors from that fitting process.

Just as one can define a dissipation ratio Γ_μ in the context of diagnosing how production $\mathcal{P}$ could be partitioned between buoyancy flux $\mathcal{B}$ and dissipation ϵ,

$$\Gamma_\mu = \frac{\chi N^2}{2\overline{\theta}_z^2 \epsilon}$$

one defines a ratio based upon downscale transports Γ_{trans}

$$\Gamma_{\text{trans}} = \frac{\alpha_i \Phi_\theta N^2}{2 C_\theta \Phi_i \overline{\theta}_z^2}$$

and visually identifies this when velocity and normalized temperature spectra are plotted together, i.e.,

$$\frac{\Phi_\theta N^2}{\Phi_i \overline{\theta}_z^2} = \frac{2C_\theta \Gamma}{\alpha_i} \cong 1.18\Gamma \tag{12}$$

Thus, for example, if the w' and normalized temperature spectra have similar levels,

$$\Gamma_{\text{trans}} \cong 0.8$$

If the downscale transports of turbulent kinetic energy and scalar variance are non-divergent, $\Gamma_{\text{trans}} = \Gamma_\mu$, i.e., Γ_{trans} is the inertial subrange equivalent of Γ_μ.

Following Bouruet-Aubertot et al. [47], we can estimate the dissipation rate of TKE and temperature variance from the temperature sensors. The dissipation rate can be estimated:

$$\varepsilon = \left(\frac{E_f}{2C_\theta \Gamma (N/(g\alpha_\theta))^2} \right)^{3/2} \tag{13}$$

where coefficients $C_\theta = 0.4$, $\Gamma = 0.2$ and thermal expansion coefficient $\alpha_\theta = 1.36 \times 10^{-4}\ ^\circ\text{C}^{-1}$. Buoyancy frequency $N = \sqrt{g\alpha_\theta(d\theta/dz) - g\beta_\theta(dS/dz)}$ was estimated from the temperature recorders with the addition of small contributions from salinity S estimated using the $\theta - S$ curve from CTD data obtained from the shipboard survey. The coefficient E_f results from fitting $\Phi_\theta = E_f k_1^{-5/3}$ using the observed temperature spectrum.

2.3. Orography

Topographic variability (orographic variability) on scales of 100 m to 10 km is required to characterize the hydrodynamic response. Measurements at a resolution of better than 100 m are available from multibeam surveys for the northern Gulf from the NOAA National Geophysical Data Center, U.S. Coastal Relief Model, at the website: http://www.ngdc.noaa.gov/mgg/coastal/crm.html (accessed on 1 April 2021).

3. Results

3.1. Time Dependence

The internal wave paradigm of flow–topography interactions in Section 1.3, whether small or large amplitude topography, is couched in terms of a quasi-stationary response to quasi-stationary (eddy) flow. The observations we obtained provide a different story, one of a time dependent response that we characterize as 'internal swash' in analogy to the surface wave swash zone. Our intent is to allude to similar behavior in direct numerical simulations and large eddy simulations of critical wave reflection and internal tide generation [48,49] in which a wave process trips over itself with shoaling and drag acting in combination. Obvious in the moored time series of temperature (Figure 4) and velocity (Figure 5) are significant contributions from inertial-diurnal frequencies. These inertial-diurnal contributions are most obvious toward the middle of the 8-day record and can be easily distinguished from the wave frequency at the slope aspect ratio (6) by simply counting wave crests and troughs. During the early part of the record, near bottom temperature and N/S currents are characterized by fluctuations having somewhat shorter time scales than those in the middle and toward the end of the time series. Modulation of high frequency turbulence in the near-bottom temperature records (Figure 6) and correlation between cross-slope velocity and temperature (Figure 7) are apparent during the early part of the record as well.

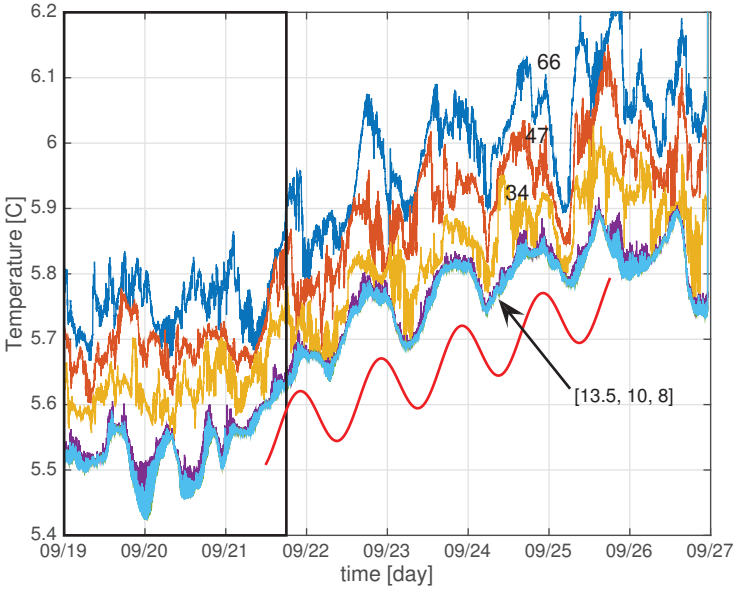

Figure 4. Time series for the 5 SBE and one RBR temperature sensors with H_{ab} indicated. Inertial-diurnal time scales are rendered as a sine wave in the red trace. These frequencies are distinguishable from the slope parallel frequency (6) as that frequency would have five periods rather than four. The box indicates the time interval of the MAVS record.

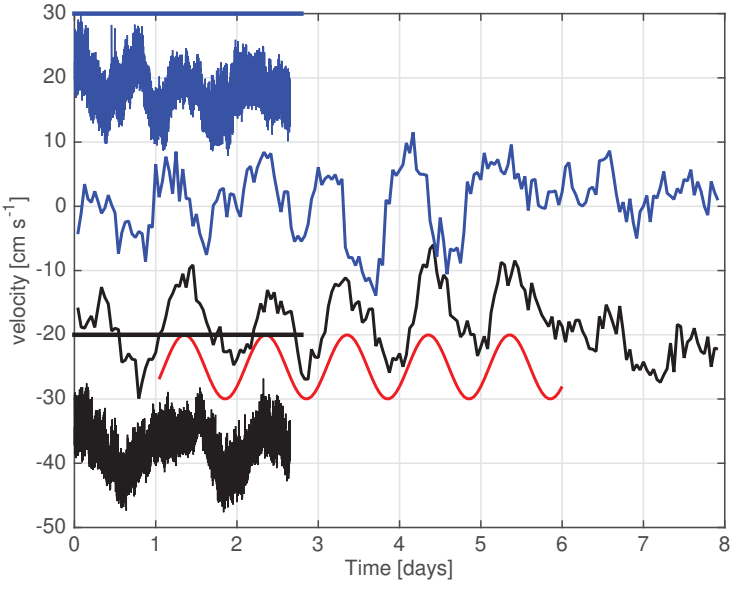

Figure 5. MAVS horizontal velocities at 10 m H_{ab} and superimposed upon the RDCP horizontal velocities at 73 m H_{ab}. Blue traces are N/S velocities, black E/W velocities. The MAVS data have been offset (by +30 cm s^{-1} in N/S and −20 cm s^{-1} in E/W). Thick lines indicate the zero crossing lines for each MAVS velocity component. Inertial-diurnal time scales are rendered as a sine wave in the red trace. These inertial-diurnal frequencies are distinguishable from the slope parallel frequency (6) as that frequency would have five periods in the space of four inertial periods.

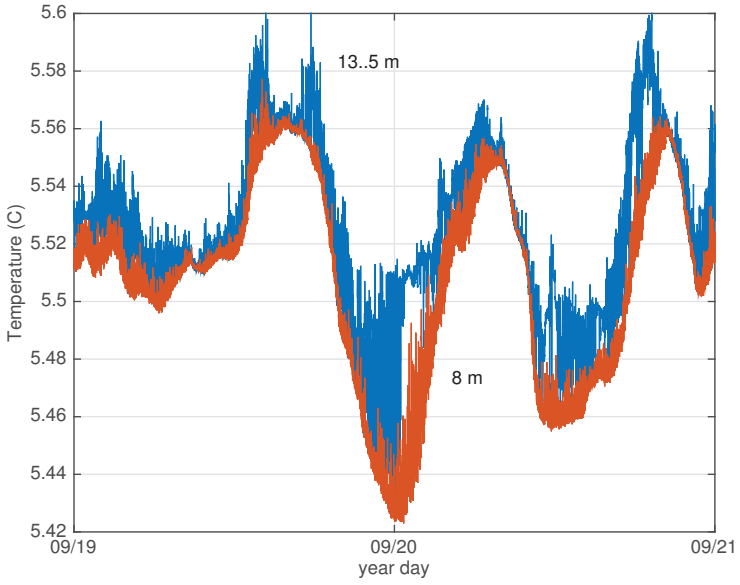

Figure 6. Time series for the bottom 2 SBE temperature sensors. High frequency variability is modulated on internal swash band time scales.

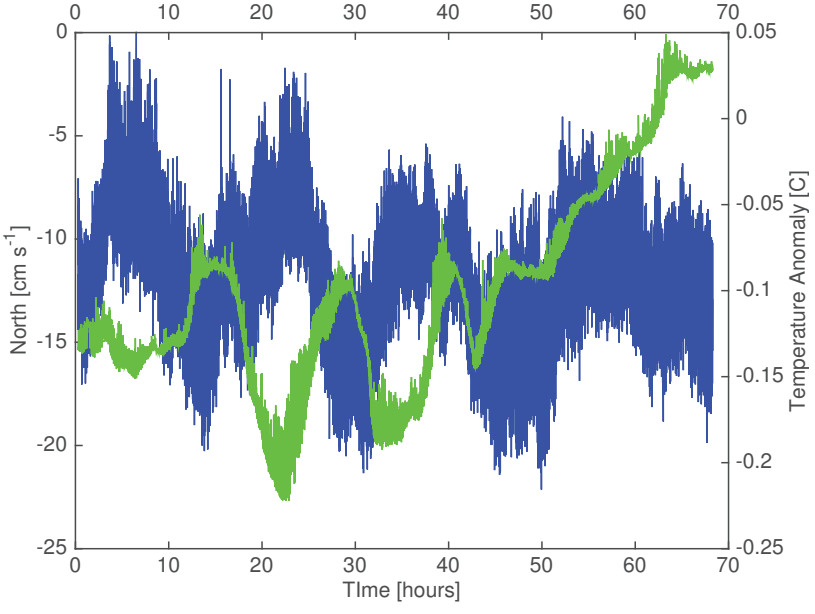

Figure 7. MAVS N/S velocity (blue trace) and RBR temperature (green trace) over the 2.8 day record. The MAVS record has been offset and the temperature record scaled so that the two traces overlay. There is an obvious anti-correlation on internal swash band time scales.

3.2. Vertical Structure

Our first objective is to quantify the bottom boundary layer height from stratification estimates in the face of this obvious time dependence. Differencing the time averaged

estimates of potential temperature from the moored temperature records provides an estimate of $\theta_z^{\text{ext}} = 0.005$ C/m and a height scale of 10 m based upon stratification falling to values between $1/2$ and $1/e$ of the external stratification estimate. Shipboard surveys (Figure 8) indicate that the weakly stratified region about the deep mooring has a height scale of approximately 15 m. Both estimates are smaller than the stratified Ekman layer metrics δ_{WM} and δ_{ZE} of approximately 30 m. The MAVS sits in a region of abruptly changing stratification, presumably near the top of the bottom boundary layer in which the velocity vector is understood to rotate quickly downslope [18,22].

The turning of the velocity vector between the MAVS (at 10 m H_{ab}) and the RDCP (at 73 m H_{ab}) over the 2.8 day MAVS record is large, Table 1, approximately 35°, relative to numerical results for a flat bottom [18]. However, it is not inconsistent with our standard parameters. From vertical integration of the along-slope momentum equation, the downslope Ekman transport $T_{\text{ekman}} = u_*^2/f$. Distributing this transport evenly over a height scale of 10 m provides a turning angle of 35° counter-clockwise viewing from above. The issue is that the observed boundary layer height scale is smaller than the asymptotic height scales δ_{WM} and δ_{ZE} and that characterizing the long-time numerical results.

The interpretation of turning of the velocity vector in association with boundary layer dynamics is not unique. In the context of a quasi-stationary internal lee wave response (Section 1.3), one anticipates a turning of 1 radian over a height scale of U/N_{ext} in the perturbation velocity field. That wave height scale clocks in as 70 m, implying a 50° turning over the two current meters in the perturbation fields. Our observations do not speak to what the magnitude of the perturbation field is in the context of a quasi-stationary internal lee wave model: what we observe is a highly time dependent internal wave band response, Figures 4–7.

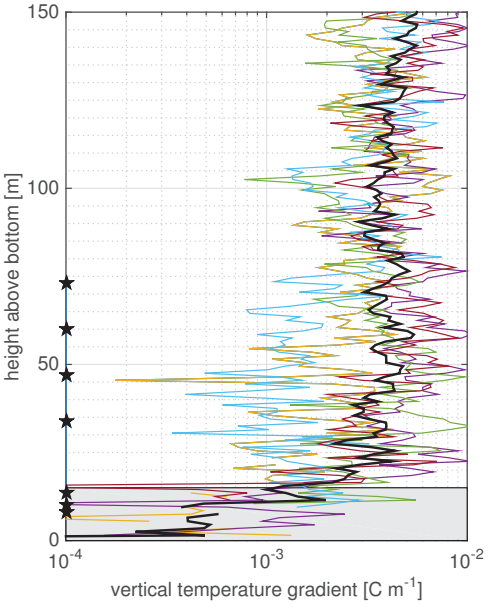

Figure 8. Vertical profiles of potential temperature gradient estimated from CTD tow-yos about the deep mooring, Figure 2. Colored traces represent the mean temperature gradients for 5 tow-yos, the thick black trace represents the mean of those five. The grey shaded region represents the reduced stratification in the bottommost 15 m, smaller than the nominal height scale of the stratified Ekman layer and slightly larger than that documented in the moored sensors. Pentagrams on the left indicate the vertical disposition of the moored instrumentation. Tow-yo sampling extends to 10–15 m H_{ab}, with 35% of the casts to within 5 m of the bottom.

3.3. Moored Data as Spectra

MAVS and RBR Spectra appear in Figure 9, in which the horizontal components have been rotated by 35° into the record mean current direction. High frequency tails of u, w, and T show respectable $-5/3$ subrange tails. Velocity spectra exhibit an increasing trend towards the Nyquist frequency which represents either motionally induced noise or the effects of vortex shedding, with potential complications from aliasing and sensor response functions. There are additional bumps in v, less prominent in u at frequencies of 0.08 and 0.3 cps. Noise in u and w is roughly 3 mm /s .

Buoyancy Reynolds numbers $\epsilon/\nu N^2$ are sufficiently large, $O(10^4)$ that one can expect the rotated velocity spectra to scale in the ratio $(U_r : V_r : W) \sim (1 : 4/3 : 4/3)$ [45]. This degree of subtlety is obscured by small noise contributions that vary amongst velocity components. Fits to the observed spectra using the response model of [38] are suggestive of locally isotropic conditions, but lie in between ratios of (1:1:1) and (1:4/3:4/3).

Estimates of both ϵ and χ are possible from the MAVS (one for each velocity axis) and co-located RBR sensor using stratification estimates provided by nearby temperature sensors. Fitting inertial subrange formulae returns $\epsilon \cong 1.2 \times 10^{-7}$ W/kg and $\chi \cong 5.4 \times 10^8$ C^{2}s^{-1}. Their combination implies a transport ratio $\Gamma_{\text{trans}} \cong 0.14$ and diapycnal diffusivity $\Gamma\epsilon/N^2 \cong 40 \times 10^{-4}$ m^2 s^{-1}. The estimated dissipation ratio is not appreciably different from that quoted for numerical simulations of shear instability [40] and does not fit with a paradigm of significant reduction in dissipation ratio at the bottom boundary articulated by [50].

Frequency spectra from the temperature recorders placed along the mooring cable fall into two distinct groups delineated by the height above the bottom. Sensors at (8.0, 10.0 13.5) m H_{ab} have reduced spectral levels within the 'Turbulent Production' frequency range $1 \times 10^{-4} < \sigma < 0.02$ cps. Sensors outside (34, 47, 60) m H_{ab} of what we have identified as the stratified Ekman layer host larger spectral levels in that frequency range. This grouping provides a potential criterion for differentiating boundary layer turbulence within the stratified Ekman layer from wave driven turbulence associated with the coupling of waves to the boundary layer. Further investigation is called for. A vertical profile of dissipation ϵ is possible from the six temperature recorders on the mooring assuming a dissipation ratio. Here, we use a value of $\Gamma = 0.2$. These averaged estimates suggest a maximum just above the current meter (13.5 m H_{ab}) and the presence of significant turbulence outside of what we have identified as the stratified Ekman layer, Table 1.

The authors in [51] define a boundary influenced regime in which turbulent length scale suppression in simple association with distance from the boundary potentially suppresses the partitioning of production into the buoyancy flux. Their boundary influenced regime occurs when $H_{\text{ab}} < 2\pi L_o$ in which the Ozmidov length scale $L_o = \sqrt{\epsilon/N^3}$ articulates the length scale at which the inertial forces of turbulence are comparable to those of gravity. Our estimates return $2\pi L_o \cong 20$ m and imply that the MAVS, placed at 10 m H_{ab}, is within this boundary influenced regime. Our transport ratio compares nicely with those of [51].

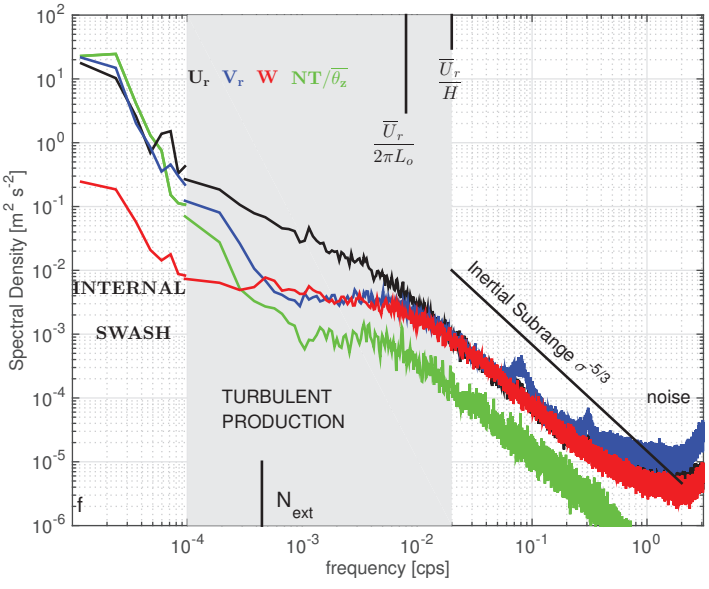

Figure 9. MAVS+RBR spectra over the 2.8 day record. Spectra use two windows. Temperature data have been interpolated onto the MAVS time base and are rendered as potential energy by multiplying the temperature time series by $N/\overline{\theta}_z$. See Figure 10 for spectra of the original time series. The frequency scale corresponding to length scale limitations on the inertial subrange $\frac{U}{H_{ab}}$ is noted. The Ozmidov length L_o is a a factor of two larger, indicating that the sensor is within a 'boundary influenced' [51] regime.

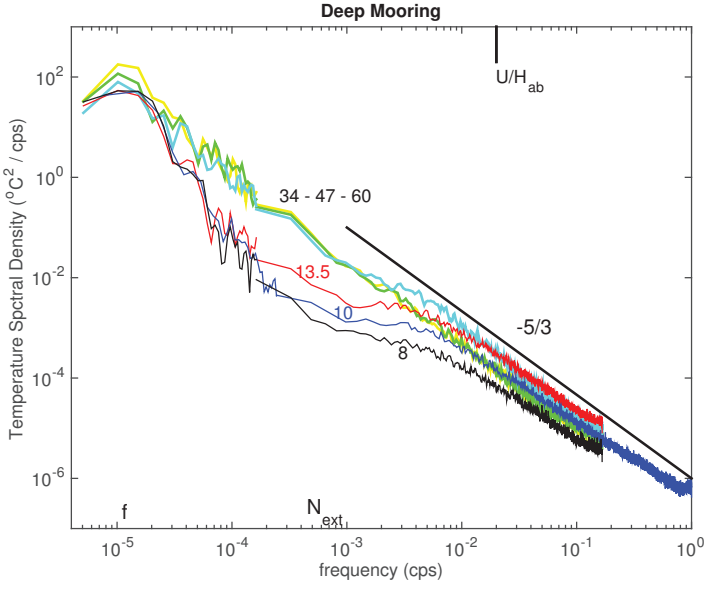

Figure 10. Spectra for the five SBE and one RBR temperature sensors. Spectra are color coded (black, blue, red, cyan, green, yellow) and labeled with their height above bottom coordinate.

3.4. Moored Data as Cospectra

In the atmospheric surface boundary layer, three-dimensional eddies are inefficient at carrying information about the surface stress aloft. From a measurement point at H_{ab}, three-dimensional eddies with vertical wavelength $2\pi H_{ab}$ have a similar horizontal wavelength and, via Taylor's frozen field hypothesis, this translates into an apparent frequency $\sigma = U/H_{ab}$. In the atmospheric boundary layer, frequencies greater than U/H_{ab} correspond to the inertial subrange and frequencies smaller than U/H_{ab} are within the production range [52]. Given the standard parameter of $U = 0.2$ m s^{-1} and $H_{ab} = 10$ m, $\sigma > 0.02$ Hz corresponds to the inertial subrange. In the atmospheric surface boundary layer, smaller scale eddies tend to be more efficient at transporting heat than momentum [52] and thus one expects temperature variance production to extend to somewhat higher frequency than U/H_{ab}. Here, we execute cospectral analyses to identify the production regimes in the MAVS record.

3.4.1. Momentum

Significant contributions to the Reynolds stress $\overline{u'w'}$ and $\overline{v'w'}$ occur where one would anticipate, at frequencies greater than $10f$ and smaller than the start of the inertial subrange, U/H_{ab}, Figures 11 and 12. In a vector format, these combine to a total of 0.5×10^{-4} m^2 s^{-2} and are directed anti-parallel to the record averaged current. The magnitude represents a 50% reduction from the bed stress using our scaling estimates of $C_d = 2.5 \times 10^{-3}$ and $U_r = 0.20$ m s^{-1}. Both direction and magnitude are plausibly consistent with numerical results for the stratified Ekman layer over a flat bottom [18], although the boundary layer height scale is quite a bit smaller than the long time result δ_{WM} and δ_{ZT}.

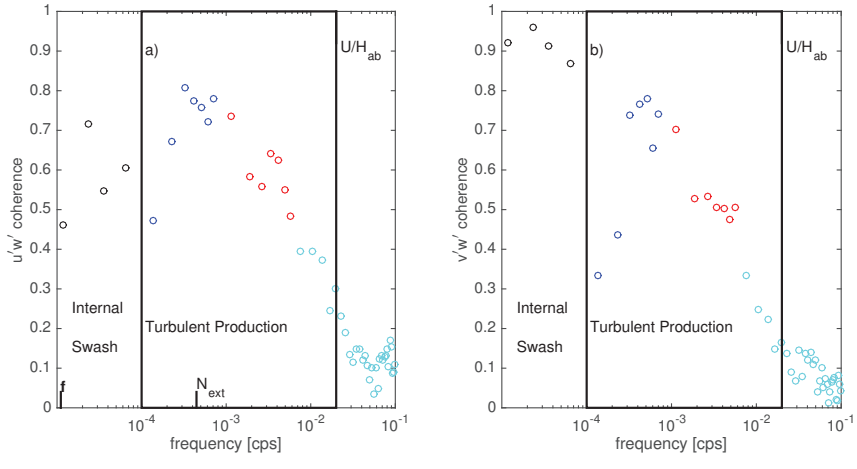

Figure 11. (**a**) $u'w'$ and (**b**) $v'w'$ coherences. Note the similarities within the 'turbulent production' and higher frequency 'inertial subrange' regimes and the difference within the 'internal swash' regime. The high meridional coherences within the 'internal swash' regime are interpreted as a coupling with internal wave motions directed upslope.

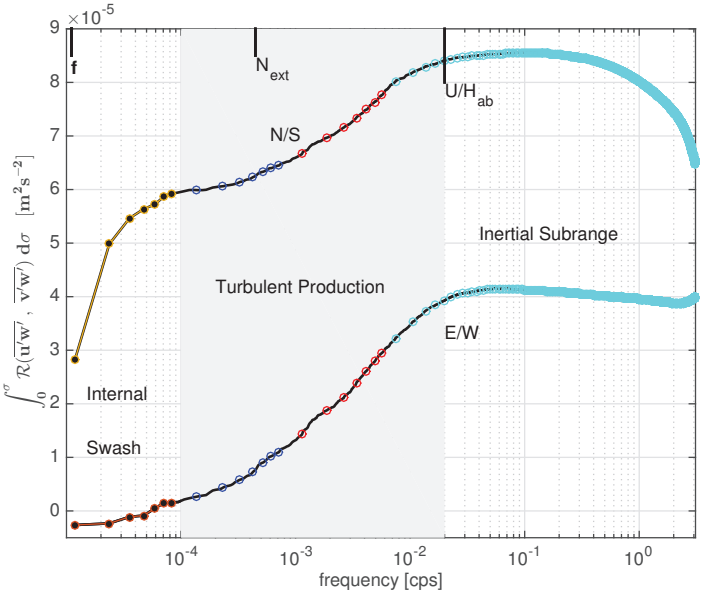

Figure 12. Integrated momentum fluxes. $\tau^{x,y}_{\text{production}} = (4 \times 10^{-5}, 2.6 \times 10^{-5})$ m^2 s^{-2}; $\tau^{x,y}_{\text{swash}} = (0, 6 \times 10^{-5})$ m^2 s^{-2}. Trends of the N/S momentum flux within the inertial subrange region are regarded as an instrumental artifact relating to vortex shedding and/or package motion.

The meridional Reynolds stress contains an even larger contribution of 0.6×10^{-4} m^2 s^{-2} in a frequency band of $f - 10f$ that we have termed 'Internal Swash'. Worthy of note is that this Reynolds stress is a significant fraction of the bed stress (nominally 1×10^{-4} m^2 s^{-2}) and is directed *directly up the mean topographic slope*. We invoke the 'internal swash's terminology to distinguish behavior in the meridional (cross-slope) and zonal (along-slope) directions. We also find a significant temperature flux in the cross-slope direction (see below) and the 'internal swash' appellation intends to evoke an analogy to a a surface wave swash zone. This notion of 'internal swash' appears in connection with numerical simulations of the critical wave reflection and near-critical internal tide generation [48,49]. Here, the data suggest an obvious hypothesis of a dynamical linkage between the downwelling Ekman boundary layer and internal wave radiation. The underlying dynamics are uncertain and deserve further attention.

3.4.2. Temperature

The temperature flux falls out of a straightforward spectral calculation, Figure 13, in which the running integral of the real part of the velocity–temperature cospectra are displayed. Beyond taking care that the MAVS and RBR time bases were aligned, the calculation of the temperature flux was 'robust'. While there are few effective degrees of freedom in a time series that is three days long when the covariance is provided by frequencies of 1–2 f, the results are robust to a variety of computational methodologies. Simply detrending the time series with polynomial fits and integrating the product of the anomaly time series provides estimates that are similar to the cospectral estimates (a factor of two smaller), and this is sufficient to conclude the following:

- Internal swash band fluxes dominate: $(\overline{v'T'}, \overline{w'T'}) = (-5 \times 10^{-4}, -4 \times 10^{-5})$ m s^{-1} C. Due to the limited duration of the record, statistical significance is marginal. A coherence of 0.7 (see Figures 14 and 15) and six degrees of freedom implies a normalized random uncertainty of 60%. The anticorrelation is obvious though (Figure 7).

- Production range fluxes are more statistically reliable, but much smaller, several percent of the respective swash band metrics. Coherences within the production band (Figure 14) are much smaller than their momentum flux counterparts (Figure 11). Moreover, relative to the mean stratification, production band fluxes are upgradient and imply restratification, Figure 16.
- Inertial subrange fluxes are negligible, as they should be within an inertial subrange.

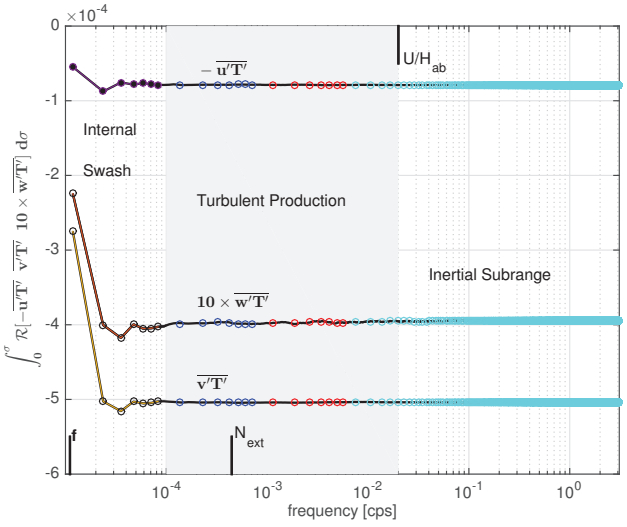

Figure 13. Running integrals of temperature fluxes in three dimensions: $(-\Re(u'T'); \Re(v'T'); 10\times\Re(w'T'))$.

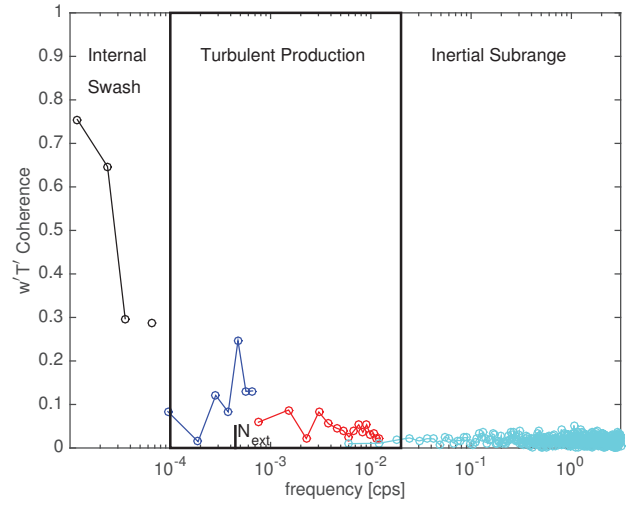

Figure 14. $w'T'$ coherence. Coherence in the production regime is small, $O(0.05)$. Color coding is associated with increased averaging within the frequency domain. Note that coherences in the production regime in Figure 11 are larger than those for the temperature flux in this figure.

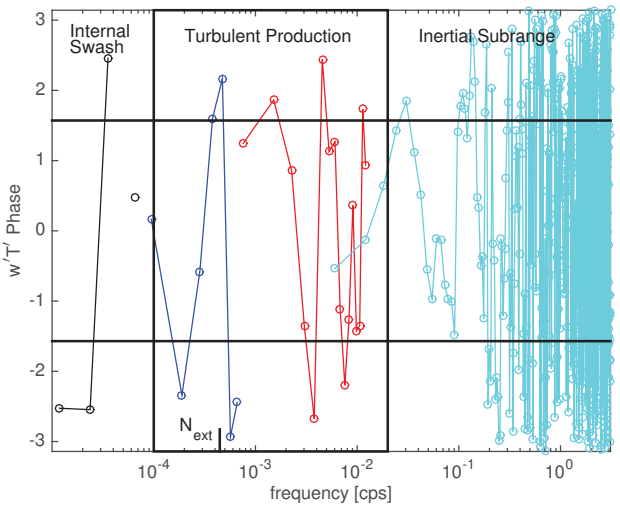

Figure 15. $w'T'$ phase. Phase in the production regime bounces between $\pm\pi/2$. Color coding is associated with increased averaging within the frequency domain.

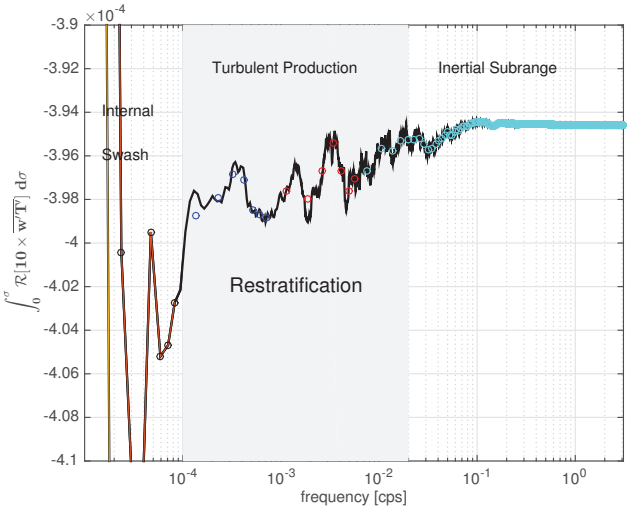

Figure 16. Running integral of the vertical temperature flux from the previous panel, with emphasis on the turbulent production region of frequency space. In this frequency band, the fluxes are upgradient, i.e., restratifying.

4. Discussion

Direct flux estimates are the gold standard of turbulence research as they let one directly address budgets. Direct estimates of turbulent momentum fluxes [1,2] and occasionally temperature fluxes [38] have been made for decades from stable platforms such as bottom landers. Here, we placed one such instrument, the MAVS, on a conventional mooring with the express intent of exploring the evolution of the bottom boundary layer to heights greater than is possible on rigid platforms. We have done so over sloping topography. This is a situation in which the intersection of isopycnals with the topography provides for a direct coupling of the boundary layer with internal waves [25] and may also introduce complexities of additional submesoscale dynamics due to the influence of

rotation [36]. Below, we discuss how the coupling was manifested in the observations and further modifications to enhance the capability of the sensors.

4.1. Momentum Fluxes

Interpretation of momentum flux estimates requires some notion of the bottom boundary condition on that flux, i.e., the bed stress. For the purpose of discussion, we use a quadratic drag formulation and the measured current at 10 m H_{ab}. The bed stress metric is thus 1×10^{-4} m^2 s^{-2}. There are two distinct frequency bands that contribute to the measured momentum fluxes.

The first frequency band characterized turbulent fluxes between 10 f and U/H_{ab}, with the upper bound being similar to measurements in the atmospheric surface boundary layer [53]. As expected, this flux is directed anti-parallel to the 10 m current. The flux is half the magnitude of the nominal bedstress. This decrease from the nominal bedstress is consistent with a boundary layer height scale of approximately 10 m in both nearby CTD casts (Figure 8) and moored temperature sensors. The veering of the velocity vector at 10 m in comparison to a current meter at 70 m was 35° in the downslope direction (Figure 17), again consistent with the nominal bedstress and a 10 m bottom boundary layer height scale.

The second frequency band contributing to the momentum flux is contained within (1–10) f. We refer to this as an internal swash band, in analogy to a surface wave swash zone [48]. This internal swash momentum flux is 60% of the nominal bedstress and directed upslope, Figure 17. The direction is aligned with coupling of the boundary layer with the internal gravity wavefield in one-dimensional models [25]. The upslope orientation of this flux implicates internal gravity wave dynamics rather than submesoscale instabilities [36], which are aligned at a cross slope orientation of 45° and for which the fastest growing instabilities have no buoyancy perturbation [54]. Information concerning how the magnitude of this upslope internal swash band momentum flux might depend upon the bed stress and other environmental parameters does not appear in the literature.

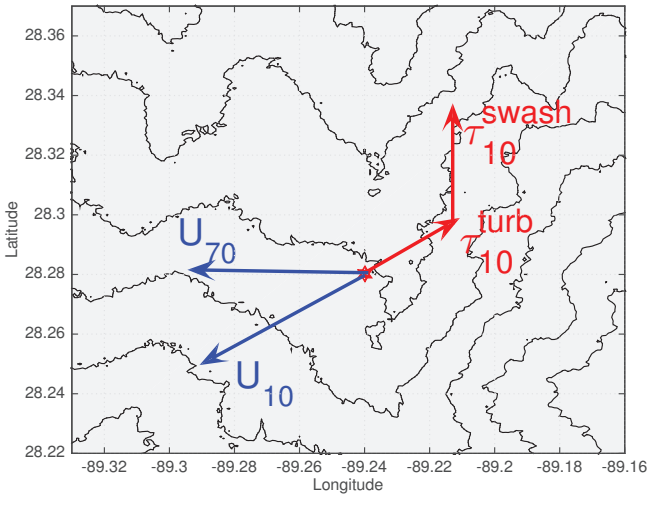

Figure 17. Horizontal velocity vectors at 10 and 70 m H_{ab} (blues, U_{10} and U_{70}) and vertical stress estimates (reds) at 10 m H_{ab}. The mooring location at 825 m water depth serves as the origin for the vectors and is denoted by a red pentagram. Bathymetry contours are at 50 m intervals. The stress vector is composed of turbulent contributions nearly antiparallel to the 10 m horizontal velocity (τ_{10}^{turb}) and a northward directed contribution from swash frequencies (τ_{10}^{swash}).

4.2. Temperature Fluxes

Temperature measurements are collocated with velocity measurements by placing the sensing element of a standalone RBR Solo temperature recorder into the measurement volume of the MAVS. This enabled two lines of enquiry. The first is an estimate of what is commonly parsed as the partitioning of TKE production $\mathcal{P}$ into TKE dissipation ϵ and the dissipation of thermal variance χ. We determined a dissipation ratio by inertial subrange arguments of $\Gamma_{\text{trans}} = 0.14$, smaller than the commonly cited value of $\Gamma_{\mu} = 0.2$. Although smaller, this implies a significant production of temperature variance. Decomposition of the temperature flux in the frequency domain provided a surprise. Estimates of production within the turbulent production band are negative, implying a restratification process in that frequency band. Production is contained within the internal swash band and dominated by frequencies of $(1-2)f$. This distribution of production and restratification within the internal wave band is similar to that documented by [55,56].

4.3. The Observed Fluxes vs. Atmospheric Surface Boundary Layer Measurements

Comprehensive accounts of momentum and buoyancy fluxes in the atmospheric surface boundary layer can be found in textbooks [53,57,58]. Over flat topography, there are a few key parameters: wind speed, roughness length, and solar insolation that determine the boundary fluxes and their distribution in the vertical. A key piece is the Obukov height scale defined by the ratio of the buoyancy and momentum flux at the bottom boundary:

$$L = \frac{-u_*^3}{kB} \tag{14}$$

where $k = 0.41$ is von Karmen's constant and B is the surface buoyancy flux. The Obukov height scale articulates the relative roles of stress and buoyancy. At values smaller than one, the boundary layer is considered stress driven. Negative values correspond to a positive buoyancy flux and convective situations. This length scale is used in the context of similarity scaling (Monin–Obukov similarity scaling) to collapse variability in flux profiles using a non-dimensional height scale H_{ab}/L, in which we have inserted H_{ab} for the sensor height. The authors in [52] demonstrate how momentum and buoyancy flux cospectra evolve as a function of this non-dimensional height over a range of values $-2.0 < H_{\text{ab}}/L < 2.0$. A key message from that study is that the buoyancy flux occurs at a slightly higher apparent frequency than the momentum flux: eddies with horizontal wavenumber smaller than H_{ab} transport buoyancy more efficiently than momentum. The lack of $w'T'$ covariance in the turbulent production regime stands in stark contrast to the atmospheric data. It is a statement about the importance of the internal swash phenomena to boundary mixing and our lack of understanding about the coupling of the internal wavefield with the bottom boundary layer. This assuredly has consequences for turbulent closure schemes such as [59] that need to be addressed. A way forward is to define a slope Obukov length scale by substituting the depth integrated cross-slope Ekman buoyancy transport for B, e.g., Ref. [29]. For our standard parameters, $H_{\text{ab}}/L \cong -0.45$ If we had taken a drag coefficient half as large, $H_{\text{ab}}/L \cong -0.9$.

4.4. Speculation about the Ocean's Planetary Boundary Layer

Below, we explore some consequences of our flux estimates, equating an appropriately scaled version of the temperature flux with a buoyancy flux and relating the 10 m current to the bed stress using a drag coefficient of 0.0025. The reader should review Section 3.4.2 as concerns the statistical reliability of the flux estimates and understand the speculative nature of this sub-section.

4.4.1. Ekman Balances

Here, we attempt to interpret the 10 m $H_{\rm ab}$ temperature flux estimates in terms of Ekman dynamics and one-dimensional models of the bottom boundary layer over a planar slope [26]. The downslope Ekman transport is

$$T_{ekman} = \frac{u_*^2}{f} cos(\vartheta) \tag{15}$$

with turning angle ϑ. The mean temperature tendency equation in a Cartesian coordinate system is:

$$\overline{\theta}_t + \overline{v}\partial_y\theta + \overline{w}\partial_z\theta + \partial_z\overline{w'T'} + \partial_y\overline{v'T'} \cong 0\ . \tag{16}$$

Integrating over the Ekman layer and taking the 10 m measurements as being representative of that integral provides the wherewithal for a scale assessment of the mean temperature balance. This suggests comparing

$$T_{\rm ekman}\frac{\partial\theta}{\partial y} : \overline{w'T'} + \overline{v'T'}\alpha \tag{17}$$

Here, we invoke the one-dimensional result [26] that the upslope gradient $\theta_{\|} = \alpha\theta_z^{ext}$ and have equated $\theta_{\|}$ with θ_y. We find a plausible order of magnitude agreement between the left-hand side,

$$T_{\rm ekman}\ \alpha\ (\frac{\partial\theta}{\partial z})_{ext} \cong 1.2 \times 0.0025/64 = 5 \times 10^{-5}$$

and, from the right-hand side,

$$\overline{w'T'} = 4 \times 10^{-5}$$

with smaller contributions from

$$\overline{v'T'}\alpha = 7 \times 10^{-6}$$

We are led to an appreciation that the downslope temperature advection is essentially balanced by swash band temperature fluxes. This is understood to be a general result in the context of the one-dimensional model: the residual between downslope advection and upslope fluxes gives rise to a smaller cross-isopycnal upwelling [60]. Whether these temperature fluxes result in local dissipation is a different question.

If we had taken a drag coefficient half as large, temperature transport in the Ekman layer would be four times smaller than the temperature flux.

4.4.2. Production–Dissipation

In a steady production–dissipation balance of the temperature variance equation,

$$(\overline{v'T'}, \overline{w'T'}) \cdot (\theta_y, \theta_z) = -\chi/2$$

Our estimates of production (1.4×10^{-7} C^2 s^{-1}) and dissipation ($\chi/2 = 2.6 \times 10^{-8}$ C^2 s^{-1}) differ by a factor of five, with production estimates in excess of dissipation. A fundamental concern is the contribution of nonlinear transport terms in the temperature variance budget (9) [38].

4.4.3. Diapycnal Advection

Since there is neither advection nor stirring of density along a surface of constant density, if one can ignore nonlinearities in the equation of state, one arrives at the remarkably simple balance [50,61]:

$$\tilde{\mathbf{e}} = -\frac{\nabla\cdot\mathbf{F}_\rho}{\|\nabla\rho\|}\mathbf{n}_\rho \tag{18}$$

in which $\tilde{\mathbf{e}}$ is the mean diapycnal velocity and $\mathbf{F}_\rho$ is the density flux. The factor $\mathbf{n}_\rho$ is a unit vector normal to the mean isopycnal surface and the gradient operators serve to pick out that part of the flux that is normal to the mean isopycnals.

This balance plays a central role in recent speculation about global ocean upwelling [50,62,63], in which these authors all invoke a decreasing density flux magnitude with decreasing height above the bottom, starting at the top of the nominal boundary layer, despite observations that demonstrate high universal increase of dissipation with decreasing H_{ab}. These arguments link diapycnal upwelling to the decreasing buoyancy flux magnitude within the bottom boundary layer.

The logic behind these arguments implicitly assumes that horizontal and vertical temperature fluxes have a similar order of magnitude and that balances in the temperature (buoyancy) variance Equation (9) are local (i.e., the nonlinear transport terms can be neglected) [42]. With such assumptions, the no-flux bottom boundary condition can be reduced to a requirement that the vertical buoyancy flux tends toward zero as the bottom is approached [50]. The data presented here demonstrate otherwise on both accounts: horizontal temperature fluxes dominate the vertical and call into question the implicit assumption of an isotropic closure. The swash band fluxes do not balance dissipation and suggest a potentially important role of the nonlinear transport terms in redistributing turbulence within the boundary layer.

An allure of arguments prescribing the vertical structure of the buoyancy flux within the boundary layer is the notion of potential length scale limitations in a stress driven turbulent field leading to reduced dissipation ratios. This seems a rather intuitive notion for boundary layer turbulence as the boundary is approached, but there is an equally intuitive notion to argue for precisely the opposite: the downwelling Ekman layer hosts a convective process and internal swash can be parsed as episodic convection with such intermittent convective events dominating the variance budgets. One anticipates $O(1)$ dissipation ratios to characterize convection, rather than values decreasing from a nominal $\Gamma_\mu = 0.20$ to zero.

The fallacy [42] underlying these [50] upwelling arguments may originate in the fact that the no-flux bottom boundary condition controls the stratification only on scales smaller than the log-layer [29,64], rather than the O(100) m envisioned by those authors [50,62,63]. Clearly, further work needs to be done.

4.5. Assessments

In one-dimensional models of the downwelling Ekman layer [19,25,28,29], the downslope advection of buoyancy can result in convectively unstable conditions [65]. Information about the downslope buoyancy advection can be carried aloft to heights in excess of the penetration depth of the turbulent momentum flux by coupling with the internal wave mode at the slope frequency (Equation (6)), providing a time dependent response. The topography about the mooring contrasts sharply with the planar sloping boundary assumed by the one-dimensional models. The mooring was placed just in the lee of a topographic crest. We anticipate that there may be elements of downslope acceleration in response to pressure gradients across the topography, also referred to as form drag. This downslope acceleration could act to decrease the boundary layer height scale. The boundary layer height documented by the mooring (10 m) is slightly smaller than that in the CTD Tow-Yos about the mooring, Figure 8.

If we had taken a drag coefficient half as large as our standard parameter, there would be less disparity between the stratified Ekman layer height scale δ_{strat}, now 14 m, and that identified in the mooring (10 m) and quite similar to that in the Tow-Yo data. One could further argue that the appropriate scaling velocity in the farfield of the log layer (taken as 0.2 m s^{-1}) should be reduced by a thermal wind contribution (a reduction of about 0.015 m s^{-1}).

If we had taken a drag coefficient half as large as our standard parameter, the nominal veering angle associated with the Ekman layer would be a factor of four smaller than

documented by the moored data. This could be compensated by asserting that the time mean velocity estimates contain a significant contribution from an upward propagating near-inertial wave phase locked to the topography, in addition to the obvious near-inertial time dependent response.

However, there is still something significant to explain: the stratified Ekman layer height scale ignores convective forcing related to cross-slope buoyancy transports which continue over a far longer time scale than required for the equilibration of the stratified Ekman layer over a flat bottom. This implies a ventilation or restratification process that keeps pace with the downslope advection driven by the bed stress. The temperature flux estimates locate this process in the internal swash band. If we had taken a drag coefficient half as large as our standard parameter, the internal swash band temperature fluxes would exceed the downslope Ekman temperature transport by a factor of four.

4.6. Sensor Performance

This study is based upon the use of a prototype sensor tested as part of a boundary mixing program on the northern continental slope of the Gulf of Mexico. As an instrument test, it suggests that there are no intrinsic limitations to using such flux sensors on conventional moorings. This opens up a world of exploration. Further improvements to the sensor package include:

- Recording serial output of an RBR Solo with MAVS to eliminate the potential for time base issues.
- Our implementation of the SBE-7/8 micro temperature and conductivity units was not successful, but our experience does not speak to conceptual issues.
- An alternate route to estimating a salinity flux is to utilize estimates of absolute travel time for speed of sound fluctuations [66] in combination with a direct temperature measurement.
- Motionally induced noise could be reduced by using faired cable.
- Developing a dynamical mooring model to understand how to avoid resonances that lead to large amplitude strumming.
- Increasing sampling rate by a factor of two or so would place aliased strumming induced noise into its natural frequency band.
- A longer sensing element for the temperature sensor would remove the instrument case from the vicinity of the MAVS sampling volume and reduce the potential for flow blockage.
- Any discussion of either turbulent or internal swash band momentum fluxes is referenced to the bed stress. Typically, one wants such a measurement near the top of the log-layer, less than one meter H_{ab}. Due to the need for releases and some amount of chain to take up shock loading when the anchor hits bottom, the closest one can manage to place a sensor on a conventional mooring is roughly 6 m H_{ab}. Conventional moorings will likely need to be paired with bottom landers.
- a drawback of the VN100 motion package we employed is that it requires a 17 s boot time, which restricts sampling schemes.

Author Contributions: Conceptualization, K.L.P., A.J.W.III and Z.W.; methodology, K.L.P.; validation, K.L.P., B.W. and Z.W.; formal analysis, K.L.P.; investigation, K.L.P., F.T., A.J.W.III and B.W.; resources, K.L.P., F.T. and A.J.W.III; data curation, K.L.P., B.W. and Z.W.; writing—original draft preparation, K.L.P.; writing—review and editing, Z.W. and B.W.; visualization, K.L.P. and B.W.; supervision, K.L.P.; project administration, K.L.P.; funding acquisition, K.L.P. and Z.W. All authors have read and agreed to the published version of the manuscript.

Funding: Funding for GoMIX was provided by BP through the Gulf of Mexico Research Initiative (GoMRI), and is administered by the Consortium for Ocean Leadership. K.L.P., B.W., Z.W. and F.T. recognize funding from GoMIX/GoMRI contract # SA12-09/GoMRI-006.

Data Availability Statement: The GoMIX data used in this study are available via the GoMRI GRIIDC data base (https://data.gulfresearchinitiative.org, accessed on 19 May 2021).

Acknowledgments: The skill and cooperation of the masters and crew of R/V Pt. Sur, operated by the Louisiana Universities Marine Consortium (LUMCON), were essential to the success of the cruises from which the data reported herein were obtained.

Conflicts of Interest: One of us, Albert Williams, is a principal of Nobska Development, Inc. who provided the MAVS current meter used in obtaining some of these measurements. Modifications to the standard MAVS were made in support of the special needs for this and subsequent deployments, including SBE 7 and 8 sensor logging and subsequently incorporation of RBR temperature measurements but not logged internally in MAVS in this experiment. Other authors declare no conflict of interest.

Abbreviations

The following abbreviations are used in this manuscript:

BBL	Bottom Boundary Layer
TKE	Turbulent Kinetic Energy
MAVS	Modular Acoustic Velocity Sensor

References

1. Gross, T.F.; Williams, A.J., III; Grant, W.D. Long-term in situ calculations of kinetic energy and Reynolds stress in a deep sea boundary layer. *J. Geophys. Res. Oceans* **1986**, *91*, 8461–8469. [CrossRef]
2. McPhee, M.G.; Smith, J.D. Measurements of the turbulent boundary layer under pack ice. *J. Phys. Oceanogr.* **1976**, *6*, 696–711. [CrossRef]
3. Thwaites, F.; Williams, A. Development of a modular acoustic velocity sensor. In Proceedings of the OCEANS 96 MTS/IEEE Conference Proceedings, The Coastal Ocean-Prospects for the 21st Century, Fort Lauderdale, FL, USA, 23–26 September 1996; Volume 2, pp. 607–612.
4. Joye, S.B. Deepwater Horizon, 5 years on. *Science* **2015**, *349*, 592–593. [CrossRef]
5. Gros, J.; Socolofsky, S.A.; Dissanayake, A.L.; Jun, I.; Zhao, L.; Boufadel, M.C.; Reddy, C.M.; Arey, J.S. Petroleum dynamics in the sea and influence of subsea dispersant injection during Deepwater Horizon. *Proc. Natl. Acad. Sci. USA* **2017**, *114*, 10065–10070. [CrossRef] [PubMed]
6. McNutt, M.K.; Camilli, R.; Crone, T.J.; Guthrie, G.D.; Hsieh, P.A.; Ryerson, T.B.; Savas, O.; Shaffer, F. Review of flow rate estimates of the Deepwater Horizon oil spill. *Proc. Natl. Acad. Sci. USA* **2012**, *109*, 20260–20267. [CrossRef] [PubMed]
7. Socolofsky, S.A.; Adams, E.E.; Sherwood, C.R. Formation dynamics of subsurface hydrocarbon intrusions following the Deepwater Horizon blowout. *Geophys. Res. Lett.* **2011**, *38*. [CrossRef]
8. Ledwell, J.R.; He, R.; Xue, Z.; DiMarco, S.F.; Spencer, L.J.; Chapman, P. Dispersion of a tracer in the deep Gulf of Mexico. *J. Geophys. Res. Oceans* **2016**, *121*, 1110–1132. [CrossRef]
9. Kantha, L. Barotropic tides in the Gulf of Mexico. *Wash. DC Am. Geophys. Union Geophys. Monogr. Ser.* **2005**, *161*, 159–163.
10. Polzin, K.; Toole, J.; Ledwell, J.; Schmitt, R. Spatial variability of turbulent mixing in the abyssal ocean. *Science* **1997**, *276*, 93–96. [CrossRef]
11. Polzin, K.L. An abyssal recipe. *Ocean Model.* **2009**, *30*, 298–309. [CrossRef]
12. Zhang, X.; DiMarco, S.F.; Smith, D.C., IV; Howard, M.K.; Jochens, A.E.; Hetland, R.D. Near-resonant ocean response to sea breeze on a stratified continental shelf. *J. Phys. Oceanogr.* **2009**, *39*, 2137–2155. [CrossRef]
13. Zhang, X.; Smith, D.C., IV; DiMarco, S.F.; Hetland, R.D. A numerical study of sea-breeze-driven ocean Poincare wave propagation and mixing near the critical latitude. *J. Phys. Oceanogr.* **2010**, *40*, 48–66. [CrossRef]
14. Hamilton, P.; Lugo-Fernandez, A. Observations of high speed deep currents in the northern Gulf of Mexico. *Geophys. Res. Lett.* **2001**, *28*, 2867–2870. [CrossRef]
15. Oey, L.; Lee, H. Deep eddy energy and topographic Rossby waves in the Gulf of Mexico. *J. Phys. Oceanogr.* **2002**, *32*, 3499–3527. [CrossRef]
16. Hamilton, P. Topographic Rossby waves in the Gulf of Mexico. *Prog. Oceanogr.* **2009**, *82*, 1–31. [CrossRef]
17. Spencer, L.J.; DiMarco, S.F.; Wang, Z.; Kuehl, J.J.; Brooks, D.A. Asymmetric oceanic response to a hurricane: Deep water observations during Hurricane Isaac. *J. Geophys. Res. Oceans* **2016**, *121*, 7619–7649. [CrossRef]
18. Taylor, J.R.; Sarkar, S. Stratification effects in a bottom Ekman layer. *J. Phys. Oceanogr.* **2008**, *38*, 2535–2555. [CrossRef]
19. Weatherly, G.L.; Martin, P.J. On the structure and dynamics of the oceanic bottom boundary layer. *J. Phys. Oceanogr.* **1978**, *8*, 557–570. [CrossRef]
20. Zilitinkevich, S.; Esau, I. On integral measures of the neutral barotropic planetary boundary layer. *Bound. Layer Meteorol.* **2002**, *104*, 371–379. [CrossRef]
21. Zilitinkevich, S.; Baklanov, A. Calculation of the height of the stable boundary layer in practical applications. *Bound. Layer Meteorol.* **2002**, *105*, 389–409. [CrossRef]

22. Perlin, A.; Moum, J.; Klymak, J.; Levine, M.; Boyd, T.; Kosro, P. Organization of stratification, turbulence, and veering in bottom Ekman layers. *J. Geophys. Res. Oceans* **2007**, *112*. [CrossRef]
23. Caldwell, D.; Van Atta, C.; Helland, K. A laboratory study of the turbulent Ekman layer. *Geophys. Fluid Dyn.* **1972**, *3*, 125–160. [CrossRef]
24. Pollard, R.T.; Rhines, P.B.; Thompson, R.O. The deepening of the wind-mixed layer. *Geophys. Fluid Dyn.* **1973**, *4*, 381–404. [CrossRef]
25. Brink, K.H.; Lentz, S.J. Buoyancy arrest and bottom Ekman transport. Part I: Steady flow. *J. Phys. Oceanogr.* **2010**, *40*, 621–635. [CrossRef]
26. Garrett, C.; MacCready, P.; Rhines, P. Boundary mixing and arrested Ekman layers: Rotating stratified flow near a sloping boundary. *Annu. Rev. Fluid Mech.* **1993**, *25*, 291–323. [CrossRef]
27. Trowbridge, J.; Lentz, S. Asymmetric behavior of an oceanic boundary layer above a sloping bottom. *J. Phys. Oceanogr.* **1991**, *21*, 1171–1185. [CrossRef]
28. Umlauf, L.; Smyth, W.D.; Moum, J.N. Energetics of bottom Ekman layers during buoyancy arrest. *J. Phys. Oceanogr.* **2015**, *45*, 3099–3117. [CrossRef]
29. Ruan, X.; Thompson, A.F.; Taylor, J.R. The Evolution and Arrest of a Turbulent Stratified Oceanic Bottom Boundary Layer over a Slope: Downslope Regime. *J. Phys. Oceanogr.* **2019**, *49*, 469–487. [CrossRef]
30. Bretherton, F.P. Momentum transport by gravity waves. *Q. J. R. Meteorol. Soc.* **1969**, *95*, 213–243. [CrossRef]
31. Baines, P.G. *Topographic Effects in Stratified Flows*; Cambridge University Press: Cambridge, UK, 1997.
32. Thorpe, S.A. The generation of internal waves by flow over the rough topography of a continental slope. *Proc. R. Soc. Lond. Ser. A Math. Phys. Sci.* **1992**, *439*, 115–130.
33. Leaman, K.D.; Sanford, T.B. Vertical energy propagation of inertial waves: A vector spectral analysis of velocity profiles. *J. Geophys. Res.* **1975**, *80*, 1975–1978. [CrossRef]
34. Benthuysen, J.; Thomas, L.N. Friction and diapycnal mixing at a slope: Boundary control of potential vorticity. *J. Phys. Oceanogr.* **2012**, *42*, 1509–1523. [CrossRef]
35. Hoskins, B. The role of potential vorticity in symmetric stability and instability. *Q. J. R. Meteorol. Soc.* **1974**, *100*, 480–482. [CrossRef]
36. Allen, J.; Newberger, P. On symmetric instabilities in oceanic bottom boundary layers. *J. Phys. Oceanogr.* **1998**, *28*, 1131–1151. [CrossRef]
37. Trivett, D.; Terray, E.; Williams, A. Error analysis of an acoustic current meter. *IEEE J. Ocean. Eng.* **1991**, *16*, 329–337. [CrossRef]
38. Shaw, W.J.; Trowbridge, J.H.; Williams, A.J., III. Budgets of turbulent kinetic energy and scalar variance in the continental shelf bottom boundary layer. *J. Geophys. Res. Oceans* **2001**, *106*, 9551–9564. [CrossRef]
39. Horne, E.P.W.; Toole, J.M. Sensor response mismatches and lag correction techniques for temperature-salinity profilers. *J. Phys. Oceanogr.* **1980**, *10*, 1122–1130. [CrossRef]
40. Gregg, M.; D'Asaro, E.; Riley, J.; Kunze, E. Mixing Efficiency in the Ocean. *Annu. Rev. Mar. Sci.* **2018**, *10*, 443–473. [CrossRef]
41. Osborn, T.R.; Cox, C.S. Oceanic fine structure. *Geophys. Fluid Dyn.* **1972**, *3*, 321–345. [CrossRef]
42. Polzin, K.L.; McDougal, T. Mixing at the Ocean's Bottom Boundary. In *Ocean Mixing*; Meredith, M., Naveira Garabato, A., Eds.; Elsevier: Amsterdam, The Netherlands, 2021.
43. Kolmogorov, A.N. The local structure of turbulence in incompressible viscous fluid for very large Reynolds numbers. *CR Acad. Sci. URSS* **1941**, *30*, 301–305.
44. Sreenivasan, K.R. On the universality of the Kolmogorov constant. *Phys. Fluids* **1995**, *7*, 2778–2784. [CrossRef]
45. Gargett, A.; Osborn, T.; Nasmyth, P. Local isotropy and the decay of turbulence in a stratified fluid. *J. Fluid Mech.* **1984**, *144*, 231–280. [CrossRef]
46. Sreenivasan, K.R. The passive scalar spectrum and the Obukhov–Corrsin constant. *Phys. Fluids* **1996**, *8*, 189–196. [CrossRef]
47. Bouruet-Aubertot, P.; Van Haren, H.; Lelong, M.P. Stratified inertial subrange inferred from in situ measurements in the bottom boundary layer of the Rockall channel. *J. Phys. Oceanogr.* **2010**, *40*, 2401–2417. [CrossRef]
48. Slinn, D.N.; Riley, J. A model for the simulation of turbulent boundary layers in an incompressible stratified flow. *J. Comput. Phys.* **1998**, *144*, 550–602. [CrossRef]
49. Sarkar, S.; Scotti, A. From topographic internal gravity waves to turbulence. *Annu. Rev. Fluid Mech.* **2017**, *49*, 195–220. [CrossRef]
50. Ferrari, R.; Mashayek, A.; McDougall, T.J.; Nikurashin, M.; Campin, J.M. Turning Ocean Mixing Upside Down. *J. Phys. Oceanogr.* **2016**, *46*, 2239–2261. [CrossRef]
51. Holleman, R.C.; Geyer, W.R.; Ralston, D.K. Stratified Turbulence and Mixing Efficiency in a Salt Wedge Estuary. *J. Phys. Oceanogr.* **2016**, *46*, 1769–1783. [CrossRef]
52. Kaimal, J.; Wyngaard, J.; Izumi, Y.; Cote, O. Spectral characteristics of surface-layer turbulence. *Q. J. R. Meteorol. Soc.* **1972**, *98*, 563–589. [CrossRef]
53. Kaimal, J.C.; Finnigan, J.J. *Atmospheric Boundary Layer Flows: Their Structure and Measurement*; Oxford University Press: New York, NY, USA, 1994.
54. Thomas, L.N. On the effects of frontogenetic strain on symmetric instability and inertia–gravity waves. *J. Fluid Mech.* **2012**, *711*, 620. [CrossRef]
55. van Haren, H.; Oakey, N.; Garrett, C. Measurements of internal wave band eddy fluxes above a sloping bottom. *J. Mar. Res.* **1994**, *52*, 909–946. [CrossRef]

56. Gemmrich, J.R.; van Haren, H. Internal wave band eddy fluxes above a continental slope. *J. Mar. Res.* **2002**, *60*, 227–253. [CrossRef]
57. Stull, R.B. *An Introduction to Boundary Layer Meteorology*; Springer Science & Business Media: New York, NY, USA, 2012; Volume 13.
58. Garratt, J.R. The atmospheric boundary layer. *Earth Sci. Rev.* **1994**, *37*, 89–134. [CrossRef]
59. Mellor, G.L.; Yamada, T. A hierarchy of turbulence closure models for planetary boundary layers. *J. Atmos. Sci.* **1974**, *31*, 1791–1806. [CrossRef]
60. Garrett, C. An isopycnal view of near-boundary mixing and associated flows. *J. Phys. Oceanogr.* **2001**, *31*, 138–142. [CrossRef]
61. McDougall, T.J. Dianeutral advection. In *Parameterization of Small-Scale Processes: Proc. 'Aha Huliko' a Hawaiian Winter Workshop*; Hawaii Institute of Geophysics Special Publication: Honolulu, HI, USA, 1989; pp. 289–315.
62. de Lavergne, C.; Madec, G.; Le Sommer, J.; Nurser, A.G.; Naveira Garabato, A.C. On the consumption of Antarctic Bottom Water in the abyssal ocean. *J. Phys. Oceanogr.* **2016**, *46*, 635–661. [CrossRef]
63. McDougall, T.J.; Ferrari, R. Abyssal Upwelling and Downwelling Driven by Near-Boundary Mixing. *J. Phys. Oceanogr.* **2017**, *47*, 261–283. [CrossRef]
64. Kaiser, B.; Pratt, L.J. The transition to turbulence within internal tide boundary layers in the abyssal ocean. In Proceedings of the Ocean Sciences Meeting 2020, San Diego, CA, USA, 16–21 February 2020.
65. Moum, J.; Perlin, A.; Klymak, J.; Levine, M.; Boyd, T.; Kosro, P. Convectively driven mixing in the bottom boundary layer. *J. Phys. Oceanogr.* **2004**, *34*, 2189–2202. [CrossRef]
66. Shaw, W.J.; Williams, A.J.; Trowbridge, J.H. Measurement of turbulent sound speed fluctuations with an acoustic travel-time meter. In Proceedings of the OCEANS 96 MTS/IEEE Conference Proceedings, The Coastal Ocean-Prospects for the 21st Century, Fort Lauderdale, FL, USA, 23–26 September 1996; pp. 105–110.

fluids

MDPI

Article

Note on the Bulk Estimate of the Energy Dissipation Rate in the Oceanic Bottom Boundary Layer

Xiaozhou Ruan

Department of Earth, Atmospheric, and Planetary Sciences, Massachusetts Institute of Technology, Cambridge, MA 02139, USA; xruan@mit.edu

Abstract: The dissipation of the kinetic energy (KE) associated with oceanic flows is believed to occur primarily in the oceanic bottom boundary layer (BBL), where bottom drag converts the KE from mean flows to heat loss through irreversible mixing at molecular scales. Due to the practical difficulties associated with direct observations on small-scale turbulence close to the seafloor, most up-to-date estimates on bottom drag rely on a simple bulk formula ($C_d U^3$) proposed by G.I. Taylor that relates the integrated BBL dissipation rate to a drag coefficient (C_d) as well as a flow magnitude outside of the BBL (U). Using output from several turbulence-resolving direct numerical simulations, it is shown that the true BBL-integrated dissipation rate is approximately 90% of that estimated using the classic bulk formula, applied here to the simplest scenario where a mean flow is present over a flat and hydrodynamically smooth bottom. It is further argued that Taylor's formula only provides an upper bound estimate and should be applied with caution in the future quantification of BBL dissipation; the performance of the bulk formula depends on the distribution of velocity and shear stress near the bottom, which, in the real ocean, could be disrupted by bottom roughness.

Keywords: turbulence; bottom boundary layer; Ekman layer; energy dissipation

Citation: Ruan, X. Note on the Bulk Estimate of the Energy Dissipation Rate in the Oceanic Bottom Boundary Layer. *Fluids* **2022**, *7*, 82. https://doi.org/10.3390/fluids7020082

Academic Editors: Joseph J. Kuehl, Pengfei Xue and Fabrice Veron

Received: 8 January 2022
Accepted: 16 February 2022
Published: 18 February 2022

Publisher's Note: MDPI stays neutral with regard to jurisdictional claims in published maps and institutional affiliations.

1. Introduction

Large-scale ocean currents are primarily powered by atmospheric winds and astronomical tidal forces at rates well quantified through satellite observations [1]. The work done by winds acting on the large-scale ocean currents inputs kinetic energy (KE) at a rate of around 0.8–0.9 TW [1–3], but the subsequent fate of this KE flux remains elusive. A large fraction of the KE input is converted into a vigorous mesoscale eddy field through the baroclinic instabilities of the large-scale currents and accounts for approximately 90% of the total ocean KE [4]. It is a topic of active research how the mesoscale energy is eventually dissipated at molecular scales. A prime candidate is thought to be bottom drag, i.e., the generation of vigorous turbulence along the ocean seafloor, which effectively transfers energy to smaller dissipative scales. Problematically, attempts to estimate the energy dissipated through bottom drag have resulted in widely differing estimates [1,5–7]

Bottom drag is experienced by oceanic flows above the seafloor, where a stress develops that brings the flow to zero. This occurs in a thin bottom boundary layer (BBL) characterized by enhanced shear and turbulence. The bottom stress τ_b is given by:

$$\tau_b \equiv \rho_0 \nu \left.\frac{\partial u}{\partial z}\right|_{z=0}, \tag{1}$$

where z is the vertical coordinate relative to the bottom, ν is the molecular viscosity, ρ_0 is a reference density (seawater density varies by no more than a few percent across the global ocean) and $u(z)$ is the velocity component parallel to the seafloor. The bottom friction is often expressed in terms of a friction velocity defined as

$$u_\tau \equiv \sqrt{\tau_b / \rho_0}. \tag{2}$$

In the real turbulent ocean, it is difficult to estimate the bottom stress using Formula (1), because it requires detailed knowledge of rapid shear fluctuations very close to the boundary. Instead, the bottom stress is typically calculated using an empirical quadratic drag law

$$\tau_b = \rho_0 C_d U^2, \tag{3}$$

where C_d is a drag coefficient and U is the magnitude of the mean flow above the BBL, the so-called "far-field" velocity. This formula relates the bottom stress to dynamic pressure (proportional to U^2) associated with the mean flow [8].

Taylor went a step further and proposed to estimate the KE dissipation within the BBL, $\mathcal{D}$, as the product of the bottom stress and the "far-field" velocity [9]:

$$\mathcal{D} \equiv \int_{\mathrm{BBL}} \epsilon(z)\, dz \simeq \frac{\tau_b}{\rho_0} U = C_d U^3, \tag{4}$$

where ϵ is the point-wise KE dissipation rate defined as

$$\epsilon = \frac{\nu}{2} S_{ij} S_{ij}, \tag{5}$$

and $S_{ij} = \partial u_i/\partial x_j + \partial u_j/\partial x_i$ is the rate of strain tensor. Taylor used this bulk formula to estimate the dissipation experienced by barotropic tides over continental shelves and set U to be the barotropic tidal velocity [9]. This bulk formula was later used to estimate the dissipation of sub-inertial flows in the global ocean and returned values anywhere between 0.2 and 0.83 TW [1,5–7]. Based on these estimates, bottom drag could be a dominant sink of the 0.8–0.9 TW KE input by winds or a second-order process.

In this study, we will take a closer look at the reasoning and assumptions behind Taylor's KE dissipation formula (Equation (4)) and compare this bulk estimate with explicitly diagnosed KE dissipation rates from turbulence-resolving direct numerical simulations (DNS). We find that although the formula slightly overestimates the integrated BBL energy dissipation rate, it provides satisfying bulk estimates in idealized numerical simulations of flows over a smooth flat bottom. The difference between the two depends on the distribution of velocity and shear stress close to the seafloor, which implies a possibly larger discrepancy when the inner layer BBL structure is disrupted by bottom roughness in the real ocean. The DNS data are described in Section 2. In Section 3, we illustrate how the vertical profiles of stress and velocity shear determine the performance of Taylor's formula. Our hypothesis is confirmed by computing the vertical profiles of shear, stress and KE dissipation from the DNS in Section 4. In Section 5, we derive a heuristic formula that predicts the performance of Taylor's formula at a realistically large frictional Reynolds number Re_τ. The implications of our work for oceanographic estimates of energy dissipation in the BBL are discussed in Section 6.

2. Data and Methods

The data analyzed in this study come from four DNS of a mean flow over a smooth flat bottom—two without rotation [10] and two with rotation [11]—the so-called bottom Ekman layer. The simulations are characterized using frictional Reynolds number $\mathrm{Re}_\tau = u_\tau \delta/\nu = \delta/\delta_\nu$, where $\delta_\nu = \nu/u_\tau$ is the viscous length scale. The bottom boundary condition is no-slip in all simulations, and the top boundary condition is a prescribed velocity equal to the free-stream flow. The diagnostics are obtained by horizontally averaging over the model domain once the solutions have achieved a statistically steady state. More details about the simulations are given in Table 1.

Table 1. Summary of the DNS experiments. Note that the drag coefficient C_d in each run can be obtained using $C_d = (u_\tau/U)^2$ considering $\tau_b = \rho_0 C_d U^2$ and $u_\tau \equiv \sqrt{\tau_b/\rho_0}$.

No.	$\mathbf{Re_\tau(Re_f)}$	u_τ/U	Type	$\mathcal{D}/C_dU^3$
1	830	4.08×10^{-2}	non-rotating	0.8614
2	1271	3.85×10^{-2}	non-rotating	0.8638
3	943	5.61×10^{-2}	rotating	0.9082
4	1765	5.21×10^{-2}	rotating	0.9178

For the rest of the paper, we will use δ as the boundary layer thickness for both setups. In the non-rotating case, δ denotes the distance across the boundary layer from the bottom wall to a point where the flow velocity has essentially reached the 'free-stream' velocity (99% of U); in the rotating case, we adopt the common Ekman layer scaling, $\delta = u_\tau/f$, where f is the Coriolis frequency. Considering the difference in the definition of boundary layer thickness, we will use $\mathrm{Re}_\tau = u_\tau\delta/\nu$ for the non-rotating BBL and $\mathrm{Re}_f = u_\tau^2/f\nu$ for the rotating BBL, where the boundary layer thickness is replaced with the Ekman layer scaling. Note, however, that these two Reynolds numbers are comparable, as will be shown in Section 4. Finally, all the diagnostics are non-dimensionalized by the appropriate combination of frictional variables ν and u_τ; for instance, the non-dimensional dissipation rate is given by $\epsilon^+ = \epsilon\nu/u_\tau^4$.

3. The Impact of the Vertical Shear Profile on BBL Dissipation

We start by computing the integrated BBL dissipation rate in a non-rotating BBL for idealized vertical profiles of velocity and shear stress in order to illustrate their impacts on the bulk estimates. We assume a horizontal flow u above a solid bottom, and that all variables are independent of horizontal position and vary only with distance above the bottom. The total energy dissipation rate (per unit mass) within the BBL can simply be calculated as the vertical integral of the product of u and the vertical gradient of total shear stress τ:

$$\mathcal{D} = -\int_0^\delta u\frac{\partial\tau}{\partial z}\,dz = \int_0^\delta \tau\frac{\partial u}{\partial z}\,dz = \int_0^\delta C_dU^2\left(\frac{\delta - z}{\delta}\right)\frac{\partial u}{\partial z}\,dz. \tag{6}$$

where τ includes both viscous and Reynolds stresses and we integrated by parts using the fact that the velocity u vanishes at $z = 0$ and the shear stress vanishes at $z = \delta$. The shear stress has been approximated as a linearly decaying profile in z [12]:

$$\tau(z) = \tau_b\left(\frac{\delta - z}{\delta}\right). \tag{7}$$

Taylor's formula follows from Equation (6) only if the velocity profile u is uniform and equal to the far-field velocity U, but this is not the case in reality. Instead, the velocity profile decays to zero within the BBL due to the no-slip bottom boundary condition. If we assume, for simplicity, that the velocity profile is linear in z up to $z = \delta_s$, where it reaches the far-field velocity U, and remains constant above (Figure 1) (in other words, we only consider the large velocity shear confined in a thin layer of thickness δ_s near the bottom and we ignore any negligibly small changes above), the integral in Equation (6) can be rewritten as:

$$\mathcal{D} = \int_0^{\delta_s} C_dU^2\left(\frac{\delta - z}{\delta}\right)\frac{U}{\delta_s}\,dz = C_dU^3(1 - \frac{1}{2}\frac{\delta_s}{\delta}). \tag{8}$$

For this admittedly idealized piece-wise linear velocity profile, Taylor's formula is recovered only in the limit where the velocity shear is confined to a layer much thinner than the BBL ($\delta_s \ll \delta$).

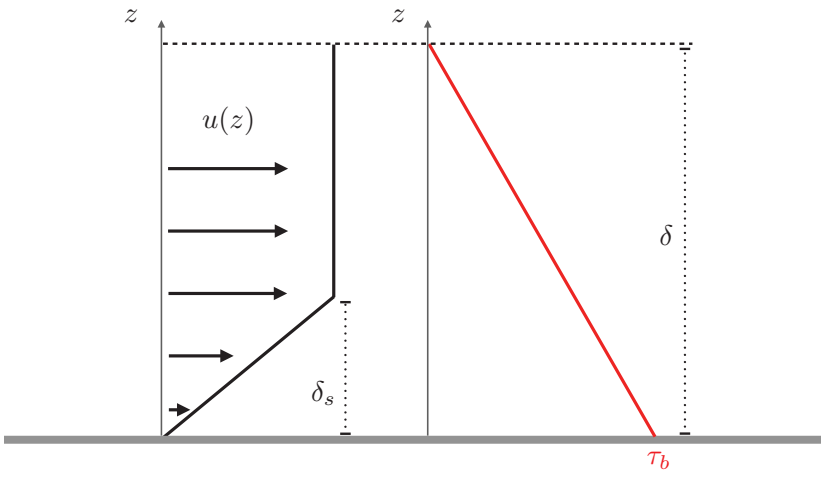

Figure 1. Schematic of idealized distribution of velocity and shear stress in the non-rotating bottom boundary layer (BBL). On the left is the mean velocity profile as a function of depth, where a constant shear layer of thickness δ_s is present. On the right is the linearly decaying profile of shear stress, where it takes the bottom stress value $\tau = \tau_b$ at $z = 0$ and $\tau = 0$ at $z = \delta$.

The vertical profiles of velocity and shear stress in the DNS of non-rotating BBL are shown in Figure 2 for two different Re_τ. Supporting the main idealization associated with our heuristic model introduced above, two observations can be made: (i) the largest velocity shear is confined within a thin layer near the bottom (Figure 2a and dashed lines in Figure 2b); (ii) the decay of the total shear stress follows a rather linear profile (solid lines in Figure 2b). As Re_τ increases, the layer accounting for the large velocity shear becomes thinner and closer to the wall. While the shear layer thickness is always thinner than δ, and progressively more so for increasing Re_τ, it clearly differs from the limit where the shear layer is infinitesimally thin, as assumed in Taylor's formula. We will evaluate the impact of this discrepancy in the next section.

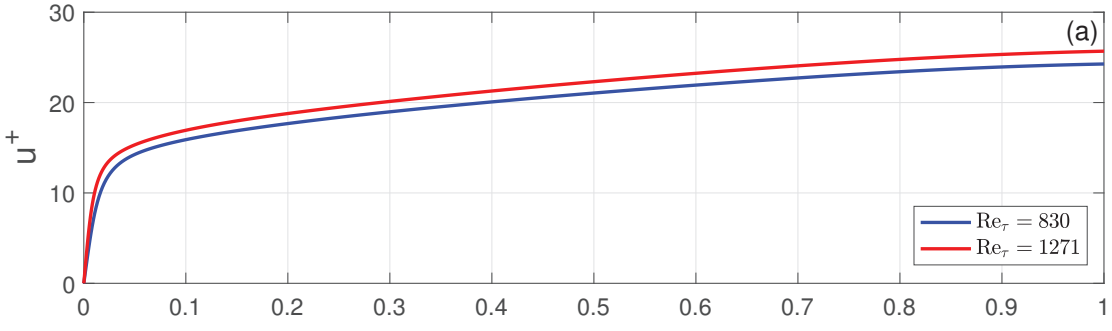

Figure 2. *Cont.*

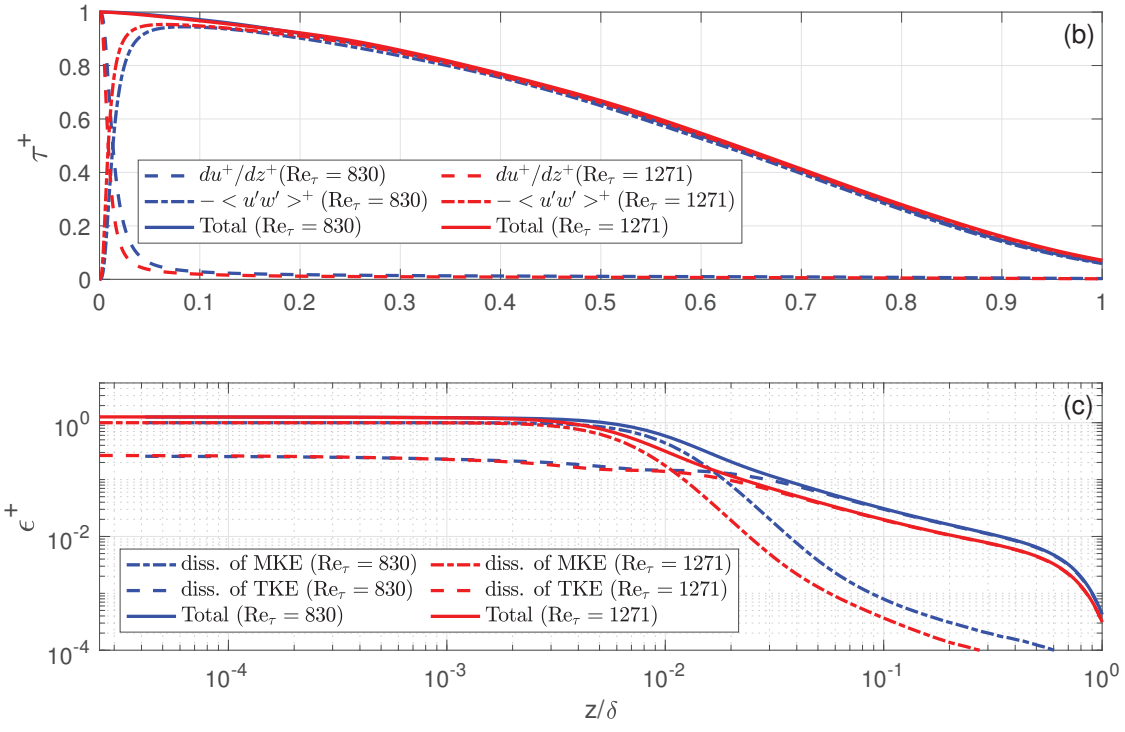

Figure 2. Profiles of non-dimensional velocity (**a**), shear stress including both viscous stress $\mathrm{du}^+/\mathrm{dz}^+$ and Reynolds stress $< u'w' >^+$ (**b**) and dissipation rate (**c**) as a function of z/δ (depth normalized by the boundary layer thickness) in the DNS of non-rotating BBL.

4. Vertical Structures of the BBL

4.1. Non-Rotating BBL

Along with the thin layer containing the large velocity shear is enhanced viscous stress and the associated dissipation of mean kinetic energy (MKE) within the BBL (Figure 2b,c). The viscous stress is dominant for $z/\delta \lessapprox 0.02$ due to both the enhanced velocity shear and the damping of Reynolds stress in the presence of the solid bottom. Again, the distribution of the total shear stress provides support for the linear approximation made in the idealized heuristic model in the last section. As Re_τ increases, both the viscous and Reynolds stress become closer to the bottom, but the structure of the total shear stress remains relatively unchanged (Figure 2b).

The dissipation of MKE acts as an additional route to energy dissipation and has been typically thought to be negligible in turbulent flows away from boundaries with moderate to large Reynolds numbers. It cannot be ignored, however, in the BBL, where the velocity shear is confined close to the bottom. In this case, MKE dissipation contributes around 40% of the total energy dissipation rate. On the other hand, the dissipation of turbulent kinetic energy (TKE) becomes dominant beyond $z/\delta = 0.02$ and remains so all the way to the top of the BBL. The transition point between the dissipation of MKE and TKE becomes closer to the bottom with larger Re_τ.

From the simulations, we can calculate the ratios between the true KE dissipation rate (using Equation (5)) integrated across the BBL and those estimated with Taylor's

bulk formula: τ_b can be directly obtained from Equation (1) in each run, as with the drag coefficient C_d and friction velocity u_τ (Table 1). The ratio of the two can be written as:

$$\frac{\mathcal{D}}{C_d U^3} = \frac{u_\tau^3 \int_{\mathrm{BBL}} \epsilon^+(z^+)\, dz^+}{u_\tau^2\, U} = \frac{u_\tau}{U} \int_{\mathrm{BBL}} \epsilon^+(z^+)\, dz^+. \tag{9}$$

The calculated $\mathcal{D}/C_d U^3$ ratios for the two simulations of non-rotating BBL are 86.1% and 86.4%, respectively (Table 1). These ratios imply that the δ_s/δ ratio in Equation (8) is around 0.28; this depth of shear layer δ_s roughly corresponds to $\epsilon^+ = 10^{-2}$ (Figure 2c). We will examine the performance of Taylor's formula in the rotating BBL next.

4.2. Rotating BBL

When rotation is introduced, the simulated velocity profiles show a spiral structure as they approach the far-field mean flow (Figure 3a). One noticeable difference from the non-rotating BBL is the more bottom-confined or concave profiles for both velocity shear and shear stress (Figure 3a,b), compared with the more linear shear profile in the non-rotating BBL. The rest of the structures remain similar in the BBL with or without rotation.

In the two simulations of rotating BBL, the true integrated KE dissipation rate is 90.8% and 91.8% of those estimated using Taylor's bulk formula (using Equation (9)), higher than those for the non-rotating BBL for comparable Re_f. This better performance could be explained by the more bottom-confined velocity shear and shear stress profiles.

In summary, Taylor's bulk formula provides reasonable first-order estimates for the true integrated dissipation rate. In fact, $\mathcal{D}/C_d U^3 \approx 0.9$, which is the equivalent of $\delta_s/\delta \approx 0.2$, is consistent with the observations that the log-layer, where the largest velocity shear and shear stress reside, roughly occupies 20% of the BBL thickness for both the rotating and non-rotating BBLs (Figure 4). This 20% has also been shown to hold for natural turbulent flows with much larger Re_τ [13], which implies that Taylor's formula could provide a reasonable integrated dissipation estimate in the real ocean, given that the log-layer structure remains intact.

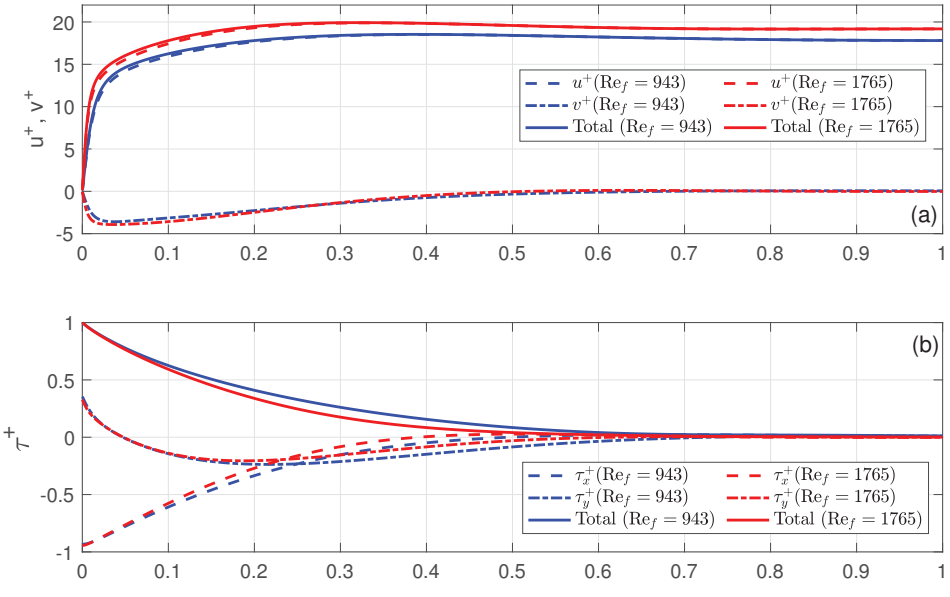

Figure 3. *Cont.*

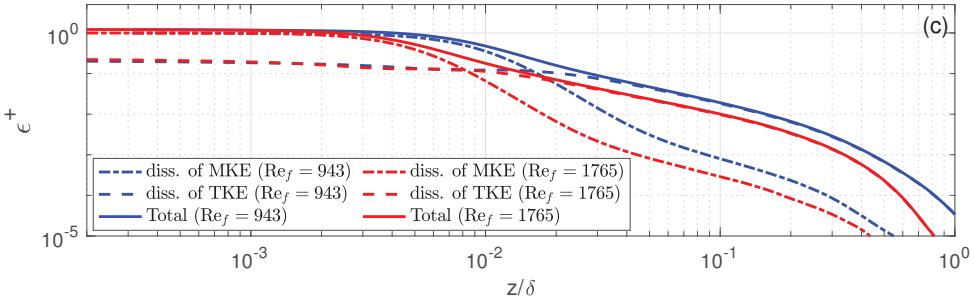

Figure 3. Profiles of non-dimensional velocity (**a**), shear stress including both viscous stress du^+/dz^+ and Reynolds stress $< u'w' >^+$ (**b**) and dissipation rate (**c**) as a function of z/δ (depth normalized by the boundary layer thickness) in the DNS of rotating BBL.

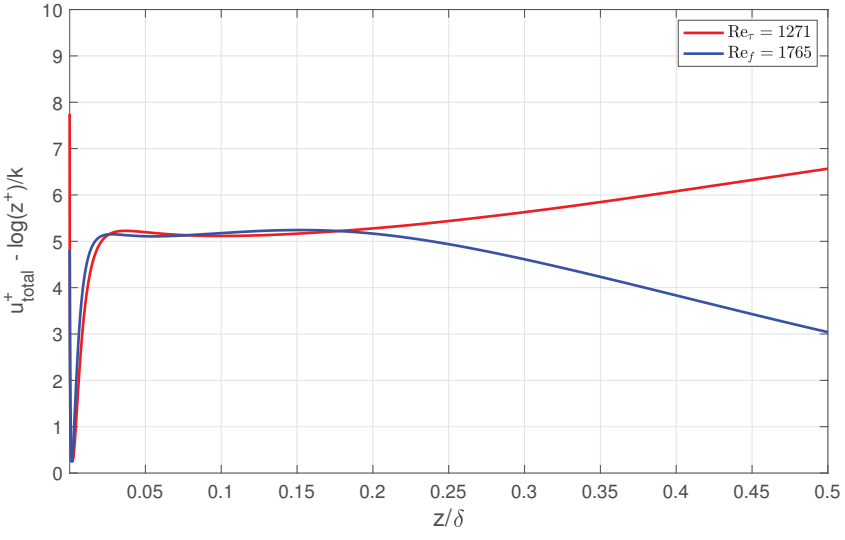

Figure 4. The difference between non-dimensional velocity in the simulations and a logarithmic function of depth (z^+), where the relatively flat lines indicate the location of the logarithmic layer. Both the rotating and non-rotating profiles are shown here.

5. An Empirical Formula for Large Re_τ

To improve on the prediction of the heuristic model and extend the findings to realistically large Re_τ for real ocean applications, we repeat the analysis in Section 3 but with a more physical velocity profile derived by van Driest [14]. Note that the prediction is only performed for the non-rotating BBL since relevant analytical profiles for the rotating BBL structures are still lacking. The analytical shear profile is introduced based on mixing length arguments:

$$\frac{\partial u^+}{\partial z^+} = \frac{2(1 - z^+/Re_\tau)}{1 + [1 + 4(1 - z^+/Re_\tau)(l_m^+)^2]^{1/2}} \tag{10}$$

where

$$l_m^+ = kz^+[1 - exp(-z^+/\zeta)] \tag{11}$$

is a mixing length that decreases rapidly close to the wall, representing the damping of the log-layer mixing length kz^+ due to the presence of the solid boundary. $k = 0.41$ is the von

Kármán constant and ζ is a constant with a typical value of 26. Figure 5 demonstrates that the analytical profile captures well the velocity shear from the numerical simulations.

Substituting van Driest's analytical Formula (10) into the integral formula for the BBL dissipation given in Equation (6) and again assuming a linear decaying function for the total shear stress, we obtain:

$$\mathcal{D} = C_d U^2 u_\tau \int_0^{\mathrm{Re}_\tau} \left(1 - \frac{z^+}{\mathrm{Re}_\tau}\right) \frac{\partial u^+}{\partial z^+} \, \mathrm{d}z^+ = \mathrm{I}(\mathrm{Re}_\tau) \, \frac{u_\tau}{U} \, C_d U^3, \tag{12}$$

where $\mathrm{I}(\mathrm{Re}_\tau)$ is a growing function of Re_τ given by the integral expression:

$$\mathrm{I}(\mathrm{Re}_\tau) = \int_0^{\mathrm{Re}_\tau} \frac{2(1 - z^+/\mathrm{Re}_\tau)^2}{1 + [1 + 4(1 - z^+/\mathrm{Re}_\tau)(l_m^+)^2]^{1/2}} \, \mathrm{d}z^+. \tag{13}$$

Finally, the ratio of the integrated BBL dissipation rate based on van Driest's analytical expression and that proposed by Taylor is given by:

$$\mathcal{R} \equiv \frac{\mathcal{D}}{C_d U^3} = \mathrm{I}(\mathrm{Re}_\tau) \frac{u_\tau}{U}. \tag{14}$$

Pope [12] showed that $U/u_\tau = k^{-1} \ln(\mathrm{Re}_\tau) + D$, where D is a constant that depends on the problem geometry. Thus, the ratio in Equation (14) can be expressed as a function of Re_τ only:

$$\mathcal{R}(\mathrm{Re}_\tau) = \frac{\mathrm{I}(\mathrm{Re}_\tau)}{k^{-1} \ln(\mathrm{Re}_\tau) + D}. \tag{15}$$

The prediction of $\mathcal{R}(\mathrm{Re}_\tau)$ to realistically large Re_τ is shown in Figure 6 with two different choices of D. For our two non-rotating BBL simulations, D is found to be around 8 based on the U/u_τ ratios given in Table 1, but we need to adjust the D value to 5 when estimating the integrated dissipation rate to match the existing simulation results. This adjustment for higher-order statistics (i.e., dissipation) may be justified as a way to compensate for the idealizations introduced in the heuristic model, such as possible deviations from the assumed perfect linear profile of shear stress. While it is indeed the case that the ratio approaches one for infinite Re_τ, the convergence for larger Re_τ becomes very slow and our non-rotating BBL results are very close to the "saturated" value of $\mathcal{R} = 0.9$ (Figure 6). It is unclear whether the prediction for the rotating BBL follows a similar asymptotic trend; it is likely that the calculated $\mathcal{R}$ values for the rotating BBL presented here are already in the slow-converging regime considering that the velocity shear is more confined to the solid bottom compared with the non-rotating BBL at comparable Reynolds numbers. This will need to be addressed in future studies.

Formula (15) quantifies the amount by which Taylor's formula overpredicts the integrated dissipation taking place over a flat BBL. To appreciate the oceanographic implications of this result, it is worth applying the formula to parameters typical of oceanic BBL: $C_d = 1 \times 10^{-3}$, $U = 0.15$ m/s, $\delta = 10$ m and $\nu = 1.5 \times 10^{-6}$ m^2/s. With these values, $\mathrm{Re}_\tau = 3 \times 10^4$ and the formula gives $\mathcal{R} = \frac{\mathcal{D}}{C_d U^3} = 0.90$. The degree to which results based on flat walls may be used over the rugged ocean bottom will be discussed in the next section.

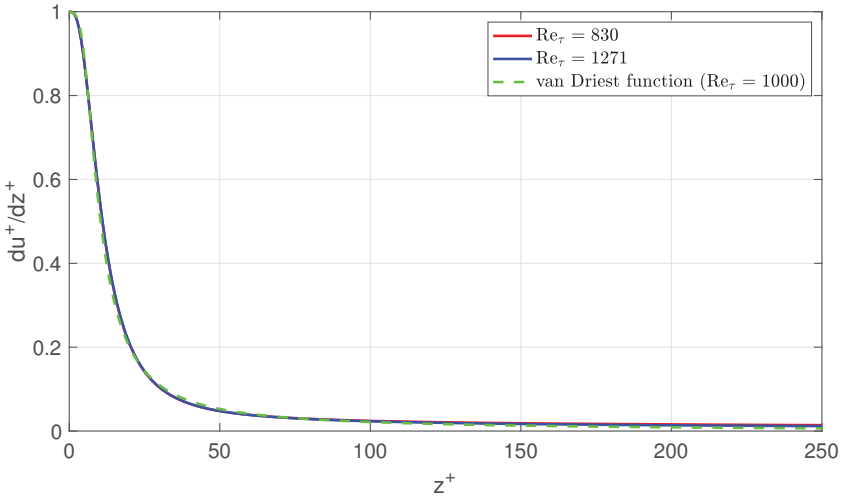

Figure 5. The non-dimensional velocity shear as a function of z^+ for the DNS of non-rotating BBL. The dashed green curve is the van Driest function with $\zeta = 26$ and Re_τ=1000 (Equation (10)).

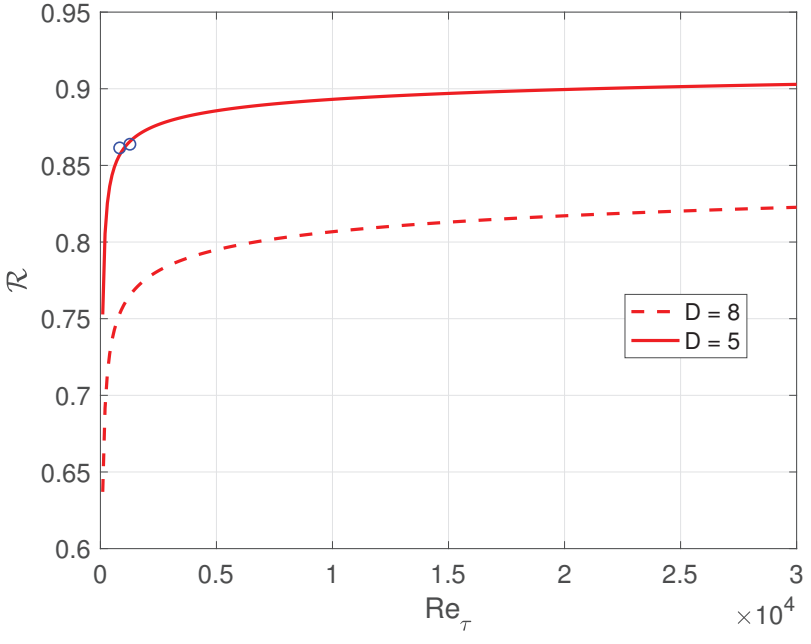

Figure 6. The predicted ratio $\mathcal{R}$ (Equation (15)) as a function of Re_τ. The blue circles mark the ratios from the two non-rotating BBL runs.

6. Conclusions and Discussion

Four DNS experiments were used to demonstrate that the KE dissipation rate in the BBL over a flat wall is less than predicted by the celebrated formula proposed by Taylor [9]: $\mathcal{D} \simeq C_d U^3$, where C_d is a constant drag coefficient and U the "far-field" velocity above the BBL. Taylor's estimate should be treated as an upper and singular limit of the true BBL-integrated KE dissipation rate. The discrepancy arises due to the assumption that the shear in the BBL is confined to an infinitesimally thin layer within the viscous sublayer

in Taylor's formula. It is shown that the shear actually extends far above the viscous sublayer to approximately 20% of the BBL thickness for even the largest frictional Reynolds numbers Re_τ expected in natural flows. Taylor's formula could thus be improved to be $\mathcal{D} \approx 0.9 \times C_d U^3$ for a more accurate prediction. We note that this is a modest correction compared with the other uncertainties in real ocean applications. The local uncertainties associated with the drag coefficient C_d and the identification of the far-field velocity U when using Taylor's formula could introduce much larger errors in problems encountered in the real ocean. Nonetheless, we believe that the findings in this study will be helpful in future BBL dissipation estimates, especially in cases where C_d and U are well measured or when their local variations can be ignored in large-scale BBL dissipation quantification.

Admittedly, Taylor's formula provides a good first-order estimate for the integrated BBL dissipation rate. However, the evaluation performed in this note only applies to a smooth bottom where the viscous and log-layers are intact. The ocean seafloor is far from flat. Corrugations on scales smaller than the BBL thickness, typical of the ocean seafloor, could modify or even destroy the inner layer structures [15]. The small roughness can be accounted for by introducing a roughness parameter that quantifies the characteristic height of the corrugations, z_o. This results in a modification of the log-layer away from the bottom: $u(z) = \frac{u_\tau}{\kappa} \log \frac{z}{z_o}$, e.g., [12,16]. It remains to be studied whether the disrupted viscous sublayer and the modified log-layer structure could have an impact on the energy dissipation estimate. Moreover, the log-layer could be completely destroyed when the roughness is large. A common parameter to consider here is the blockage ratio δ/k, where k is the roughness height. This non-dimensional parameter measures the direct effect of the roughness on the log-layer, where most of the mean shear is concentrated. Previous studies have shown that δ/k has to be at least 40 for a general log-layer structure to hold [15]. This suggests that Taylor's formula could fail over rough seafloors where the velocity shear is no longer concentrated close to the wall. Detailed velocity measurements near the seabed are very sparse and the existence of log-layer structures has only been reported over a few locations over the continental shelf, e.g., [17–19]; more observations are needed to assess the applicability of Taylor's formula in the global ocean over more complex topography.

The DNS experiments presented here do not include stratification. This may not be the most problematic simplification of our work, because stratification is expected to be quite weak in oceanic BBL. Stratification is indeed very weak in the inner layer close to the seafloor due to enhanced mixing, e.g., [20,21]. Stratification may, however, be strong enough in the outer layer to suppress turbulent overturns larger than the Ozmidov scale $L_o = (\epsilon/N^3)^{1/2}$ (N being the Brunt–Väisälä frequency) and lead to a modification of the shear profile [18,19]. However, we showed that the bulk of the KE dissipation occurs in the log-layer, and not in the outer layer, where the distance to the bottom is the dominant limit on the eddy overturn size rather than the Ozimdov scale. Thus, we expect the influence of stratification on the integrated dissipation rate to be small. In real ocean applications, however, stratification may pose problems in identifying the far-field flow U, especially when over a sloping bottom [22–25].

In addition to small-scale roughness, BBL dissipation can be modified by the presence of large-scale slopes, such as along the flanks of ridges and seamounts [26–28], detachment of BBL at large Froude numbers, e.g., [29], and the development of a whole gamut of hydrodynamic subemsoscale instabilities and hydraulic jumps, e.g., [30,31]. Clearly, a full quantitative picture of BBL dissipation in the ocean remains far from complete. Our work has only shown that Taylor's formula should be used with caution and treated as an upper limit of the integrated BBL dissipation rate in the case of a mean flow over the seafloor. Future examinations are needed to account for seafloor roughness and more realistic velocity and stress profiles before applying Taylor's formula in global energy dissipation studies.

Funding: This research was funded by NSF Award OCE-1756324.

Data Availability Statement: The non-rotating and rotating BBL data used in this study are available at https://www.mech.kth.se/~pschlatt/DATA/ (accessed on 2 November 2020) and https://www.rs.tus.ac.jp/t2lab/db/ekm/ekm.html (accessed on 2 November 2020).

Acknowledgments: I thank Raffaele Ferrari and Stephen Griffies for the helpful discussions and comments that improved the manuscript.

Conflicts of Interest: The author declares no conflict of interest.

Abbreviations

The following abbreviations are used in this manuscript:

KE	Kinetic Energy
BBL	Bottom Boundary Layer
DNS	Direct Numerical Simulation
MKE	Mean Kinetic Energy
TKE	Turbulent Kinetic Energy

References

1. Wunsch, C.; Ferrari, R. Vertical mixing, energy, and the general circulation of the oceans. *Annu. Rev. Fluid Mech.* **2004**, *36*, 281–314. [CrossRef]
2. Wunsch, C. The work done by the wind on the oceanic general circulation. *J. Phys. Oceanogr.* **1998**, *28*, 2332–2340. [CrossRef]
3. Scott, R.B.; Xu, Y. An update on the wind power input to the surface geostrophic flow of the World Ocean. *Deep. Sea Res. Part Oceanogr. Res. Pap.* **2009**, *56*, 295–304. [CrossRef]
4. Ferrari, R.; Wunsch, C. Ocean circulation kinetic energy: Reservoirs, sources, and sinks. *Annu. Rev. Fluid Mech.* **2009**, *41*, 253–282. [CrossRef]
5. Sen, A.; Scott, R.B.; Arbic, B.K. Global energy dissipation rate of deep-ocean low-frequency flows by quadratic bottom boundary layer drag: Computations from current-meter data. *Geophys. Res. Lett.* **2008**, *35*. [CrossRef]
6. Arbic, B.K.; Shriver, J.F.; Hogan, P.J.; Hurlburt, H.E.; McClean, J.L.; Metzger, E.J.; Scott, R.B.; Sen, A.; Smedstad, O.M.; Wallcraft, A.J. Estimates of bottom flows and bottom boundary layer dissipation of the oceanic general circulation from global high-resolution models. *J. Geophys. Res. Ocean.* **2009**, *114*. [CrossRef]
7. Wright, C.J.; Scott, R.B.; Furnival, D.; Ailliot, P.; Vermet, F. Global observations of ocean-bottom subinertial current dissipation. *J. Phys. Oceanogr.* **2013**, *43*, 402–417. [CrossRef]
8. Tritton, D.J. *Physical Fluid Dynamics*; Springer Science & Business Media: Berlin/Heidelberg, Germany, 2012.
9. Taylor, G.I. I. Tidal friction in the Irish Sea. *Philos. Trans. R. Soc. London. Ser. Contain. Pap. Math. Phys. Character* **1920**, *220*, 1–33.
10. Schlatter, P.; Örlü, R. Assessment of direct numerical simulation data of turbulent boundary layers. *J. Fluid Mech.* **2010**, *659*, 116–126. [CrossRef]
11. Miyashita, K.; Iwamoto, K.; Kawamura, H. Direct numerical simulation of the neutrally stratified turbulent Ekman boundary layer. *J. Earth Simulator* **2006**, *6*, 3–15.
12. Pope, S.B. *Turbulent Flows*; Cambridge University Press: Cambridge, UK, 2001.
13. Marusic, I.; Monty, J.P.; Hultmark, M.; Smits, A.J. On the logarithmic region in wall turbulence. *J. Fluid Mech.* **2013**, *716*. [CrossRef]
14. Van Driest, E.R. On turbulent flow near a wall. *J. Aeronaut. Sci.* **1956**, *23*, 1007–1011. [CrossRef]
15. Jiménez, J. Turbulent flows over rough walls. *Annu. Rev. Fluid Mech.* **2004**, *36*, 173–196. [CrossRef]
16. Tennekes, H.; Lumley, J.L. *A first Course in Turbulence*; MIT Press: Cambridge, MA, USA, 2018.
17. Caldwell, D.; Chriss, T. The viscous sublayer at the sea floor. *Science* **1979**, *205*, 1131–1132. [CrossRef] [PubMed]
18. Sanford, T.B.; Lien, R.C. Turbulent properties in a homogeneous tidal bottom boundary layer. *J. Geophys. Res. Ocean.* **1999**, *104*, 1245–1257. [CrossRef]
19. Perlin, A.; Moum, J.N.; Klymak, J.; Levine, M.D.; Boyd, T.; Kosro, P.M. A modified law-of-the-wall applied to oceanic bottom boundary layers. *J. Geophys. Res. Ocean.* **2005**, *110*. [CrossRef]
20. Perlin, A.; Moum, J.; Klymak, J.; Levine, M.; Boyd, T.; Kosro, P. Organization of stratification, turbulence, and veering in bottom Ekman layers. *J. Geophys. Res. Ocean.* **2007**, *112*. [CrossRef]
21. Ruan, X.; Thompson, A.F.; Flexas, M.M.; Sprintall, J. Contribution of topographically generated submesoscale turbulence to Southern Ocean overturning. *Nat. Geosci.* **2017**, *10*, 840. [CrossRef]
22. MacCready, P.; Rhines, P.B. Buoyant inhibition of Ekman transport on a slope and its effect on stratified spin-up. *J. Fluid Mech.* **1991**, *223*, 631–661. [CrossRef]
23. Brink, K.H.; Lentz, S.J. Buoyancy arrest and bottom Ekman transport. Part I: Steady flow. *J. Phys. Oceanogr.* **2010**, *40*, 621–635. [CrossRef]
24. Ruan, X.; Thompson, A.F.; Taylor, J.R. The Evolution and Arrest of a Turbulent Stratified Oceanic Bottom Boundary Layer over a Slope: Downslope Regime. *J. Phys. Oceanogr.* **2019**, *49*, 469–487. [CrossRef]

25. Ruan, X.; Thompson, A.F.; Taylor, J.R. The evolution and arrest of a turbulent stratified oceanic bottom boundary layer over a slope: Upslope regime and PV dynamics. *J. Phys. Oceanogr.* **2021**, *51*, 1077–1089. [CrossRef]
26. Callies, J. Restratification of abyssal mixing layers by submesoscale baroclinic eddies. *J. Phys. Oceanogr.* **2018**, *48*, 1995–2010. [CrossRef]
27. Wenegrat, J.O.; Callies, J.; Thomas, L.N. Submesoscale baroclinic instability in the bottom boundary layer. *J. Phys. Oceanogr.* **2018**, *48*, 2571–2592. [CrossRef]
28. Ruan, X.; Callies, J. Mixing-driven mean flows and submesoscale eddies over mid-ocean ridge flanks and fracture zone canyons. *J. Phys. Oceanogr.* **2020**, *50*, 175–195. [CrossRef]
29. Armi, L. Some evidence for boundary mixing in the deep ocean. *J. Geophys. Res. Ocean.* **1978**, *83*, 1971–1979. [CrossRef]
30. Thurnherr, A.; St. Laurent, L.; Speer, K.; Toole, J.; Ledwell, J. Mixing associated with sills in a canyon on the midocean ridge flank. *J. Phys. Oceanogr.* **2005**, *35*, 1370–1381. [CrossRef]
31. Wenegrat, J.O.; Thomas, L.N. Centrifugal and symmetric instability during Ekman adjustment of the bottom boundary layer. *J. Phys. Oceanogr.* **2020**, *50*, 1793–1812. [CrossRef]

fluids

MDPI

Article

Interannual Bottom-Intensified Current Thickening Observed on the Continental Slope Off the Southeastern Coast of Hokkaido, Japan

Akira Nagano [1,*], Takuya Hasegawa [2,3], Keisuke Ariyoshi [4] and Hiroyuki Matsumoto [4]

[1] Research Institute for Global Change, Japan Agency for Marine-Earth Science and Technology (JAMSTEC), Yokosuka 237-0061, Japan
[2] Faculty of Environmental Earth Science, Hokkaido University, Sapporo 060-0810, Japan; takuya.hasegawa@ees.hokudai.ac.jp
[3] Graduate School of Science, Tohoku University, Sendai 980-8578, Japan
[4] Research Institute for Marine Geodynamics, Japan Agency for Marine-Earth Science and Technology (JAMSTEC), Yokosuka 237-0061, Japan; ariyoshi@jamstec.go.jp (K.A.); hmatsumoto@jamstec.go.jp (H.M.)
* Correspondence: nagano@jamstec.go.jp

Abstract: By rotary empirical orthogonal function and coastal-trapped wave mode analyses, we analyzed current velocity data, collected from 2001 to 2016. The data were obtained by an acoustic Doppler current profiler, deployed upward at a location of 41°39.909′ N, 144°20.695′ E, on a 2630-m deep continental slope seabed off the southeastern coast of Hokkaido, Japan. The results indicate that the current intensifies toward the bottom and is directed nearly toward the shore, reaching an average speed of ∼2.5 cm s^{-1} just above the bottom. The thickness of the along-slope northward component of the bottom-intensified current varied within the range of 50–350 m. We found that the current thickness change was caused by oceanic barotropic disturbances, produced by the intensification of the Aleutian Low, largely related to the El Niño–Southern Oscillation and modified through the excitation of bottom-trapped modes of coastal-trapped waves. This finding improves the prediction accuracy of the the bottom-intensified current change, being beneficial for suspended sediment studies, construction and maintenance of marine structures, planning of deep drilling, and so on.

Keywords: ocean bottom boundary layer; bottom-intensified current; coastal-trapped wave; acoustic Doppler current profiler

Citation: Nagano, A.; Hasegawa, T.; Ariyoshi, K.; Matsumoto, H. Interannual Bottom-Intensified Current Thickening Observed on the Continental Slope Off the Southeastern Coast of Hokkaido, Japan. *Fluids* **2022**, *7*, 84. https://doi.org/10.3390/fluids7020084

Academic Editors: Joseph J. Kuehl, Pengfei Xue and Fabrice Veron

Received: 30 November 2021
Accepted: 16 February 2022
Published: 19 February 2022

1. Introduction

Deep and bottom currents are critical factors in oceanographic researches and ocean engineering. For example, bottom currents suspend sediments from the seabed [1]. Besides short-term sediment gravity flows [2], the cumulative effects of long-term variations in deep and bottom currents, even those that are very weak, are thought to have substantial impacts on the distribution of suspended sediments, e.g., [3]. In addition to corrosion, deep and bottom currents impact the construction and maintenance of marine and offshore structures and deep sea drilling, e.g., [4]. Flows around marine structures produce Kármán vortices, which induce vibration of marine structures and generate turbulence, e.g., [5,6]. Such periodic and random vibrations could seriously damage structures and their functions. Accordingly, knowledge of deep and bottom currents is prerequisite to construct marine structures and perform deep drilling.

Knowledge of mid-depth and deep currents is quite limited, in comparison to sea- and near-surface currents. It is because current velocity data are derived from "snapshot" data, such as geostrophic velocity calculations based on hydrographic data [7], lowered acoustic Doppler current profiler (ADCP) observations [8–10], and moored current meter observations [11]. Even mooring observations have data coverage lengths of 2 years at most, with limitations of the installed battery life and data storage [12,13]. Thus, variations

on timescales of years and longer cannot be fully understood. The exception is the bottom pressure observation in the region off the southeast coast of Hokkaido, Japan. By using data at stations PG1 (41°42.076′ N, 144°26.486′ E) and PG2 (42°14.030′ N, 144°51.149′ E) (Figure 1a), recorded over periods of 10 years and longer, Hasegawa et al. [14,15] found that the interannual variation in bottom pressure is related to atmospheric variations that originated in the tropical dominant variation, i.e., the El Niño–Southern Oscillation (ENSO).

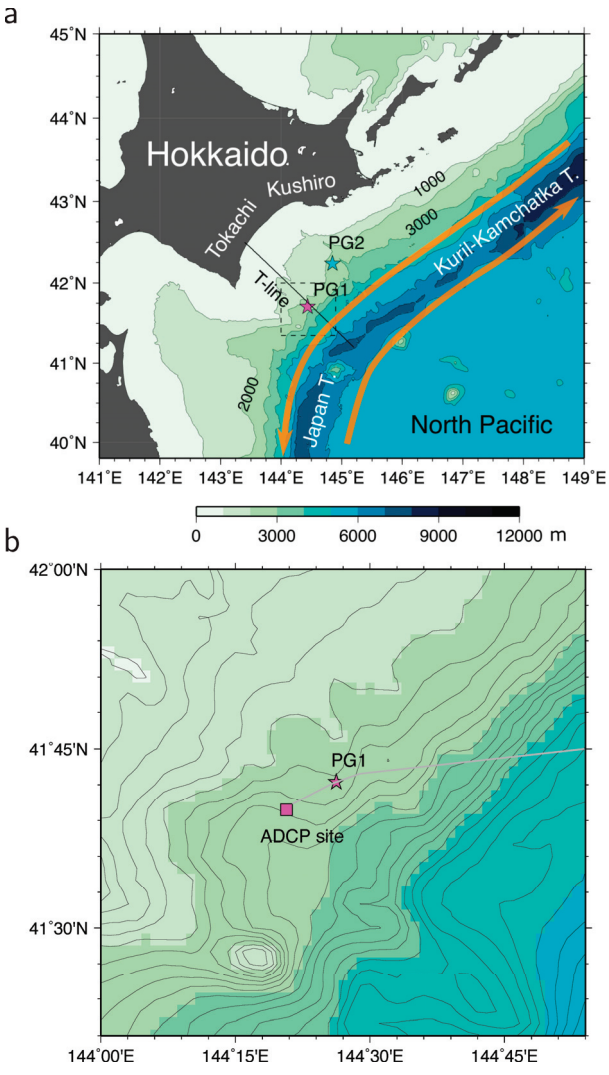

Figure 1. (**a**) Locations of the ADCP and bottom pressure gauge station PG1 (magenta star) and bottom pressure gauge station PG2 (cyan star) with sea bottom topography. Deep circulation currents are schematically illustrated by orange lines. Coastal-trapped wave (CTW) modes were computed using the topographic data at the southeastward-trending black line (called the T-line). The bottom topography contour interval is 1000 m. (**b**) Enlarged map of the region around PG1 (magenta star), enclosed by the dashed square in panel (**a**) and location of the ADCP site (magenta square). The bottom topography contour interval is 200 m. Part of the cable connecting the portable observation system (cable end station) to the land station via PG1 and PG2 is illustrated by gray line.

From the bottom pressure data alone, however, we cannot infer the vertical structure of the disturbances in the deep and bottom layers. Similarly, the single layer measurements of current velocity by current meters cannot deliver vertical current structure. Thus, variations in the current velocity structures just above the seafloor surface, even on timescales longer than the inertial period, have not been sufficiently observed. To elucidate the vertical structure of such long-term variations, we must deploy ADCPs near the bottom pressure gauge to obtain current velocity profiles in long term.

On the seabed, near the bottom pressure gauge at PG1, a portable observation system (cable end station) has been installed (Figure 1b). This system comprises of an ADCP, hydrophone, video camera, and other components and is connected to the battery pack [16]. A cable, connecting the system to a land station, transmits the collected data to land. Consequently, we were able to record an approximately 15-year-long ADCP velocity time series, which is exceptionally long and able to cover the ENSO-scale temporal variations. As described below, we obtained a reasonable time series of the current velocity vectors, ranging from near bottom depth to a height of 388 m, and found a bottom-intensified current. Such a persistent bottom-intensified current has not been documented by past investigators. Furthermore, the northward component of the bottom-intensified current was found to thicken on an interannual timescale; using an ocean general circulation model (OGCM) dataset, we also found that the current travels along the onshore continental slope region of the Japan and Kuril–Kamchatka trenches.

In theory, the current velocity variations over continental slopes cannot be represented by the baroclinic Rossby wave modes, estimated with assumption of a flat bottom ocean, as done by Nagano and Wakita [17] in a study of variations at station K2 in the interior region of the North Pacific subarctic gyre. Fluctuations over the continental slopes are substantially affected by the topography, besides density stratification, being trapped by the continental slopes on subinertial (low) frequencies. These types of waves are called coastal-trapped waves (CTWs) [18–20]. The ENSO (i.e., interannual) timescale variation imposed on the southeastern coast of Hokkaido is thought to excite the CTW mode variations over the continental slope.

In this study, by using a rotary empirical orthogonal function (EOF) analysis [21–23], we examined the characteristics of the interannual variation of the bottom-intensified current. In addition, we calculated the CTW modes by using the method of Brink and Chapman [24] and demonstrated that the observed current velocity variations can be expressed as a superposition of the CTW modes. The disturbances from the offshore region, which follow excitation by ENSO-related changes in the Aleutian Low, were found to be modified by the bottom slope, off the southeastern coast of Hokkaido. The result is a change in the bottom-intensified current thickness by excitation of the bottom-trapped modes of CTW.

2. Observation and Data

2.1. ADCP Observation

Beginning in July 1999, the Japan Agency for Marine-Earth and Technology (JAMSTEC) created the Long-Term Deep Sea Floor Observatory, off Kushiro–Tokachi in the Kuril Trench. Initiation of this project involved deploying bottom pressure gauges at PG1 and PG2, along with a portable observation system, on which the 150-kHz BBADCP (RD Instruments, Poway, CA, USA) was installed upward on the seabed, at a depth of 2630 m, located at 41°39.909′ N, 144°20.695′ E, approximately 6.7 km southwest of PG1 (Figure 1b) [16,25]. The ADCP was set to collect data every 30 min, at 48 levels, with a depth bin size of 8 m. The entire observation system has continued to collect time series data of current velocity profiles near PG1 and bottom pressure data at PG1 and PG2. The ADCP data are available from January 2001. As described below, because the distance between the ADCP station and bottom pressure gauge station PG1 (∼6.7 km) is smaller than the estimated spatial scale of current variation across the continental slope, we refer to the ADCP station as PG1. The data, and detailed accompanying information, are publicly available on the website of

the JAMSTEC Submarine Cable Data Center (http://www.jamstec.go.jp/scdc/top_e.html, accessed on 10 February 2022).

We corrected the current directions using the annual difference between true north and geomagnetic north, on the basis of the 12th generation of the International Geomagnetic Reference Field [26]. The data were interpolated onto grids at intervals of 8 m, from 2242 to 2618 m depths. The nominal accuracy of the ADCP data is 1% of the velocity, or 0.5 cm s^{-1} (Teledyne RD Instruments). The accuracy was 0.5 cm s^{-1} for the observations reported here because the observed range of current speeds was less than 10 cm s^{-1}. In this study, we calculated monthly mean values. Therefore, the random error is less than 0.06 cm s^{-1} by monthly averaging. To examine the interannual variation in current velocity, we further smoothed the data by a 15-month running mean filter.

2.2. OGCM for the Earth Simulator (OFES) Data

We used the current velocity data computed by a global OGCM, which is tuned for the the Earth Simulator (JAMSTEC), based on the Modular Ocean Model, version 3, of the National Oceanic and Atmospheric Administration/Geophysical Fluid Dynamics Laboratory [27]. This model is referred to as the OFES [28–31]. The OGCM dataset used in this study features horizontal grids of 0.1° and 54 vertical grids and is driven by sea-surface momentum, heat, and freshwater flux data, provided by the US National Centers for Environmental Prediction/National Center for Atmospheric Research (NCEP/NCAR) [32].

2.3. North Pacific Index

The North Pacific Index (NPI), which is defined as the area-weighted sea-level pressure in the region of 30° N–65° N, 160° E–140° W, is an indicator of the strength of the Aleutian Low [33]. During El Niño (La Niña) winters, the Aleutian Low becomes stronger (weaker) via atmospheric teleconnection, e.g., [34]. The NPI anomaly was calculated from the seasonal mean. To focus on the ENSO-timescale variation, smoothing was performed for the NPI anomaly using a 15-month running mean filter. Furthermore, we inverted the sign of the NPI anomaly and used the inverted values. Positive (negative) values of the inverted NPI anomaly indicate strengthening (weakening) of the Aleutian Low, principally due to El Niño (La Niña).

3. Results and Discussion

3.1. Vertical Structure of the Bottom Current

Figure 2a,b show eastward and northward components of the current velocity in a bottom layer, from 2240- to 2620-m depth, as observed by the ADCP at PG1. A southwestward flow was observed down to a depth of approximately 2500 m. This current is part of the deep circulation current flowing southward and southwestward along the northwest and west flank of the Kuril–Kamchatka, Japan, and Izu-Ogasawara trenches, studied by past investigators [35–38]. Beneath the deep circulation current, we found the bottom current lies at depths between approximately 2500 and 2620 m, which is mostly directed to the west, i.e., toward the shore, and intensifies with depth. This bottom-current structure was more clearly illustrated by averaging within the study period (Figure 3). The lower end of the deep circulation current was present at a height of approximately 110 m above the seabed. The underlying bottom current reached speeds of 2.5 cm s^{-1} just above the seabed and is along an isopleth of 2600 m (Figure 1b). Such a bottom-intensified current has not been revealed by geostrophic velocity calculation, based on snapshot hydrographic observations and vertically sparse moored current meter observations. Similar bottom-intensified currents have been reported, on the basis of snapshot observations from lowered ADCPs on the continental slope off the south coast of Shikoku [9].

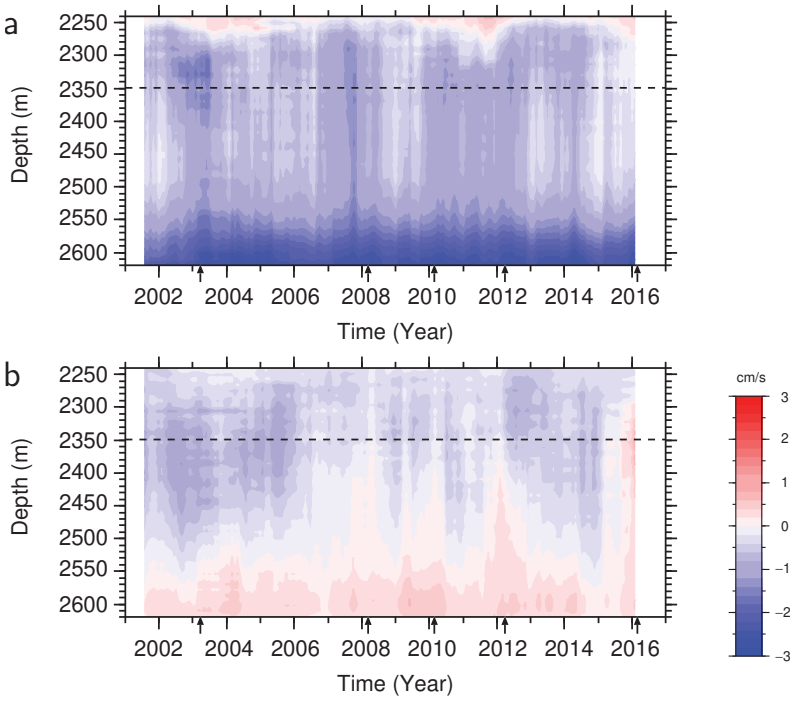

Figure 2. Time-depth diagrams of the (**a**) eastward and (**b**) northward components of the acoustic Doppler current profiler (ADCP) current velocity (cm s^{-1}), within a depth range from near the ocean bottom to 2240 m at station PG1. Smoothing was performed by a 15-month running mean filter to eliminate variations on timescales shorter than 1 year. Horizontal dashed lines indicate the 2349 m depth level, for which the current velocity fields, produced by the OFES, are illustrated in Figure 4. Arrows mark the periods for which the OFES current velocity fields are shown in Figure 4.

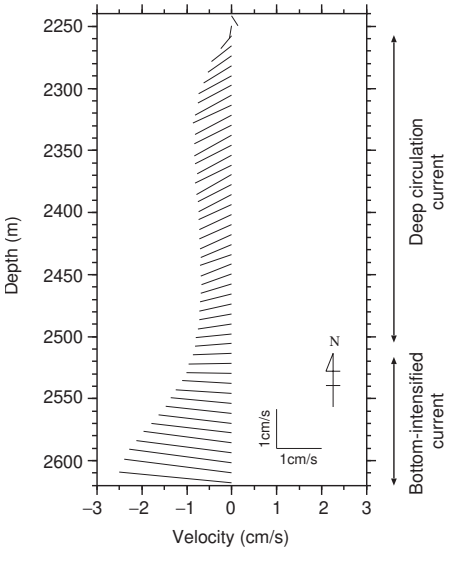

Figure 3. Mean profile of the ADCP current velocity vector at PG1. Mean values were calculated using the data collected from 2001 to 2016.

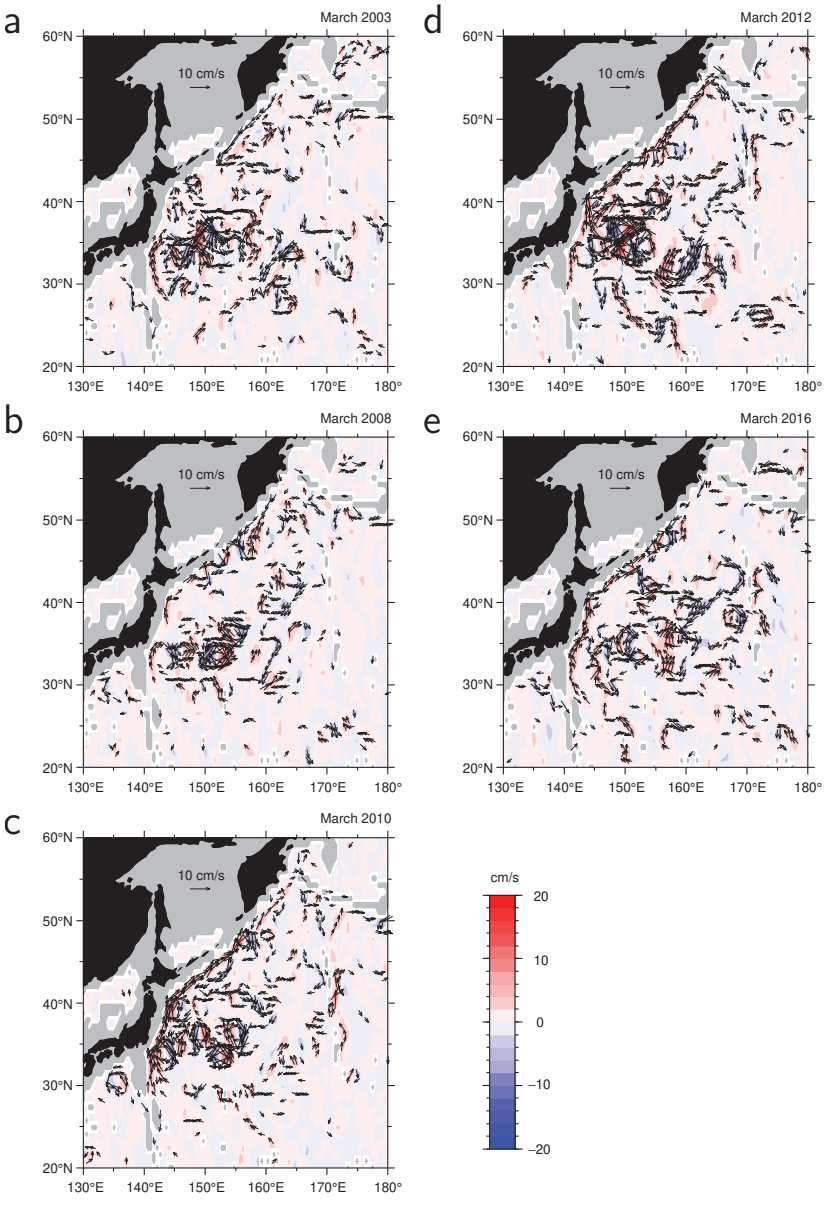

Figure 4. OFES current velocity vector (arrows) and northward velocity component (color gradient) fields at a depth of 2349 m in (**a**) March 2003, (**b**) March 2008, (**c**) March 2010, (**d**) March 2012, and (**e**) March 2016, which are marked by the arrows in Figure 2b. Panel (**a**) shows the current vector field in period of vertically shrunken state of the bottom-intensified current at PG1, and other panels display the current fields in periods of vertically extended states of the current. Velocity vectors with speeds lower than 3.0 cm s^{-1} are not shown.

The thickness of the bottom-intensified current (>50 m) at PG1 is greater than that of the bottom Ekman layer, which is roughly estimated to be 20 m at most, according to the formula used by Wimbush and Munk [39] and others. There is a topographic depression of approximately 600 m to the south of the ADCP site (Figure 1b). A cyclonic eddy is

anticipated to be trapped within the topographic depression. If this anticipation is correct, the trapped cyclonic eddy would intensify the current at the ADCP site. Then, the top of the cyclonic eddy should be shallower than the ADCP site (2630 m) and deeper than the 2400 m isopleth. In observation, the top of the bottom-intensified current is within the depth range. These findings suggest that the bottom-intensified current can be attributed to the local topography that impedes the mean southwestward deep current (Figure 1), rather than a result of turbulent diffusion.

Furthermore, as clearly shown in Figure 2b, the northward component of the bottom-intensified current extended upward, reaching a level shallower than 2400 m depth on an interannual timescale, as in the winters of 2007/2008, 2009/2010, 2011/2012, and 2015/2016. During the study period, the current thickness varied within a range from approximately 50 m during the 2002/2003 winter to 350 m during the 2015/2016 winter. For example, the OFES current velocity fields at a depth of 2349 m (horizontal dashed lines in Figure 2), in periods marked by arrows in Figure 2, are shown in Figure 4. The diminished bottom-intensified current in March 2003 had no single continuous current along the trenches (Figure 4a). Except for March 2008, the extended bottom-intensified current featured a narrow ($\sim$50 km) northward and northeastward current, exceeding 3.0 cm s^{-1}, along the Japan and Kuril–Kamchatka trenches (Figure 4c,d). In March 2008 (Figure 4b), the bottom current was vertically extended but the current speed produced by the OFES was quite low. Accordingly, this suggests that the bottom-intensified current frequently becomes elongated and trapped along the onshore continental slope of the trenches, in association with upward extension. However, we note that the OFES does not produce quantitatively accurate velocity and may not be able to sufficiently resolve the cross-shelf structure of the bottom-intensified current. The mechanism of the vertical extension of the current will be discussed in Section 3.3.

3.2. The Rotary EOF Modes of the Bottom Current Variation

To examine variations in the bottom-intensified current, we decomposed the variation in the ADCP-observed current velocity vector at PG1 by rotary EOF modes (Figure 5). The percentages of the first and second rotary EOF modes are 76% and 14%, respectively. These two rotary EOF modes explain approximately 90% of the total variance in the monthly current velocity variation. The first rotary EOF mode, i.e., the dominant mode variation, has a maximum amplitude at a depth of 2380 m (red line in Figure 5a). The upward extension of the bottom-intensified current is principally attributable to the first rotary EOF mode. As the phase of the first rotary EOF mode has a nearly constant value of approximately 90°, except in the uppermost observed layer (blue line), in which the amplitude is quite small, the first mode variation is directed along the continental slope. The second rotary EOF mode changes the phase between depths of approximately 2380 and 2410 m (blue line in Figure 5b), representing current velocity variations with smaller vertical scales than the first mode variation.

The time coefficient of the first rotary EOF mode exhibits interannual variation, with significant positive peaks in the winters of 2002/2003, 2007/2008, 2009/2010, 2011/2012, and 2015/2016 (Figure 6a). Most of these positive peaks lag behind the positive peaks of the inverted NPI anomaly (gray line), which represent the strengthening of the Aleutian Low, principally due to the occurrence of El Niño events, e.g., [34]. With a lag of 3 months, the correlation coefficient between the first rotary EOF mode and inverted NPI anomaly reaches a maximum of 0.52, which is higher than the 99% confidence limit (0.47) and, therefore, statistically significant. The time-lag is unexpectedly shorter than the time lag (30 months) between the sea surface height variation at PG1 and inverted NPI anomaly, calculated by Hasegawa et al. [14]. This very short time lag suggests that the vertical extension of the bottom-intensified current is brought about by a barotropic response in the central Pacific to ENSO-related wind variation, which is relatively rapid, in comparison to the baroclinic response [17].

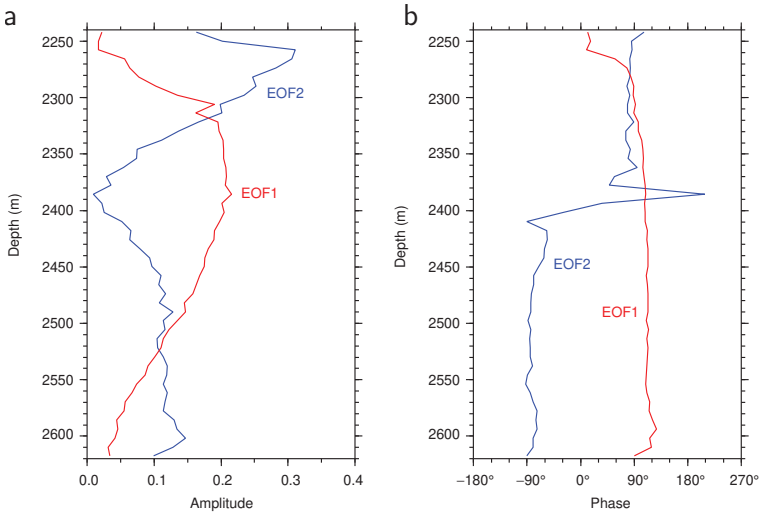

Figure 5. (**a**) Amplitudes and (**b**) phases of the first (red lines) and second (blue lines) rotary EOF modes of the ADCP current velocity at PG1, with respect to depth. In panel (**b**), counterclockwise rotation was set to correspond to the positive phase.

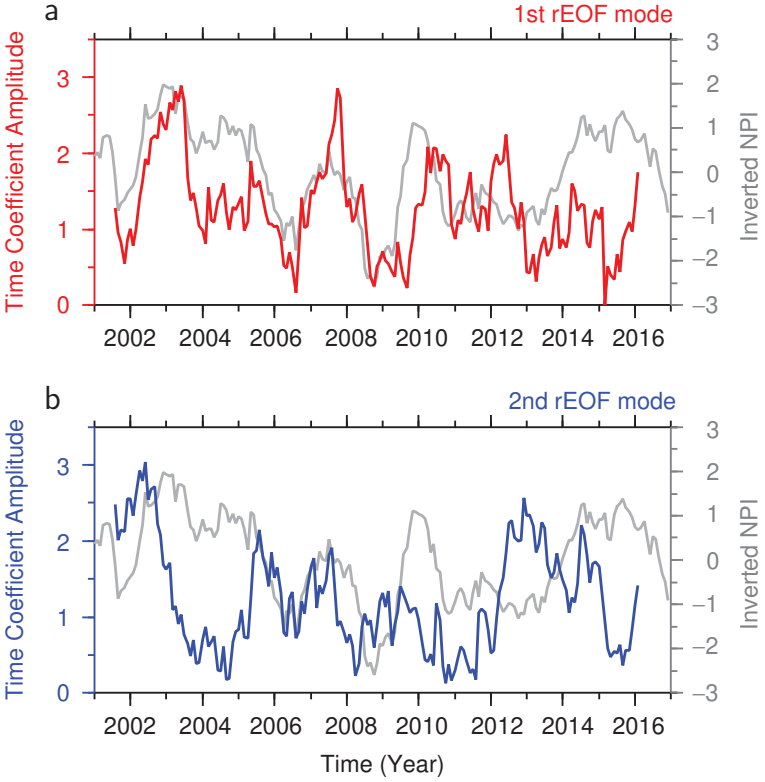

Figure 6. Amplitudes of time coefficients of the (**a**) first (red line) and (**b**) second (blue line) rotary EOF modes of the ADCP current velocity at PG1, as well as the inverted North Pacific Index (NPI) anomaly (gray line). The time coefficients and inverted NPI anomaly were normalized by the standard deviations.

The current velocity actually observed is related to the phase of the time coefficient of the first rotary EOF mode (not shown), besides the amplitude. For this reason, the positive peaks of the time coefficients (Figure 6a) do not always coincide with the upward extensions of the bottom-intensified current (Figure 2b). In Figure 7, we show the current velocity variation along the continental slope (or perpendicular to the T-line in Figure 1), constructed from the first rotary EOF mode. The first rotary EOF mode current velocity variation exhibits positive peaks that correspond to the vertical extensions of the bottom-intensified current in 2007/2008, 2009/2010, 2011/2012, and 2015/2016, as mentioned in Figure 2b. Furthermore, the negative peak of the first mode variation in 2002/2003 concurred with shrinkage of the bottom-intensified current. The correlation coefficient between the second rotary EOF mode (blue line in Figure 6b), and the inverted NPI anomaly is lower than the 99% confidence limit, even if time lags are considered.

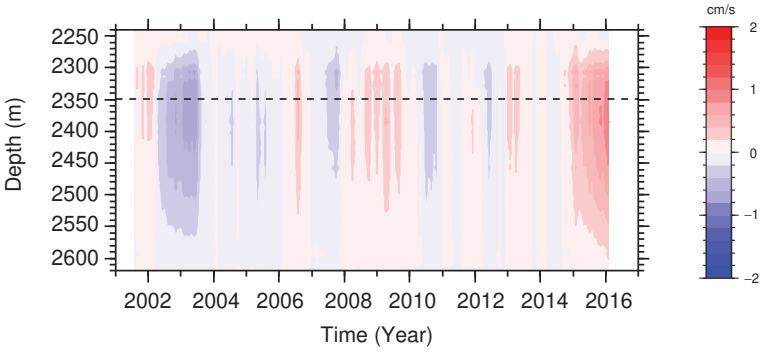

Figure 7. Time-depth diagram of current velocity variations perpendicular to the T-line in Figure 1, due to the first rotary EOF mode at PG1. The horizontal dashed line indicates the 2349 m depth level, for which the OFES current velocity fields are illustrated in Figure 4.

The ENSO-related barotropic disturbances that propagated westward in the interior region of the oceans as Rossby waves and impinged on the continental slope were strongly modified by the topography along the western boundary. Thus, we expect that the modified current disturbances over the continental slope to be expressed as a superposition of CTW mode waves.

3.3. Current Structures of Coastal-Trapped Wave Modes

We calculated eigenfunctions of CTW modes from the f-plane linearized hydrostatically balanced equations of motion and continuity for an inviscid fluid, assuming a rigid-lid condition, using the software BIGLOAD4 developed by Brink [40] and Brink and Chapman [24]. For the calculation, we used a horizontally uniform Brunt–Väisälä frequency profile, on the basis of hydrographic data at 40.5° N, 145.5° E from the World Ocean Atlas 2018 [41] and ETOPO1 [42] depth data at the T-line. Figure 8 shows the eigenfunctions of the along-slope velocity component for the first to fifth CTW modes. Aside from the first CTW mode, the calculated CTW modes are bottom-trapped. The vertical scale of these modes are mainly attributed to the density stratification. The higher the mode, the smaller the spatial scale tends to be along the T-line. Fixed to the approximate period (reciprocal of frequency) of ENSO (∼4 years), the wavelengths of these CTW mode waves were evaluated to be longer than 3×10^5 km (Figure 9). This is considerably longer than the along-trench length of the northward current on the continental slope (∼3000 km) produced in the OFES. Although the computation of the CTW modes does not account for dissipation effects, CTW disturbances in the OFES and in the real ocean must be dissipated by friction with the seabed.

The variations in the along-slope component of the bottom-intensified current are considered to be related to these CTW mode variations. To examine whether or not

the observed current velocity variations perpendicular to the T-line are represented as a superposition of the CTW modes, we performed a regression of the observed variations to the five CTW modes. The resultant variations, constructed by the five CTW modes (Figure 10), are remarkably similar to the first rotary EOF mode variation (Figure 7). The correlation coefficients between these time series are higher than 0.9 for most depth levels. Hence, the observed vertical extension of the along-slope component of the bottom-intensified current can be explained by the excitation of the bottom-trapped (second to fifth) modes of CTW, by impingement of ENSO-related barotropic Rossby wave disturbances on the continental slope off the southeast coast of Hokkaido.

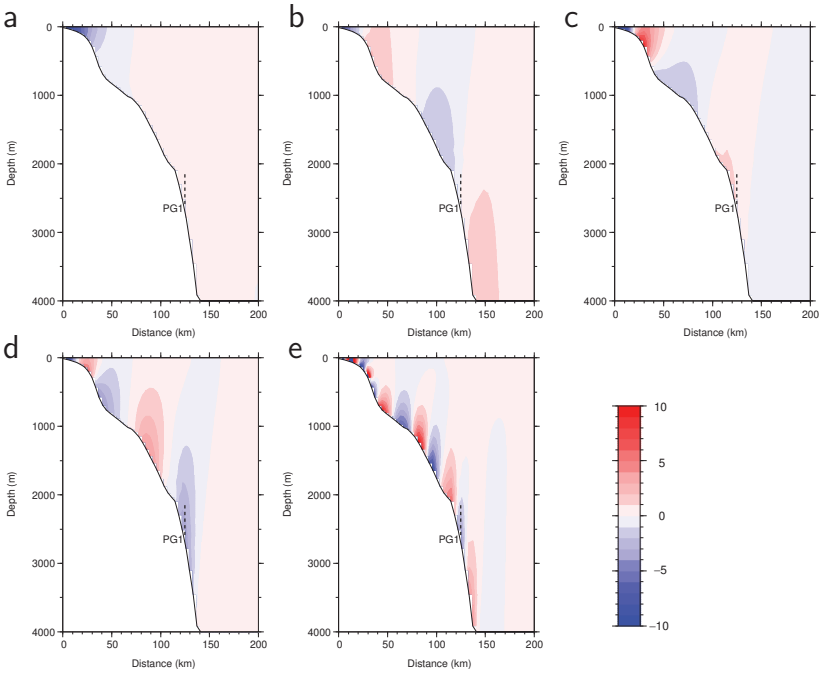

Figure 8. Sections of the eigenfunctions of the along-slope current velocity component for the (**a**–**e**) first to fifth coastal-trapped wave (CTW) modes, with a wavenumber of 1×10^{-7} m^{-1} at the T-line in Figure 1. The vertical dashed lines show the vertical range of the ADCP observation at PG1.

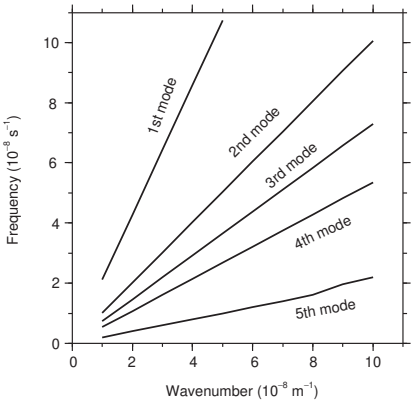

Figure 9. Dispersion relations of the lowest five coastal-trapped wave (CTW) modes at the T-line in Figure 1.

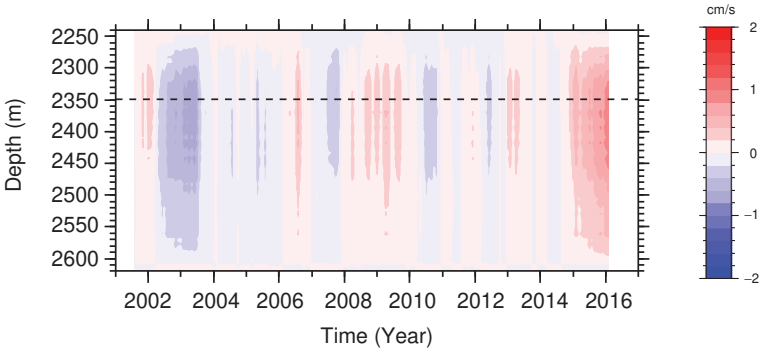

Figure 10. Time-depth diagram of current velocity variations perpendicular to the T-line (Figure 1) by the lowest five coastal-trapped wave (CTW) modes, fitted to the first rotary EOF mode variation at PG1. The horizontal dashed line indicates the 2349 m depth level, for which the OFES current velocity fields are illustrated in Figure 4.

4. Summary

By using current velocity profile data, collected near PG1 (41°39.909′ N, 144°20.695′ E), from 2001 to 2016, by an upward-looking ADCP installed on the seabed (2630-m depth), we examined changes in the current velocity structure near the ocean bottom on the continental slope off the southeast of Hokkaido, Japan. At the site, the deep circulation current, which has been observed by past investigators, e.g., [37], flows southwestward down to a depth of approximately 2520 m (a height of approximately 110 m above the seabed) on average. In the bottom layer, from approximately 2520- to 2620-m depth, the current speed increases with depth, up to 2.5 cm s^{-1} immediately above the seabed.

The thickness of the bottom-intensified current changes on an interannual timescale, within a range of 50–350 m. The OFES current velocity data show that the thickened bottom-intensified current flows northward, trapped along the onshore continental slope of the Japan and Kuril–Kamchatka trenches. The first rotary EOF mode, which accounts for 76% of the total variance of the variation, has a nearly constant phase and a peak amplitude around 2380 m depth. The first rotary EOF mode becomes enhanced (or attenuated) 3 months after the strengthening (or weakening) of the Aleutian Low, forced by the El Niño (La Niña) teleconnection. The current velocity variation along the continental slope, due to the first rotary EOF mode, represents the interannual change in the bottom-intensified current thickness.

Except for the first CTW mode, the eigenfunctions (i.e., cross-sectional structure of the along-slope current variation) of the CTW modes on the continental slope off the southeastern coast of Hokkaido are bottom-intensified. The thickness change of the bottom-intensified current is represented as the superposition of the first to fifth CTW modes, particularly of the (second to fifth) bottom-trapped modes of CTW. Hence, the observed interannual thickness changes in the bottom-intensified current are caused by oceanic barotropic disturbances, excited by changes in the Aleutian Low in the central Pacific and modified by the continental slope off the southeast coast of Hokkaido. These results are beneficial for oceanographic studies and ocean engineering, such as suspended sediment studies, the construction and maintenance of marine structures, and the planning of deep drilling.

Author Contributions: Conceptualization, A.N.; formal analysis, A.N. and T.H.; writing—original draft preparation, A.N.; writing—review and editing, T.H., K.A. and H.M.; project administration, K.A.; funding acquisition, A.N., K.A. and T.H. All authors have read and agreed to the published version of the manuscript.

Funding: This work was partly supported by the Japan Society for the Promotion of Science, Grant-in-Aid for Scientific Research (Grant Numbers: JP15H04228, JP16H06473, JP17K05660, JP18H03726, JP19H05702, JP20K04072, JP20H02236, and JP20H04349).

Institutional Review Board Statement: Not applicable.

Informed Consent Statement: Not applicable.

Data Availability Statement: ADCP data are available on the website of the JAMSTEC project "Long-Term Deep Sea Floor Observatory off Kushiro-Tokachi in the Kuril Trench" (http://www.jamstec.go.jp/scdc/top_e.html, accessed on 10 February 2022. OFES data were provided by the Asia-Pacific Data-Research Center of the International Pacific Research Center, the University of Hawaii (http://apdrc.soest.hawaii.edu/index.php, accessed on 10 February 2022). World Ocean Atlas 2018 and ETOPO1 data are published on the websites of National Centers for Environmental Information, National Oceanic and Atmospheric Administration (https://www.ncei.noaa.gov/products/world-ocean-atlas, accessed on 10 February 2022 and https://www.ngdc.noaa.gov/mgg/global/, accessed on 10 February 2022).

Acknowledgments: The authors thank the individuals concerned in the establishment of the JAMSTEC Long-Term Deep Sea Floor Observatory, off Kushiro-Tokachi in the Kuril Trench. The OFES simulation was conducted on the Earth Simulator, under the support of JAMSTEC. The authors express gratitude to Kyoko Taniguchi (JAMSTEC) for correcting the manuscript. Additionally, the authors thank the guest editors (Joseph J. Kuehl and Morgan Xiang) for inviting us to the present special session, as well as the anonymous reviewers for helpful comments.

Conflicts of Interest: The authors declare no conflict of interest.

Abbreviations

The following abbreviations are used in this manuscript:

ADCP	Acoustic Doppler current profiler
CTW	Coastal-trapped wave
ENSO	El Niño–Southern Oscillation
EOF	Empirical orthogonal function
JAMSTEC	Japan Agency for Marine-Earth and Technology
NPI	North Pacific Index
OFES	Ocean general circulation model for the Earth Simulator
OGCM	Ocean general circulation model

References

1. McCane, I.N. Local and Global Aspects of the Bottom Nepheloid Layers in the World Ocean. *Neth. J. Sea Res.* **1986**, *20*, 167–181. [CrossRef]
2. Bomberg, J.; Ariyoshi, K.; Hautala, S.; Johnson, H.P. The Finicky Nature of Earthquake Shaking-triggered Submarine Sediment Slope Failures and Sediment Gravity Flows. *J. Geophys. Res.* **2021**, *126*, e2021JB022588. [CrossRef]
3. Komaki, K.; Nagano, A. Monitoring the deep western boundary current in the western North Pacific by echo intensity measured with lowered acoustic Doppler current profiler. *Mar. Geophys. Res.* **2019**, *40*, 515–523. [CrossRef]
4. Mao, L.; Zeng, S.; Liu, Q.; Wang, G.; He, Y. Dynamical mechanics behavior and safety analysis of deep water riser considering the normal drilling condition and hang-off condition. *Ocean Eng.* **2020**, *199*, 106996. [CrossRef]
5. Williamson, C.H.K.; Govardhan, R. Vortex-induced Vibrations. *Annu. Rev. Fluid Mech.* **2004**, *36*, 413–455. [CrossRef]
6. Davidson, P.A. *Turbulence: An Introduction for Scienctist and Engineers*, 2nd ed.; Oxford University Press: Oxford, UK, 2015.
7. Kawabe, M.; Fujio, S.; Yanagimoto, D.; Tanaka, K. Water masses and currents of deep circulation southwest of the Shatsky Rise in the western North Pacific. *Deep-Sea Res. I* **2009**, *56*, 1675–1687. [CrossRef]
8. Komaki, K.; Kawabe, M. Deep-circulation current through the Main Gap of the Emperor Seamounts Chain in the North Pacific. *Deep-Sea Res. I* **2009**, *56*, 305–313. [CrossRef]
9. Nagano, A.; Ichikawa, H.; Ichikawa, K.; Konda, M. Bottom Currents on the continental slope off Shikoku. In Proceedings of the OCEANS 2008—MTS/IEEE Kobe Techno-Ocean, Kobe, Japan, 8–11 April 2008; pp. 1–4. [CrossRef]
10. Nagano, A.; Ichikawa, K.; Ichikawa, H.; Yoshikawa, Y.; Murakami, K. Large ageostrophic currents in the abyssal layer southeast of Kyushu, Japan, by direct measurement of LADCP. *J. Oceanogr.* **2013**, *69*, 259–268. [CrossRef]
11. Kawabe, M.; Yanagimoto, D.; Kitagawa, S. Variations of deep western boundary currents in the Melanesian Basin in the western North Pacific. *Deep-Sea Res. I* **2006**, *53*, 942–959. [CrossRef]
12. Taira, K.; Teramoto, T. Bottom Currents in Nankai Trough and Sagami Trough. *J. Oceanogr. Soc. Jpn.* **1985**, *41*, 388–398. [CrossRef]

13. Weatherly, G.L.; Kelly, E.A., Jr. Storms and flow reversals at the HEBBLE site. *Mar. Geol.* **1985**, *66*, 205–218. [CrossRef]
14. Hasegawa, T.; Nagano, A.; Matsumoto, H.; Ariyoshi, K.; Wakita, M. El Niño-related sea surface elevation and ocean bottom pressure enhancement associated with the retreat of the Oyashio southeast of Hokkaido, Japan. *Mar. Geophys. Res.* **2019**, *40*, 505–512. [CrossRef]
15. Hasegawa, T.; Nagano, A.; Ariyoshi, K.; Miyama, T.; Matsumoto, H.; Iwase, R.; Wakita, M. Effect of Ocean Fluid Changes on Pressure on the Seafloor: Ocean Assimilation Data Analysis on Warm-core Rings off the Southeastern Coast of Hokkaido, Japan on an Interannual Timescale. *Front. Earth Sci.* **2021**, *9*, 600930. [CrossRef]
16. Hirata, K.; Aoyagi, M.; Mikada, H.; Kawaguchi, K.; Kaiho, Y.; Iwase, R.; Morita, S.; Fujisawa, I.; Sugioka, H.; Mitsuzawa, K.; et al. Real-time geophysical measurements on the deep seafloor using submarine cable in the southern Kurile subduction zone. *IEEE J. Ocean Eng.* **2002**, *27*, 170–181. [CrossRef]
17. Nagano, A.; Wakita, M. Wind-driven decadal sea surface height and main pycnocline depth changes in the western subarctic North Pacific. *Prog. Earth Planet. Sci.* **2019**, *6*, 59. [CrossRef]
18. Gill, A.E.; Clarke, A.J. Wind-induced upwelling, coastal currents and sea-level changes. *Deep-Sea Res.* **1974**, *21*, 325–345. [CrossRef]
19. Huthnance, J.M. On Coastal Trapped Waves: Analysis and Numerical Calculation by Inverse Iteration. *J. Phys. Oceanogr.* **1978**, *8*, 74–92. [CrossRef]
20. Gill, A.E. *Atmosphere-Ocean Dynamics*; Academic Press: London, UK, 1982.
21. Denbo, D.W.; Allen, J.S. Rotary Empirical Orthogonal Function Analysis of Currents near the Oregon Coast. *J. Phys. Oceanogr.* **1984**, *14*, 35–46. [CrossRef]
22. Thomson, R.E.; Emery, W.J. *Data Analysis Methods in Physical Oceanography*, 3rd ed.; Elsevier: Amsterdam, The Netherlands, 2014. [CrossRef]
23. Nagano, A.; Wakita, M.; Fujiki, T.; Uchida, H. El Niño-related Vertical Mixing Enhancement under the Winter Mixed Layer at Western Subarctic North Pacific Station K2. *J. Geophys. Res.* **2021**, *126*, e2020JC016913. [CrossRef]
24. Brink, K.H.; Chapman, D.C. *Programs for Computing Properties of Coastal-trapped Waves and Wind-driven Motions Over the Continental Shelf and Slope*; Technical Report WHOI-87-24; Woods Hole Oceanographic Institution: Woods Hole, MA, USA, 1987; p. 02543.
25. Kawaguchi, K.; Hirata, K.; Mikada, H.; Kaiho, Y.; Iwase, R. An expendable deep seafloor monitoring system for earthquake and tsunami observation network. In Proceedings of the 2000 MTS/IEEE Conference, Providence, RI, USA, 11–14 September 2000; pp. 1719–1722.
26. Thèbault, E.; Finlay, C.C.; Beggan, C.D.; Alken, P.; Aubert, J.; Barrois, O.; Bertrand, F.; Bondar, T.; Boness, A.; Brocco, L.; et al. International Geomagnetic Reference Field: The 12th generation. *Earth Planets Space* **2015**, *67*, 79. [CrossRef]
27. Pacanowski, R.C.; Griffies, S.M. *MOM 3.0 Manual*; Geophysical Fluid Dynamics Laboratory/National Oceanic and Atmospheric Administration: Princeton, NJ, USA, 2000.
28. Masumoto, Y.; Sasaki, H.; Kagimoto, T.; Komori, N.; Ishida, A.; Sasai, Y.; Miyama, T.; Motoi, T.; Mitsudera, H.; Takahashi, K.; et al. A five-year-eddy-resolving simulation of the world ocean—Preliminary outcomes of OFES (OGCM for the Earth Simulator). *J. Earth Simulator* **2004**, *1*, 35–56.
29. Sasai, Y.; Ishida, A.; Yamanaka, Y.; Sasaki, H. Chlorofluorocarbons in a global ocean eddy-resolving OGCM: Pathway and formation of Antarctic Bottom Water. *Geophys. Res. Lett.* **2004**, *31*, L12305. [CrossRef]
30. Sasaki, H.; Sasai, Y.; Kawahara, S.; Furuichi, M.; Araki, F.; Ishida, A.; Yamanaka, Y.; Masumoto, Y.; Sakuma, H. A series of eddy-resolving ocean simulations in the world ocean: OFES (OGCM for the Earth Simulator) project. In Proceedings of the Oceans '04 MTS/IEEE Techno-Ocean '04 (IEEE Cat. No.04CH37600), Kobe, Japan, 9–12 November 2004; Volume 3, pp. 1535–1541. [CrossRef]
31. Sasaki, H.; Nonaka, M.; Masumoto, Y.; Sasai, Y.; Uehara, H.; Sakuma, H. An eddy-resolving hindcast simulation of the quasi-global ocean from 1950 to 2003 on the Earth Simulator. In *High Resolution Numerical Modelling of the Atmosphere and Ocean*; Ohfuchi, W., Hamilton, K., Eds.; Springer: New York, NY, USA, 2008; pp. 157–185. [CrossRef]
32. Kalnay, E.; Kanamitsu, M.; Kistler, R.; Collins, W.; Deaven, D.; Gandin, L.; Iredell, M.; Saha, S.; White, G.; Woollen, J.; et al. The NCEP/NCAR 40-year reanalysis project. *Bull. Am. Meteorol. Soc.* **1996**, *77*, 437–471. [CrossRef]
33. Trenberth, K.E.; Hurrel, J.W. Decadal atmosphere-ocean variations in the Pacific. *Clim. Dynam.* **1994**, *9*, 303–319. [CrossRef]
34. Mezzina, B.; Palmeiro, F.M.; Garcia-Serrano, J.; Bladé, I.; Batté, L. Multi-model assessment of the late-winter stratospheric response to El Niño and La Niña. *Clim. Dyn.* **2021**. [CrossRef]
35. Hallock, Z.R.; Teague, W.J. Evidence for a North Pacific Deep Western Boundary Current. *J. Geophys. Res.* **1996**, *101*, 6617–6624. [CrossRef]
36. Mitsuzawa, K.; Holloway, G. Characteristics of deep currents along trenches in the northwest Pacific. *J. Geophys. Res.* **1998**, *103*, 13085–13092. [CrossRef]
37. Owens, W.B.; Warren, B.A. Deep circulation in the northwest corner of the Pacific Ocean. *Deep-Sea Res. I* **2001**, *48*, 959–993. [CrossRef]
38. Fujio, S.; Yanagimoto, D. Deep current measurements at 38° N east of Japan. *J. Geophys. Res.* **2005**, *110*. [CrossRef]
39. Wimbush, M.; Munk, W. The benthic boundary layer. In *The Sea*; Maxwell, A.E., Ed.; John Wiley: New York, NY, USA, 1970; Volume 4, pp. 731–758.

40. Brink, K.H. A Comparison of Long Coastal Trapped Wave Theory with Observations off Peru. *J. Phys. Oceanogr.* **1982**, *12*, 897–913. [CrossRef]
41. Garcia, H.E.; Boyer, T.P.; Baranova, O.K.; Locarnini, R.A.; Mishonov, A.V.; Grodsky, A.; Paver, C.R.; Weathers, K.W.; Smolyar, I.V.; Reagan, J.R.; et al. *World Ocean Atlas 2018: Product Documentation*; Ocean Climate Laboratory NCEI/NESDIS/NOAA: Princeton, NJ, USA, 2019.
42. Amante, C.; Eakins, B.W. *ETOPO1 1 Arc-Minute Global Relief Model: Procedures, Data Sources and Analysis*; Technical Report, NESDIS NGDC-24; NOAA: Boulder, CO, USA, 2009.

fluids

MDPI

Article

Influence of Turbulence Effects on the Runup of Tsunami Waves on the Shore within the Framework of the Navier–Stokes Equations

Andrey Kozelkov [1,2], Elena Tyatyushkina [1,2], Vadim Kurulin [1,2] and Andrey Kurkin [2,*]

[1] Russian Federal Nuclear Center-All-Russian Research Institute of Experimental Physics, 607188 Nizhny Novgorod, Russia; askozelkov@mail.ru (A.K.); leno4ka-07@mail.ru (E.T.); kurulin@mail.ru (V.K.)
[2] Department of Applied Mathematics, Nizhny Novgorod State Technical University n.a. R.E. Alekseev, 603155 Nizhny Novgorod, Russia
* Correspondence: aakurkin@nntu.ru

Abstract: This paper considers turbulence effects on tsunami runup on the shore in tsunami simulations using the system of three-dimensional Navier–Stokes equations. The turbulence effects in tsunami propagation and runup are studied by solving the problem of a wave propagating in a nonuniform-bottom pool and collapsing with a barrier. To solve this problem, we used the turbulence model, RANS SST (Reynolds-averaged Navier–Stokes shear stress transport). We compared the wave profiles at different times during wave propagation, runup, and collapse. To quantify the turbulence effects, we also compared the forces acting on the basin bottom. We demonstrated that the turbulence had almost no effect on the shape of the wave and the way of its propagation (except collapse). However, turbulence effects during the runup and collapse became noticeable and could boost the flow (increasing the pressure force and the total force) by up to 25 percent.

Keywords: tsunami; numerical simulation; Navier–Stokes equations; Volume of Fluid Method (VOF method); LOGOS software package

Citation: Kozelkov, A.; Tyatyushkina, E.; Kurulin, V.; Kurkin, A. Influence of Turbulence Effects on the Runup of Tsunami Waves on the Shore within the Framework of the Navier–Stokes Equations. *Fluids* **2022**, *7*, 117. https://doi.org/10.3390/fluids7030117

Academic Editors: Pengfei Xue, Fabrice Veron and Joseph J. Kuehl

Received: 9 February 2022
Accepted: 14 March 2022
Published: 20 March 2022

1. Introduction

The Navier–Stokes equations are the most complete set of equations to describe viscous fluids, which takes into account their complex flow structure. Tsunami waves possess a number of physical properties that become evident only in the three-dimensional scenario and must be considered in their simulations. Such structures develop when the wave runs up near the shore, breaks, comes onshore, and travels overland, interacting with the coastal infrastructure. Numerical simulations of tsunami waves based on the set of three-dimensional Navier–Stokes equations [1] make it possible to explore turbulence effects during tsunami propagation and arrival on the shore, which cannot be studied by means of two-dimensional models. At present, there are a number of publications in which tsunami waves are simulated using a variety of turbulence models [2–7]. Is it really necessary to incorporate turbulence in such simulations? The issue of turbulence effects on tsunami simulations requires some additional analysis. In the models based on the nonlinear shallow-water and Boussinesq equations, turbulence is parametrized by empirical relations borrowed from the steady flow theory rather than from the wave theories, whereas turbulence is a substantial three-dimensional unsteady process [5]. Three-dimensional simulations open up the prospect of using the known and well-tested fluid turbulence models [8–15] and eddy-resolving models [16,17]. To explore the effect of turbulence on the wave as it propagates and comes onshore, in this work, we use one of the most widely used turbulence models, RANS SST [18].

In the paper, we present the results of studying the turbulence effects during tsunami propagation and runup on the shore by solving the problem of a wave propagating in

a nonuniform-bottom basin and breaking with a barrier. We describe the mathematical model, which is based on the Reynolds-averaged three-dimensional Navier–Stokes equations [11,19] and the VOF technique (Volume of Fluid Method) [20,21]. This model has been adapted for tsunami simulations [22,23]. We also describe the SST turbulence model (TM) and present the problem statement, setup the specifications, and the mesh model constructed. To assess the turbulence effects, we compare the wave profiles for each setup, calculated both with and without the use of the turbulence model. To quantify the turbulence effects, we also compare the forces acting on the basin bottom (pressure force, friction, and total force).

2. Mathematical Model

Let us consider a flow of substance consisting of an arbitrary number of components in different physical states. For simplicity, we assume that the components (water and air) are described by the same field of velocities and pressures, that there are no phase transitions, the components are incompressible, there are no sinks or sources, and the heat exchange processes are negligible. At this point, we ignore the effects of Earth's rotation and sphericity. As a result, the system of Reynolds-averaged Navier–Stokes equations in the Cartesian coordinates takes the following form (the averaging signs are omitted):

$$\begin{cases} \frac{\partial}{\partial x_i}(u_i) = 0, \\ \rho\frac{\partial u_i}{\partial t} + \rho\frac{\partial}{\partial x_j}(u_i u_j) = -\frac{\partial p}{\partial x_i} + \frac{\partial}{\partial x_j}(\tau_{ij} + \tau^t{}_{ij}) + \rho g_i, \\ \frac{\partial \alpha_w}{\partial t} + \frac{\partial}{\partial x_i}(u_i \alpha_w) = 0, \end{cases} \quad (1)$$

where i, j are the subscripts indicating that the vector components belong to the Cartesian coordinates, $i, j = \{x, y, z\}$; ρ is the mixture density calculated as $\rho = \rho_w \alpha_w + \rho_a \alpha_a$; w (water) is the subscript indicating the quantities belonging to the "water" phase; a (air) is the subscript indicating the quantities belonging to the "air" phase; α_w / α_a is the volume fraction of water/air, respectively; u_i is the component of the velocity vector, $i = \{x, y, z\}$; t is time; p is pressure; x_i is the component of the vector of the Cartesian coordinates, $i = \{x, y, z\}$; τ_{ij} is the tensor of viscous stresses, which, according to the Boussinesq hypothesis, takes the form of:

$$\tau_{ij} = \mu\left(\frac{\partial u_i}{\partial x_j} + \frac{\partial u_j}{\partial x_i} - \frac{2}{3}\frac{\partial u_k}{\partial x_k}\delta_{ij}\right),$$

μ_t is the dynamic viscosity; δ_{ij} is the Kronecker delta; and g_i is the component of the gravitational acceleration vector.

The set of Equation (1) is not closed because we do not know how one of the basic variables in this system, τ^t_{ij}, is related to the averaged flow parameters. This relationship, representing the contribution of turbulent fluctuations to the main flow, can be defined through some additional relations, generally referred to as turbulence models. The turbulence models are described in refs [8,9,11,16,18,19,24].

Here, we use the differential turbulence models, which employ empirical relations for the coefficient of turbulent viscosity μ_t, the Boussinesq hypothesis, and Fourier's law for the stress tensor:

$$\tau^t{}_{ij} = 2\mu_t\left(S_{ij} - \frac{1}{3}I_{ij}\nabla\cdot\vec{u}\right) + \frac{2}{3}kI_{ij}, \;\; S_{ij} = \frac{1}{2}\left(\frac{\partial u_i}{\partial x_j} + \frac{\partial u_j}{\partial x_i}\right).$$

Here, k is the kinetic energy of turbulence, μ_t is turbulent viscosity, I_{ij} is an identity matrix.

The first two equations in Equation (1) are the equations of conservation of mass and momentum, and the third one is the volume fraction transport equation of the liquid phase. For the "air" phase, the volume fraction transport equation must not be solved, because, according to the principles of the VOF method, the volume fraction α_a is calculated from the relationship $\alpha_w + \alpha_a = 1$.

Before discretizing Equation (1), it makes sense to use transformations to improve the accuracy and stability of the solution. The momentum equation is written in a half-divergent form, because, as shown in [21], this representation compensates for the approximation errors associated with the imperfect fulfillment of the mass balance condition in the computation cells and resolves the shape of the free-surface more accurately:

$$\rho\frac{\partial u_i}{\partial t}+\frac{\partial}{\partial x_j}(u_iu_j\rho)-u_i\frac{\partial}{\partial x_j}(u_j\rho)=-\frac{\partial p}{\partial x_i}+\frac{\partial}{\partial x_j}\tau_{ij}+\rho g_i$$

Thus, the system of Equation (1) has the following final form:

$$\begin{cases}\frac{\partial u_i}{\partial x_i}=0,\\ \rho\frac{\partial u_i}{\partial t}+\frac{\partial}{\partial x_j}(u_iu_j\rho)-u_i\frac{\partial}{\partial x_j}(u_j\rho)=-\frac{\partial p}{\partial x_i}+\frac{\partial}{\partial x_j}(\tau_{ij}+\tau^t{}_{ij})+\rho g_i,\\ \frac{\partial\alpha_w}{\partial t}+\frac{\partial}{\partial x_i}(u_i\alpha_w)=0.\end{cases} \quad (2)$$

Equation (2) enables simulations of tsunami waves, their propagation, and subsequent runup on the shore. The use of the VOF method, underlying Equation (2), allows for running numerical experiments on arbitrary geometry meshes.

To carry out the turbulence simulations, one must add some relationships to the system of Equation (2) to complete the problem. In this paper, we use for this purpose the RANS SST turbulence model, the classic formulation of which is presented in [18].

Equation (2) is discretized by the finite volume method on an arbitrary unstructured mesh and solved numerically by a fully implicit method [16,25] based on the known SIMPLE algorithm. The modeling of the free-surface flows implies some modifications of the SIMPLE algorithm developed specifically for three-dimensional tsunami simulations [22]. The basic formulations of the SIMPLE algorithm, its boundary conditions, and implementation in the LOGOS software package (a program complex for engineering analysis, focused on solving the problems of computational fluid and gas dynamics, as well as heat transfer on an arbitrary unstructured grid using parallel computing algorithms) are described in detail in [22,25,26]. This method has been widely verified, both for the free-surface problems [27] and for the problems directly associated with tsunami waves [28]. This particular form of the method has already been used to simulate historical [29] and hypothetical tsunami waves [30].

3. Turbulence Effects on the Wave Runup on the Shore

In order to explore turbulence effects on the propagation and transformation of a wave as it comes onshore, we simulate numerically the process of a wave traveling in a tank and collapsing with a barrier [28,31]. This problem deals with a wave moving in a tank (the wave is generated on the left boundary of the tank) having a length of 22 m and a depth of h_0 = 0.2 m. The bottom of the tank has a slope starting from x = 10 m and a barrier. Figure 1 shows the problem geometry.

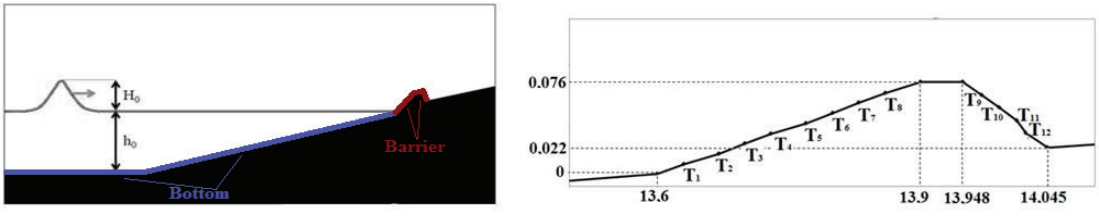

Figure 1. Schematic representation of the problem.

Elevation coordinates of the barrier are given in Table 1.

Table 1. Elevation coordinates of the barrier.

Point (Figure 1, Right)	Coordinates	Point (Figure 1, Right)	Coordinates	Point (Figure 1, Right)	Coordinates
T_1	(13.63, 0.008) m	T_5	(13.77, 0.042) m	T_9	(13.97, 0.065) m
T_2	(13.67, 0.017) m	T_6	(13.80, 0.050) m	T_{10}	(13.99, 0.055) m
T_3	(13.70, 0.025) m	T_7	(13.83, 0.059) m	T_{11}	(14.01, 0.044) m
T_4	(13.73, 0.033) m	T_8	(13.86, 0.067) m	T_{12}	(14.02, 0.034) m

The problem domain was discretized with a three-dimensional unstructured computational mesh consisting of truncated polyhedrons (Figure 2).

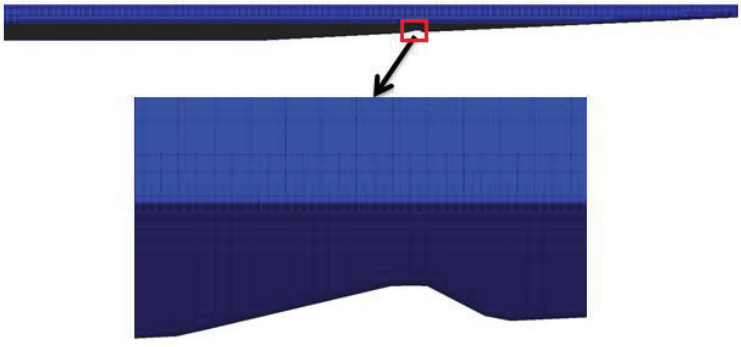

Figure 2. Computational mesh.

The problem was solved for different values of the Reynolds number Re (Table 2):

$$\mathrm{Re} = \frac{\rho u L}{\mu},$$

where u is the characteristic velocity, m/s; L is the characteristic dimension, m; μ is the dynamic viscosity, kg/(m·s).

Table 2. Problem setups.

Setup No.:	Reynolds Number	H_0, m
1	2.8×10^4	0.02
2	1.92×10^5	0.07
3	5.4×10^5	0.12
4	7.2×10^5	0.15

The characteristic dimension L, in this problem, is represented by the undisturbed water depth (corresponding to h_0 in Figure 1) and by the characteristic velocity u, the wave velocity, $u(x,0) = \sqrt{\frac{g}{h_0}}\eta(x,0)$, η is the displacement of the water surface. The Reynolds number is varied by controlling the flow velocity in the wave, which in turn, is controlled by varying the wave amplitude, H_0.

The problem is simulated for two flow cases: calculation without the use of a turbulence model and calculation with the use of the SST TM.

3.1. Setup 1

Figure 3 shows a comparison of the wave profiles for both cases calculated using the LOGOS software package for the Reynolds number Re = 2.8×10^4.

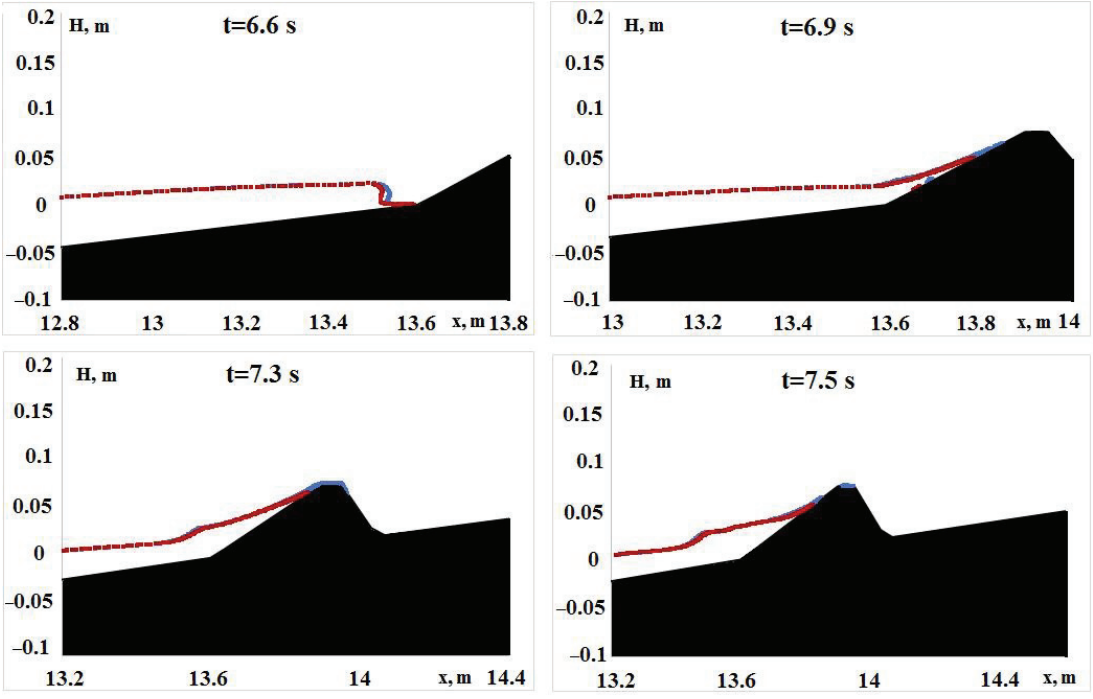

Figure 3. Comparison of the wave profiles for setup 1 (■—without TM, ■—with TM).

The subplots indicate that the wave runs up onto the barrier and then moves back. In the case without TM, the wave runs up onto the barrier at the time of 6.7 s with a small part of the fluid running over the barrier. In the same case with TM, the wave hits the barrier a little later (0.1 s) and does not run over it. This difference is explained by the fact that TM introduces additional viscosity into the solution, which represents the effect of the turbulent vortex flows and increases the viscous stress on the tank bottom, which has its effect on the runup velocity, intensity, dispersion, and nonlinear properties of the wave.

Let us present some quantitative estimates of the effect of turbulence on the propagation and runup of the wave. Figure 4 shows comparative profiles of the forces acting on the bottom. The areas on the bottom where the forces were calculated, ('Bottom'—during propagation, 'Barrier'—during runup and roll-over), are shown in Figure 1. The comparison is made for the total force F_s acting on the wall, and separately for the force of pressure F_p and the force of friction F_τ.

The total force is defined as $F_s = F_P + F_\tau$, где $F_P = p \cdot S$, p is the pressure acting on the surface area S, $F_\tau = \mu_{eff}(\partial u_i / \partial x_j)$, $\mu_{eff} = \mu + \mu_t$.

The plots show that the total force and the pressure force acting on the 'Bottom' wall in the setup with Re = $2.8 \cdot \times 10^4$ are nearly the same for both flow cases. The force of pressure in the case without TM on the 'Barrier' wall and the total force are about 5% higher than those in the case with TM, which, in our opinion, is attributed to the more active runup onto the barrier in the calculation without TM in the absence of turbulent vortex flows in the flow core. The maximum friction force is two orders higher in the calculation with TM, but the contribution of friction to the total force for this flow case is negligibly small.

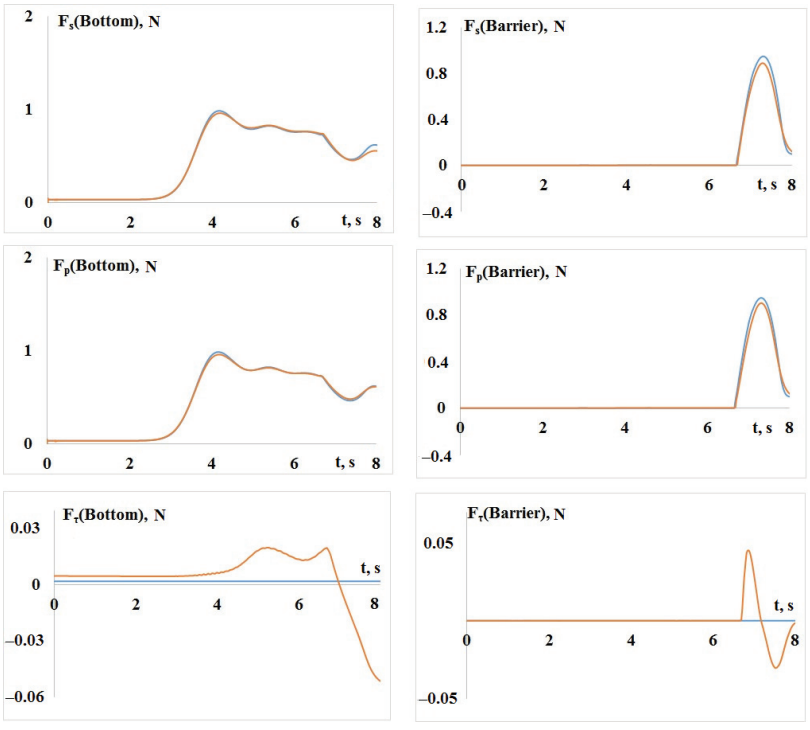

Figure 4. Comparison of the forces acting on the channel bottom in the slope and barrier zones (—without TM, —with TM).

3.2. Setup 2

Figure 5 shows a comparison of the wave profiles for both flow cases calculated by using the LOGOS software package for the Reynolds number, Re = 1.92×10^5.

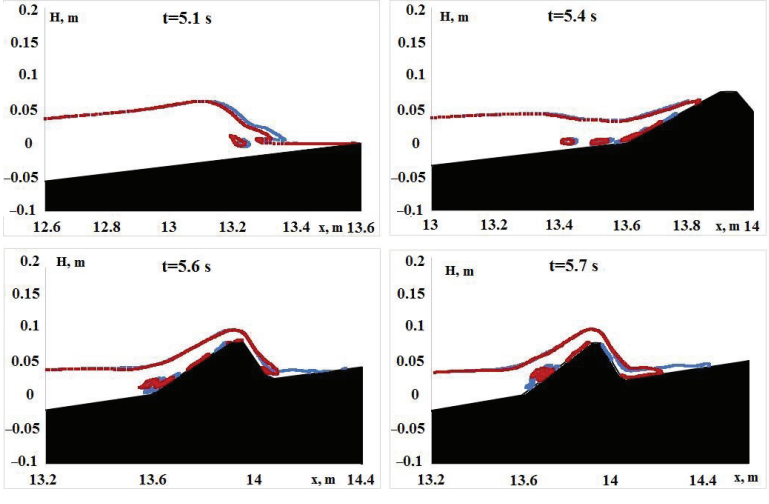

Figure 5. Comparison of the wave profiles for setup 2 (—without TM, —with TM).

The figures suggest that the wave in the first part of the slope first breaks and then runs up onto the barrier and flows over it. In the calculation with the turbulence model, the wave runs up onto the barrier with some delay in time. In order to explore the turbulence effects in greater detail, let us show the time series of the free-surface position and turbulent viscosity for the case with TM (Figure 6).

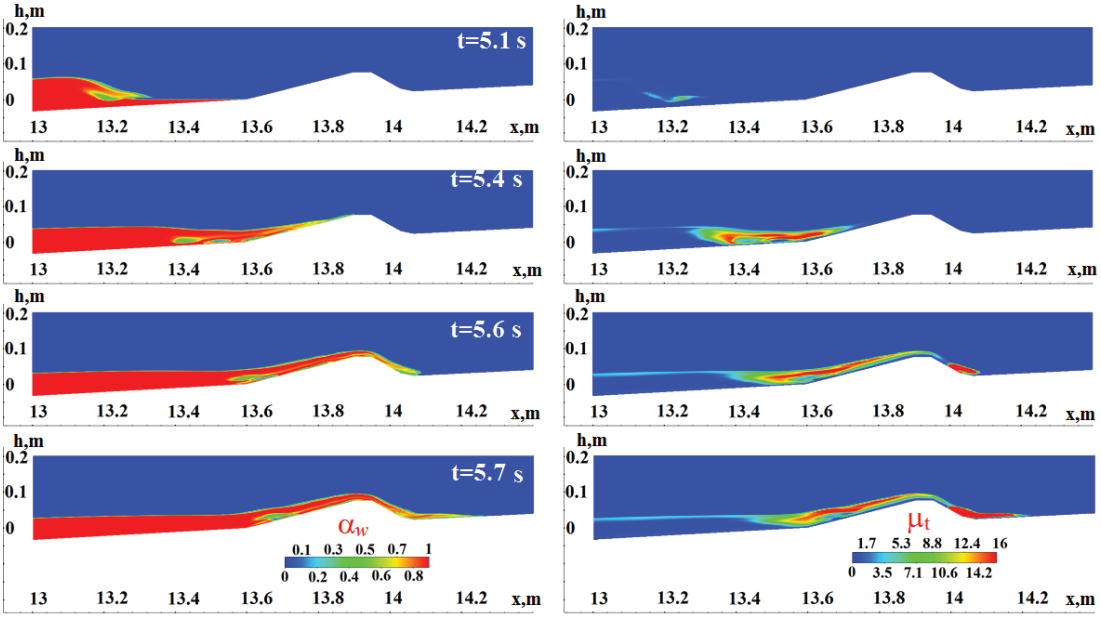

Figure 6. Time series of the free-surface position and turbulence viscosity.

The subplots show that the maximum turbulent viscosity is generated when the wave runs up and then collapses behind the barrier. The turbulent viscosity is not generated during the wave propagation, which points to the fact that TM has almost no effect at this stage.

Let us present some quantitative estimates of the effect of turbulence on the propagation and runup of the wave. Figure 7 shows comparative profiles of the forces acting on the bottom (in the slope and barrier zones) for setup 2 (Table 1). The profiles indicate that the pressure force on the 'Bottom' during the wave propagation in both calculations is nearly identical. One can see a peak at the time moment when the wave breaks. The friction force in the 'Bottom' zone in the case with TM is about 10 times higher than in the case without TM. However, its magnitude is low, and its contribution to the total force is very small.

The force of pressure acting on the 'Barrier' is nearly identical in both calculations. The total force in the case with TM, however, is on average 10 percent higher than in the case without TM due to the friction force.

3.3. Setup 3

Figure 8 shows a comparison of the wave profiles for both flow cases calculated by using the LOGOS software package for the third setup with the Reynolds number, $\mathrm{Re} = 5.4 \times 10^5$.

The plots indicate that the wave runs up onto the barrier and then the fluid flows over it. In the calculation with TM, the wave runs up onto the barrier with some delay in time. In this setup, as the Reynolds number increases, one can observe more chaotic wave structures with a large number of bubbles.

Let us show the snapshots of the free-surface position and turbulent viscosity of the case with TM (Figure 9).

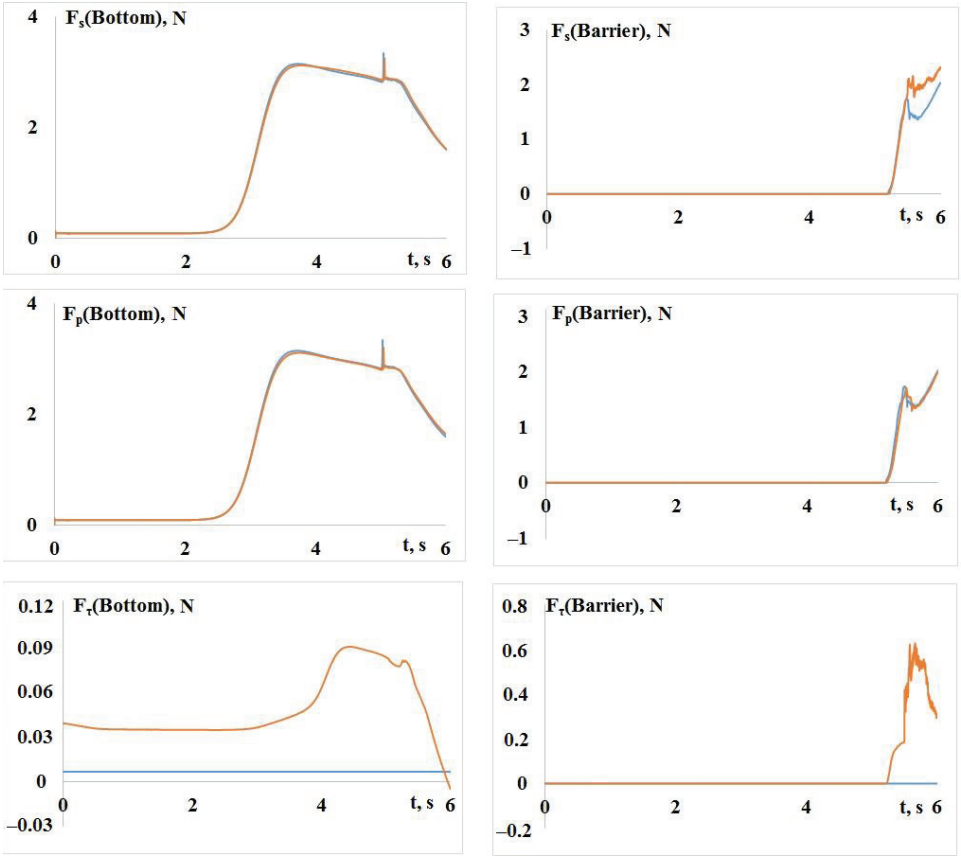

Figure 7. Comparison of the forces acting on the channel bottom in the slope and barrier zones for setup 2 (—without TM, —with TM).

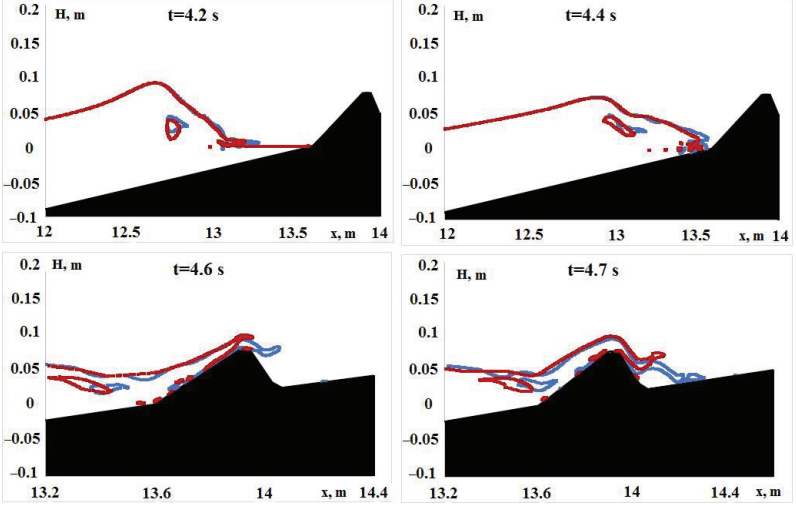

Figure 8. Comparison of the wave profiles for setup 3 (—without TM, —with TM).

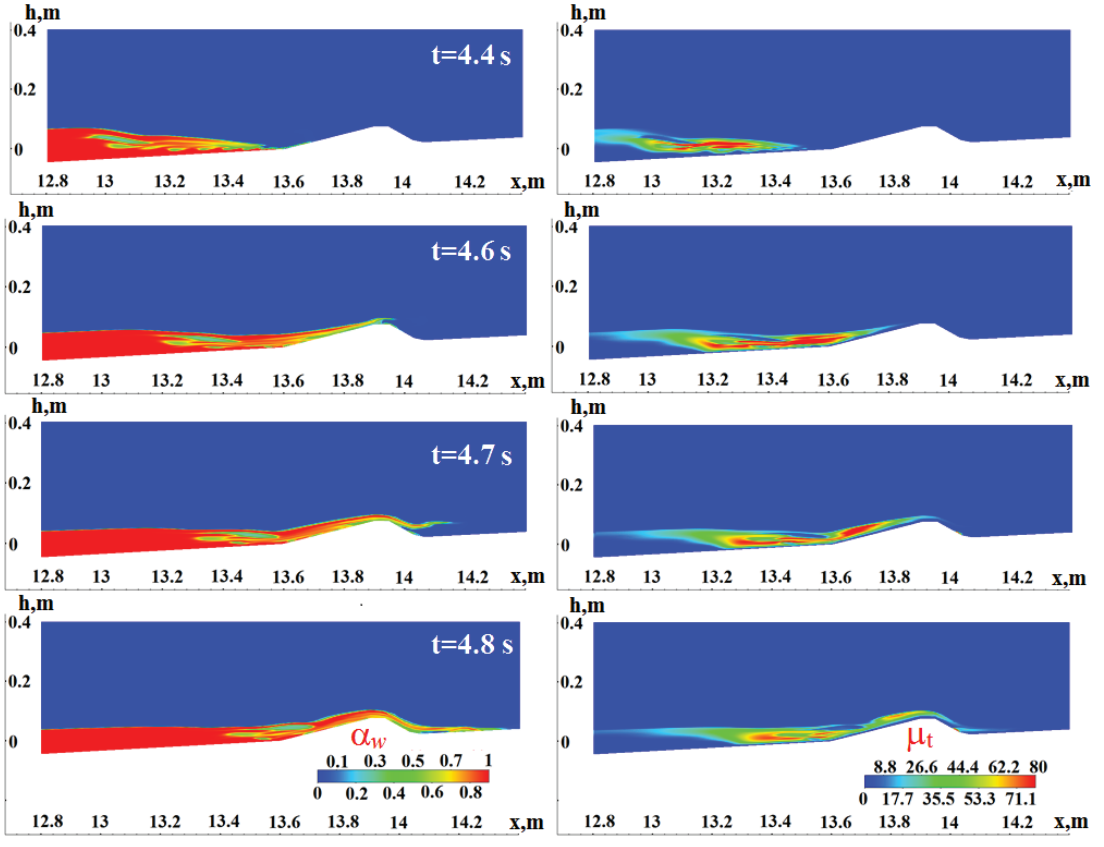

Figure 9. Time series of the free-surface position and turbulence viscosity for setup 3.

The figures show that the maximum turbulent viscosity is generated when the wave runs up and then overcomes the barrier. Let us present some quantitative estimates of the effect of turbulence on the propagation and runup of the wave. Figure 10 shows comparative profiles of the forces acting on the bottom for setup 3.

The profiles indicate that the force of pressure acting on the 'Bottom' wall during the wave propagation in both calculations is nearly identical. One can see a peak at the time when the wave collapses. The difference in the magnitude of the total force in both calculations does not exceed 3%. The contribution of the friction force to the total force is very small.

The pressure force produced by the wave as it runs up onto the 'Barrier' zone is about 15% higher in the case with TM. The total force in the calculation with TM is about 25% higher. The total force in the case with TM is higher due to the friction force, whose contribution to the total force is about 13%.

3.4. Setup 4

Figure 11 shows a comparison of the wave profiles for both cases calculated using the LOGOS software package for the Reynolds number, Re = 7.2×10^5.

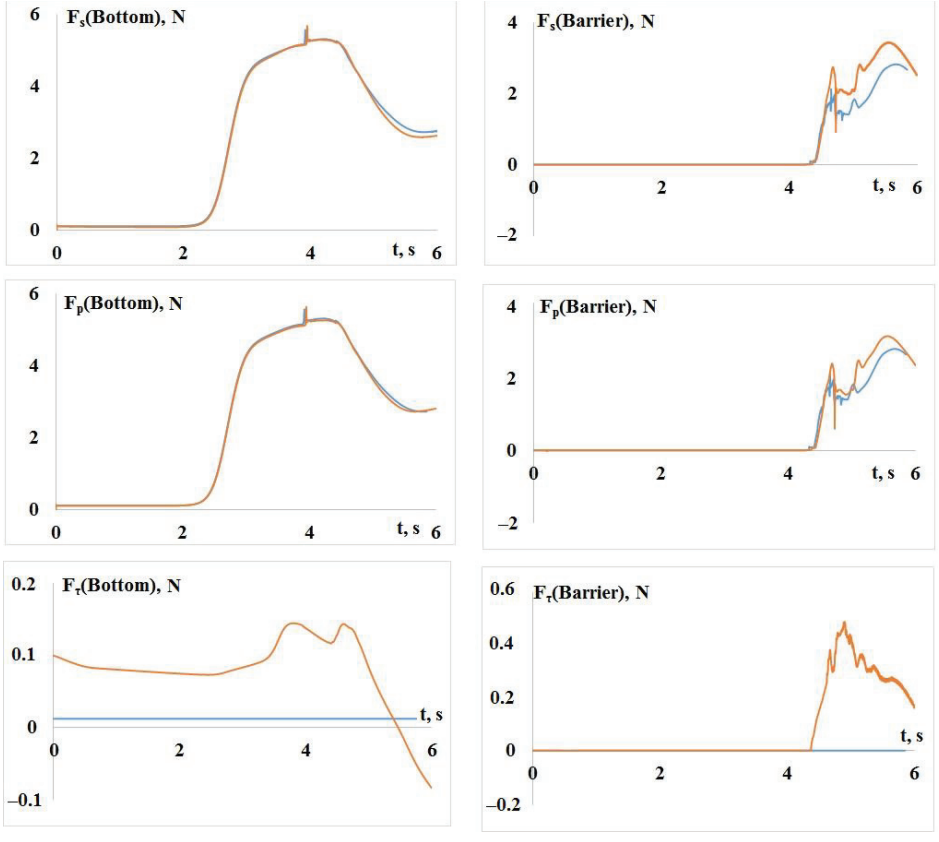

Figure 10. Comparison of the forces acting on the channel bottom in the slope and barrier zones for setup 3 (—without TM, —with TM).

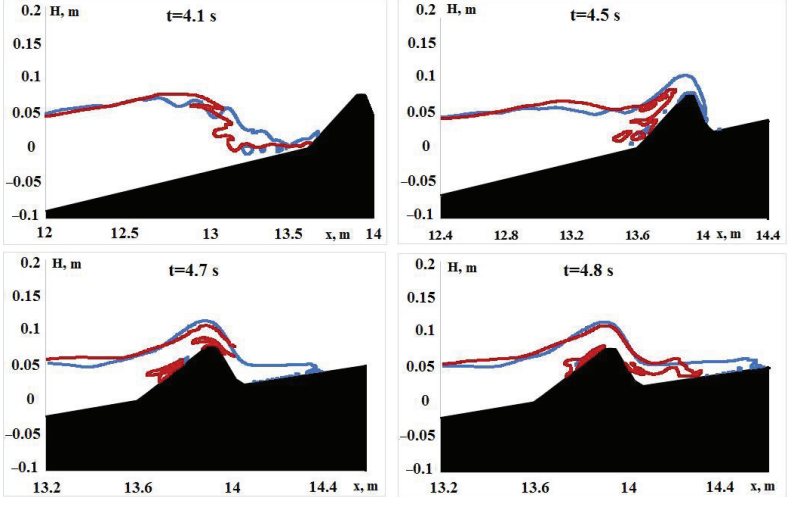

Figure 11. Comparison of the wave profiles for setup 4 (—without TM, —with TM).

The subplots indicate that the wave runs up onto the barrier and then goes over it. In the case of TM, the wave arrives with some delay in time, and, as a result, the way it overcomes the barrier is different, as shown below in the force plots.

Let us show the snapshots of the free-surface position and turbulent viscosity of the case with TM (Figure 12).

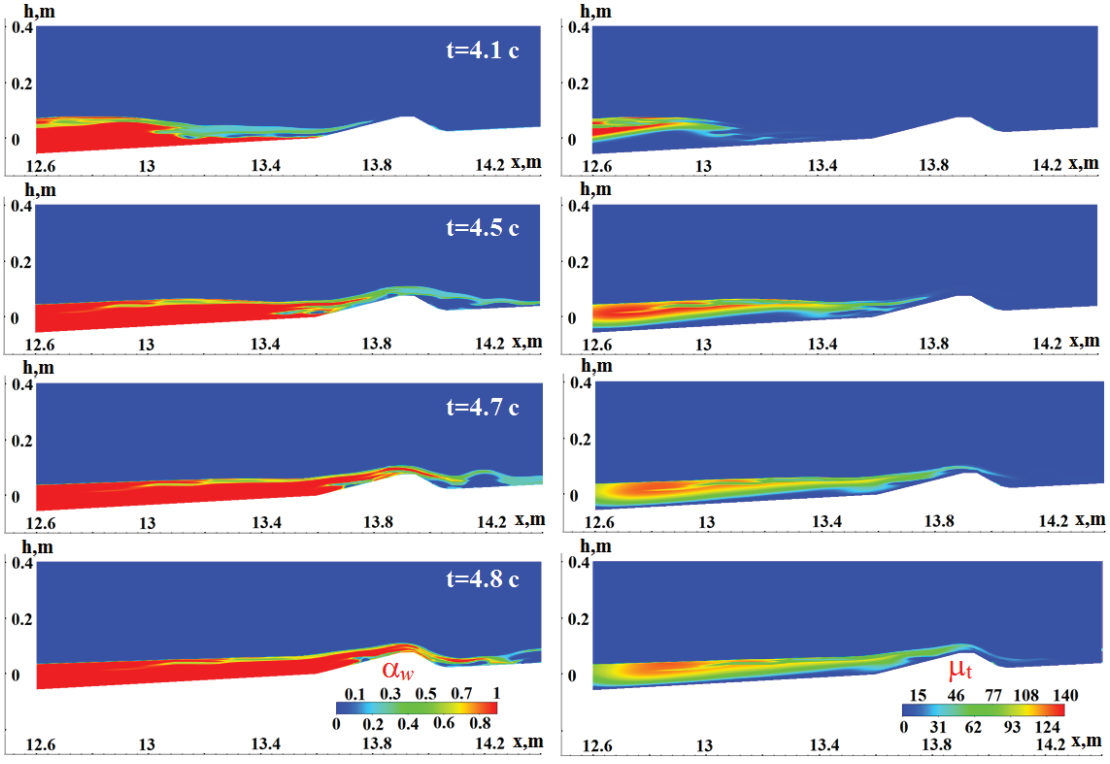

Figure 12. Time series of the free-surface position and turbulence viscosity for setup 4.

The subplots show that the maximum turbulent viscosity, in this case, is generated when the wave breaks over the slope.

Some quantitative estimates of the effect of turbulence on the propagation and runup of the wave are presented in Figure 13, which shows comparative profiles of the forces acting on the bottom for setup 4.

The profiles indicate that the pressure force acting on the 'Bottom' zone during the wave propagation in both calculations is nearly identical. The difference in the magnitude of the total force in both calculations does not exceed 3%. The contribution of the friction force to the total force is very small.

The pressure force produced by the wave as it runs up onto the 'Barrier' is about 10% higher in the case with TM. On average, the total force in the calculation is 18% higher. The total force in the case with TM is higher due to the force of friction, the contribution of which to the total force is about 8%.

Generally speaking, the presented results and quantitative estimates of the forces of friction and pressure and the total force acting on the channel bottom suggest that turbulence has almost no effect on the shape and way of propagation in the phase of wave propagation (without breaking). However, turbulence effects during the runup and breaking become noticeable and can boost the flow (increase the force of its pressure and the total force) by up to 25%.

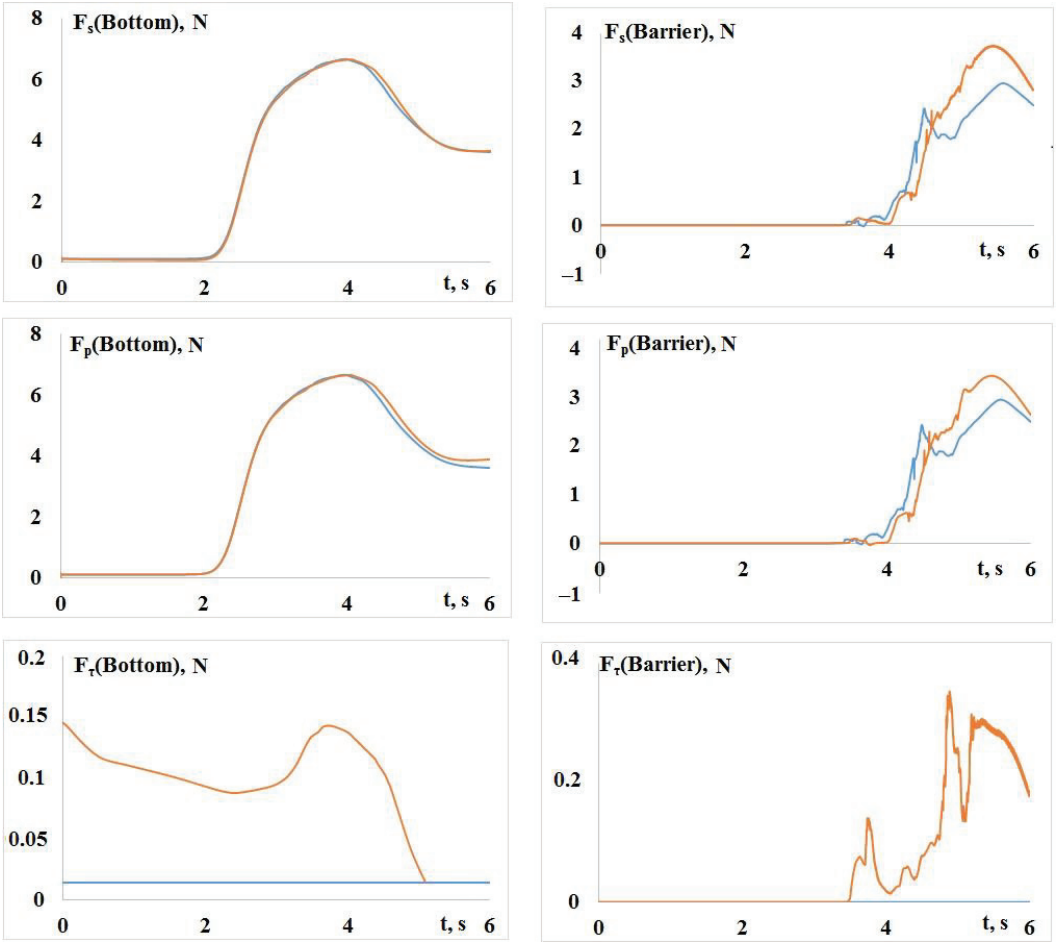

Figure 13. Comparison of the forces acting on the channel bottom in the slope and barrier zones for setup 4 (—without TM, —with TM).

4. Conclusions

The paper provides a description of wave transformation and its interaction with an inclined bottom and a barrier. It is demonstrated within the mathematical model based on the three-dimensional Navier–Stokes equations, the VOF method, and the RANS SST turbulence model. The turbulence effects in the phases of wave propagation and runup are studied. We compare the wave profiles at different times during wave propagation, runup, and collapse. The wave profiles are compared for the cases with and without TM. We demonstrate that, in the case with TM, the wave runs up onto the barrier a little later. The use of TM introduces additional viscosity into the solution, which represents the effect of turbulent vortex flows and increases the viscous stress on the tank bottom, which has its effect on the runup velocity, intensity, dispersion, and nonlinear properties of the wave. We show that turbulence has almost no effect on the shape of the wave and the way of its propagation (except the breaking itself). Turbulence effects during the runup and breaking, however, become noticeable and can boost the flow (increase the force of its pressure and the total force) by up to 25%.

Author Contributions: Conceptualization, A.K. (Andrey Kozelkov) and A.K. (Andrey Kurkin).; data curation, E.T. and V.K.; formal analysis, A.K. (Andrey Kozelkov) and V.K.; investigation, E.T., A.K. (Andrey Kozelkov), A.K. (Andrey Kurkin) and V.K.; methodology, A.K. (Andrey Kozelkov), A.K. (Andrey Kurkin) and V.K.; software, E.T. and V.K.; supervision, A.K. (Andrey Kurkin); validation, E.T.; visualization, E.T.; writing—original draft, A.K. (Andrey Kozelkov) and A.K. (Andrey Kurkin) . All authors have read and agreed to the published version of the manuscript.

Funding: The reported study was funded by the Ministry of Science and Higher Education of the Russian Federation (project No. FSWE-2021-0009) and the Council of the grants of the President of the Russian Federation for the state support of Leading Scientific Schools of the Russian Federation (Grant No. NSH-70.2022.1.5).

Conflicts of Interest: The authors declare no conflict of interest.

References

1. Landau, L.D.; Lifshitz, E.M. *Fluid Mechanics: V. 6*; Elsevier: Amsterdam, The Netherlands, 2013; p. 558.
2. Kim, D.C.; Kim, K.O.; Pelinovsky, E.N.; Didenkulova, I.I.; Choi, B.H. Three-dimensional tsunami runup simulation for the port of Koborinai on the Sanriku coast of Japan. *J. Coast. Res.* **2013**, *65*, 266–271. [CrossRef]
3. Yuk, D.; Yim, S.C.; Liu, P.L.-F. Numerical modeling of submarine mass-movement generated waves using RANS model. *Comput. Geosci.* **2006**, *32*, 927–935. [CrossRef]
4. Zhao, Q.; Armfield, S.; Tanimoto, K. Numerical simulation of breaking waves by a multi-scale turbulence model. *Coast. Eng.* **2004**, *51*, 53–80. [CrossRef]
5. Choi, B.H.; Kim, D.C.; Pelinovsky, E.; Woo, S.B. Three-dimensional simulation of tsunami run-up around conical island. *Coast. Eng.* **2007**, *54*, 618–629. [CrossRef]
6. Pelinovsky, E.; Choi, B.H.; Talipova, T.; Woo, S.B.; Kim, D.C. Solitary wave transformation on the underwater step: Asymptotic theory and numerical experiments. *Appl. Math. Comput.* **2010**, *217*, 1704–1718. [CrossRef]
7. Choi, B.H.; Pelinovsky, E.; Kim, D.C.; Didenkulova, I.; Woo, S.-B. Two- and three-dimensional computation of solitary wave runup on non-plane beach. *Nonlinear Processes Geophys.* **2008**, *15*, 489–502. [CrossRef]
8. Garbaruk, A.V.; Strelets, M.K.; Travin, A.K.; Shur, M.L. *Up-to-Date Approaches to Turbulence Simulations: A Study Guide*; Publishing House of Peter the Great St./Petersburg Polytechnic University: Saint Petersburg, Russia, 2016; p. 233.
9. Volkov, K.N.; Emelyanov, V.N. *Large Eddy Simulations in Calculations of Turbulent Flows*; Fizmatlit: Moscow, Russia, 2008; p. 368.
10. Belov, I.A.; Isaev, S.A. *Simulations of Turbulent Flows: A Study Guide*; Publishing House of Baltic State Technical University: Saint Petersburg, Russia, 2001; p. 108.
11. Lesieur, M. *Turbulence in Fluids*, 4th ed.; Springer: Dordrecht, The Netherlands, 2008; p. 558.
12. Tanaka, H.; Tinh, N.X.; Sana, A. Transitional Behavior of a Flow Regime in Shoaling Tsunami Boundary Layers. *J. Mar. Sci. Eng.* **2020**, *8*, 700. [CrossRef]
13. Sana, A.; Tanaka, H. Numerical modeling of a turbulent bottom boundary layer under solitary waves on a smooth surface. *Coast. Eng. Proc.* **2018**, *36*, 152266. [CrossRef]
14. Tinh, N.X.; Tanaka, H. Study on boundary layer development and bottom shear stress beneath a tsunami. *Coast. Eng. J.* **2019**, *61*, 574–589. [CrossRef]
15. Sana, A.; Tanaka, H. Two-equation turbulence modeling of an oscillatory boundary layer under steep pressure gradient. *Can. J. Civ. Eng.* **2010**, *37*, 648–656. [CrossRef]
16. Kozelkov, A.S.; Kurulin, V.V.; Tyatyushkina, E.S.; Puchkova, O.L. Application of the detached-eddy simulation model for viscous incompressible turbulent flow simulations on unstructured grids. *Math. Models Comput. Simul.* **2014**, *26*, 81–96.
17. Kozelkov, A.; Kurulin, V.; Emelyanov, V.; Tyatyushkina, E.; Volkov, K. Comparison of convective flux discretization schemes in detached-eddy simulation of turbulent flows on unstructured meshes. *J. Sci. Comput.* **2016**, *67*, 176–191. [CrossRef]
18. Menter, F.R.; Kuntz, M.; Langtry, R. Ten Years of Industrial Experience with the SST Turbulence Model. In *Turbulence, Heat and Mass Transfer*, 4th ed.; Hanjalic, K., Nagano, Y., Tummers, M., Eds.; Begell House Inc.: Danbury, CT, USA, 2003; pp. 625–632.
19. Zaikov, L.A.; Strelets, M.K.; Shur, M.L. A comparison between one- and two-equation differential turbulence models in application to separated and attached flows: Flow in channels with counter. *High Temp.* **1996**, *34*, 713–725.
20. Ubbink, O. Numerical Prediction of Two Fluid Systems with Sharp Interfaces. Ph.D. Thesis, Imperial College of Science, Technology & Medicine, London, UK, 1997.
21. Khrabry, A.I.; Zaytsev, D.K.; Smirnov, E.M. Numerical simulations of free-surface flows based on the VOF method. *Trans. Krylov State Res. Cent.* **2003**, *78*, 53–64.
22. Kozelkov, A.S. The Numerical Technique for the Landslide Tsunami Simulations Based on Navier-Stokes Equations. *J. Appl. Mech. Tech. Phys.* **2017**, *58*, 1192–1210. [CrossRef]
23. Kozelkov, A.S.; Efremov, V.R.; Kurkin, A.A.; Pelinovsky, E.N.; Tarasova, N.V.; Strelets, D.Y. Three dimensional numerical simulation of tsunami waves based on the Navier-Stokes equations. *Sci. Tsunami Hazards* **2017**, *36*, 183–196.

24. Kozelkov, A.S.; Kurulin, V.V.; Lashkin, S.V.; Shagaliev, R.M.; Yalozo, A.V. Investigation of supercomputer capabilities for the scalable numerical simulation of computational fluid dynamics problems in industrial applications. *Comput. Math. Math. Phys.* **2016**, *56*, 1506–1516. [CrossRef]
25. Chen, Z.J.; Przekwas, A.J. A coupled pressure-based computational method for incompressible/compressible flows. *J. Comput. Phys.* **2010**, *229*, 9150–9165. [CrossRef]
26. Kozelkov, A.S.; Lashkin, S.V.; Efremov, V.R.; Volkov, K.N.; Tsibereva, Y.A.; Tarasova, N.V. An implicit algorithm of solving Navier–Stokes equations to simulate flows in anisotropic porous media. *Comput. Fluids* **2018**, *160*, 164–174. [CrossRef]
27. Kozelkov, A.S.; Kurkin, A.A.; Sharipova, I.L.; Kurulin, V.V.; Pelinovsky, E.N.; Tyatyushkina, E.S.; Meleshkina, D.P.; Lashkin, S.V.; Tarasova, N.V. A minimum basic set of validation problems for free-surface flow simulation methods. *Trans. NNSTU N.A. R.E. Alekseev.* **2015**, *2*, 49–69.
28. Tyatyushkina, E.S.; Kozelkov, A.S.; Kurkin, A.A.; Pelinovsky, E.N.; Kurulin, V.V.; Plygunova, K.S.; Utkin, D.A. Verification of the LOGOS Software Package for Tsunami Simulations. *Geosciences* **2020**, *10*, 385. [CrossRef]
29. Kozelkov, A.S.; Kurkin, A.A.; Pelinovsky, E.N.; Kurulin, V.V.; Tyatyushkina, E.S. Modeling the Disturbances in the Lake Chebarkul Caused by the Fall of the Meteorite in 2013. *Fluid Dyn.* **2015**, *50*, 828–840. [CrossRef]
30. Kozelkov, A.S.; Kurkin, A.A.; Pelinovsky, E.N.; Kurulin, V.V. Modeling the cosmogenic tsunami within the framework of the Navier-Stokes equations with sources of different type. *Fluid Dyn.* **2015**, *50*, 306–313. [CrossRef]
31. Hsiao, S.-C.; Lin, T.-C. Tsunami-like solitary waves impinging and overtopping an impermeable seawall: Experiment and RANS modeling. *Coast. Eng.* **2010**, *57*, 1–18. [CrossRef]

fluids

MDPI

Article

Flow Past Mound-Bearing Impact Craters: An Experimental Study

Diego Gundersen [1], Gianluca Blois [1,*] and Kenneth T. Christensen [1,2,3,†]

[1] Department of Aerospace and Mechanical Engineering, University of Notre Dame, Notre Dame, IN 46556, USA; dgunders@nd.edu (D.G.); Kenneth.Christensen@iit.edu (K.T.C.)
[2] Department of Civil and Environmental Engineering and Earth Sciences, University of Notre Dame, Notre Dame, IN 46556, USA
[3] CO_2 Storage Division, International Institute for Carbon-Neutral Energy Research (I2CNER), Kyushu University, Fukuoka 819-0385, Japan
* Correspondence: gblois@nd.edu
† Current Affiliation: Department of Mechanical, Materials, and Aerospace Engineering, Illinois Institute of Technology, Chicago, IL 60616, USA.

Abstract: An experimental investigation into the flow produced by mound-bearing impact craters is reported herein. Both an idealized crater and a scaled model of a real martian crater are examined. Measurements were performed using high-resolution planar particle image velocimetry (PIV) in a refractive-index matching (RIM) flow environment. Rendering the crater models optically invisible with this RIM approach provided unimpeded access to the flow around and within each crater model. Results showed that the mean flow within the idealized crater exhibits more structural complexity compared to its moundless counterpart. Second-order statistics highlighted regions of minimal and elevated turbulent stresses, the latter of which revealed a complex interaction between shear layers that are present at the upstream and downstream parts of the rim and the central mound. Periodic vortex shedding of quasi-spanwise vortices from the upstream rim was revealed by POD-filtered instantaneous flow fields. Vertical flapping of this shear layer resulted in vortices occasionally impinging on the inner wall of the downstream rim. Further, conditional averaging analysis suggested periodic lateral oscillations of wall-normal vortices within the crater rim region reminiscent of those observed for flow inside spherical dimples. These results have implications for intra- to extra-crater mass and momentum exchange, and for sediment transport processes. Lastly, experiments with the Gale Crater model showed both similarities with and differences from the primary flow features found for the idealized model.

Keywords: impact crater; index matching; complex topography

Citation: Gundersen, D.; Blois, G.; Christensen, K.T. Flow Past Mound-Bearing Impact Craters: An Experimental Study. *Fluids* **2021**, *6*, 216. https://doi.org/10.3390/fluids6060216

Academic Editors: Joseph J. Kuehl, Pengfei Xue and Fabrice Veron

Received: 28 April 2021
Accepted: 3 June 2021
Published: 9 June 2021

1. Introduction

Some of the richest records of Mars's evolution are preserved in the sedimentary strata deposited within depressed topographic features, mostly represented by impact craters [1–3]. A number of early studies focused on simple martian impact craters indicated that wind-driven erosional and depositional processes may have played major roles in their post-impact evolution [4,5]. More recently, attention has shifted towards craters that have central sedimentary mounds [6]. Although less common, these craters are considered key to paleo-environmental reconstruction studies, as a valuable rock record is thought to be preserved not only within the crater floors but also within the strata forming these unique sedimentary features. Conveniently, when mounds are eroded, ancient signatures of past environmental conditions are exposed and accessible to robotic imaging and sampling. One of the best documented and most well-known examples of these outcrops can be found within Gale Crater, a ∼150 km impact crater hosting a large sedimentary deposit, a ∼5 km tall sedimentary mound, Aeolis Mons, emerging at the center of the crater. Gale is believed

to hold evidence of past and potentially current subsurface water presence on Mars, and as such, it is the target of an ongoing exploration by the NASA rover Curiosity [7,8].

The processes controlling crater mound formation and subsequent erosion are the subjects of ongoing research [6,9,10]. These efforts are key to developing robust paleo-environmental reconstruction theories and predicting future environmental conditions, and are thus central to exploration missions. Several theories exist as to the formation of a central mound, those pointing to wind processes as the predominant driving mechanisms being among the most compelling [6,9,10]. Kite et al. [9] suggested that radially-directed slope winds, arising from strong intracrater temperature and density gradients, are responsible for both the formation of the mound and for its partial erosion. A complementary theory proposed by Day et al. [10] suggested that stages of mound formation progress from a sediment-filled crater, to the development of an initial moat, to a retreating central mound, to an isolated hill. This hypothesis, based upon the dominance of unidirectional regional winds, has been numerically tested by Anderson and Day [11], who linked the exhumation of the moat to the erosive action induced by an arch-shaped three-dimensional flow structure wrapping around the central mound. Geologic surface features, such as wind streaks, yardangs (sharp irregular ridges lying parallel to the prevailing winds), and dune fields provide additional inference to the prevailing wind directions over a given period of time. The distribution and orientations of these features, both within and around Gale, support the flow reconstruction proposed by Anderson and Day [11], and indicate that northerly regional winds, as opposed to katabatic (slope) winds, may have played a dominant role in the transport of sediments inside Gale Crater [6,12]. The pressure-driven regional winds impinging upon Gale Crater are dominant in the meridional direction, having estimated velocity magnitudes in the range of 1–20 m/s, though most commonly in the range of 5–7 m/s producing a mature planetary boundary layer thickness of 7–10 km [13–15]. It is reasonable to assume that a combination of density-driven slope winds and synoptic winds contribute to the formation and erosion of mounded craters, with the former mechanism being negligible for smaller craters.

As mentioned earlier, the notion that craters may be sculpted by winds is not new. Greeley et al. [4,5] studied the morphological evolution of simple craters driven by unidirectional winds and provided evidence of a link between erosional/depositional patterns and flow. Greeley et al. [5] performed sediment transport experiments in a wind tunnel using idealized crater geometries (both erodible craters and solid craters with loose sand) and compared the resulting morphological patterns to those observed in martian craters. Outside of the crater, they observed a region of deposition on the upwind side of the windward crater rim and erosion on the flanks of the crater. When wind velocity was above a certain threshold (dependent on grain size), erosional depressions originated in the lee of the crater rim in the form of a "bilobate" pattern. For each grain size, they also noted that as free-stream velocity was increased, the bilobate depressions became longer and wider, and moved toward the centerline, eventually merging in a single larger erosional region. A small triangular-shaped region in which erosion was relatively less present was observed near the lee of the crater. At the highest free-stream velocities considered, a trilobate depositional pattern was found downwind of the crater, suggesting a regime transition. Greeley et al. [5] proposed that the bilobate depressions were produced by the action of a horseshoe vortex wrapped around the leading edge of the crater rim, and counter-rotating, quasi-streamwise trailing vortices originating from the crater sides and emanating downstream. Within the crater, sand was first deposited in the downwind portion of the crater floor. However, as the experiment reached steady state conditions, sand tended to be transported upstream and accumulated in the lee of the windward crater rim. The downwind portion of the crater's inner surface, including the floor and wall, was consistently eroded, regardless of the initial configuration of the experiment.

Some of the experiments performed by Greeley et al. [5] allowed inference as to the primary sediment pathways. In particular, a reverse flow along the centerline of the intracrater region was consistently seen to move sediment upwind, explaining the erosion

in the downwind portion of the crater's inner surface. Moreover, sediment accumulated inside the crater in a horseshoe pattern wrapped around the upwind inner wall and trailing downwind. Sand was eventually carried upward over the crater rim along the lateral sides and the leeward rim. Greeley et al. [5] interpreted these observations as the action of a large recirculating region extending across the entire intracrater and sustaining both the reverse flow along the floor and the uplift along the lateral walls.

Martian craters are immersed in a very thin atmosphere, which makes physical modeling highly challenging, especially if sediment transport is involved. Nonetheless, Greeley et al. [5], who used a standard atmospheric wind tunnel, demonstrated that experimental approaches are extremely valuable for understanding first-order flow physics. As mentioned earlier, in order to assess the applicability of their results to large scale craters, Greeley et al. [5] provided a qualitative comparison between the erosional patterns produced in their experiments and field observations of martian and terrestrial craters. They used photographs of small martian craters in which erosional/depositional patterns were indicated by the exposure/burial of more cohesive substrates. As additional corroboration, Greeley et al. [5] found that the patterns obtained experimentally were also consistent with those observed in terrestrial field studies. By inferential analogy, the similarity between experimental and field patterns provides compelling evidence supporting the notion that martian crater evolution may be primarily driven by aeolian processes.

Besides the work of Greeley et al. [5] and Anderson and Day [11], there have been few other studies focused on elucidating the flow dynamics associated with geometries similar to impact craters. A number of studies were dedicated to dimples, which are more closely related to rimless bowl-shaped craters [16–20]. In industrial applications, dimples are used to enhance heat transfer exchange, as they offer the advantage of minimizing pressure loss compared to ribs and fins [20–22]. These studies have highlighted the complexity of the flow structure associated with such depressions. The mean flow structure within a dimple is characterized by a flow separation at the leading edge producing a three-dimensional monocore recirculation, symmetric about the centerline, occupying $\sim$90% of the cavity and generating low and high surface pressures at the upstream and downstream halves of the dimple cavity, respectively [19,22]. While the mean flow does not seem to be strongly dependent on Reynolds number (Re), the flow complexity does increase with the depth-to-diameter ratio, causing the flow to be highly unsteady and multi-modal [17–19]. A combination of high-frequency and low-frequency modes were observed. Low-frequency, periodic, self-sustained lateral oscillations of the large-scale vortex structure were found to position the axis of the large vortex structure in the range $\pm 45^{\circ}$. More interestingly, periodical outbursts of vortex pairs producing turbulent ejections of mass from the downstream rim were observed at higher frequencies, first in qualitative flow visualization experiments [17,20], and then this was confirmed through POD (proper orthogonal decomposition) analysis of LES (large eddy simulation) data by Turnow et al. [19]. Recent particle image velocimetry (PIV) experiments performed by Zhou et al. [22] over a spherical dimple quantitatively investigated the shear layer produced by the separation at the upstream edge. They concluded that the Kelvin–Helmholtz vortices populating the shear layer are responsible for the exchange of momentum between the free-stream and the dimple cavity. While studies on dimples may be directly applicable to ancient simple craters sculpted into rimless depressions by extremely long erosion processes, they cannot be applied to raised rim craters, particularly such craters with central mounds.

While much work has been done to understand flow around and within simple craters and dimples, our understanding of the flow around mound-bearing martian craters remains poor. To the best of our knowledge, no experimental study has probed the flow within complex craters with raised rims and central mounds, and no study has reported on the flow over a model of a real martian crater. The objective of this study was to start addressing these gaps by investigating the intracrater and extracrater flow structure induced by a unidirectional turbulent boundary layer on mounded craters via laboratory measurements. Herein, the craters were assumed to be subjected to external unidirectional

winds. High spatial resolution particle image velocimetry (PIV) measurements were performed on two mounded craters: an idealized crater shape based upon a mathematical model that was previously employed by Anderson and Day [11], and a model of a real crater sourced from a digital elevation map (DEM) of Gale Crater. The initial results presented in Sections 3–5 provide a detailed description of flow responding to the idealized crater model. The results presented in Section 6 characterize flow around the Gale Crater model as a means of determining how well idealized models can inform our understanding of more realistic topographies.

2. Materials and Methods

2.1. Facility

Laboratory experiments were performed on physical models in the refractive-index-matched (RIM) flow facility at Notre Dame [23] wherein idealized and realistic crater models were fabricated and exposed to a turbulent unidirectional flow. The PIV method [24] was used to resolve the flow both within and outside of each crater model. Figure 1 presents perspective views of the experimental setup illustrating the relative orientation of the camera and laser sheet (which defines the measurement plane and the field of view, FOV) used to image flow in wall-normal and wall-parallel planes. A high-resolution digital camera captured the positions of tracer particles dispersed in the flow at two sequential times to infer the instantaneous fluid velocity field within the FOV. The tracer particles were illuminated over a targeted flow region with pulsed laser light formed into a thin sheet that defines the measurement plane. The laser pulses were synchronized to the capture rate of the imaging camera. Optical access to the flow around complex topography such as that of a crater is difficult to attain in the measurement planes, as illustrated in Figure 1, owing to protruding geometric features (e.g., the crater ridge) which obstruct views of the interior. This fundamental limitation can be overcome by fabricating transparent crater models from a material (acrylic) whose optical refractive index (RI) matches that of the working fluid in the RIM flow facility [23]. This RIM approach overcomes issues of optical access and in the current work allowed full-field imaging of the flow in and around the topographically complex crater models. By fine-tuning the fluid temperature to optimize the match between the solid and fluid RIs, each crater model immersed in the working fluid optically "disappeared" and light was able to pass through the model with minimal reflection or refraction. This experimental protocol therefore enabled unobstructed and unaberrated optical access to all regions of the flow produced by the crater, allowing its full quantification via PIV measurements.

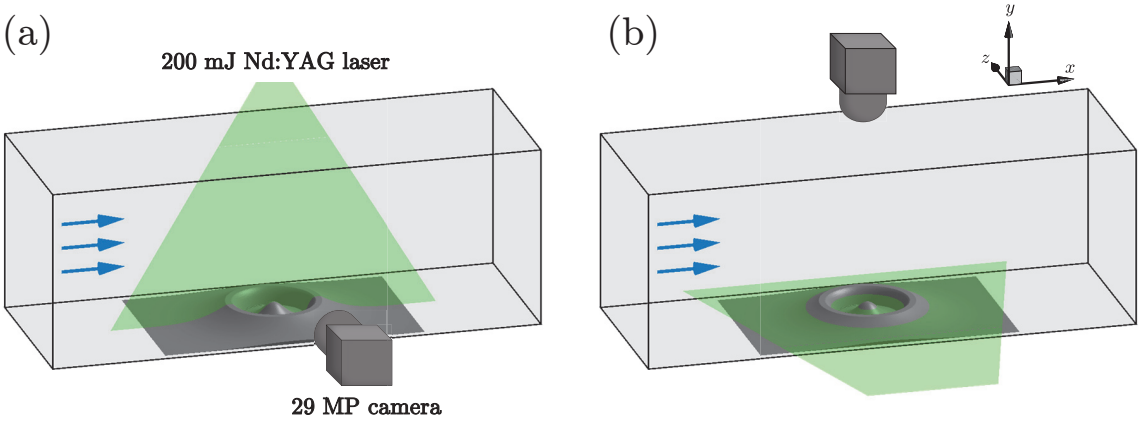

Figure 1. Perspective views of the imaging setup used for the (**a**) wall-normal and (**b**) wall-parallel PIV measurements.

The flow facility used for this study employs an aqueous solution of sodium iodide (∼63% NaI by weight) as the working fluid for which a number of transparent resins can be used for the fabrication of the models [23]. This solid/fluid combination is ideal in a broad range of flow applications because of the relatively minor safety concerns associated with this liquid, and its physical properties, including a relatively high specific weight (∼1.9) and low kinematic viscosity (only 10% higher than that of water). The latter characteristic enables high-Reynolds-number flows to be studied. Figure 2 illustrates the efficacy of this RIM approach. Here, a model of Gale Crater was molded from an acrylic resin (Uoptic2) whose RI can be matched to that of the NaI solution. In Figure 2a, the model is simply immersed in air and therefore fully visible. In Figure 2b, the same crater model is partially immersed in the NaI solution. As their RIs under the fluid interface are nearly the same, light passed through the model without reflection or refraction and thus it appeared as if it had disappeared. In the figure, the grid pattern positioned behind the model is visible and undistorted through the portion of the model that was immersed in the NaI solution. The optical transparency of this immersed portion of the model illustrates the measurement principle which is based upon rendering the fluid–solid system a continuum from an optical standpoint. By eliminating all sources of reflection and refraction, the flow within and around the intracrater region can be optically accessed and quantitatively resolved.

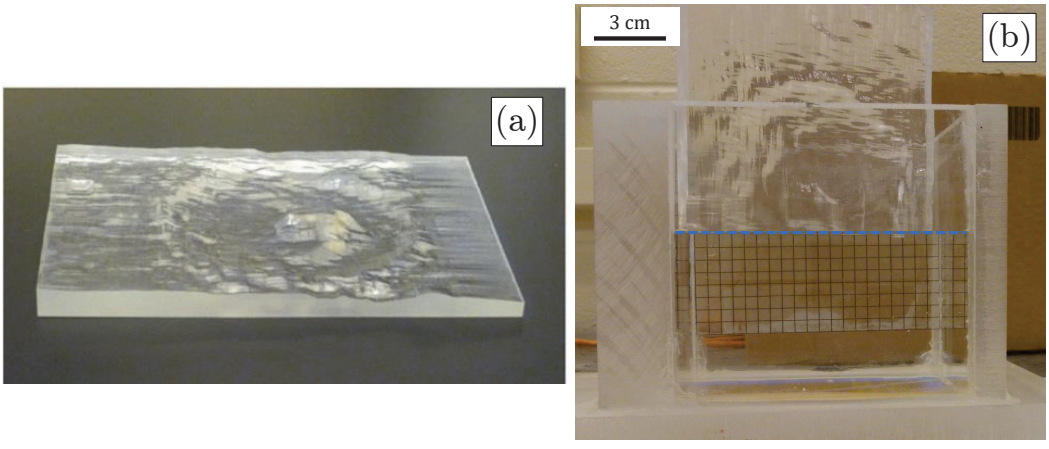

Figure 2. Photos of the realistic crater model (**a**) immersed in air and (**b**) partially immersed in an NaI solution. The dashed line in (**b**) demarcates the air–fluid interface.

2.2. Crater Models

Transparent models of craters like that shown in Figure 2 were fabricated using the protocol detailed in Blois et al. [23]. First, a positive topography was 3D printed with the same geometry of the final model. A two-part silicone solution was poured around the 3D printed positive and cured to create the mold. Finally, a clear acrylic resin whose RI matches that of the NaI working fluid (RI $\approx$ 1.49) was poured into the silicone mold and appropriately degassed and cured.

Two models were fabricated: a synthetic crater shape based upon mathematical models [11] that served as a proxy of a real crater and a digital elevation model (DEM) of Gale Crater. Anderson and Day [11] performed numerical simulations of flow over idealized crater morphologies with stages ranging from a fully-filled to an empty crater. The model used in the present study corresponds to the middle of that morphological range, with the crater surface having been defined by a combination of Gaussian curves with standard deviations of 0.4 (outer rim surface), 0.05 (inner rim surface), and 0.03 (mound). The physical model fabricated for this study had a crater rim height of 10 mm and a diameter of 50 mm, and the mound height was 90% of the rim height, as shown in Figure 3a,c.

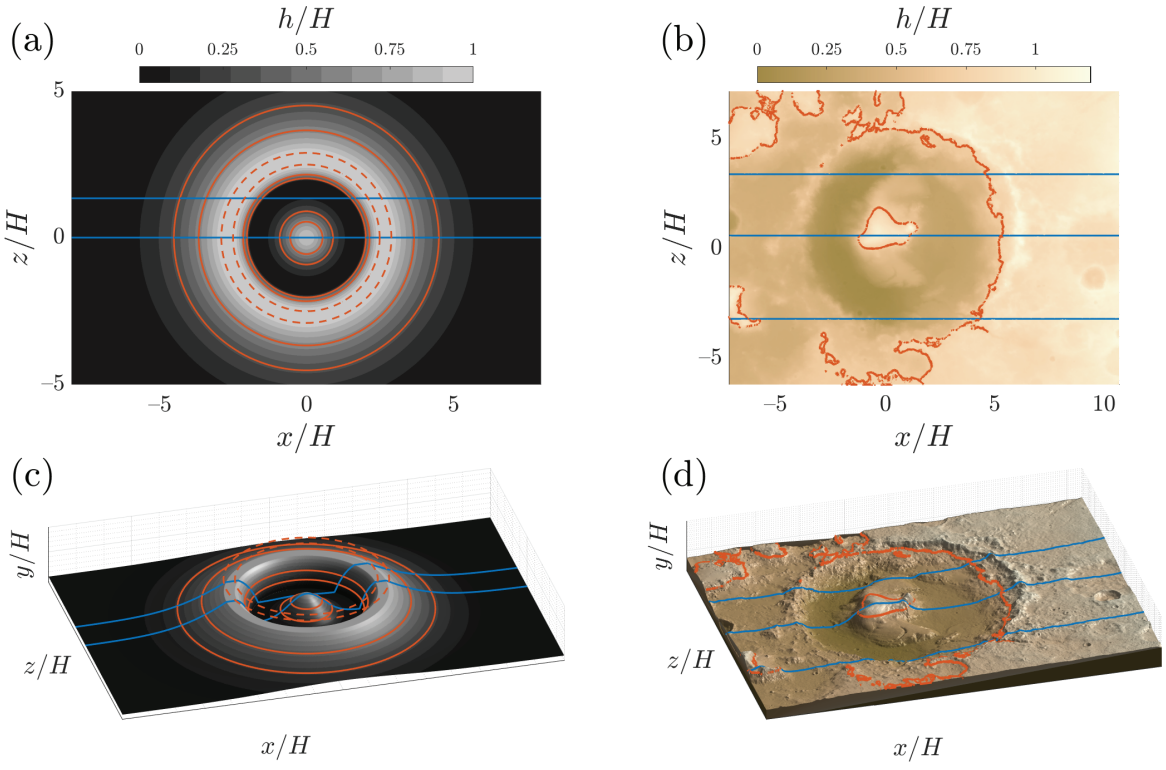

Figure 3. Elevation maps of (**a**) the idealized crater model and (**b**) the Gale Crater model. (**c**,**d**) Isometric views of the idealized and Gale Crater models, respectively. Solid red lines demarcate the intersections of the wall-parallel PIV measurement planes with the surface, and the blue lines identify the spanwise positions of the wall-normal PIV measurement plane locations. H is the model elevation, corresponding to the rim height.

The DEM used for the Gale Crater model was sourced from the High-Resolution Stereoscopic Camera (HRSC) experiment on Mars Express [25]. The geometry of the model ensured that the resulting experimental datasets contained realistic information on intracrater flows relevant to aeolian abrasion of actual intracrater mounds. As such, a low-pass filter was applied to the DEM. In addition, the vertical scale was exaggerated by a factor of three in order to satisfy the constraints of the facility. The morphology of this Gale Crater model is shown in Figure 3b,d. This model had a crater rim height of 10 mm, a diameter of 87 mm, and a mound height of 7.9 mm.

In both models, the rim was the most protruding feature, and its height, denoted by H, indicates the model elevation. Once fabricated, each model was mounted flush along the bottom wall of the RIM facility test section for testing. In the case of the Gale model, the upstream portion of the topography included in the DEM was modified to eliminate any abrupt transition that would contaminate the flow. Each model was mounted approximately 1.7 m downstream of the inlet and the flow was tripped at the inlet of the test section with a 3.5 mm-diameter cylinder secured to the channel floor to ensure a mature turbulent boundary at the measurement location. In this regard, each model was fully immersed within a turbulent boundary layer, with a $\delta/H > 5$, where δ is the boundary layer thickness obtained from independent measurements with no crater model present (see Table 1).

Given the three-dimensionality of the crater's geometry, flow was measured in five different planes to capture key elements of its three-dimensional structure. The locations of these PIV measurement planes are illustrated in Figure 3. Here, x, y, and z represent the

streamwise, wall-normal, and spanwise directions, respectively; and blue and red lines denote the intersections between the streamwise–wall-normal ($x-y$; wall-normal) and streamwise–spanwise ($x-z$; wall-parallel) PIV measurement planes and each model's surface, respectively. Data were collected at two wall-normal measurement planes—one positioned at the centerline ($z/H=0$) and the other offset in the spanwise direction by about half of the crater rim radius ($z/H=1.3$). Measurements were also made in three wall-parallel planes positioned near the model base ($y/H=0.3$), just above the crater half-height ($y/H=0.6$) and just above its rim ($y/H=1.1$). For each model, data were collected at four free-stream velocities ($U_\infty=0.25$, 0.49, 0.73, and 0.97 m/s), corresponding to four crater Reynolds numbers, Re_H ($Re_H=2200$, 4500, 6700. and 8900, where $Re_H=U_\infty H/\nu$) in each measurement plane. The primary flow parameters of the incoming turbulent boundary layer for each free-stream velocity are reported in Table 1, with the friction Re being defined as $Re_\tau=u_\tau\delta_{99}/\nu$, where u_τ is the friction velocity, and $Re_\delta=U_\infty\delta_{99}/\nu$. As the discussion of the results focuses primarily on the highest-speed case, a more detailed list of the experimental parameters for this flow condition is presented in Table 2. As described in Section 3, all of these flow parameters were obtained from mean velocity profiles measured with the model (i.e., smooth-wall data).

Table 1. Characteristics of the incoming flow for each free-stream condition.

U_∞ (m/s)	δ_{99} (mm)	u_τ (m/s)	Re_H	Re_τ	Re_δ
0.25	54.1	0.011	2200	540	12,000
0.49	56.7	0.020	4500	1040	25,000
0.73	52.2	0.029	6700	1380	35,000
0.97	56.5	0.038	8900	1920	50,000

Table 2. Characteristics of the incoming flow for the highest Re case ($Re_H=8900$).

Channel cross Section	112 × 112 mm
Flow development length	1.7 m
Working fluid kinematic viscosity ν	1.1 $\times 10^{-6}$ m^2/s
Free-stream velocity U_∞	0.97 m/s
Re_H	8900
Free-stream turbulence intensity	2.4%
δ_{99}	56.5 mm
Re_δ	50,000
u_τ	0.038 m/s
Re_τ	1920

2.3. Particle Image Velocimetry

To enable PIV measurements, the flow was seeded with 11 μm silver-coated hollow-glass spheres (see Blois et al. [23] for details). The tracer particles were illuminated with a dual-cavity, Quantel Evergreen Nd:YAG laser (Lumibird, formerly Quantel-Keopsys group, Bozeman, MT, USA) at an energy of 200 mJ/pulse formed into a thin light sheet (∼1 mm thickness) and oriented in the various $x-y$ and $x-z$ measurement planes mentioned previously (see Figure 3). A 29-megapixel, frame-straddle CCD camera (TSI, Inc., Shoreview, MN, USA) with an array size of 6592 × 4400 pixels was used to image the 285 × 101 mm and 242 × 114 mm wall-parallel and wall-normal fields of view, respectively. The camera was positioned such that the model was centered at roughly a third of the total streamwise field of view in order to best capture the full extent of the shear-layer dynamics. At each

measurement location, 4000 time-delayed pairs of PIV images were collected at a sample frequency of 0.5 Hz to ensure statistical independence of the samples.

The vector fields were processed using commercial software DaVis 8.4.0 (LaVision GmbH, Göttingen, Germany) with a normalized multi-pass iterative cross-correlation scheme with decreasing interrogation window size, starting with two passes with a 64 × 64 pixel spot size, followed by three passes with a 16 × 16 pixel spot size. The final spatial resolution of the vector fields was ∼0.6 mm (0.06 H). Direct correlation was used in evaluating interrogation windows that intersected with the surface of the model to avoid spurious results owing to the solid–fluid interface. Finally, spurious vectors were identified and removed using a universal outlier detection scheme [26]. Holes were filled via linear interpolation. Less than 5% of vectors within the shear layer were a result of interpolation, indicating the high-quality nature of the PIV velocity fields.

3. Effect of Reynolds Number

Before discussing the complex 3D structure of the flow field, we explore the possibility of Re dependence for the idealized crater model across the range of Re achievable in the flow facility. To this end, the incoming turbulent boundary layers are first characterized at various Re, and their structural differences are discussed. Any Re effects on the flow perturbed by the presence of the crater are then explored by comparing profiles of mean velocity and turbulence statistics obtained at fixed streamwise positions around the crater at different Re.

Characteristics of the incoming turbulent boundary layers at the four measured Re were assessed by acquiring data in the absence of the crater models, hereafter referred to as smooth-wall flow. These measurements were conducted at free-stream velocities in the range $0.25 \leq U_\infty \leq 0.97$ m/s (corresponding to $12,000 \leq Re_\delta \leq 50,000$), as reported in Table 1. Figure 4 presents profiles of the smooth-wall mean streamwise velocity, scaled in inner units (i.e., $y^+ = yu_\tau/\nu$ and $U^+ = U/u_\tau$); the primary boundary layer parameters are reported in Tables 1 and 2. Here, the friction velocity u_τ was obtained using the fitting method proposed by Chauhan et al. [27], who established a composite boundary layer mean velocity profile defined by the sum of an inner profile and a wake function. The profiles were parameterized by u_τ, δ, and a wake parameter Π that were determined via linear regression. Leveraging 95% confidence intervals [28], these estimates of δ and u_τ have associated uncertainties of approximately ±3% and ±0.2%, respectively. This former variability, along with the free-stream turbulence levels, slightly favorable pressure gradient in the RIM facility, and trip used to regularize the boundary-layer transition to turbulence, together account for the slight irregularities noted in δ over the Re measured.

For reference, the red dashed line in Figure 4 represents the logarithmic law given by $U^+ = \frac{1}{\kappa}\log(y^+) + B$, which typically resides in the range $100 \lesssim y^+ \lesssim 0.2\delta^+$ (where $\kappa = 0.384$ and $B = 4.17$ as in [27]). While the three higher Re cases display a clear log region of increasing extent with Re (indicative of the growing range of scales from small to large with increasing Re), the $Re_\tau = 540$ case is devoid of a log layer, as the upper limit for this case is $y^+ = 101$, which aligns with the lower of the log layer ($y^+ = 100$). As such, there is limited separation of turbulent spatial scales between the smaller and larger scales for this case. In contrast, for the three higher Re cases, each reflects a well-defined log region of increasing extent with Re, consistent with an increasing separation between the smaller and larger flow scales with Re. These results therefore suggest that, while all four boundary layers are turbulent, the lowest Re tested is nearly devoid of a log layer, which implies a minimal inertial subrange in the velocity spectra, and therefore weak separation at best between the smaller and larger flow scales.

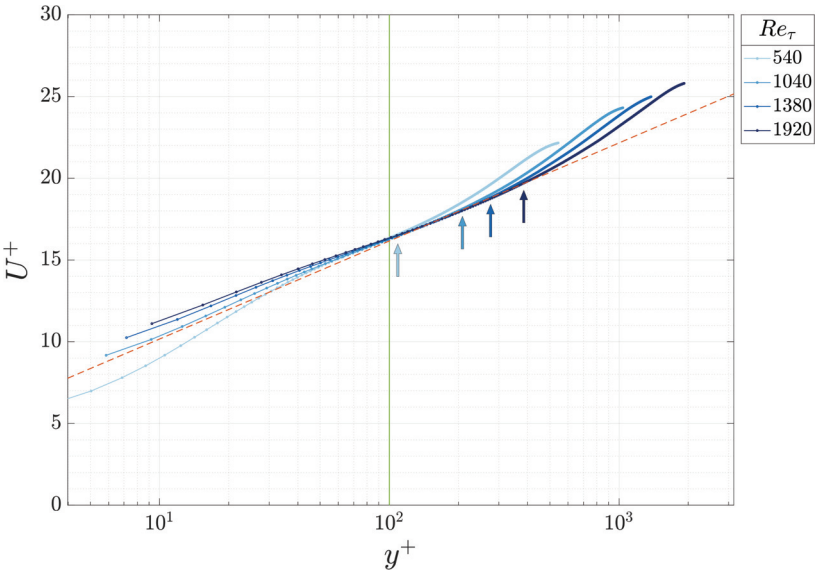

Figure 4. Profiles of the incoming mean streamwise velocity scaled in inner units, U^+, for four different Re_τ. The red dashed line is the log law curve, $U^+ = \frac{1}{\kappa}\log(y^+) + B$, with $\kappa = 0.384$ and $B = 4.17$ [27]. The vertical arrows demarcate the $y^+ = 0.2Re_\tau$ outer edges of the log layers for the correspondingly colored profiles, whereas the green vertical line demarcates the inner boundary of the log layer at $y^+ = 100$.

Differences are also noted in the near-wall region, where these profiles should display universality. These differences are artifacts related to the limited spatial resolution of the measurements. PIV interrogation windows are fixed in physical units and the interrogation window size is limited by particle seeding density, which was kept constant for all experiments. Near-wall scales become smaller with *Re*, as reflected in a reduced y_* with *Re*. As such, a growing mean velocity gradient exists within a fixed interrogation window size for increasing *Re*. For that reason, the near-wall velocity gradient cannot be accurately captured within the PIV interrogation windows, resulting in an overestimation of the mean velocity with increasing *Re*, as noted in Figure 4. While these measurement limitations impeded full characterization of the very near-wall behavior of the incoming boundary layer (i.e., within 1 mm of the wall), they did not impede documentation of flow around the crater, as this was dominated by motions that scaled with the crater dimensions (i.e., over ten times larger than this very near-wall flow).

The dependence of the mean flow field around the idealized crater on *Re* was studied at the four aforementioned *Re* conditions by comparing velocity profiles at fixed streamwise locations. For brevity, comparisons of wall-normal profiles at the crater centerline ($z/H = 0$) are presented at four streamwise locations (see Figure 5a). These streamwise positions were chosen to capture a representative range of intracrater and extracrater flow patterns, and for consistency, will be used for all of the wall-normal profiles shown herein. Figure 5b,c illustrates wall-normal profiles of the mean streamwise and wall-normal velocity components normalized by U_∞. The horizontal dashed lines demarcate the elevations of the crater surface at the corresponding measurement locations. Here we focus the discussion on the similarities between the profiles at different *Re*, and a more detailed discussion of the physics suggested by these data is forthcoming.

Overall, the profiles at different *Re* compare well, particularly for the three highest *Re* in both the streamwise (Figure 5b) and wall-normal (Figure 5c) mean velocity components. However, the lowest *Re* deviates from these trends in both components, indicating perhaps

that the lower level of turbulence maturity of the incoming turbulent boundary layer for this *Re*, as previously discussed, may have been responsible for the observed disparities.

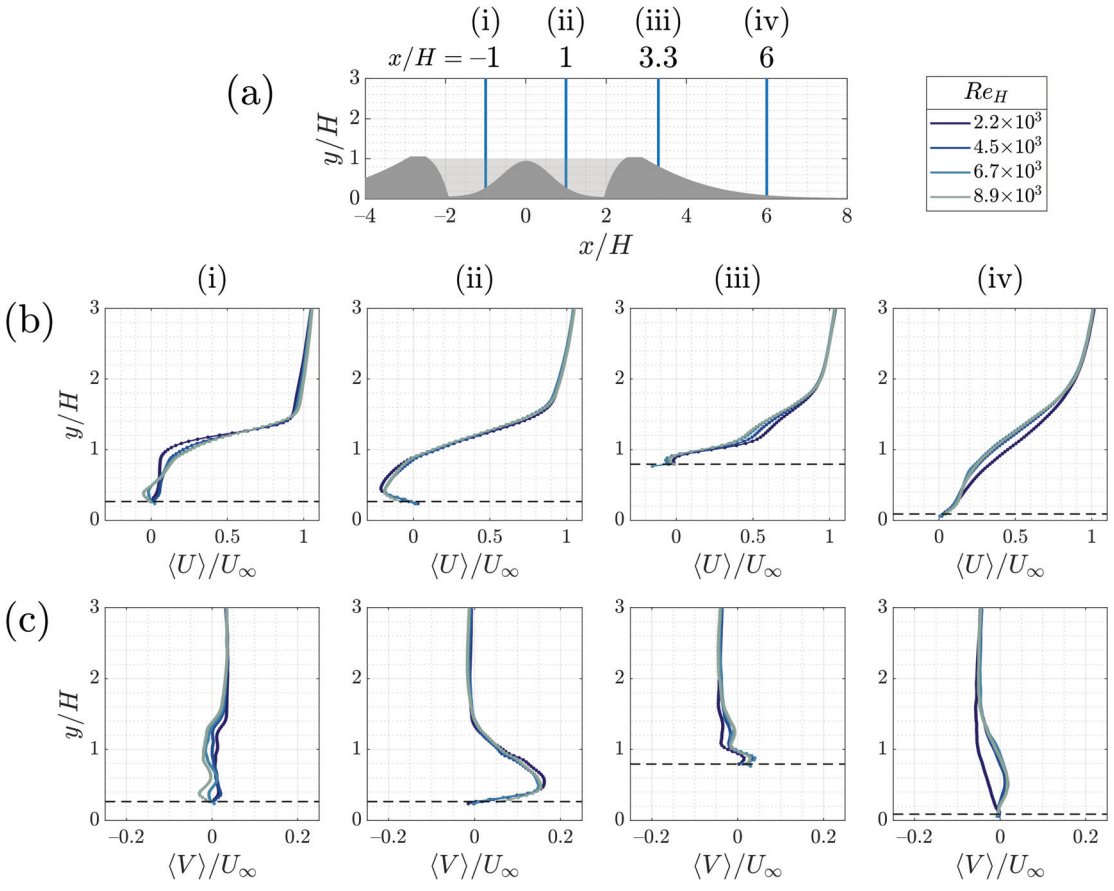

Figure 5. Profiles of normalized mean velocity components along the crater centerline for four different *Re*. Data are normalized by the free-stream velocity, U_∞. (**a**) A reference of the streamwise locations of the profiles. The four streamwise locations from which data were extracted: $x/H =$ (**i**) -1, (**ii**) 1, (**iii**) 3.3, and (**iv**) 6; (**b**) streamwise component, $\langle U\rangle$; (**c**) wall-normal component, $\langle V\rangle$. The horizontal dashed lines in (**b**,**c**) demarcate the elevations of the model's surface at the corresponding $x/H =$ profile locations.

Normalized wall-normal profiles of turbulent stresses for the same *Re* cases and locations are shown in Figure 6. Again, normalization with U_∞ seems to produce a reasonable collapse with the exception of the low-*Re* case, which shows a slightly larger departure than that observed in the mean velocities. Qualitatively, all profiles show the existence of a shear layer due to flow separation at the upstream rim. Profiles at (i) $x/H = -1$ show a peak of all turbulent fluctuations just above the rim. At this location, intracrater stresses increase with *Re*. This is particularly evident for the wall-normal Reynolds normal stress, showing a very mild $\langle v'v'\rangle$ peak at $x/H = -1$ (Figure 6c). All peaks increase downstream of the mound at (ii) $x/H = 0$, suggesting that the fluctuations in the original shear layer are amplified by the interaction with the mound. Some *Re* effects are also noted at this location, with the lowest *Re* exhibiting the largest normalized fluctuations. The profiles at (iii) $x/H = 3.3$ are positioned in the near-wake region. Two peaks emerge in all profiles at this location, suggesting an additional flow separation and an interaction between two distinct shear layers, with an increase in magnitude with

Re. Finally, in the far wake, (iv) $x/H = 6$, the double peak disappears and the profiles exhibit a less pronounced peak whose magnitude increases and at a higher elevation with increasing *Re*.

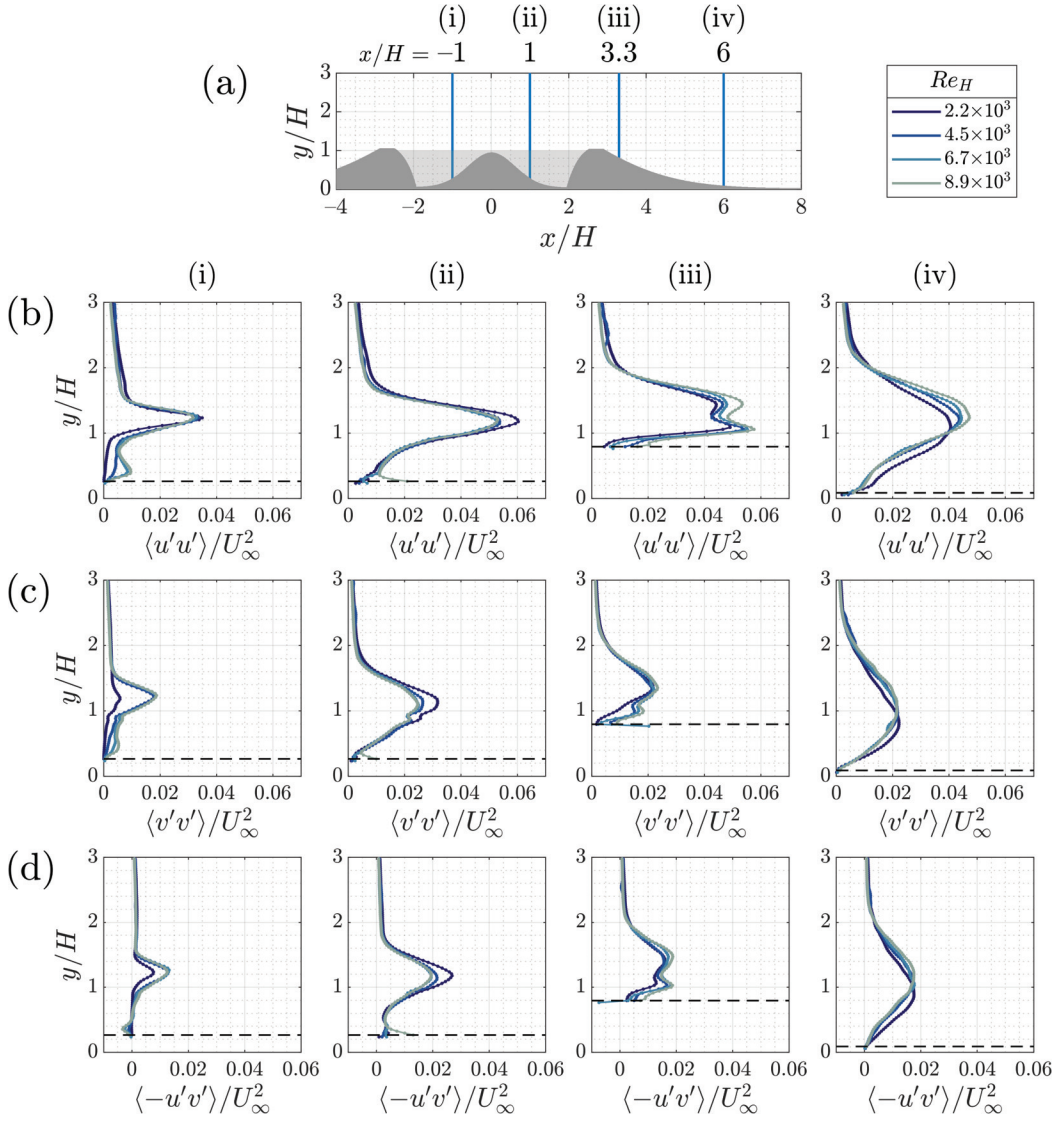

Figure 6. Normalized profiles of Reynolds stresses along the crater centerline for four different *Re*. (**a**) A reference for the streamwise locations of the profiles; (**b**) streamwise stresses, $\langle u'u' \rangle / U_\infty^2$; (**c**) wall-normal stresses, $\langle v'v' \rangle / U_\infty^2$; (**d**) shear stresses, $\langle -u'v' \rangle / U_\infty^2$. The horizontal dashed lines in (**b**,**c**) demarcate the elevations of the model's surface at the corresponding $x/H =$ profile locations.

Dependence on *Re* was also examined in the wall-parallel measurement planes, with a particular interest in any impact on flow three-dimensionality. Here we focus on the measurement plane positioned just above the crater rim (top-plane, $y/H = 1.1$), which is the most influenced by the boundary layer thickness and thus shows the largest disparities. Figure 7 presents spanwise profiles of normalized mean streamwise and spanwise veloc-

ities at the same selected streamwise locations considered above (Figure 7a). While the profiles show qualitative similarities, the comparison shows clear *Re* trends, particularly accentuated at the most upstream location, (i) $x/H = -1$. At this streamwise location, increasing *Re* results in increased momentum along the crater centerline (Figure 7b) accompanied by a stronger lateral flow deflection (Figure 7c). The profiles of $\langle U \rangle$ at all locations embody three local minima, located at the centerline and at $z/H = 2$ and -2 (Figure 7b). With increasing *Re*, these peaks become more pronounced, suggesting that the flow perturbation induced by the crater increases slightly with *Re*. The profiles of the mean spanwise velocity, $\langle W \rangle$, also suggest the existence of a *Re* trend, with higher *Re* inducing increased lateral flow deflections above the crater (Figure 7c).

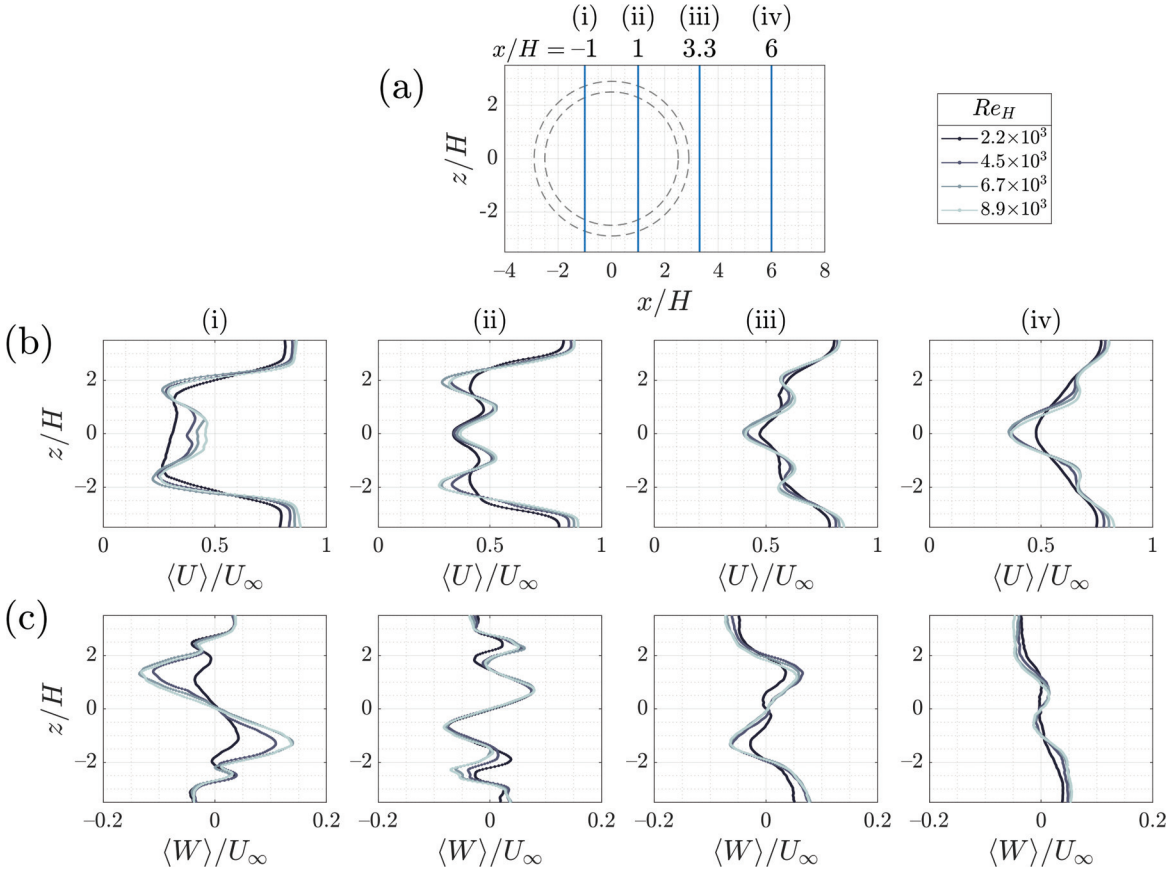

Figure 7. Spanwise profiles of normalized mean velocity components at the top plane ($y/H = 1.1$) for four different *Re*. Data are normalized by the free-stream velocity, U_∞. (**a**) A reference for the streamwise locations of the profiles showing the four streamwise locations from which data were extracted: (**b**) streamwise component, $\langle U \rangle$; (**c**) spanwise component, $\langle W \rangle$.

In summary, these comparisons across the *Re* cases considered suggest some differences among *Re*—most notably, deviations between the lowest *Re* case and the three higher *Re* cases (which match well). The lack of consistency in this regard aligns well with differences noted between the incoming flow at the lowest *Re* and those of the three higher *Re* cases, given the former has virtually no logarithmic layer. This suggests that the weak turbulent scale separation in the incoming boundary layer, found in the lowest *Re* case, may have been responsible for the trends observed. However, our results suggest that this dependence decays with increasing *Re* as the log layer of the incoming turbulent boundary

layer matures and scale separation grows. As such, the remaining results and analysis delving into the flow around mounded craters focus on the highest *Re* results, in an effort to minimize the dissonance between observations in our physical models and the actual flow in full-scale impact craters.

4. Mean Flow Structure

4.1. Flow Topology

Given the 3D structural complexity of the flow under study, a description of the mean flow topology is first explored via critical point analysis. Critical points in a 2D velocity field are defined as locations where both components of the velocity are zero; are classified based on the signs of the real and imaginary components of the eigenvalues λ of the local velocity gradient tensor, $\nabla \mathbf{u}$ [29]; and include foci, nodes, and saddle points. In a two-dimensional flow plane, there are two eigenvalues of the local velocity gradient tensor, yielding two real components, $\lambda_{r1,r2}$, and two imaginary components, $\lambda_{i1,i2}$, along with the property that $\lambda_i = \lambda_{i1} = -\lambda_{i2}$. Foci and nodes are further denoted as either attracting or repelling based upon the signs of the real components. A focus is defined as a critical point where $\lambda_i \neq 0$ and $\lambda_{r1,r2}$ have the same sign and is repelling or attracting if $\lambda_{r1,r2} > 0$ or $\lambda_{r1,r2} < 0$, respectively. A critical point is a node if $\lambda_i = 0$ and $\lambda_{r1,r2}$ have the same sign and is repelling or attracting if $\lambda_{r1,r2} > 0$ or $\lambda_{r1,r2} < 0$, respectively. Lastly, a saddle point is defined as a critical point where $\lambda_i = 0$ and $\lambda_{r1,r2}$ have opposite signs. For additional details on critical point analysis, the reader is referred to Chong et al. [29].

Figure 8 presents the mean flow topology, both identified critical points, and mean streamlines, for the highest *Re* case in both the wall-normal and wall-parallel measurement planes. These results reveal significant complexity in the mean flow structure and indicate a strong three-dimensionality of the flow. This is true particularly within the intracrater space, where several flow features appear and each measurement plane reveals a unique flow pattern.

Let us focus first on the mean flow topology in the wall-normal measurement planes (Figure 8a,b): No reverse flow is observed in the stoss (upstream side) of the crater. This is inconsistent with observations by Greeley et al. [5] who examined the stagnation region of a simple crater and found that reverse flow was tied to sediment deposition. This difference may or may not be associated with the presence of a mound in the current work, as the shape of the leading edge of the crater could also alter this behavior. In this regard, the crater studied herein is more streamlined than that employed by Greeley et al. [5] and thus produced a lower adverse pressure gradient. Further downstream, flow separates both at the upstream and downstream rims along the crater centerline (Figure 8a). The leeside presents no clear signs of a flow reattachment point nor of recirculating flow at the centerline. Instead, a near-wall critical point (found to be a repelling node) is visible at $x/H = 5.3$ on the lee side, from which streamlines emit outwardly (Figure 8a). Within the crater, topological analysis suggests the presence of an unstable focus and a node upstream of the mound, whereas streamlines downstream of the mound reveal an outwardly-directed flow departing from a node located near the surface of the downstream rim (Figure 8a). The centerline topology of the mounded crater is dramatically different from that of simple craters, due to its having dimple-like cavities with either with raised or flat rims [4,22]; simple craters are characterized by a single recirculation cell and a stagnation point on the internal surface of the downstream rim at approximately the same location occupied by the repelling node of the case studied herein.

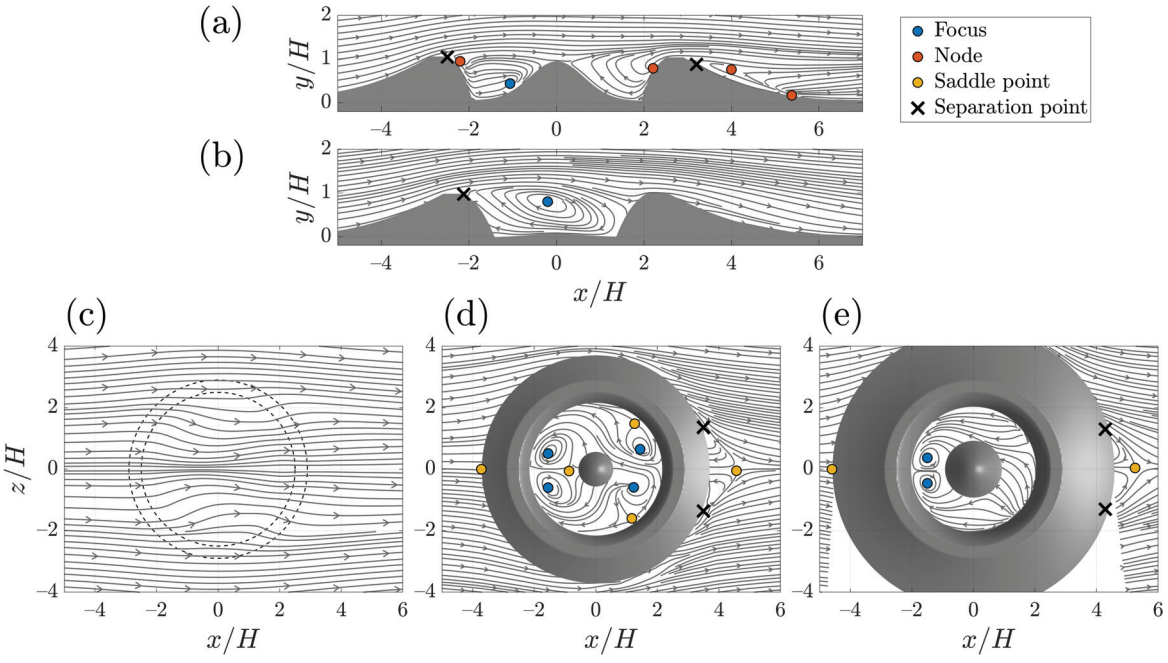

Figure 8. Mean streamlines and distribution of critical points (i.e., $\langle U \rangle = \langle V \rangle = 0$) in different measurement planes calculated using the Chong et al. [29] formulation. (**a**,**b**) Streamwise wall-normal planes; (**c**,**d**) streamwise wall-parallel planes; (**a**) centerline plane, $z/H = 0$; (**b**) offset plane, $z/H = 1.3$; (**c**) top-plane, $y/H = 1.1$ (the location of the crater rim is indicated by the dashed lines for reference); (**d**) mid-plane, $y/H = 0.6$; and (**e**) bottom-plane plane, $y/H = 0.3$. $Re_H = 8.9 \times 10^3$.

The offset wall-normal plane (Figure 8b) exhibits a large region of coherent swirling flow occupying the entire crater interior. This mean-flow vortex is oblate and titled downward, with a focus located at roughly $x/H = 0$, $y/H = 0.8$. Interestingly, the streamlines neither converge nor diverge downstream of this point, classifying it by topological analysis as a "center," which is mathematically defined as a critical point where $\lambda_{r1} = \lambda_{r2} = 0$ and $\lambda_i \neq 0$.

The wall-parallel measurement planes reveal rich flow patterns. While no critical points were detected in the plane above the crater (Figure 8c), the streamlines suggest that the topographic perturbation imparted by the crater on the mean flow extends above its rim. The flow past the upstream rim converges toward the mound, and after passing it, the flow diverges, suggesting a decelerated/accelerated flow sequence devoid of abrupt transitions. Below the rim (Figure 8d,e), the intracrater and extracrater flows are physically separated by the crater wall, and the patterns are dramatically different from the plane above the crater. Outboard of the crater, the mean flow is quite similar. Figure 8d,e reveals a stagnation point upstream of the crater located at the crater centerline, as expected, due to symmetry of the flow. The mean flow then detaches along the lateral sides of the crater at $x/H \approx 3$, which creates a triangular zone of reverse flow in the lee of the crater culminating in a saddle point. This configuration is reminiscent of the leeward shadow zone identified by Greeley et al. [5] as a deposition region for a simple raised-rim crater.

Unlike the extracrater region, mean flow in the crater's interior varies significantly between the two planes examined. In the wall-parallel mid-plane (Figure 8d), four swirling motions with identified foci are noted in the mean flow. Streamlines show that these vortices are symmetric and counter-rotating about the centerline, with the vortices in the first and third quadrants rotating in a clockwise manner, and the vortices in the second and fourth quadrants have counterclockwise rotation. The upstream pair of vortex cells

converges along the centerline and forms a saddle point just upstream of the mound at $x/H = -0.9$. The downstream pair rotates in the opposite direction and instead the flow collides with the lateral sides of the rim interior, resulting in near-surface saddle points. The mean flow in the lower measurement plane at $y/H = 0.3$ (Figure 8e) shows that the upstream pair of vortices penetrates deeper into the crater's interior, whereas the downstream vortex pair leaves an imprint in the form of diverging streamlines.

4.2. Mean Flow

Contours of mean streamwise and wall-normal velocity in the two streamwise–wall-normal planes are shown in Figure 9, with mean streamlines overlaid. Results suggest the typical behavior of a topographically forced flow whereby $\langle U \rangle$ shows decelerated flow upstream [30,31], accelerated flow above the crater, and a momentum deficit in the wake (Figure 9a,b). Likewise, $\langle V \rangle$ features an upward push followed by downward recovery (Figure 9c,d). While the crater depression does not alter this overall pattern significantly, it introduces distinct features that are worth noting. First, a complex afterbody region (i.e., low momentum region bounded by the shear layer) forms, involving both the intracrater region and the lee of the crater. This feature sets a raised rim crater apart from simple topographies such as hills and bedforms in which the afterbody develops only on the lee side. Moreover, unlike rimless craters and dimples, in which wall-normal momentum is induced by shear layer instabilities, here vertical flow is instead topographically induced by the rim and mound.

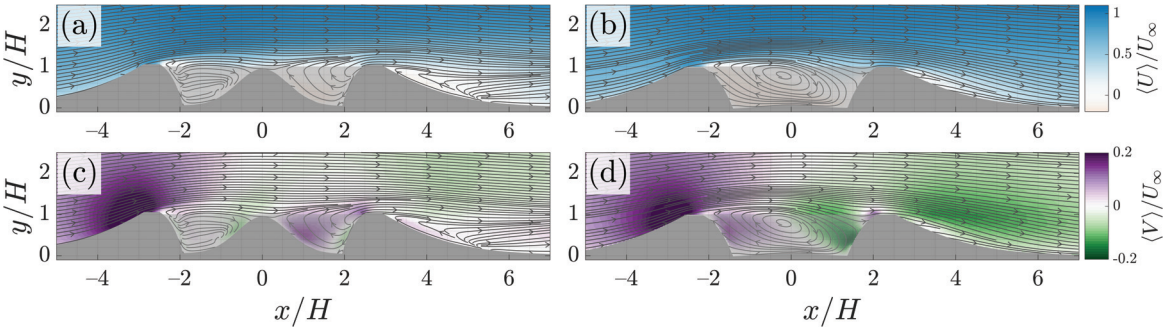

Figure 9. Contours of in-plane mean: (**a**,**b**) streamwise, $\langle U \rangle$, and (**c**,**d**) wall-normal, $\langle V \rangle$, velocity normalized by free-stream velocity U_∞ in the (**a**,**c**) centerline, $z/H = 0$, and (**b**,**d**) offset, $z/H = 1.3$, planes. Mean streamlines are overlaid. $Re_H = 8.9 \times 10^3$.

Flow is significantly different at the two spanwise measurement locations. While the upwelling flow ($V > 0$) is slightly stronger at the centerline, the downwelling flow ($V < 0$) is significantly stronger at the sides (Figure 9c,d). These results highlight alternating regions of upwelling and downwelling flow within the crater which are key to understanding the interactions between the outer- and intra-crater flow occurring across the shear layer. Finally, a region of upwelling flow appears downstream of the reattachment point in the lee of the crater (Figure 9c). This region of positive $\langle V \rangle$ is contrasted by a region of negative $\langle V \rangle$ of larger magnitude in the wall-normal offset plane (Figure 9d). This shift in sign is indicative of a secondary motion in the wake, consistent with the action of quasi-streamwise vortices emanating downstream from the crater sides as proposed by Greeley et al. [5].

Figure 10 presents the distribution of mean streamwise, $\langle U \rangle$, and spanwise, $\langle W \rangle$, velocity components in the three different wall-parallel planes with mean streamlines overlaid. The mean velocity distribution is symmetric about the centerline for $\langle U \rangle$ and asymmetric in $\langle W \rangle$. Therefore, only the top half (i.e., $z > 0$) of the measurement domain is shown. Results are described starting from the plane located just above the crater rim ($y/H = 1.1$), as shown in Figure 10e,f.

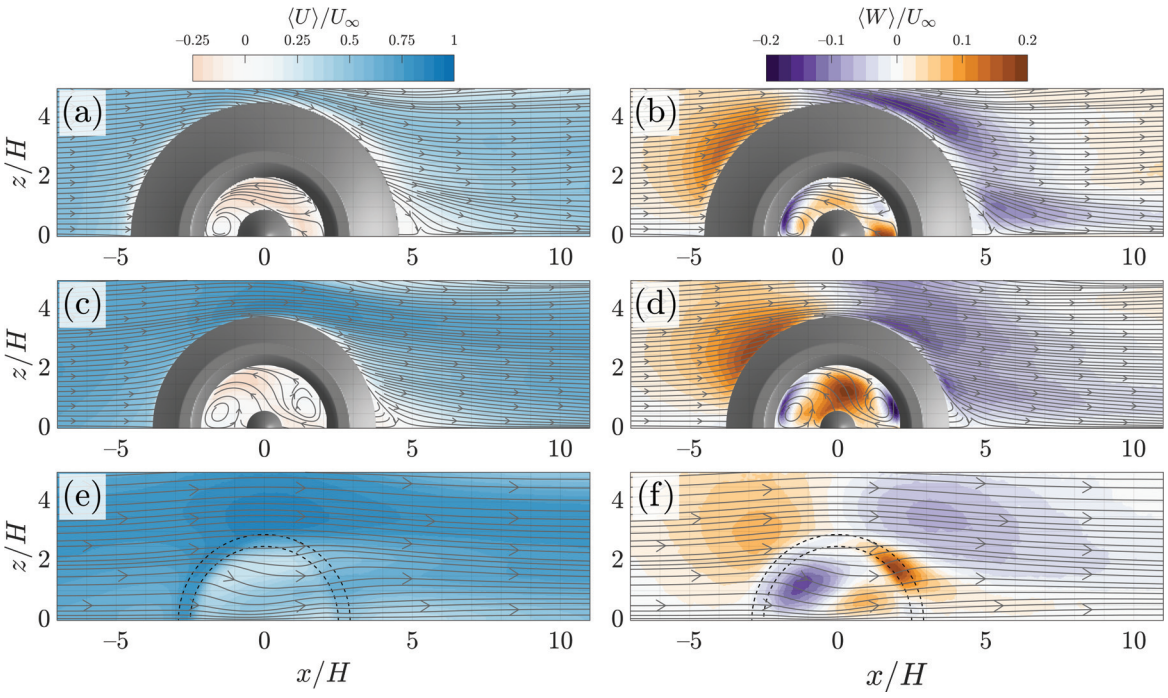

Figure 10. Contours of normalized $\langle U \rangle$ (**left**) and $\langle W \rangle$ (**right**) on the wall-parallel measurement planes located at (**a**,**b**) $y/H = 0.3$, (**c**,**d**) $y/H = 0.6$, and (**e**,**f**) $y/H = 1.1$. The location of the crater rim is indicated by the dashed lines for reference. $Re_H = 8.9 \times 10^3$.

The mean streamwise velocity (Figure 10e) around the crater rim shows a slight deceleration of the flow approaching the crater, an acceleration along the crater's sides, and a slight momentum deficit in the crater's wake displaying an elongated pattern concentrated at the spanwise centerline and ranging from about $x/H = 0$ to $x/H = 8$. The flow just above the intracrater region shows a crescentic region of momentum deficit along the flanks of the crater rim. The values of $\langle W \rangle$ in Figure 10f quantify the lateral deflection induced by the crater, which is entirely beneath this measurement plane. Results show that the extracrater flow is first deflected laterally outward and then laterally inward, as expected. The $\langle W \rangle$ distribution just above the intracrater region, though less obvious, shows a more complex behavior. There exist three distinct pockets of elevated magnitude of $\langle W \rangle$ within the bounds of the crater rim. First, the flow converges laterally inwards (i.e., $\langle W \rangle < 0$), toward the mound peak at $x = 0$. Downstream of the mound, $x > 0$, the flow is directed laterally outwards ($\langle W \rangle > 0$). Finally, this lateral outward motion is enhanced above the downstream rim.

For the mid-plane at $y/H = 0.6$ (Figure 10c,d), the flow outside and inside the crater are physically separated. The flow outside the crater displays essentially the same patterns as noted in the higher elevation plane, but with increased magnitude in $\langle W \rangle$. In contrast, the flow within the crater is more complex and characterized by the recirculation regions previously identified in the topological analysis. These results quantify the magnitude of the motion indicated by the streamlines and reveal that the reverse flow inside the crater is elevated, particularly near the crater floor (Figure 10a). The mound seems to induce a lateral deflection of this reverse flow that prevents the formation of the two large recirculation regions often seen in dimples [22]. Instead, these cells split and form two counter-rotating cells near the upstream rim that persist near the crater floor.

4.3. Turbulent Stresses

Contours of the in-plane Reynolds normal ($\langle u'u' \rangle$ and $\langle v'v' \rangle$) and shear ($\langle -u'v' \rangle$) stresses in the wall-normal centerline and spanwise offset planes are shown in Figure 11. The shear layer, identified by regions with elevated $\langle -u'v' \rangle$, is clearly three-dimensional as indicated by the distinct patterns noted at the different spanwise measurement planes [32]. Along the crater centerline, the shear layer, which first forms due to flow separation from the upstream rim, grows in strength and thickness with downstream distance. The presence of the mound appears to alter the evolution of the shear layer at the centerline, principally by amplifying the turbulent fluctuations and its growth rate. The shear layer eventually reaches the downstream rim at $x/H = 2.5$. The lower portion of the shear layer impinges into the inner crater wall, and the upper portion interacts with another shear layer formed from the crest of the downstream rim. The crater's turbulent wake thus results from the interaction between multiple shear layers. The main orientation of the wake at the centerline is horizontal, which results in a sheltered region in the crater lee side along the centerline with near-zero turbulent fluctuations. In the laterally offset plane, the shear layer does not appear to be significantly influenced by the mound, and $\langle u'u' \rangle$ on the rim interior wall and in the near-wake of the crater is reduced (Figure 11b).

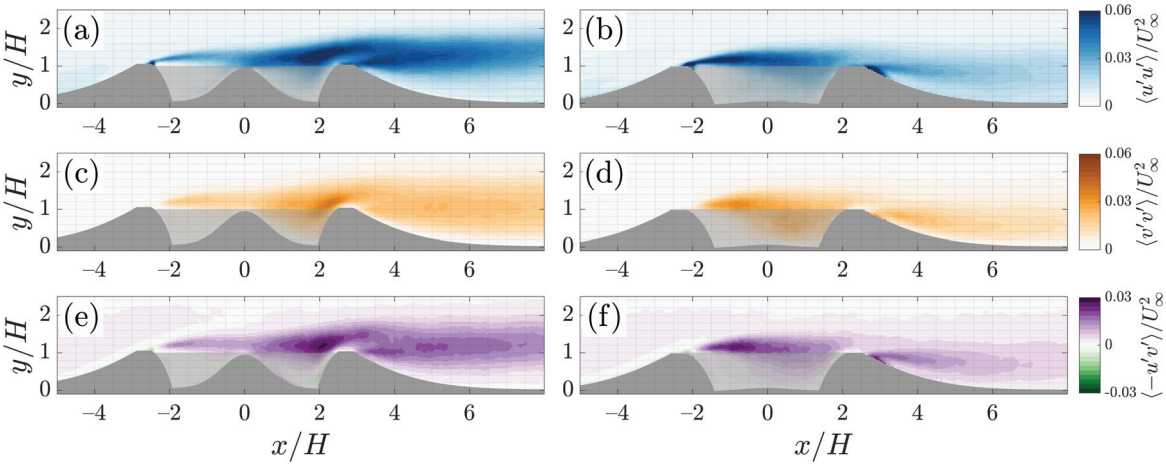

Figure 11. Contours of Reynolds stresses normalized by U_∞^2 at the centerline plane (**left column**) and offset plane (**right column**). (**a**,**b**) $\langle u'u' \rangle$, (**c**,**d**) $\langle v'v' \rangle$, and (**e**,**f**) $\langle -u'v' \rangle$. $Re_H = 8.9 \times 10^3$.

The wall-normal Reynolds normal stresses, $\langle v'v' \rangle$, in the centerline plane (Figure 11c) exhibit a notable peak that occurs near the downstream crater rim and seems to mostly affect the inner area of the wall ($x/H = 2.3$, $y/H = 1.15$). Qualitative comparison of $\langle v'v' \rangle$ in the two measurement planes (Figure 11c,d) suggests that the intensity of the vertical velocity fluctuations is maximal at the centerline. This observation also holds for the Reynolds shear stresses reported in Figure 11e,f, suggesting overall increased turbulent activity at the centerline. Taken together, these results indicate that the peak of wall-normal velocity fluctuations may create a preferential momentum exchange path linking the intracrater flow to the overlying flow. It is reasonable to conjecture that this area is not only associated with intense erosion activity of the inner wall, as previously suggested by Greeley et al. [5], but may also create an escape path for the sediments exhumed from the crater moat, similarly to the upwash mass exchange mechanism described by Zhou et al. [22] for dimple cavities.

A quantitative comparison between the two wall-normal planes is reported in Figure 12, wherein profiles of the in-plane Reynolds stresses at selected streamwise locations are presented. The centerline plane displays larger stress magnitudes at streamwise positions downstream of the mound compared to the laterally offset plane, though this pattern is

reversed upstream of the mound. These results also show that the maxima in the turbulent stresses in the laterally offset plane are located closer to the wall, which is particularly pronounced in the near-wake region. These observations indicate that the turbulent processes flanking the central mound, likely responsible for the erosion of the lateral moat, act more effectively in the erosion of the bottom wall, and that the enhanced turbulent shear layer aligned with the mound may be more responsible for the transport of sediments in suspension being exhumed away from the crater. This interpretation of these results is consistent with previously proposed theories [4,11].

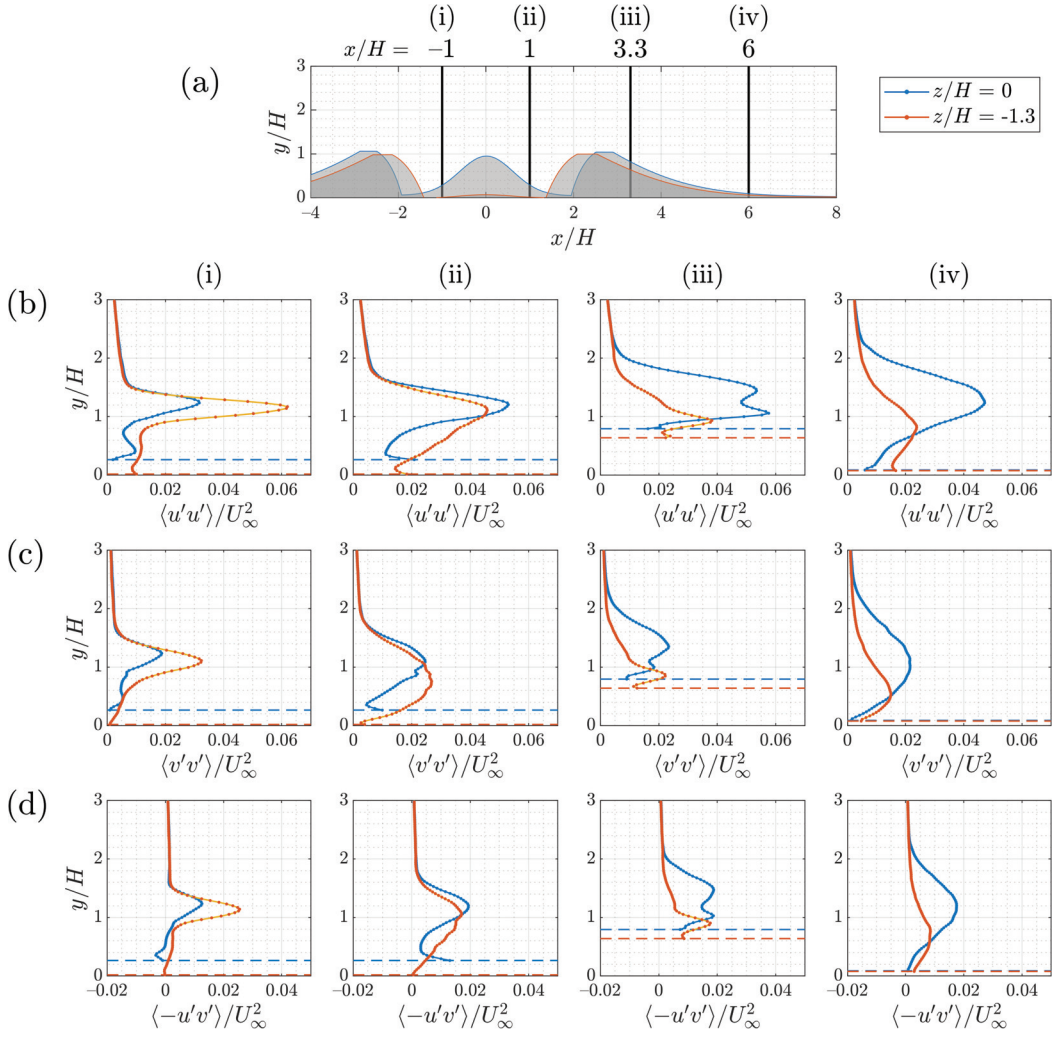

Figure 12. (**a**) A schematic of the crater rim profile at the two spanwise locations showing the reference of the streamwise positions of the profiles. (blue) Centerline plane, $z/H = 0$; (red) offset plane, $z/H = 1.3$. (b-d) Vertical profiles of Reynolds stresses normalized by U_∞^2 at the streamwise locations at $x/H =$ (**i**) −1, (**ii**) 1, (**iii**) 3.3, and (**iv**) 6. (**b**) $\langle u'u' \rangle / U_\infty^2$, (**c**) $\langle v'v' \rangle / U_\infty^2$, and (**d**) $\langle -u'v' \rangle / U_\infty^2$. The dashed lines in (**b**–**d**) demarcate the locations of the model's surface. $Re_H = 8.9 \times 10^3$.

The interaction between shear layers in the same plane is highlighted by the presence of double maxima in the profiles of turbulent stresses in the near wake ($x/H = 3.3$) of the

centerline plane in Figure 12b(iii). These two peaks are located $0.06H$ and $0.44H$ above the surface and are most likely the signature of the interaction between the shear layers originating at the upstream and at the downstream rims. The presence of two peaks begins at the downstream crater rim edge ($x/H = 2.8$) and persists up to $x/H \approx 4.2$. A similar behavior was also observed by Buckles et al. [32] in their study of flow over a surface with sinusoidally varying elevation. In the laterally offset plane at the same streamwise location, there is one clear peak in the Reynolds stresses at $y/H = 0.93$ and an inflection point at $y/H = 1.3$. The inflection point appears to be a signature of the peak in the centerline plane at $y/H = 1.44$ (Figure 12b(iii)).

The sheltered area in the upstream intracrater region is apparent in the attenuated stresses at (ii) $x/H = 1$ in the elevations below the rim height ($y = H$). This sheltered region is mostly absent in the offset plane at the same streamwise location and elevation, which may indicate that the 3D volume of elevated turbulent stresses wraps around the mound in a horseshoe-like pattern. This is further substantiated by the distributions of wall-parallel Reynolds stresses shown in the following section.

Finally, the turbulent stresses persist far downstream of the crater. The maxima of $\langle -u'v' \rangle$ and $\langle v'v' \rangle$ at $10H$ downstream of the rim (not shown herein) are about 85% of the peak value of that at the downstream rim, and 70% for $\langle u'u' \rangle$. The wall-normal position of maximum Reynolds stress in the centerline plane shifts upwards for increasing downstream distance and is particularly pronounced in the $\langle u'u' \rangle$ profiles. This upwards shift of peak stress magnitude following a local maximum in elevation is reminiscent of that observed by Jackson and Hunt [33] in flow over a hill.

The in-plane Reynolds normal stresses in the wall-parallel planes (i.e., $\langle u'u' \rangle$ and $\langle w'w' \rangle$) are symmetric about the crater centerline ($z = 0$), and the in-plane Reynolds shear stress ($\langle -u'w' \rangle$) is anti-symmetric about the centerline. For this reason, only the top half ($z > 0$) of the contours are presented in this section for the mid-plane ($y/H = 0.6$) and the plane sitting just above the crater ($y/H = 1.1$) in Figure 13.

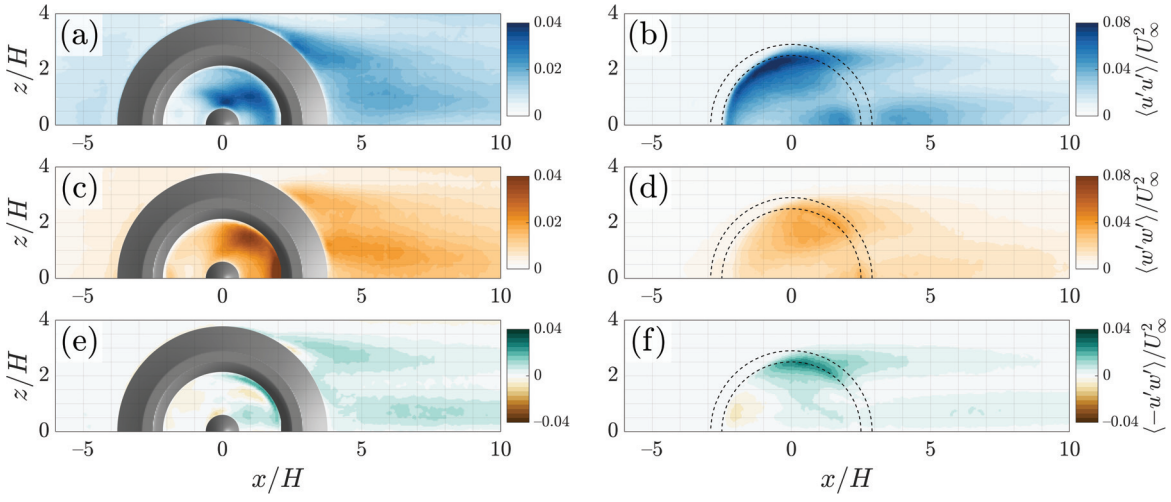

Figure 13. Contours of normalized (**a**,**b**) $\langle u'u' \rangle$, (**c**,**d**) $\langle w'w' \rangle$, and (**e**,**f**) $\langle -u'w' \rangle$ in the wall-parallel measurement planes at (**a**,**c**,**e**) $y/H = 0.6$ and (**b**,**d**,**f**) $y/H = 1.1$. The dashed circles demarcate the location of the crater rim. $Re_H = 8.9 \times 10^3$.

Focusing first on $\langle u'u' \rangle$ inside the crater: Elevated values are noted on the lateral sides of the central mound (Figure 13a). These regions are characterized by intense $\langle u'u' \rangle$ near the inner downstream crater wall and are interpreted as the signature of horseshoe vortices flanking the crater interior and exterior, as previously suggested by Anderson and Day [11]. Likewise, on the exterior of the crater, streaks of enhanced $\langle u'u' \rangle$ emanate from near the point of flow separation. These regions are quite consistent with the bilobate erosional

patterns reported by Greeley et al. [4]. The extracrater streaks surround two additional streamwise elongated regions of relatively high magnitude $\langle u'u' \rangle$ that are aligned with the previously mentioned high stresses within the crater. As such, they may be a residual of the downwashing flow emanating from the central mound.

The spanwise Reynolds normal stress, $\langle w'w' \rangle$, in the mid-plane (Figure 13c), shows three distinct regions of increased magnitude within the crater, all located near the downstream wall. These stresses at the centerline are particularly elevated, confirming that this region is likely exposed to increased erosion and transport of sediments induced by turbulent processes. The spanwise extent of this region is most likely due to flow impinging into the wall surface with a mound-induced spanwise flapping. The elongated shape of this region also suggests that the spanwise fluctuations at the centerline may effectively mobilize sediments supplied by the moat erosion processes towards the centerline, where the vertical velocity fluctuations would provide a lifting mechanism.

Finally, the in-plane Reynolds shear stress, $\langle -u'w' \rangle$ (Figure 13e) reveals the presence of four streaks of elevated magnitude in the wake of the crater, which is consistent with the spatial distribution of $\langle u'u' \rangle$. Adjacent streaks possess the same sign, suggesting that they originate from distinct flow separations. It is conjectured that, while the external layers are produced by separation around the crater rim, the ones closer to the centerline may be produced by a distinct set of secondary flow structures originating from within the crater moat, conceptually consistent with that reported by Anderson and Day [11].

Contours of the in-plane turbulent stresses in the wall-parallel plane just above the crater rim ($y/H = 1.1$; Figure 13b,d,f) reveal that the interior of the crater rim is flanked by areas of elevated magnitudes of $\langle u'u' \rangle$ in a crescent-shaped pattern (Figure 13b) near the rim. Additional streamwise fluctuations are concentrated at the centerline and seem to originate from the mound. These two independent sources of turbulence produce a complex pattern downstream. In contrast, $\langle w'w' \rangle$ and $\langle -u'w' \rangle$ (Figure 13d,f) reveal regions of elevated stresses are present on either side of the mound and slightly downstream of it. The propagation of these stresses downstream is very limited as they seem to dissipate quickly. Secondary regions of $\langle -u'w' \rangle$ are visible at the centerline, near the upstream rim at $z/H \approx \pm 1$, and in the wake of the crater. The latter, in particular, presumably produced by the mound, seem to produce very elongated streaks.

4.4. Turbulence Production

While the results in the previous section reveal complex spatial distributions of turbulent activity, it is of interest to determine the mechanisms of turbulence production. The incompressible, steady-state turbulent kinetic energy equation can be written as [34,35]

$$\underbrace{\overline{u_i}\frac{\partial k}{\partial x_i}}_{\text{Advection}} = -\underbrace{\overline{u_i'u_j'}\frac{\partial U_i}{\partial x_j}}_{\text{Production } P} - \underbrace{\frac{1}{2}\frac{\partial \overline{u_i'u_j'u_j'}}{\partial x_i}}_{\text{Transport } T} + \underbrace{\nu\frac{\partial^2 k}{\partial x_j^2}}_{\text{Diffusion } D} - \underbrace{\frac{1}{\rho}\frac{\partial \overline{u_i'p'}}{\partial x_i}}_{\text{Pressure-gradient } \Pi} - \underbrace{\nu\overline{\frac{\partial u_i'}{\partial x_j}\frac{\partial u_i'}{\partial x_j}}}_{\text{Dissipation } \epsilon}, \quad (1)$$

where k is the turbulence kinetic energy, $\frac{1}{2}\langle u_i u_i \rangle$. The present analysis focuses on the turbulence production term, P. The sign convention used here is such that the production is defined as $P = -\langle u_i'u_j' \rangle \partial U_i/\partial x_j$, for $i, j = 1, 2, 3$, and therefore represents the summative contributions of six independent terms accounting for different combinations of Reynolds stresses and mean velocity gradients. In this context, the production term represents energy transfer to and from the mean flow from and to the turbulence. In particular, $P > 0$ denotes energy transfer from the mean flow to the turbulence and $P < 0$ represents energy lost by the turbulence and gained by the mean flow.

Contours of turbulence production are shown in Figure 14 for the various measurement planes. Since the measurements were conducted with planar, two-component PIV, the out-of-plane components are not included in the summation. As such, the values of P measured herein are surrogates of the total production. This is especially true for the wall-parallel plots in Figure 14c,d, which neglect the wall-normal term that is the dominant

contribution to the total production. For this reason, the surrogate turbulence production values in the wall-normal planes, P_{x-y}, and in the wall-parallel planes, P_{x-z}, were computed from the resolved velocities and velocity gradients in the two measurement plane orientations and are defined as

$$P_{x-y} = -\langle u'u' \rangle \frac{\partial U}{\partial x} - \langle u'v' \rangle \frac{\partial U}{\partial y} - \langle u'v' \rangle \frac{\partial V}{\partial x} - \langle v'v' \rangle \frac{\partial V}{\partial y}, \quad \text{and}$$

$$P_{x-z} = -\langle u'u' \rangle \frac{\partial U}{\partial x} - \langle u'w' \rangle \frac{\partial U}{\partial z} - \langle u'w' \rangle \frac{\partial W}{\partial x} - \langle w'w' \rangle \frac{\partial W}{\partial z}.$$

However, a general picture of the three-dimensional distribution can be inferred by combining the two orthogonal orientations.

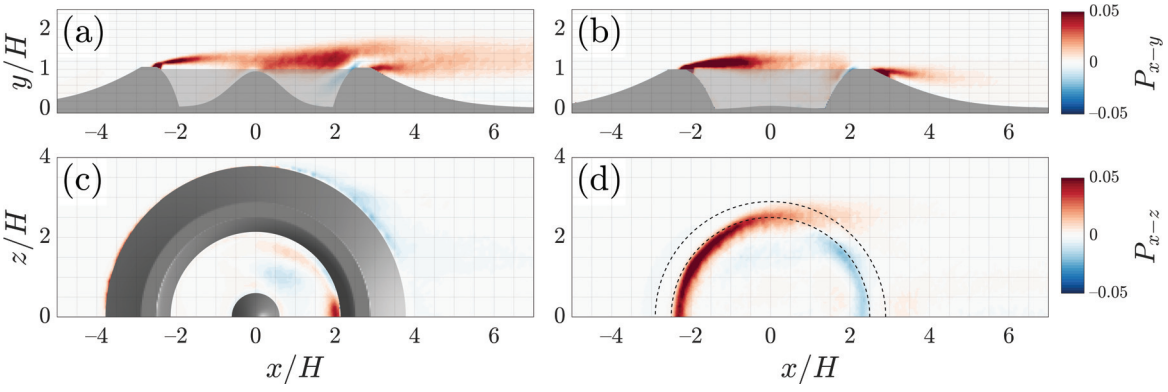

Figure 14. Turbulence production P in the wall-normal measurement planes at (**a**) $z/H = 0$ and (**b**) $z/H = 1.3$, and the wall-parallel planes at (**c**) $y/H = 0.6$ and (**d**) $y/H = 1.1$. Values of P are normalized by U_∞^3/H. $Re_H = 8.9 \times 10^3$.

The $\langle u'v' \rangle \partial U/\partial y$ contribution to the wall-normal production, P_{x-y}, dominates throughout most of the domain, while the $\langle u'v' \rangle \partial V/\partial x$ and $\langle v'v' \rangle \partial V/\partial y$ terms make negligible contributions. The effect of the mound on the flow is more prominent than in the contours of the Reynolds stresses, in that the turbulence production sharply increases at $x/H \approx 0$ in the centerline plane (Figure 14a). The highest values of production are found in the offset wall-normal plane (Figure 14b), in which the peak in production is located just downstream of the rim. The impingement of the shear layer into the interior surface of the rim is also clearly visible in this metric. One region of particular interest is the region of negative turbulence production (i.e., energy transfer from the turbulence to the mean flow) in the centerline plane at the inner wall (at $x/H \approx 2$), near the downstream rim. As seen in Figure 11e, the Reynolds shear stress is near zero in this region. The negative values of P therefore arise from the $\langle u'u' \rangle \partial U/\partial x$ and $\langle v'v' \rangle \partial V/\partial y$ terms, and are found at elevations above and below the rim, respectively. Examination of the wall-parallel planes confirms that turbulence production is negative near the rim at $y/H = 1.1$ (Figure 14d); however, the positive turbulence production, P_{x-z}, in the mid-plane (Figure 14c) at the interior side of the rim offsets the negative P_{x-y} noted in the centerline plane.

The upstream and downstream regions of positive and negative P_{x-z}, respectively, near the rim in the $y/H = 1.1$ plane (Figure 14d) are primarily due to the $\langle u'u' \rangle \partial U/\partial x$ term. The region of positive turbulence production is a combination of high values of $\langle u'u' \rangle$ in the shear layer emanating from the upstream rim and the flow decelerating as it encounters the high-pressure crater interior and thus causing $\partial U/\partial x$ to be negative. The region of negative turbulence production is likely due to flow accelerating over the downstream interior surface that results in $\partial U/\partial x$ being positive. Finally, the $\langle u'v' \rangle \partial U/\partial y$ term accounts for the positive turbulence production noted on the lateral flanks of the rim.

4.5. Flow Rotation

The flow in this study is characterized by multiple recirculation regions and complex flow separations. In order to better understand the nature and origins of these features, the spatial distribution of the rotational component of the flow is examined using a Galilean invariant metric. We computed swirling strength, λ_{ci}, which is derived from the local velocity gradient tensor, $\nabla \mathbf{u}$. In general, this tensor has one real eigenvalue, λ_r, and a pair of complex eigenvalues of the form $\lambda_{cr} \pm i\lambda_{ci}$, where λ_{ci}, the imaginary part of the complex eigenvalue of the velocity gradient tensor, is a scalar quantity. In this context, it only measures the magnitude of the local flow rotation. As the complex eigenvalues only occur as conjugate pairs, the sign of the rotation cannot be discerned directly from λ_{ci}. However, as suggested by Wu and Christensen [36], the sign of the local instantaneous fluctuating vorticity can be assigned to λ_{ci} to provide the rotational sense. For example, the swirling strength in the streamwise–wall-normal plane, wherein rotation is around the z axis, can be defined as

$$\lambda_{ci,z} = \lambda_{ci,z} \frac{\omega_z}{|\omega_z|}. \tag{2}$$

Figure 15 presents contours of the ensemble-averaged swirling strength in the three wall-parallel measurement planes, $\langle \lambda_{ci,y} \rangle$. Four distinct longitudinal streaks of pronounced magnitude can be observed in the wake of the crater in all of the planes. The two upper planes offer a clearer picture of the wake structure and insight into its formation (Figure 15b,c). The streaks in the region $z > 0$ rotate primarily in a clockwise fashion and the streaks in the region $z < 0$ have counterclockwise rotation. Despite having the same rotational sign, streaks on the same side of the crater centerline appear to originate from distinct mechanisms. While the external streak seems to emanate from the rim outer wall, the internal one appears to originate from within the crater, presumably generated by rotational flow induced by separation from the mound.

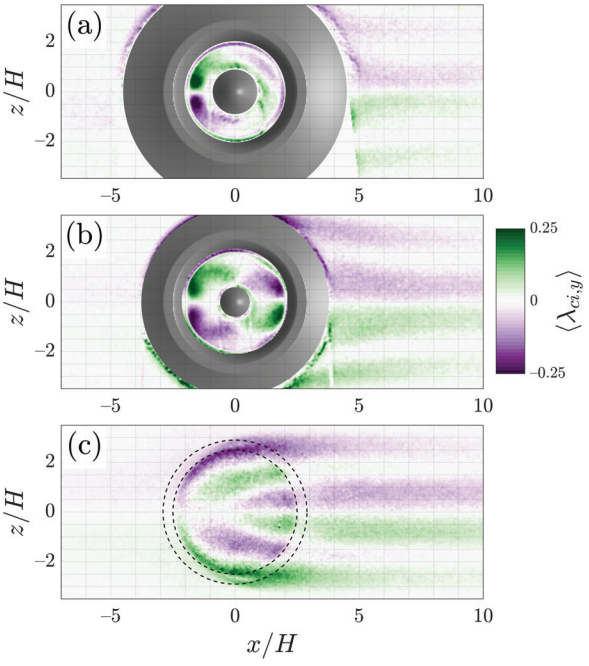

Figure 15. Mean swirling strength $\langle \lambda_{ci,y} \rangle$ in the wall-parallel measurement planes located at (**a**) $y/H = 0.3$, (**b**) $y/H = 0.6$, and (**c**) $y/H = 1.1$. $Re_H = 8.9 \times 10^3$.

Figure 15b quantifies the swirling strength of the four counter-rotating intracrater vortices, previously revealed in the mid-plane by mean flow streamlines (see Figure 8d). In the region above the crater, the upstream recirculation regions stretch into elongated streaks of elevated magnitude of $\langle \lambda_{ci,y} \rangle$ (Figure 15c). Closer to the crater floor, in the $y/H = 0.3$ plane, only the two upstream intracrater vortices are visible (Figure 15a). Taken together, these results suggest that quasi-wall-normal vortices, originating in the upstream portion of the intracrater, are bent into quasi-streamwise structures wrapping around the mound. This 3D arch-shaped structure remains confined within the boundaries of the crater rim. A second 3D arched vortex, with opposite rotational sign, also originates in the downstream portion of the crater due to the presence of the mound. This structure, which also emerges as quasi-vertical and then bends into a quasi-streamwise direction, originates at higher elevation and propagates beyond the crater rim and into the far wake.

Finally, these results offer insights into the link between the near-floor plane (Figure 15a) and the mid-plane (Figure 15b). The positive rotation in the upstream region of the intracrater above the centerline (second quadrant) near the floor wraps around the mound. Some residual positive rotation remains visible in the fourth quadrant (Figure 15a). This pattern suggests that the mound allows the passage of rotational fluid near the crater floor. The rotation reaches the diametrically opposed quadrant and is then amplified, at higher elevations, by the shear separating from the mound which has the same rotational sense.

5. Visualization of Coherent Flow Structures

The turbulent stresses and swirling strength fields presented so far provide a statistical imprint of the distribution of the turbulent vortices that populate the flow. We now consider instantaneous flow fields to identify the nature, scales, and relative locations of individual turbulent vortices. We again turn to swirling strength as a way of identifying instantaneous vortices in the measured flow fields, given its ability to isolate pure rotation in regions of high shear [37]. To aid in identifying larger-scale instantaneous turbulent structures, the instantaneous velocity fields were low-pass filtered using proper orthogonal decomposition (POD). In POD, an optimal set of basis functions are determined that maximize the energy content in the fewest number of modes, with the lowest-order modes being the most energetic and largest in spatial scale, and increasing mode number representing less-energetic and smaller-scale motions. A low-pass filter can be achieved by truncating these modes at a fixed mode number and discarding all remaining modes. As such, reconstruction of velocity fields with the first few POD modes can thus be used to extract and visualize the large-scale motions in the flow [38,39].

Figure 16 presents examples of reconstructed instantaneous flow fields in the wall-normal centerline and laterally offset planes. These results were obtained from POD-filtered velocity fields that embody 50% (left column) and 80% (right column) of the turbulent kinetic energy (TKE). Here, velocity vectors represent the in-plane instantaneous filtered velocity field (only every other vector is plotted to aid visualization) and contours represent the in-plane instantaneous swirling strength, $\lambda_{ci,z}$, to aid in vortex identification. The reconstruction of the velocity field with a higher number of modes (higher TKE cutoff) identifies smaller-scale features with larger magnitudes of $\lambda_{ci,z}$ that are concentrated over smaller regions. It is important to note that, while the identification of smaller-scale features may help with understanding some of the most intricate flow dynamics, these structures likely have second-order effects relative to the larger-scale motions.

In the centerline plane (Figure 16a,b), a trail of vortices, clearly noted as regions of elevated swirling strength magnitude, emanates from the upstream rim. The spacing between the vortices indicates that shedding of these structures occurs in a somewhat periodic fashion. As they move downstream, the vortices become larger and therefore have reduced rotational intensity. The wall-normal position of the vortices varies across the instantaneous velocity fields, indicating that this shear layer may undergo vertical flapping. This mechanism is enhanced downstream of the mound, and in the lee side, presumably due to the interaction between different shear layers. For example, the 80% TKE

reconstruction suggests the entrainment of small turbulent vortices into the downstream intracrater region, impinging into the rim wall. In the offset planes, results show that diffusion and flapping are highly increased right after the shedding from the upstream rim, suggesting enhanced momentum exchange around the mound (Figure 16a,b).

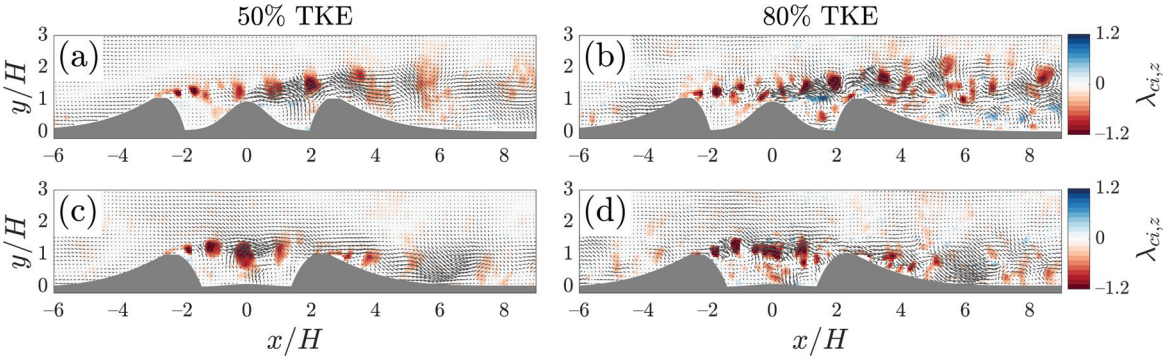

Figure 16. Contours of representative instantaneous spanwise swirling strength, $\lambda_{ci,z}$, for the high-speed case in the (**a**,**b**) centerline wall-normal measurement plane and (**c**,**d**) spanwise offset wall-normal measurement plane. The fields were reconstructed with numbers of modes corresponding to 50% (**left column**) and 80% (**right column**) of the total kinetic energy. Vectors show the corresponding fluctuating velocity components u' and v' at every other grid point. $Re_H = 8.9 \times 10^3$.

Figures 16 and 17 present low-pass filtered instantaneous velocity fields and associated swirling strength in the wall-parallel mid-plane and the plane aloft the rim. These results were obtained from POD-filtered velocity fields that embodied 30% (left column) and 50% (right column) of the TKE, respectively. Vortices with opposite rotational sense (pairs) appear on either side of the crater centerline, $z/H = 0$ (Figure 17a,b). While within the crater vortical pairs have similar streamwise positions, they seem to be offset in the wake, suggesting an alternating shedding mechanism. In the intracrater region, while well-defined recirculation regions appear in the mean flow, the instantaneous flow is marked by multiple vortices (Figure 17a,b). In the upstream portion of the crater, these vortices are concentrated near the inner wall. In the downstream portion of the crater, they are located near the centerline. In the $y/H = 1.1$ plane (Figure 17c,d), vortices can be seen emanating from the lateral sides of the crater surface and from the mound. The latter seem to form a trail of diffusing vortex pairs in the wake near the centerline. In the example reported in Figure 17c,d, pairs of adjacent vortices of opposite signs appear at $x/H \approx 2.5$, and in a lower swirl magnitude at $x/H \approx 6.5$.

The patches of swirling motion in Figures 16 and 17 are reminiscent of the "vortex-loops" that are found in the wake of a wall-mounted hemisphere [40–42]. These structures are occasionally referred to as recirculation arch vortices. The regions of pronounced $\lambda_{ci,z}$ in the offset wall-normal plane (Figure 16c,d) tend to be closer to the wall and be of lesser magnitude compared to those on the centerline plane. Savory and Toy [41] proposed the location of the lateral free shear layer to be centered at the local maxima of $\partial U/\partial z$. Contours of $\partial U/\partial z$ (not shown) display four streaks of pronounced magnitude near the same locations as the streaks in Figure 13e.

Now that instantaneous vortices can be identified in this manner, their occurrence and spatial distributions can be assessed in order to gain insight on their dynamics. We limit our focus to the intracrater region within the wall-parallel measurement planes below the crater rim in an attempt to understand the dynamics of the four-cell recirculation pattern identified previously. To this end, a vortex detection algorithm similar to those used by [43,44] was utilized to isolate in-plane vortices and then pinpoint the locations of the associated vortex cores within each low-pass filtered instantaneous velocity field. The $\lambda_{ci,y}$ fields were calculated using the POD-filtered velocity with a number of modes corresponding to 50% of the TKE. Vortices were defined as regions where $|\lambda_{ci,y}| \geq 1.5\lambda_{ci}^{rms}$,

where the root-mean-square velocity is $\lambda_{ci}^{rms} = \langle(\lambda_{ci} - \langle\lambda_{ci}\rangle)^2\rangle^{1/2}$, where the brackets denote ensemble averaging. The threshold value of $1.5\lambda_{ci}^{rms}$ was chosen based on the value used by Wu and Christensen [36] in their study of prograde and retrograde spanwise vortices in turbulent channel flow. Regions composed of fewer than nine pixels were removed in order to filter out noise in the data. The vortex cores are classified as the locations of the maximum $|\lambda_{ci,y}|$ within each region. Once the vortex locations were cataloged, a probability density was calculated based on their spatial distribution.

Figure 18 presents the probability densities of the instantaneous locations of wall-normal vortex cores with positive rotation in the wall-parallel planes at $y/H = 0.3$ and $y/H = 0.6$. These results show that at $y/H = 0.6$, counter-clockwise vortices form almost exclusively in the 2nd and 4th quadrants. Most vortex cores are detected in the proximity of the inner wall with a smaller number forming near the mound. Vortices form in a broad range of angular locations, between roughly $-45°$ and $0°$ in the fourth quadrant and between $90°$ and $180°$ in the second quadrant. This result suggests that the locations of the vortices in these quadrants undergo lateral oscillations reminiscent of that reported by Turnow et al. [19] for a dimple. At the plane near the crater floor, $y/H = 0.3$, the results show a more intricate scenario. In addition to the second and fourth quadrants, positive vortices also form in the first quadrant. In this latter quadrant, vortex cores appear closer to the mound. These results are consistent with the previous observation in Figure 15a, indicating that the passage of these structures, which leaves an imprint in the mean swirling strength, may represent the bridge between the second and fourth quadrants. This area is associated with reverse flow, which suggests that the wall-normal rotation originates in the fourth quadrant due to flow separation at the mound and is then transferred to the second quadrant through this near-floor passage.

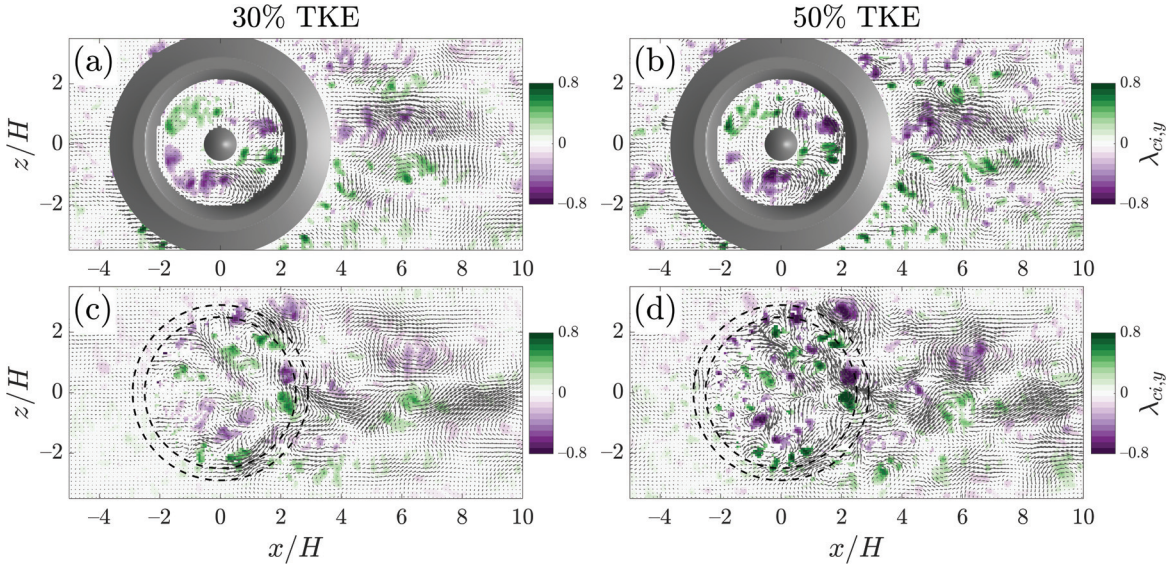

Figure 17. Contours of representative instantaneous wall-normal swirling strength, $\lambda_{ci,y}$, in the wall-parallel measurement planes located at (**a**,**b**) $y/H = 0.6$ and (**c**,**d**) $y/H = 1.1$. The fields were reconstructed with numbers of modes corresponding to 30% (**left column**) and 50% (**right column**) of the TKE. Vectors show the corresponding fluctuating velocity components u' and w' at every other grid point. $Re_H = 8.9 \times 10^3$.

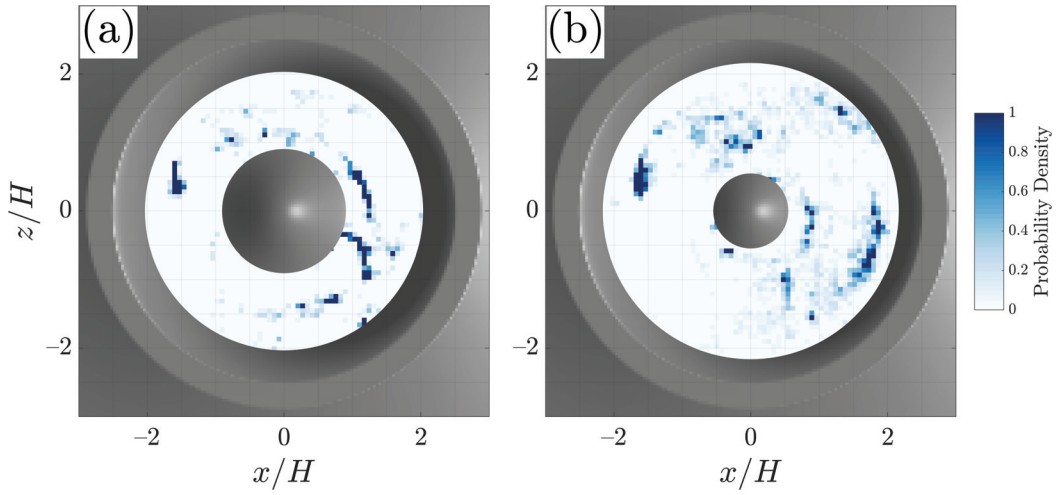

Figure 18. Probability density functions of wall-normal vortex core locations in the wall-parallel measurement planes located at (**a**) $y/H = 0.3$ and (**b**) $y/H = 0.6$. Only wall-normal vortices with positive rotation are counted. $Re_H = 8.9 \times 10^3$.

6. Comparison with Realistic Crater Geometry

While the focus of this study is on a specific idealized crater morphology, we conclude by attempting to provide a comparison with a realistic crater geometry. Doing so, especially in a quantitative manner, is difficult because of obvious geometrical differences. It must also be noted that the boundary conditions chosen for the Gale Crater model are arbitrary. In fact, several assumptions must be made when modeling a real crater. For example, the boundary layer thickness must be estimated based on available data. More importantly, the uncertainty on the incoming flow direction is problematic, which is further complicated by the lack of any topographic symmetry. Moreover, the topography upstream of the crater should be faithfully included in the model to produce the most accurate incoming boundary layer. As such, while the crater orientation was chosen following the literature on dominant synoptic winds, the results presented herein are not expected to faithfully reflect the real scenario. Our study was instead meant to be idealized study of a realistic topography.

The geometries of the idealized and Gale Crater models differed in a few key aspects. First, the aspect ratio of the Gale model, defined here as the ratio between its diameter and rim height, was $D/H \approx 10$, as opposed to $D/H = 5.5$ of the idealized crater. Additionally, the location of Gale's mound was upstream compared to the symmetric geometry of the idealized crater. Finally, the flat surfaces located far upstream and downstream, corresponding respectively to the northern and southern sides, had a $0.5H$ difference in elevation. The primary geometric properties of both models are summarized in Table 3.

Table 3. Geometric properties of the idealized crater model and of Gale Crater model. The abbreviations US and DS refer to the upstream and downstream sides, respectively. All physical units are in mm.

Geometric Parameters	Idealized Crater Model	Gale Crater Model
Diameter	55	87
Rim height	10	4.2 (US), 8.5 (DS)
Mound height	9	7.9
US - DS elevation difference	0	3.0
Aspect ratio (D/H_{rim})	5.5	10.2

Figure 19 presents a side-by-side comparison of the mean flow produced by the idealized crater model at the centerline and that of Gale Crater model at a plane roughly

cutting through the crater's center. Despite the obvious topographical differences and the aforementioned lack of symmetry, the two flows in Figure 19 display some common flow features that are worth highlighting. The streamlines indicate that the flow induced by Gale Crater is qualitatively similar to that of the ideal model, as the models exhibit similar topology and share some critical points, though with different spatial locations. For example, Gale's flow displays three separation points (upstream rim, mound, and downstream rim). However, the strong asymmetry in elevation produces a significantly different flow separation in the upstream crater depression, where a reattachment point and a recirculation region appear. A repelling node resides near the downstream interior surface of Gale Crater, topologically resembling the one discussed for the idealized case. As previously noted, we interpreted this node as the point at which fluid flows from the crater interior to the overlying flow. As such, this point may be the key to understanding the escaping flow paths and the boundary of the erosion region, both of which are important to crater exhumation processes. Finally, both craters exhibit regions of recirculating flow in the crater wake, with Gale's being smaller but more apparent.

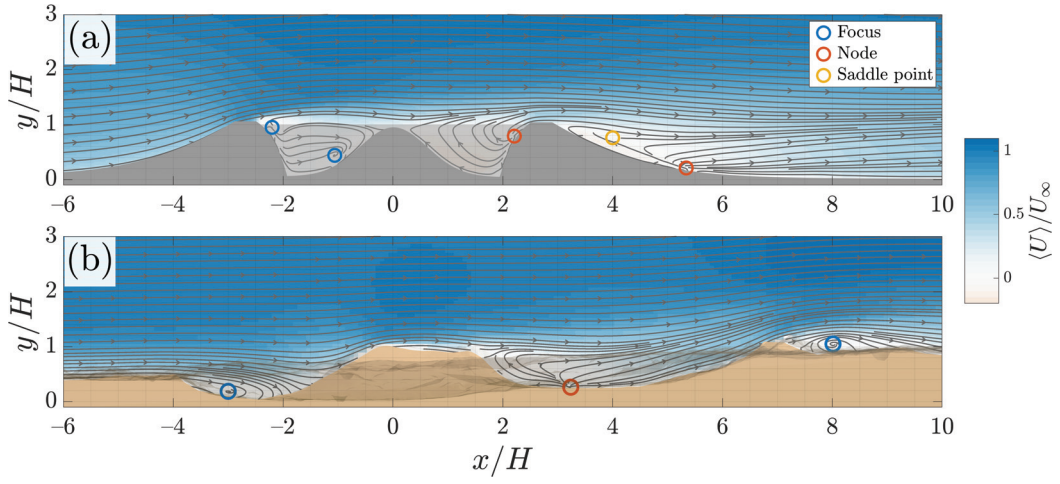

Figure 19. Contours of the in-plane mean streamwise velocity $\langle U \rangle$ normalized by free-stream velocity U_∞ for the (**a**) idealized crater model ($Re_H = 8.9 \times 10^3$) and (**b**) Gale Crater model ($Re_H = 4.6 \times 10^3$). Critical points are also shown in a similar manner as Figure 8.

A comparison of the Reynolds stress component distributions between the idealized crater model and the Gale Crater model is shown in Figure 20. Three distinct shear layers are noted in both cases and formed due to the presence of the two rims and the mound. Of particular interest is the impingement of the shear layer into the downstream internal wall of each crater. First, the distance between the mound and the downstream rim is significantly larger for Gale's model ($x/H \approx 7.5$) than for the ideal model ($x/H \approx 2.5$). This contributes to decreased the stresses on the internal wall, which are located downstream of the peak in stress. Additionally, unlike the idealized case which features rather horizontal shear layers, in the case of Gale, the adverse pressure gradient induced by the downstream interior surface causes the shear layers from the mound to veer upwards, further reducing the potentially erosive impact of this shear layer impingement.

In addition, the lower aspect ratio of the Gale Crater model leads to overall lower Reynolds stress magnitudes compared to the idealized case, as the realistic model obstructs the flow to a lesser degree. As such, the color bar limits in Figure 20 have been adjusted accordingly in order to make clearer comparisons. Finally, Gale's mound protrudes to roughly the same elevation as the downstream rim, similarly to the idealized model where the mound protrudes to an elevation equal to 90% of the rim height. However, due to

the low protruding upstream rim, Reynolds stresses in the upstream intracrater region are reduced and the upstream shear layer impinges into the mound at a lower point (Figure 20b) compared to the idealized case. The implication of this behavior on the flow emanating from the mound is that the two shear layers do not have the same degree of interaction, as observed in the idealized case, where results showed an enhancement of the combined turbulence levels. The lower turbulent stresses' intensity observed for Gale's model may have been, at least in part, due to this lack of interaction.

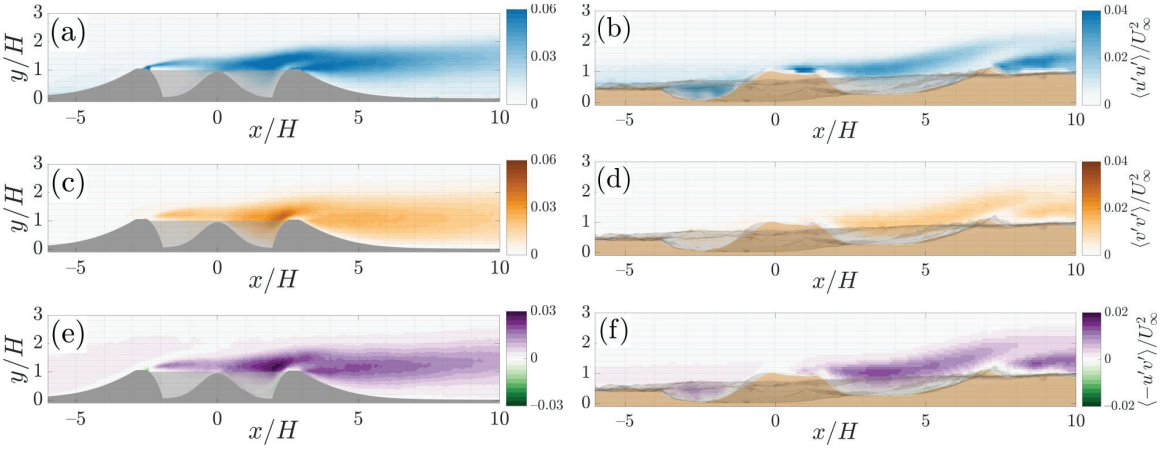

Figure 20. Contours of normalized Reynolds stress components in the idealized (**left**) and Gale Crater models (**right**). (**a**,**b**) $\langle u'u' \rangle$, (**c**,**d**) $\langle v'v' \rangle$, and (**e**,**f**) $\langle -u'v' \rangle$.

7. Discussion

The multi-plane measurement approach used herein has allowed inference as to some of the mechanics and implications of this flow. In particular, the identification of certain flow patterns can help to explain mass and momentum exchange processes across the shear layer, which has implications for heat transfer applications and sediment transport phenomena. Additionally, identification of vortex locations and statistical analysis of the spatial range of occurrence can provide insights into the dynamics of the flow.

7.1. Implications for Mass and Momentum Exchange

Our results suggest that turbulence drives the exchange of fluid across the shear layer by creating preferential mass and momentum exchange paths connecting the intracrater and extracrater flows. We conjecture that the two large spanwise recirculation regions on the sides of the mound entrain fluid from the overlying flow into the crater interior. Fluid enters the crater presumably near the downstream rim, where relatively high levels of vertical mixing are coupled with downward mean flow. The flow acceleration in this region is also likely associated with a pressure unbalance that favors downward flow, similarly to the flow inside a dimple [22]. Entrainment likely occurs periodically following the flapping of the shear layer and the passage of the structures shown in Figure 16d,f. To maintain continuity, the same mass of fluid must be periodically ejected into the overlying flow. Ejection presumably occurs at the crater centerline downstream of the mound, where there exist localized regions of elevated $\langle v'v' \rangle$ (Figure 11c) and upwardly directed mean flow (Figure 9c).

Figure 9c,d indicates that in the region spanning roughly from $x/H = 0$ to $x/H = 2.5$ and near $y = H$, $\langle V \rangle$ is positive in the centerline plane (Figure 9c) and negative in the offset plane (Figure 9c). This suggests that fluid tends to be entrained from the overlying flow in a spanwise-inward fashion and ejected near the symmetry plane. This explanation is corroborated by the mean spanwise velocity $\langle W \rangle$ and streamlines in the wall-parallel

mid-plane (Figure 10d), which show that the flow tends inwards towards the centerline near the downstream inner rim at $x/H = 2.1$. This inwardly concentration of flow (i.e., $\langle W \rangle < 0$) towards the centerline is also found within the recirculation region in the wake of the crater as noted in Figure 10d.

7.2. Implications for Erosion Deposition Patterns

As the present study was performed on fixed crater models with no mobile sediments, no direct conclusions can be drawn as to the morphodynamics implications of these measurements. However, a number of hypotheses can be made based upon similar studies involving deformable craters. Greeley et al. [4,5] performed a number of experimental and numerical studies to understand the morphodynamics of simple craters subjected to unidirectional turbulent winds. Schematics summarizing their primary observations are shown in Figure 21. The arrows in and around the crater in Figure 21a represent the inferred sediment pathways overlaid on the erosion and deposition patterns observed in their work, and Figure 21b presents a conceptual three-dimensional flow model. Some of these qualitative flow patterns are consistent with the mean velocity streamlines in the present results, particularly for the extracrater flow. Large differences are to be expected for the intracrater flow due to the presence of a mound. It should be noted that the *Re* of Greeley et al. [4,5] ($Re_H = 200 - 250$) are an order of magnitude smaller than those studied herein. However, their approach linking flow features to erosion/deposition patterns provides a valuable framework with which to interpret the present results and generate hypotheses on sediment dynamics in the mounded craters considered herein.

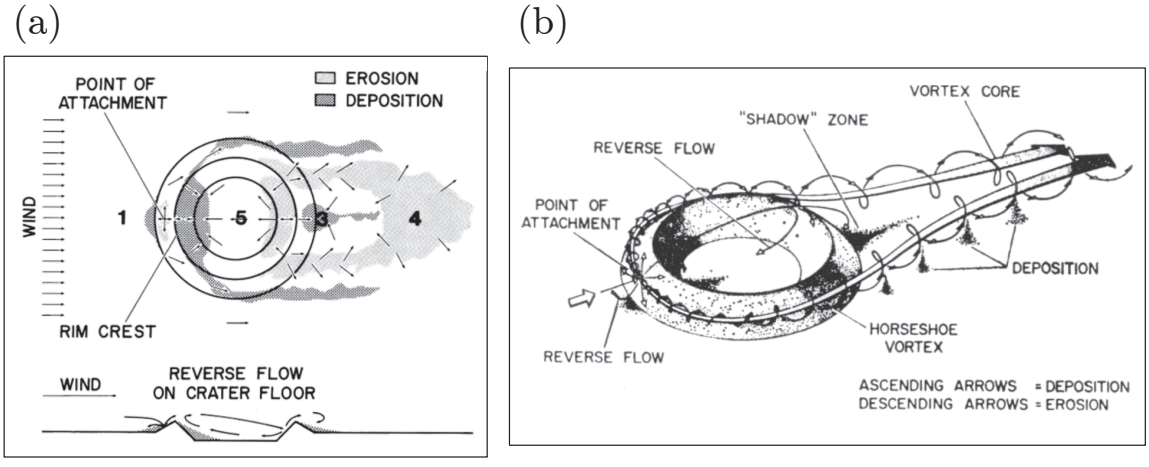

Figure 21. (**a**) Schematic of the direction of sediment movement in and around a raised rim crater [5] (Reproduced with permission from Proceedings of the Royal Society of London. Series A, Mathematical and Physical Sciences, 1974); and (**b**) the proposed flow field over a raised-rim crater, showing the horseshoe vortex and zones of relative erosion and deposition [4] (Reproduced with permission from Proceedings of Science, 1974).

In Zone 1 (as it is demarcated in Figure 21a), a small region of deposition is visible at the toe of the crater. Zone 3 is identified as area of high deposition, and Zone 4 is an area of high erosion. The elevated erosion was conjectured by Greeley et al. [4,5] to be caused by a horseshoe vortex that flanks the crater and converges in Zone 4 (as conceptualized in Figure 21b). Lastly, Zone 5 is located in the intracrater region, with elevated levels of deposition on the upstream surface and erosion on the downstream surface. Overall, we expected Zones 1, 3, and 4 as proposed by Greeley et al. [4,5] to be quite similar for the mounded crater considered herein.

Zone 1 was observed by Greeley et al. [5] to be a low-momentum region characterized by the incoming flow separating and reattaching on the upstream surface of the crater ("attachment point" in Figure 21a) and forming a small spanwise flow recirculation. They proposed that deposition was due to reverse flow produced by the recirculation. The present measurements did not identify a similar complex flow topology upstream of the crater. However, the present results suggest that this region remains favorable to deposition since it is associated with low momentum and low Reynolds stresses. Differences in flow patterns, more likely due to the slope of the crater rim employed than to the presence of the mound, have limited sediment transport implications. Likewise, in the lee side of the crater, upstream of the saddle point, increased deposition can be inferred by the triangular sheltered zone characterized by low Reynolds stresses (Figure 11). In this region, corresponding to Zone 3 as defined by Greeley et al. [5], mean reverse inwardly directly flow is indicated by the streamlines and values of the mean velocity components (Figure 10b,d,f).

The far wake of a mounded crater may be quite different from that reported by Greeley et al. [5] and the behavior observed in Zone 4, owing to the interaction arising in the mounded case between the shear layer produced by the mound and that produced by the rim. Multiple streaks of elevated $\lambda_{ci,y}$ and in-plane Reynolds stresses can be identified in the wall-parallel distributions shown in Figures 13 and 15, respectively. While the lateral streaks, produced by flow separation at the lateral sides of the crater, are common to craters with a devoid of mounds, the central streaks are not. These latter streaks are likely imprints of the shear layers spawned by the mound, as suggested by observation of instantaneous vortices with elevated wall-normal swirling strength emanating from the mound (Figure 17). While the exact morphodynamic implications of these features are unknown at this point, it is reasonable to conjecture that all streaks characterized by elevated Reynolds stresses may be associated with erosional patterns.

Finally, Zone 5 is also likely different due to the mound, which modifies turbulent patterns, and therefore sediment paths. However, many similarities may remain. For example, one of the most compelling conclusions drawn from the present results is that the interior face of the downstream rim of the crater is likely to be a region of erosion, similarly to the simple crater case of Greeley et al. [5]. This conjecture is supported by the elevated Reynolds stresses and turbulence production found in this surface region, likely due to the impingement of the shear layer. First, a localized region of elevated $\langle v'v' \rangle$ is visible in the wall-normal centerline plane (Figure 11c). In addition, a small localized region of high spanwise Reynolds normal stress, $\langle w'w' \rangle$, appears near the downstream rim. The elevated normal stresses in the vertical and lateral directions may be products of the "splatting" effect of flow impinging on the interior rim, in which the flow impinges on the surface and is diverted in opposite directions. In addition to elevated stress levels, there exist elevated values of turbulence production in this region (Figure 14c) as a result of the $-\langle w'w' \rangle \partial W/\partial z$ term, which indicates that the flow impinging into the rim causes large spatial gradients in the spanwise direction in addition to introducing increased levels of turbulence. It is reasonable to expect that, unlike the simple crater case, erosional patterns are extended to the sides of the mound, as suggested by increased Reynolds normal stresses in these areas.

Finally, the upstream interior face of the rim is also believed to be a depositional site, similar to a simple crater. Greeley et al. [5] explained the deposition observed in this area by pointing out the reverse flow induced by the recirculation region illustrated in Figure 21a. In the present case, the formation of similar flow feature is inhibited by the presence of the mound. However, an alternative upward path wrapping around the mound is still formed (see Figure 10a–d). More importantly, this region is characterized by very low turbulent stresses, suggesting that once deposited in this region, sediment is unlikely to be re-mobilized.

7.3. Lateral Oscillation of Intracrater Flow

The offset wall-normal measurement plane presented herein provides insights into the three-dimensional nature of the flow. The mean streamlines within the crater in the $z/H = 1.3$ plane illustrate a large-scale recirculation region within the crater with clockwise rotation. This feature is reminiscent of the flow reported by Isaev et al. [16] in their study of flow around a spherical dimple. These numerical results identified two large-scale vortex cells that are symmetric about the centerline in the detached zone within the crater. This large region of swirling flow has also been suggested in past studies of sediment transport within and around raised-rim craters [4,5]. Greeley et al. [4,5] suggested that within the crater, sediment on the interior side of the downstream surface is carried by reversed flow and deposited on the interior side of the upstream surface, thereby contributing to erosion and deposition on the downstream and upstream rims, respectively.

Liu and Li [45] and Isaev et al. [16] found multiple characteristic flow structures in numerical simulations of flow over a spherical dimple. Among others, they identified counter-rotating vortices in the offset and centerline wall-normal planes, and symmetric and asymmetric "tornado-like" vortices. These findings indicate there are insights to be gained by examining instantaneous swirling strength in addition to the mean flow statistics, as done herein in Figure 17. Using a vortex tracking algorithm, the spatial distribution of vortices within the intracrater wall-parallel planes was assessed and quantified in probability densities of vortex position in Figure 18. The results show that the intracrater vortices vary considerably in their distribution around the intracrater circumference. In particular, the vortices primarily reside within their respective quadrants in the wall-parallel mid-plane (Figure 18b). In the near-wall plane (Figure 18a), the vortices have more spatial coverage and are often located in quadrants outside of their mean locations.

8. Conclusions

An experimental study of flow responding to mounded craters is presented in this paper. Measurements were performed for an idealized crater geometry and for a scaled model of Gale Crater. High-resolution 2D-PIV measurements of flow within and outside each crater model were conducted by rendering the crater models optically invisible in a refractive-index matched flow environment. Data were acquired in multiple planes to assess the three-dimensionality of the flow and at four *Re* based on the crater rim height in the range of $2.3 \times 10^3 \leq Re_H \leq 8.9 \times 10^3$.

The mean flow and associated flow topology for an idealized, mounded crater illustrate the complexity and three-dimensionality of the flow structure, revealing significant structural differences from a simple crater without a mound, particularly within the intracrater space. First, the formation of the spanwise monocore recirculation region observed by Greeley et al. [4] in simple craters is partially prevented in mounded craters by the presence of the mound. Measurements show, instead, a more complex structure where flow in the regions upstream and downstream of the mound presents unique topological features. The offset planes indicate that a portion of the monocore cell exists on the side of the mound. Finally, wall-parallel measurements showed that the two large recirculating cells with quasi-vertical axes are replaced by a more complex structure in which the flow varies dramatically in the vertical direction. Perhaps the most interesting feature was found at the mid-plane and was represented by four counter-rotating recirculating regions that were offset from the centerline in the spanwise direction. Taken together, these results suggest that the mound obstructs the near-floor reverse flow typical of spherical depressions and induces a lateral deflection that results in a distinctive four-cell structure.

Unlike dimples and rimless craters, where vertical mass exchange is mostly induced by turbulent mixing along the shear layer, topographic effects of the protruding rim and mound for the cases examined herein resulted in enhanced and more complex vertical mass fluxes. Turbulence statistics indicated that flow separation processes play a key role in the exchange of momentum and kinetic energy. Separation occurs at multiple locations, resulting in a turbulent mixing layer that is the result of a series of interactions and merg-

ing processes between independent shear layers. This is particularly true at the crater, centerline where the shear layer, originally separating at the upstream rim, undergoes a series of interactions: it first interacts with the flow separated at the mound; subsequently, the merged shear layer impinges on the interior of the downstream crater wall and eventually interacts with the flow emanating from the downstream rim. Consistently with the case of a simple crater, localized regions of elevated turbulent stresses were found on the interior face of the downstream crater wall, both at the centerline and at lateral locations. These observations suggest an extended area of potential erosional activity caused by the shear layer impinging onto this wall. Finally, distributions of Reynolds stresses in the wake of the crater showed longitudinal streaks of elevated magnitude that suggested independent trains of vortices emanating from the side of crater and from the mound. The former is consistent with the horseshoe structure suggested by Greeley et al. [4] for simple raised-rim craters and was presumably responsible for the bilobate erosion patterns observed in their experiments. The implications of the streaks near the centerline, which extended further downstream, are unknown and will require additional investigation.

Analysis of the instantaneous flow fields via POD filtering allowed examination of the the shear layer and allowed us to identify the most energetic turbulent structures. These structures were responsible for most of the transport of momentum, which has implications for relevant phenomena such as transport of sediments and heat. Examples of instantaneous swirling strength fields showcased the spanwise vortices that populate the shear layers. Instantaneous swirling strength fields displayed a periodic trail of vortices, suggesting a consistent shedding mechanism from the upstream crater rim. The results indicated intense vertical flapping of the shear layer associated with vortices emanating from the mound. These vortices traveled along slightly different trajectories. While some vortices convected above the rim, others advected downward towards the interior wall of the crater, transferring their energy into the solid surface and thus presumably driving erosion in this area. Additionally, within the crater rim, probability densities of wall-normal vortex core locations at the mid-plane, identified via conditional averaging analysis, showed that the two pairs of intracrater vortices exhibited lateral oscillations within their respective quadrants, suggesting the occurrence of a low-frequency oscillating mechanism reminiscent of that observed in dimple depressions. The same analysis near the crater floor provided insights into the link between the circulation patterns at different elevations. The results suggested the existence of a path along which rotational fluids from opposite quadrants were transferred. This path, visible at the lower plane, wrapped around the mound, and was associated with a region of reverse flow suggesting that, for example, for $x/H > 0$, the wall-normal rotation originated in the fourth quadrant due to flow separation at the mound and was then transferred to the second quadrant through this near-floor passage.

Finally, experiments were performed on a Gale Crater model to clarify how well the observations from the idealized crater measurements reflect the flow around a realistic crater geometry. The primary flow features in the Gale Crater model closely resembled those of the idealized crater model, including the presence of two critical points within the crater in the form of a focus and a node. Additionally, turbulence statistics revealed that the flow over the Gale model exhibits a similar dynamic of three distinct co-interacting shear layers that are formed due to the presence of the mound, the upstream rim, and the downstream rim. As such, the idealized geometry is a useful analogue to geometries based on real impact craters and can be effectively used to understand the basic mechanics of the flow.

As highlighted in previous studies [46], the crater rim protrusion, the depth of the crater floor, and the height and diameter of the mound are key geometrical parameters that can significantly modify the flow around and within a crater. As such, the results reported herein are directly tied to the specific topographies considered and cannot be extended to craters with different geometries. However, crater idealizations facilitate parametric studies in which the effects of each parameter can be isolated and observed within a

representative range of variability. Such an approach would provide insights into the mechanistic behavior of these flows and their dependence on geometry and classification criteria based on topographic metrics.

Author Contributions: D.G., G.B. and K.T.C. have equally contributed to the development of the present paper, including the conceptualization, methodology, data acquisition and analysis, interpretation of the results, and manuscript preparation. All authors have read and agreed to the published version of the manuscript.

Funding: This research received no external funding.

Conflicts of Interest: The authors declare no conflict of interest.

References

1. Malin, M.C.; Edgett, K.S. Sedimentary rocks of early Mars. *Science* **2000**, *290*, 1927–1937. [CrossRef] [PubMed]
2. Squyres, S.W.; Arvidson, R.E.; Bell, J.; Calef, F.; Clark, B.; Cohen, B.; Crumpler, L.; De Souza, P.; Farrand, W.; Gellert, R.; et al. Ancient impact and aqueous processes at Endeavour Crater, Mars. *Science* **2012**, *336*, 570–576. [CrossRef] [PubMed]
3. Wray, J.J. Gale crater: The Mars Science Laboratory/Curiosity rover landing site. *Int. J. Astrobiol.* **2013**, *12*, 25–38. [CrossRef]
4. Greeley, R.; Iversen, J.D.; Pollack, J.B.; Udovich, N.; White, B. Wind Tunnel Simulations of Light and Dark Streaks on Mars. *Science* **1974**, *183*, 847–849. [CrossRef]
5. Greeley, R.; Iversen, J.; Pollack, J.; Udovich, N.; White, B. Wind tunnel studies of Martian aeolian processes. *Proc. R. Soc. Lond. A Math. Phys. Sci.* **1974**, *341*, 331–360.
6. Bennett, K.A.; Bell, J.F., III. A global survey of Martian central mounds: Central mounds as remnants of previously more extensive large-scale sedimentary deposits. *Icarus* **2016**, *264*, 331–341. [CrossRef]
7. Grotzinger, J.; Gupta, S.; Malin, M.; Rubin, D.; Schieber, J.; Siebach, K.; Sumner, D.; Stack, K.; Vasavada, A.; Arvidson, R.; et al. Deposition, exhumation, and paleoclimate of an ancient lake deposit, Gale crater, Mars. *Science* **2015**, *350*. [CrossRef]
8. Williams, R.M.; Grotzinger, J.P.; Dietrich, W.; Gupta, S.; Sumner, D.; Wiens, R.; Mangold, N.; Malin, M.; Edgett, K.; Maurice, S.; et al. Martian fluvial conglomerates at Gale crater. *Science* **2013**, *340*, 1068–1072. [CrossRef]
9. Kite, E.S.; Lewis, K.W.; Lamb, M.P.; Newman, C.E.; Richardson, M.I. Growth and form of the mound in Gale Crater, Mars: Slope wind enhanced erosion and transport. *Geology* **2013**, *41*, 543–546. [CrossRef]
10. Day, M.; Anderson, W.; Kocurek, G.; Mohrig, D. Carving intracrater layered deposits with wind on Mars. *Geophys. Res. Lett.* **2016**, *43*, 2473–2479. [CrossRef]
11. Anderson, W.; Day, M. Turbulent flow over craters on Mars: Vorticity dynamics reveal aeolian excavation mechanism. *Phys. Rev. E* **2017**, *96*, 043110. [CrossRef]
12. Day, M.; Kocurek, G. Observations of an aeolian landscape: From surface to orbit in Gale Crater. *Icarus* **2016**, *280*, 37–71. [CrossRef]
13. Fonseca, R.M.; Zorzano-Mier, M.P.; Martín-Torres, J. Planetary boundary layer and circulation dynamics at Gale Crater, Mars. *Icarus* **2018**, *302*, 537–559. [CrossRef]
14. Rafkin, S.C.; Pla-Garcia, J.; Kahre, M.; Gomez-Elvira, J.; Hamilton, V.E.; Marín, M.; Navarro, S.; Torres, J.; Vasavada, A. The meteorology of Gale Crater as determined from Rover Environmental Monitoring Station observations and numerical modeling. Part II: Interpretation. *Icarus* **2016**, *280*, 114–138. [CrossRef]
15. Tyler, D., Jr.; Barnes, J. Mesoscale modeling of the circulation in the Gale Crater region: An investigation into the complex forcing of convective boundary layer depths. *Int. J. Mars Sci. Explor.* **2013**, *8*, 58–77.
16. Isaev, S.; Leont'ev, A.; Frolov, D.; Kharchenko, V. Identification of self-organizing structures by the numerical simulation of laminar three-dimensional flow around a crater on a plane by a flow of viscous incompressible fluid. *Tech. Phys. Lett.* **1998**, *24*, 209–211. [CrossRef]
17. Terekhov, V.I.; Kalinina, S.; Mshvidobadze, Y.M. Heat transfer coefficient and aerodynamic resistance on a surface with a single dimple. *J. Enhanc. Heat Transf.* **1997**, *4*, 131–145. [CrossRef]
18. Ligrani, P.; Harrison, J.; Mahmmod, G.; Hill, M. Flow structure due to dimple depressions on a channel surface. *Phys. Fluids* **2001**, *13*, 3442–3451. [CrossRef]
19. Turnow, J.; Kornev, N.; Isaev, S.; Hassel, E. Vortex mechanism of heat transfer enhancement in a channel with spherical and oval dimples. *Heat Mass Transf.* **2011**, *47*, 301–313. [CrossRef]
20. Won, S.Y.; Zhang, Q.; Ligrani, P.M. Comparisons of flow structure above dimpled surfaces with different dimple depths in a channel. *Phys. Fluids* **2005**, *17*, 045105. [CrossRef]
21. Van Nesselrooij, M.; Veldhuis, L.; Van Oudheusden, B.; Schrijer, F. Drag reduction by means of dimpled surfaces in turbulent boundary layers. *Exp. Fluids* **2016**, *57*, 1–14. [CrossRef]
22. Zhou, W.; Rao, Y.; Hu, H. An experimental investigation on the characteristics of turbulent boundary layer flows over a dimpled surface. *J. Fluids Eng.* **2016**, *138*. [CrossRef]
23. Blois, G.; Bristow, N.; Kim, T.; Best, J.; Christensen, K. Novel Environment Enables PIV Measurements of Turbulent Flow around and within Complex Topographies. *J. Hydraul. Eng.* **2020**, *146*, 04020033. [CrossRef]

24. Adrian, R.J.; Westerweel, J. *Particle Image Velocimetry*; Number 30; Cambridge University Press: Cambridge, UK, 2011.
25. Jaumann, R.; Neukum, G.; Behnke, T.; Duxbury, T.C.; Eichentopf, K.; Flohrer, J.; Gasselt, S.; Giese, B.; Gwinner, K.; Hauber, E.; et al. The high-resolution stereo camera (HRSC) experiment on Mars Express: Instrument aspects and experiment conduct from interplanetary cruise through the nominal mission. *Planet. Space Sci.* **2007**, *55*, 928–952. [CrossRef]
26. Westerweel, J.; Scarano, F. Universal outlier detection for PIV data. *Exp. Fluids* **2005**, *39*, 1096–1100. [CrossRef]
27. Chauhan, K.A.; Monkewitz, P.A.; Nagib, H.M. Criteria for assessing experiments in zero pressure gradient boundary layers. *Fluid Dyn. Res.* **2009**, *41*, 021404. [CrossRef]
28. Marusic, I.; Monty, J.P.; Hultmark, M.; Smits, A.J. On the logarithmic region in wall turbulence. *J. Fluid Mech.* **2013**, *716*, R3. [CrossRef]
29. Chong, M.S.; Perry, A.E.; Cantwell, B.J. A general classification of three-dimensional flow fields. *Phys. Fluids A Fluid Dyn.* **1990**, *2*, 765–777. [CrossRef]
30. Blois, G.; Best, J.L.; Sambrook Smith, G.H.; Hardy, R.J. Effect of bed permeability and hyporheic flow on turbulent flow over bed forms. *Geophys. Res. Lett.* **2014**, *41*, 6435–6442. [CrossRef]
31. Bristow, N.; Blois, G.; Best, J.; Christensen, K. Cross-plane Stereo-PIV measurements in a refractive index matched flume of to elucidate the turbulent flow structure over 3D bedforms. In Proceedings of the APS Meeting Abstracts, Denver, CO, USA, 19–21 November 2017.
32. Buckles, J.; Hanratty, T.J.; Adrian, R.J. Turbulent flow over large-amplitude wavy surfaces. *J. Fluid Mech.* **1984**, *140*, 27–44. [CrossRef]
33. Jackson, P.; Hunt, J. Turbulent wind flow over a low hill. *Q. J. R. Meteorol. Soc.* **1975**, *101*, 929–955. [CrossRef]
34. Pope, S.B. *Turbulent Flows*; Cambridge University Press: Cambridge, UK, 2000.
35. Tennekes, H.; Lumley, J.L. *A First Course in Turbulence*; MIT Press: Cambridge, MA, USA, 2018.
36. Wu, Y.; Christensen, K. Population trends of spanwise vortices in wall turbulence. *J. Fluid Mech.* **2006**, *568*, 55–76. [CrossRef]
37. Zhou, J.; Adrian, R.J.; Balachandar, S.; Kendall, T. Mechanisms for generating coherent packets of hairpin vortices in channel flow. *J. Fluid Mech.* **1999**, *387*, 353–396. [CrossRef]
38. Berkooz, G.; Holmes, P.; Lumley, J.L. The proper orthogonal decomposition in the analysis of turbulent flows. *Annu. Rev. Fluid Mech.* **1993**, *25*, 539–575. [CrossRef]
39. Sirovich, L. Turbulence and the dynamics of coherent structures. I. Coherent structures. *Q. Appl. Math.* **1987**, *45*, 561–571. [CrossRef]
40. Savory, E.; Toy, N. Hemisphere and hemisphere-cylinders in turbulent boundary layers. *J. Wind Eng. Ind. Aerodyn.* **1986**, *23*, 345–364. [CrossRef]
41. Savory, E.; Toy, N. The separated shear layers associated with hemispherical bodies in turbulent boundary layers. *J. Wind Eng. Ind. Aerodyn.* **1988**, *28*, 291–300. [CrossRef]
42. Acarlar, M.; Smith, C. A study of hairpin vortices in a laminar boundary layer. Part 1. Hairpin vortices generated by a hemisphere protuberance. *J. Fluid Mech.* **1987**, *175*, 1–41. [CrossRef]
43. Ganapathisubramani, B.; Longmire, E.K.; Marusic, I. Experimental investigation of vortex properties in a turbulent boundary layer. *Phys. Fluids* **2006**, *18*, 055105. [CrossRef]
44. Gao, Q.; Ortiz-Duenas, C.; Longmire, E. Analysis of vortex populations in turbulent wall-bounded flows. *J. Fluid Mech.* **2011**, *678*, 87. [CrossRef]
45. Liu, J.; Li, J. Numerical prediction of flow structure and heat enhancement with different dimple depth. *Appl. Mech. Mater.* **2014**, *574*, 147. [CrossRef]
46. Steele, L.J.; Kite, E.S.; Michaels, T.I. Crater mound formation by wind erosion on Mars. *J. Geophys. Res. Planets* **2018**, *123*, 113–130. [CrossRef]

fluids

MDPI

Article

Direct Numerical Simulation of Sediment Transport in Turbulent Open Channel Flow Using the Lattice Boltzmann Method

Liangquan Hu [1,2,3], Zhiqiang Dong [1,4], Cheng Peng [5,*] and Lian-Ping Wang [1,2,3,*]

[1] Guangdong Provincial Key Laboratory of Turbulence Research and Applications, Center for Complex Flows and Soft Matter Research and Department of Mechanics and Aerospace Engineering, Southern University of Science and Technology, Shenzhen 518055, China; hulq@sustech.edu.cn (L.H.); 11849518@mail.sustech.edu.cn (Z.D.)
[2] Southern Marine Science and Engineering Guangdong Laboratory (Guangzhou), Guangzhou 511458, China
[3] Guangdong-Hong Kong-Macao Joint Laboratory for Data-Driven Fluid Mechanics and Engineering Applications, Southern University of Science and Technology, Shenzhen 518055, China
[4] Harbin Institute of Technology, Harbin 515063, China
[5] Key Laboratory of High Efficiency and Clean Mechanical Manufacture, Ministry of Education, School of Mechanical Engineering, Shandong University, Jinan 250061, China
* Correspondence: pengcheng@sdu.edu.cn (C.P.); wanglp@sustech.edu.cn (L.-P.W.)

Abstract: The lattice Boltzmann method is employed to conduct direct numerical simulations of turbulent open channel flows with the presence of finite-size spherical sediment particles. The uniform particles have a diameter of approximately 18 wall units and a density of $\rho_p = 2.65\rho_f$, where ρ_p and ρ_f are the particle and fluid densities, respectively. Three low particle volume fractions $\phi = 0.11\%$, 0.22%, and 0.44% are used to investigate the particle-turbulence interactions. Simulation results indicate that particles are found to result in a more isotropic distribution of fluid turbulent kinetic energy (TKE) among different velocity components, and a more homogeneous distribution of the fluid TKE in the wall-normal direction. Particles tend to accumulate in the near-wall region due to the settling effect and they preferentially reside in low-speed streaks. The vertical particle volume fraction profiles are self-similar when normalized by the total particle volume fractions. Moreover, several typical transport modes of the sediment particles, such as resuspension, saltation, and rolling, are captured by tracking the trajectories of particles. Finally, the vertical profiles of particle concentration are shown to be consistent with a kinetic model.

Keywords: sediment transport; turbulent open channel flows; direct numerical simulation; lattice Boltzmann method

Citation: Hu, L.; Dong, Z.; Peng, C.; Wang, L.-P., Direct Numerical Simulation of Sediment Transport in Turbulent Open Channel Flow Using the Lattice Boltzmann Method. *Fluids* **2021**, *6*, 217. https://doi.org/10.3390/fluids6060217

Academic Editors: Joseph J. Kuehl, Pengfei Xue and Fabrice Veron

Received: 1 April 2021
Accepted: 4 June 2021
Published: 9 June 2021

1. Introduction

Sediment transport is common in rivers, lakes, estuaries, and seacoasts. In these hydraulic systems, the flow regime is turbulent. Both the dynamics of the sediments and the properties of the turbulent flows could be affected by sediment-turbulence interactions. Therefore, gaining a deeper comprehension of sediment-turbulence interactions can help us better understand the transport phenomenon.

In the past, many experimental measurements were conducted to investigate sediment-turbulence interactions. Rashidi et al. [1] experimentally investigated a Plexiglas rectangular channel with solid particles of various sizes. They found that large particles (with a mean diameter at 1100 µm) increased the Reynolds stress and turbulence intensity, while small particles (with a mean diameter at 120 µm) led to opposite modulations. The particle-fluid interactions in an open channel turbulent boundary layer were explored by Baker and Coletti [2]. The spherical hydrogel particles had a diameter of approximately 9% of the channel depth and were slightly denser than the fluid. Their results showed that the turbulent activities were damped near the wall by the particles; however, in the outer region of

the flow, the sweep and ejection motions of the turbulence were enhanced. Righetti and Romano [3] studied a closed-circuit rectangular Plexiglas open channel with glass spheres ($\rho_p/\rho_f = 2.6$) of two different sizes (mean diameters at 100 µm and 200 µm). They reported that the particle mean streamwise velocity was smaller than its fluid counterpart except for particles that resided very close to the wall. The inception motion of sediment particles (mean diameter ranges from 20.8 mm to 83.2 mm) in a recirculating flume was examined by Dwivedi et al. [4], and their results revealed that the inception was highly correlated with strong sweep flow structures for both shielded and exposed particles.

Besides the experimental studies, numerical simulations of sediment-laden flows also attract increasing attention. In principle, the transport of particles in a fluid flow could be modeled by three approaches: Eulerian method [5], Lagrangian point-particle method [6], and interface-resolved simulation [7]. The Eulerian method treats the particles as a continuum and the particle-fluid interactions are described by drag force correlations. This method fails to fully consider the particle-particle interactions and cannot track the movement of each particle. The Lagrangian point-particle method is applicable to situations where the particle size is much smaller than the Kolmogorov length scale and particles are dilute. This method assumes particles are point masses without volume. Drag force correction models are also needed to account for particle-fluid interactions. The interface-resolved simulation is the only appropriate method when particle sizes are comparable to or larger than the Kolmogorov length scale. This method considers the particle finite-size effect and resolves directly the disturbance flows around each particle. Consequently, the particle-turbulence interactions are fully resolved by the interface-resolved direct numerical simulations (IRDNS).

As one of the first simulations of the IRDNS, Pan and Banerjee [8] investigated a turbulent open channel flow seeded with finite-size particles of different sizes. They found that the ejection-sweep cycles were affected primarily through the suppression of sweeps by the smaller particles and enhancement of sweep activity by the larger particles. Simulations of horizontal open channel flow laden with finite-size heavy particles at a low solid volume fraction were performed by Kidanemariam et al. [9], and their results implied that the particles formed elongated streamwise structures, resembling aligned chains. The results of Ji et al. [10] indicated that the particle movements were closely related to the turbulent events and the protruding bed roughness can undermine the near-wall streaky structures. In the investigations of Yousefi et al. [11], the dynamics of a single sediment particle in a turbulent open channel flow over a fixed porous bed was explored. They reported that particles could resuspend or saltate if the Galileo number Ga was less than 150, while particles tend to only roll on the bed if Ga was greater than 150. Here, the Galileo number is defined as $Ga = \sqrt{(\rho_p/\rho_f - 1)gD^3}/\nu$, where g is the gravitational acceleration, D is the particle diameter, and ν is the fluid kinematic viscosity. Ga is related to the ratio of the particle effective gravity to the viscous force. Derksen et al. [12] studied turbulent open channel flows laden with solid particles. Their results showed that the particle motion was strongly related to the strength of the turbulent fluctuations. Although these previous studies have provided some insight into understanding sediment-turbulence interactions, the problem is still poorly understand, and many questions remain unanswered. For example, how do heavy particles modulate the turbulent flow? How does turbulence affect the dynamics of individual sediment particles near the bed surface? These questions motivate us to conduct the present study.

On the other hand, most of these aforementioned IRDNS of sediment-laden flows are based on directly solving the Navier–Stokes equations. Compared to the conventional N-S solvers, the lattice Boltzmann method (LBM) has bettter flexibility in treating the boundary conditions. Specifically, using the interpolated bounce-back (IBB) schemes to treat the no-slip boundary condition can easily ensure a second-order accuracy, which has been shown to result in more accurate results in particulate flow simulations than the commonly used diffused-interface immersed boundary method (IBM) [13]. This relatively new approach has been convincingly validated and benchmarked in various particle-laden turbulent

flows, such as homogeneous isotropic flows [14], pipe flows [15], and channel flows [16]. In light of these previous studies, we chose the IBB-based LBM as our numerical method to conduct IRDNS to investigate sediment-turbulence interactions in the present study.

The remainder of this paper is organized as follows. Section 2 briefly introduces LBM and its treatments of finite-size particles. In Section 3, simulation settings and code validation are given. The fluid statistics, flow structures, particle statistics, and particle dynamics are analyzed in Section 4. Finally, the major conclusions are recapitulated in Section 5.

2. Numerical Methodology

2.1. Problem Description

In this work, a horizontal turbulent open channel flow seeded with rigid, spherical, and finite-size sediment particles is investigated. As shown in Figure 1, spatial coordinates x, y, and z stand for the streamwise, wall-normal, and spanwise directions, respectively. The channel has a size of $L_x \times L_y \times L_z = 6H \times H \times 2H$, where H is the channel height. Mean flow and gravitational force are directed in the positive x and negative y directions, respectively. Periodic boundary conditions are applied in the streamwise and spanwise directions. A no-slip boundary condition is imposed at the bottom wall ($y = 0$) and free-slip condition [17] is assumed at the top boundary ($y = H$). The friction Reynolds number is set to be $Re_\tau = u_\tau H/\nu = 180$, where $u_\tau = \sqrt{\langle \tau_w \rangle / \rho_f}$ is the wall friction velocity and $\langle \tau_w \rangle$ is the time-averaged wall shear stress.

The normalized diameter of the finite-size sediment particles is $D/H = 0.1$. The particle-to-fluid density ratio is $\rho_p/\rho_f = 2.65$, which is a typical density ratio between sediment and water in reality (i.e., $\rho_p = 2650$ kg/m^3, $\rho_f = 1000$ kg/m^3) [18]. The Shields number is defined as $\Theta = \rho_f u_\tau^2/[(\rho_p - \rho_f)gD]$, indicating the ratio of fluid shear force on the particle to the effective gravitational force. Here we set $\Theta = 0.5$, a value of relevance to sediment transport [19]. A small Shields number implies that particles will settle to the bottom under gravity, and a large Shields number implies that turbulent motion can lift off and suspend particles. In this study, one single-phase case and three sediment-laden cases with different particle volume fractions (i.e., $\phi = 0.11\%$, 0.22%, and 0.44%) are simulated. When sediment volume fractions are high, sediment particles would form a sediment layer on the bottom channel wall and serve as a rough surface. Studies of dense sediment-laden turbulent channel flows have been reported by Ji et al. [10] and Shao et al. [20]. Here we focus on sediment-turbulence interactions with relatively low sediment volume fractions as a supplement of those previous studies. As the driving force per unit volume is fixed in all cases, low sediment volume fractions are chosen to avoid introducing too large attenuation to the turbulent kinetic energy, as reported by Peng et al. [16].

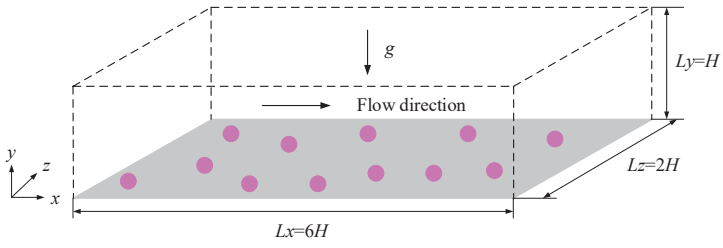

Figure 1. Schematic diagram of the open channel laden with finite-size sediment particles.

2.2. Flow Solver

LBM is applied to conduct DNS of the turbulent open channel flow in the current simulation. Unlike the traditional computational fluid dynamic approaches based on directly solving the continuum N-S equations, LBM solves the evolution of mesoscopic fluid-

particle distribution functions. Following our previous study [13], the multiple-relaxation time (MRT) LBM algorithm is chosen due to its better numerical stability compared to the single-relaxation time (SRT) LBM. The governing equation of MRT-LBM is expressed as:

$$\boldsymbol{f}(\boldsymbol{x}+\boldsymbol{c}_i\Delta t, t+\Delta t) - \boldsymbol{f}(\boldsymbol{x}, t) = -\boldsymbol{M}^{-1}\boldsymbol{S}[\boldsymbol{m}(\boldsymbol{x}, t) - \boldsymbol{m}^{eq}(\boldsymbol{x}, t)] + \boldsymbol{M}^{-1}\boldsymbol{\Psi}, \tag{1}$$

where $\boldsymbol{f}$ is the distribution function, $\boldsymbol{x}$ is the spatial location, $\boldsymbol{c}_i$ represents the discrete velocities, Δt is the time step, $\boldsymbol{M}$ is the transformation matrix that converts the distribution function $\boldsymbol{f}$ from the velocity space to the moment space $\boldsymbol{m}$, namely, $\boldsymbol{m} = \boldsymbol{M}\boldsymbol{f}$, $\boldsymbol{f} = \boldsymbol{M}^{-1}\boldsymbol{m}$, $\boldsymbol{S}$ is a diagonal matrix that contains relaxation parameters, $\boldsymbol{m}^{eq}$ is the equilibrium moments, $\boldsymbol{M}^{-1}\boldsymbol{\Psi}$ represents the effect of external body force, and $\boldsymbol{\Psi}$ denotes the mesoscopic force in the moment space.

The D3Q19 (three-dimensional lattice with 19 discrete velocities) model was most frequently used in the previous studies of particle-laden turbulent flows [14,21]. However, in the present work, the D3Q27 (three-dimensional lattice with 27 discrete velocities) model is adopted because of its better numerical stability [13]. The hydrodynamic variables, such as the local density fluctuation $\delta\rho$, pressure p, and momentum $\rho_0\boldsymbol{u}$, are calculated from the moments of the distribution function $\boldsymbol{f}$, as:

$$\delta\rho = \sum_{i=0}^{26} f_i, \quad p = \delta\rho c_s^2, \quad \rho_0\boldsymbol{u} = \sum_{i=0}^{26} f_i\boldsymbol{c}_i + \frac{1}{2}\boldsymbol{F}\Delta t, \tag{2}$$

where, in the lattice units, $c_s = 1/\sqrt{3}$ is the speed of the sound for the D3Q27 model, ρ_0=1 is the background density, $\boldsymbol{u}$ is the macroscopic fluid velocity, and $\boldsymbol{F}$ is the external body force. More detailed information about the D3Q27 MRT-LBM algorithm can be found in the work of Ref. [13].

2.3. Treatments of Particle Interface

In the LBM framework, the diffused-interface immersed boundary method (DI-IBM) and the interpolated bounce-back (IBB) scheme are two major methods used to treat the no-slip boundary condition on the moving particle surfaces. In general, DI-IBM has first-order accuracy while the IBB scheme has second-order accuracy, but the former usually yields better numerical stability [22].

In this study, the quadratic IBB scheme [23] is chosen as the default algorithm to implement the no-slip boundary condition on the particle surfaces. This scheme can guarantee the velocity field to be a second-order accuracy. The main idea of the IBB scheme is that the unknown distribution functions at boundary grid points are directly constructed based on the known ones, so that the no-slip velocity constraints can be satisfied. In order to handle the quadratic IBB scheme, at least two fluid grid points are needed. In the situations where two particles are very close to each other or a particle moves very close to the channel wall, the number of grid points in the gap becomes insufficient for the quadratic interpolation. When these scenarios occur, the linear IBB scheme [23] and the single-node IBB scheme [24] are used. These two schemes also ensure second-order accuracy in boundary treatment. During the interpolation process, the Galilean invariant momentum exchange method [25] is applied to evaluate the hydrodynamic forces and torques acting on particles. When a particle moves to a new position, some previous solid nodes could turn into fluid nodes, and the distribution functions at these uncovered nodes need to be initialized. In the present simulation, a refilling scheme referred to as "equilibrium distribution + non-equilibrium correction" [26] is adopted. The numerical accuracy and stability of the aforementioned schemes have been validated in several particle-laden turbulent flow problems [13].

2.4. Treatments of Particle Movements

When the gap between two particles, or between a particle and the channel wall, gets very narrow, the hydrodynamic interactions between the two solid objects are no longer

fully resolved. In these circumstances, a lubrication correction model [27] is introduced to handle the unresolved short-range interactions. The expression of the lubrication model is given as:

$$\boldsymbol{F}_{ij} = -6\pi\mu R[\lambda(\epsilon) - \lambda(\epsilon_0)]\boldsymbol{U}_n, \tag{3}$$

where $\boldsymbol{F}_{ij}$ is the lubrication force acting on the ith particle due to the presence of the jth particle, μ is the fluid dynamic viscosity, R is the particle radius, $\epsilon = (\delta - R)/R$ is the ratio of the gap width and the particle radius, δ is the distance between two approaching particles, ϵ_0 is the gap threshold value, and $\boldsymbol{U}_n$ is half of the longitudinal velocity of the ith particle relative to the jth particle. For particle-particle interactions, λ is defined as:

$$\lambda(\epsilon) = \frac{1}{2\epsilon} - \frac{9}{20}ln\epsilon - \frac{3}{56}\epsilon ln\epsilon + 1.346. \tag{4}$$

While for particle-wall interactions, λ is defined as:

$$\lambda(\epsilon) = \frac{1}{\epsilon} - \frac{1}{5}ln\epsilon - \frac{1}{21}\epsilon ln\epsilon + 0.9713. \tag{5}$$

When two solid objects are in physical contact, the soft-sphere collision model [28] is employed to model the collision forces. This model allows particles to have slight overlap and it is intrinsically a spring-dashpot system. The collision force predicted by this soft-sphere model is written as:

$$\boldsymbol{F}_{ssc} = (-k_n\zeta - \beta_n U_n)\boldsymbol{n}_{ij}, \tag{6}$$

$$k_n = \frac{m_e[\pi^2 + (lne_d)^2]}{(N_c\Delta t)^2}, \quad \beta_n = -\frac{2m_e lne_d}{N_c\Delta t}, \tag{7}$$

where $\boldsymbol{F}_{ssc}$ is the contact collision force, k_n is the stiffness parameter, ζ is the overlap distance, β_n is the damping coefficient, U_n is the magnitude of $\boldsymbol{U}_n$, and $\boldsymbol{n}_{ij}$ is the unit vector pointing from the jth particle to the ith particle. m_e is the effective mass involved in the collision, $m_e = 1/(1/m_i + 1/m_j)$ for particle-particle collisions, and $m_e = m$ for particle-wall collisions. e_d is the dry collision coefficient, it is set to be 0.97 [11]. $N_c\Delta t$ is the collision duration and Δt is the flow evolution time step. Here, N_c is set to be 8, it means that the sequence of initial contact, increasing overlap, zero relative motion, decreasing overlap, and end of overlap takes 8 time steps to finish. This implies that the 8 lattice time steps should be small, relative to the lubrication interaction time.

In practice, the lubrication force model and the soft-sphere collision model are implemented in a piecewise manner as follows [27]. When $\epsilon > \epsilon_0$, $\epsilon_0 = 0.125$ for particle-particle collisions and $\epsilon_0 = 0.15$ for particle-wall collisions, no lubrication correction for the hydrodynamic interactions is required. When $\epsilon_1 < \epsilon \leq \epsilon_0$, $\epsilon_1 = 0.001$, Equation (3) is activated. When $0 \leq \epsilon \leq \epsilon_1$, to avoid singularity, the lubrication correction is kept constant using ϵ_1 instead of ϵ in Equation (3). When $\epsilon_2 \leq \epsilon < 0$, $\epsilon_2 = -0.01$, the interaction forces are the combination of those calculated by Equations (3) and (6), whereas ϵ is still replaced by ϵ_1 in Equation (3). Finally, when $\epsilon < \epsilon_2$, the lubrication force becomes relatively weak compared to the contact force, the interaction forces are only evaluated by Equation (6).

After the resolved hydrodynamic force $\boldsymbol{F}_i$, modeled particle-particle/wall interaction forces, and torque $\boldsymbol{T}_i$ acting on the ith particle are obtained, the translational velocity $\boldsymbol{u}_i$, angular velocity $\boldsymbol{\omega}_i$, center position $\boldsymbol{y}_i$, and angular displacement $\boldsymbol{\theta}_i$ of the ith particle are updated as Equations (8)–(11). It should be pointed out that, in order to better resolve the collision process, a smaller particle time step $dt = 0.1\Delta t$ is adopted to update the particle motion with $\boldsymbol{F}_i$ unchanged within Δt,

$$\boldsymbol{u}_i^{t+dt} = \boldsymbol{u}_i^t + \frac{1}{M_p}[\frac{\boldsymbol{F}_i^{t+\Delta t/2} + \boldsymbol{F}_i^{t-\Delta t/2}}{2} + (\boldsymbol{F}_{ij} + \boldsymbol{F}_{ssc} + \boldsymbol{F}_g)^t]dt, \tag{8}$$

$$\boldsymbol{\omega}_i^{t+dt} = \boldsymbol{\omega}_i^t + \frac{1}{I_p}\left(\frac{\boldsymbol{T}_i^{t+\Delta t/2} + \boldsymbol{T}_i^{t-\Delta t/2}}{2}\right)dt, \tag{9}$$

$$\boldsymbol{y}_i^{t+dt} = \boldsymbol{y}_i^t + \frac{1}{2}(\boldsymbol{u}_i^t + \boldsymbol{u}_i^{t+dt})dt, \tag{10}$$

$$\boldsymbol{\theta}_i^{t+dt} = \boldsymbol{\theta}_i^t + \frac{1}{2}(\boldsymbol{\omega}_i^t + \boldsymbol{\omega}_i^{t+dt})dt, \tag{11}$$

where M_p is the particle mass, $I_p = (2/5)M_pR^2$ is the moment of inertia of particle, $\boldsymbol{F}_g = (3/4)\pi R^3(\rho_p - \rho_f)\boldsymbol{g}$ is the effective gravitational force. The contact collision process is numerically integrated over 80 time steps with dt, this ensures that the very stiff contact interaction force changes slowly each dt step, helping to improve numerical stability in treating the multiscale particle-particle or particle-wall interactions involving a large time scale contrast among the resolved hydrodynamic force, the lubrication correction force, and the contact collision force.

3. Simulation Settings and Validation

3.1. Simulation Settings

A uniform mesh of $900 \times 150 \times 300$ is used to discretize the computational domain in the x, y, and z directions, respectively. This grid mesh yields to a grid resolution of $\Delta^+ = \Delta/y_\tau \approx 1.20$, where $y_\tau = \nu/u_\tau$ is the viscous length scale (wall unit). According to the published DNS datasets, at $Re_\tau = 180$, the minimized local Kolmogorov length scale near the channel wall is approximately $\eta^+ \approx 1.5$ [29]. The current grid spacing Δ^+ is smaller than the minimum flow length scale η^+, which indicates that the grid resolution adopted in the present study is reasonably sufficient to resolve the smallest eddy structures in the turbulent flow.

All the investigated cases start with a single-phase, initial laminar flow with a given velocity field [13]. To avoid a long transition from laminar to turbulent regime, a perturbation force is introduced to stir the initial flow [13]. This perturbation force promotes the flow instability and creates vortical structures which further stretch, break, and transfer energy from the mean flow to turbulent fluctuations, and eventually turns the whole flow into turbulent motion. After that, the perturbation force is turned off and a constant driving force is activated to maintain the turbulent flow to the fully developed stage. When the turbulent open channel flow reaches its statistically steady state, the sediment particles are randomly added in the near-wall region with a particle velocity equal to the local fluid velocity. These particles interact with the surrounding fluid and particles until a new two-phase, statistically steady state is achieved.

The single-phase and particle-laden statistics are gathered and averaged along the two homogeneous directions (i.e., streamwise and spanwise directions), over around 20 large eddy turnover times ($20\ H/u_\tau$) after the statistically steady state is reached. In the present study, we mainly focus on two types of statistics. The first type is single-point statistics characterized by the wall-normal distance from the bottom wall. For example, a particle statistic $Q(j)$ of this type is first spatially averaged from the quantity $q^{(n)}(i,j,k)$ at each vertical location j as $Q^{(n)}(j) = \sum_{i=1}^{N_x}\sum_{k=1}^{N_z} q^{(n)}(i,j,k)\psi^{(n)}(i,j,k) / \sum \psi^{(n)}(i,j,k)$, where N_x and N_z are the total grid points in the streamwise and spanwise directions, respectively, and ψ is a phase indicator, which equals to 1 when (i,j,k) at time step n is inside the particle and 0 otherwise. This calculation is conducted for all the 150 j-planes in the wall-normal direction. Afterwards, $Q^n(j)$ is further time-averaged to obtain the final statistic $Q(j)$. The second type is the two-point statistics separated by a specified distance. This is also conditionally averaged in each time frame then time averaged. Throughout the remainder of this paper, we use the bracket $\langle\cdots\rangle$ to denote the first-type statistics and the overline $\overline{\cdots}$ to represent the second-type statistics.

The other notations of the fluid and particle statistics used in this paper is summarized as follows. The subscripts "f"and "p"represent the quantities associated with the fluid and particle phases, respectively. The wall-normal distance from the bottom wall is normalized

by y_τ and shown as y^+, the velocity results are normalized by u_τ and exhibited with the superscript "+". $u^+_{f,rms}/u^+_{p,rms}$, $v^+_{f,rms}/v^+_{p,rms}$, and $w^+_{f,rms}/w^+_{p,rms}$ represent the fluid/particle velocity fluctuation components in the streamwise, wall-normal, and spanwise directions, respectively. Unless otherwise specified, all figures cover the whole channel height from $y^+ = 0$ to $y^+ = 180$.

3.2. Code Validation

The statistical features of the single-phase flow are validated with the reference data of Kidanemariam et al. [9] and Liu et al. [19]. In the study of Kidanemariam et al. [9], the open channel had a size of $L_x \times L_y \times L_z = 12H \times H \times 3H$, and the computational domain was discretized by $3072 \times 257 \times 768$ grid points. The turbulent flow was solved using a finite difference method based on the N-S equations. In the work of Liu et al. [19], the open channel size was $L_x \times L_y \times L_z = 4\pi H \times H \times 2\pi H$, and the computational domain had a grid resolution of $384 \times 64 \times 384$. The turbulent flow was solved by the finite volume method based on the N-S equations.

Figure 2a shows the comparison results of the fluid mean streamwise velocity profiles. It can be seen that the present method predicts the mean streamwise velocity very well. In Figure 2b, the fluid root-mean-square (RMS) velocity fluctuation components are compared. For each component, a general good agreement is found along the whole channel height. However, slight deviations can be captured, in particular concerning the streamwise velocity fluctuation. This is perhaps due to the domain size in the streamwise direction not being long enough. Peng [13] argued that the streamwise velocity fluctuation was more related to the large-scale flow structures, which requires the size of the computational domain to be large enough, hence the contamination from the periodic boundary condition can be avoided.

Overall, reasonable agreements between the present results and the reference data are achieved, which provide evidences for the acceptable accuracy of the developed LBM codes. From now on, the sediment-turbulence interactions will be investigated in detailed in the following sections.

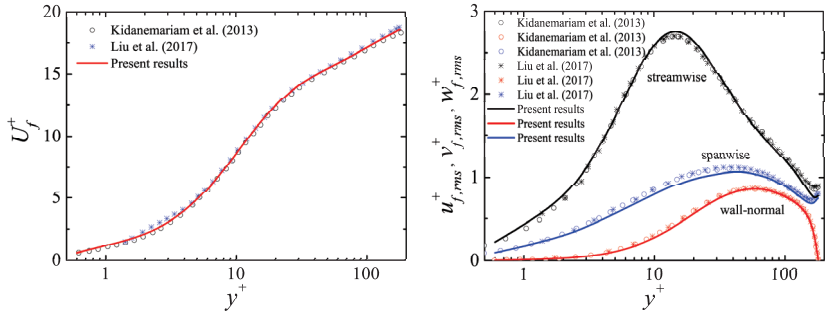

Figure 2. Comparison of results between the single-phase flow and the reference data: (**a**) Fluid mean streamwise velocity and (**b**) fluid root-mean-square (RMS) velocity fluctuation components.

4. Results and Discussion

4.1. Fluid Statistics

Figure 3a shows the fluid mean streamwise velocity profiles from different cases. It is clearly observed that the streamwise velocity is reduced by the presence of particles, which is consistent with the results reported in particle-laden turbulent pipe flows [15] and channel flows [16] with similar settings. Compared to the single-phase flow, domain-averaged velocity reductions of 5.02%, 7.11%, and 9.22% for cases $\phi = 0.11\%$, 0.22%, and 0.44% are found, respectively. Hence, the velocity reduction is more pronounced at a higher

particle volume fraction. It is also seen that all particle-laden cases make the transition from the viscous sublayer to the logarithmic region more gradual. In the logarithmic region ($U_f^+ = (1/\kappa)lny^+ + B$), the von Kármán constant κ and additive coefficient B are fitted (κ, B) = (0.4, 5.72) for the single-phase flow, and (κ, B) = (0.42, 5.37), (0.34, 2.51), and (0.42, 4.59) for cases $\phi = 0.11\%$, 0.22%, and 0.44%, respectively.

According to the stress balance in a particle-laden channel flow system [13], the fluid mean velocity changes in the sediment-laden cases from their single-phase flow counterpart are related to the change of the Reynolds stress. The Reynolds stress profiles of the four cases are compared in Figure 3b. With respect to the single-phase flow, the Reynolds stresses of the particle-laden simulations are increased in the near-wall region ($y^+ \leq 17$), but decreased in the intermediate region ($17 < y^+ \leq 60$), and remain unchanged very close to the top boundary ($175 \leq y^+ \leq 180$). Peng and Wang [15] pointed out that particles have two opposite influences on the Reynolds stress. On the one hand, particles can filter out the small-scale flow fluctuations due to their finite size. This leads to a reduction in the Reynolds stress. On the other hand, particle rotation in the spanwise direction can produce additional sweep and ejection events through bringing high-speed fluid from the outer region to the wall, and low-speed fluid from the wall to the outer region. This results in the enhancement of the Reynolds stress. Consequently, the overall modulation on the Reynolds stress depends on the competitive mechanisms between the finite size filtration-induced attenuation and the particle rotation-induced enhancement. In the current particulate flows, enhancement due to the particle rotation overwhelms the attenuation induced by the particle filtration near the wall, therefore the Reynolds stress is augmented. Far from the wall, the enhancement mechanism becomes insufficient to compensate the attenuation mechanism, therefore the Reynolds stress is damped.

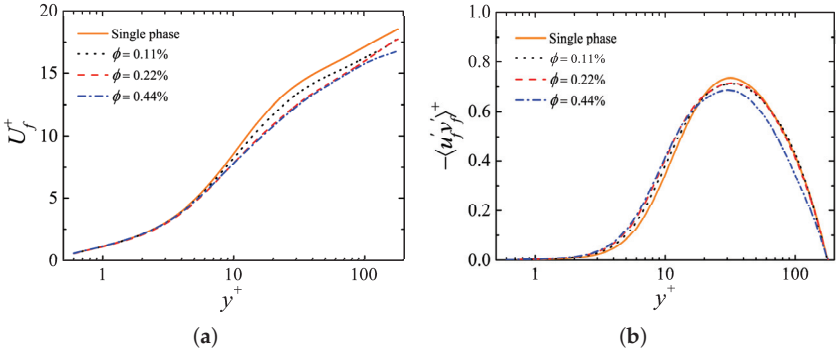

Figure 3. Comparison of results between the single-phase flow and the particle-laden flows: (**a**) Fluid mean streamwise velocity profiles and (**b**) fluid Reynolds stress profiles.

Figure 4a–c show the fluid RMS velocity fluctuation profiles. As seen from Figure 4a, the strength of the streamwise velocity fluctuation is significantly reduced by the particles. Again, a higher volume fraction leads to a stronger reduction. Shao et al. [20] attributed this reduction to the reduced strength of the large-scale streamwise vortices. Close to the wall ($y^+ \leq 30$), the wall-normal and spanwise velocity fluctuations are both increased compared to the unladen case. These increases can be explained by the fact that particles induce many small-scale vortices in the near-wall region (see Figure 5). It is also noted that the three RMS velocity fluctuation profiles become closer to each other in the particle-laden cases with respect to the single-phase flow. This behavior implies that particles make the distribution of the fluid energy towards a more isotropic state among different velocity components, and the modulation increases with the particle volume fraction.

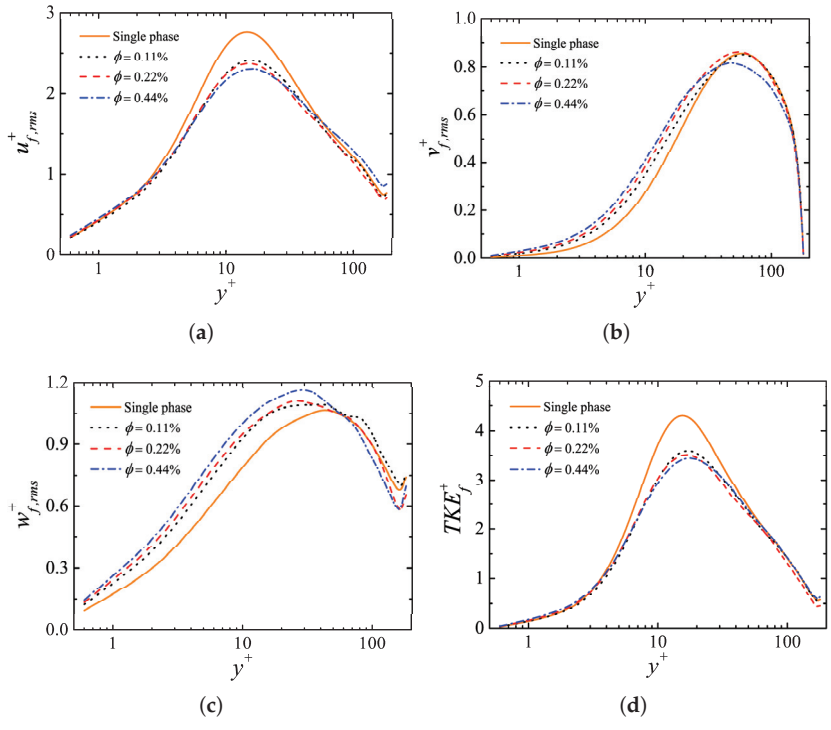

Figure 4. (**a**–**c**) Fluid RMS velocity fluctuations in the streamwise, wall-normal, and spanwise directions, respectively, and (**d**) fluid turbulent kinetic energy (TKE).

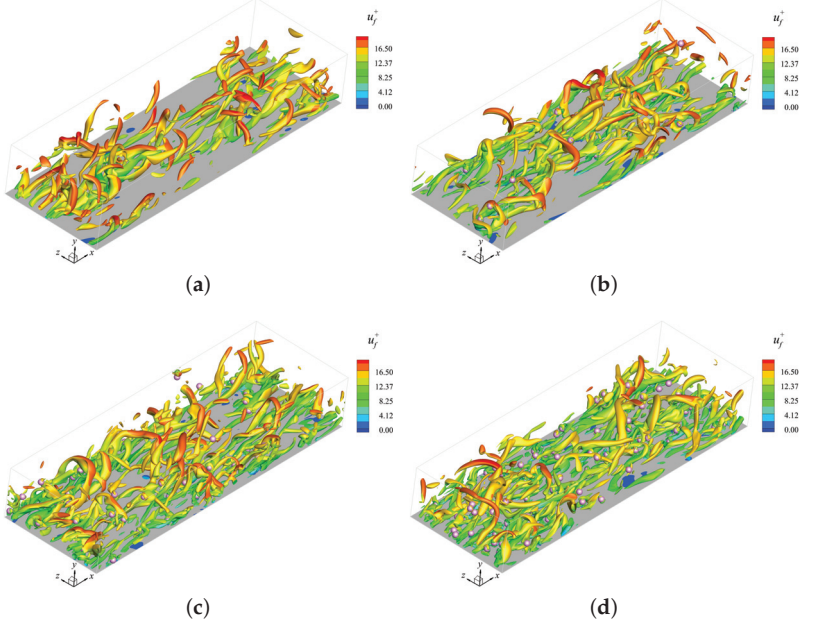

Figure 5. Vortical structures visualized by the Q-criterion at $Q/(u_\tau{}^4/\nu^2) = 0.01$ and colored by the fluid streamwise velocity: (**a**) Single phase, (**b**) $\phi = 0.11\%$, (**c**) $\phi = 0.22\%$, and (**d**) $\phi = 0.44\%$.

The fluid turbulent kinetic energy (TKE) from different cases are shown in Figure 4d. The fluid TKE is defined as $TKE_f^+ = 0.5[(u_{f,rms}^+)^2 + (v_{f,rms}^+)^2 + (w_{f,rms}^+)^2]$. With the presence of particles, the two-phase flows have lower peak values of TKEs. It indicates that the turbulence activities are generally suppressed by the particles. Overall, the addition of particles is found to result in a more homogeneous TKE distribution in the wall-normal direction, with slightly enhanced TKE in the viscous sublayer and noticeably reduced TKE in the buffer region. Similar behaviors were also found in turbulent channel flows laden with neutrally buoyant particles [13].

4.2. Flow Structures

The modulations of the fluid statistics are essentially due to the changes brought by the sediment particles to local flow structures. Figure 5 exhibits the isosurfaces of the second invariant of the velocity gradient tensor, i.e., Q-criterion, which is frequently used to visualize vortical structures in the turbulent flow [30]. The Q-criterion is defined using Einstein summation convention as $Q = (1/4)(\omega_i\omega_i - 2S_{ij}S_{ij})$, where $\omega_i = \varepsilon_{ijk}\partial_j u_k$ is the vorticity, $S_{ij} = (\partial u_i/\partial x_j + \partial u_j/\partial x_i)/2$ is the strain rate of the velocity fluctuations, and ε_{ijk} is the Levi–Civita symbol. In all cases, the large-scale hairpin vortices can be identified, but their occurrence is decreased with the increase of particle volume fraction. With the presence of particles, the suppression of the vortical structures is responsible for the reduction of the maximum value of the fluid streamwise velocity fluctuations [20], as shown in Figure 4a. Compared to the single-phase flow, the particle-laden cases show a considerable amount of small-scale vortices in the near-wall region. The number of these vortices increases monotonically with the particle volume fraction. This is because the particle-turbulence interactions are more intense at a higher particle volume fraction, which lead to more large-scale vortices breaking into small-scale ones. In the numerical work of Eshghinejadfard et al. [21], they pointed out that such small-scale vortices were stronger and more energetic in the particle-laden cases than those in the single-phase flow. These small-scale vortices are the main reason for the enhancements of the fluid wall-normal and spanwise velocity fluctuations in the proximity of the wall, as depicted in Figure 4b,c.

The streamwise vortices exchange the fluid momentum between the inner wall and the outer channel, which creates the well-known high- and low-speed velocity streaks [31]. As the streamwise vortices have been modified by the presence of sediment particles, the velocity streaks structures near the bottom channel wall could also be modulated. To explore this effect, snapshots of the streaky structures at $y^+ = 13.8$ plane are plotted in Figure 6. The reason for choosing this location is because it corresponds to the position with the maximum particle concentration, as depicted in Figure 7a. As shown, the presence of particles breaks the slender low-speed streaks into many smaller ones. Interestingly, the velocity streaks can still be recognized at the highest volume fraction $\phi = 0.44\%$. It is also observed that particles have a tendency to reside in the low-speed streaks. This phenomenon can be explained by the fact that the streamwise vortices tend to drive particles into the low-speed velocity regions. The above observation is in agreement with the simulation results of Kidanemariam et al. [9] ($D/H = 0.04$, $\phi = 0.05\%$, $\rho_p/\rho_f = 1.7$, and $\Theta = 0.19$) and Shao et al. [20] ($D/H = 0.05$ and 0.1, ϕ ranges from 0.79% to 7.08%, $\rho_p/\rho_f = 1.5$, and $\Theta = 0.11$ and 0.22) for heavy finite-size particles.

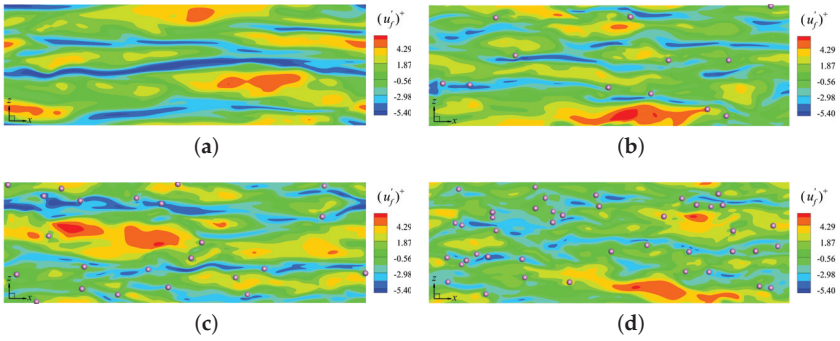

Figure 6. Snapshots of the streaky structures at $y^+ = 13.8$ plane: (**a**) Single phase, (**b**) $\phi = 0.11\%$, (**c**) $\phi = 0.22\%$, and (**d**) $\phi = 0.44\%$. Particles in contact with this plane are also shown.

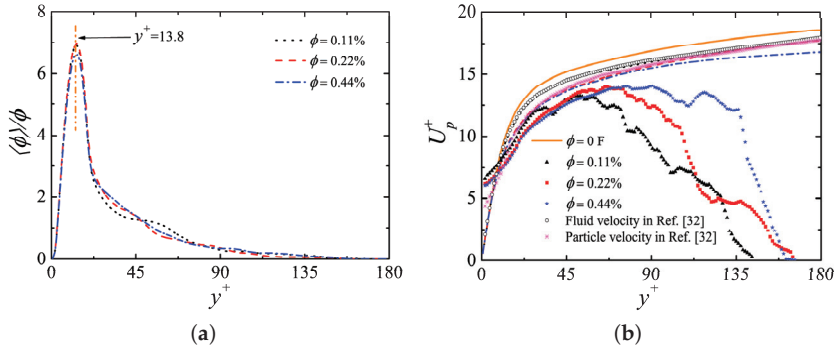

Figure 7. (**a**) Distributions of particle local volume fraction as function of the wall-normal locations and (**b**) particle mean streamwise velocity profiles. In (**b**), the corresponding profiles of the fluid phase are also shown for comparison (lines). Besides, mean velocity profiles of the fluid and the particles in Ref. [32] (see Figure 7a in their paper) are also added for comparison.

In order to quantitatively evaluate the effect of particles on the streaky structures, the two-point autocorrelation functions at $y^+ = 13.8$ plane are examined. Figure 8 illustrates the autocorrelations of velocity fluctuation components as a function of the spanwise and streamwise separations. The spanwise autocorrelation coefficient is calculated as $R_{zz}(\Delta z) = \overline{u'(x,y,z)u'(x,y,z+\Delta z)}/\overline{u'(x,y,z)u'(x,y,z)}$, where Δz is the spanwise separation and $u'(x,y,z)$ is the instantaneous streamwise velocity fluctuation. The streamwise autocorrelation coefficient is computed as $R_{xx}(\Delta x) = \overline{u'(x,y,z)u'(x+\Delta x,y,z)}/\overline{u'(x,y,z)u'(x,y,z)}$, where Δx is the streamwise separation. As stated by Kim et al. [33], the streak spacing is roughly twice the spanwise location of the minimum point of R_{zz}. It is found in Figure 8a that the streak spacing decreases from $\Delta z^+ \approx 120$ in the single-phase flow to $\Delta z^+ \approx 100$ for a volume fraction of $\phi = 0.44\%$. This result confirms the qualitative comparisons between Figure 6a,d. As observed from Figure 8b, the values of R_{xx} are substantially decreased by the existence of particles, which verifies the observations in Figure 6 that particles alters the near-wall turbulent structures to a less organized state.

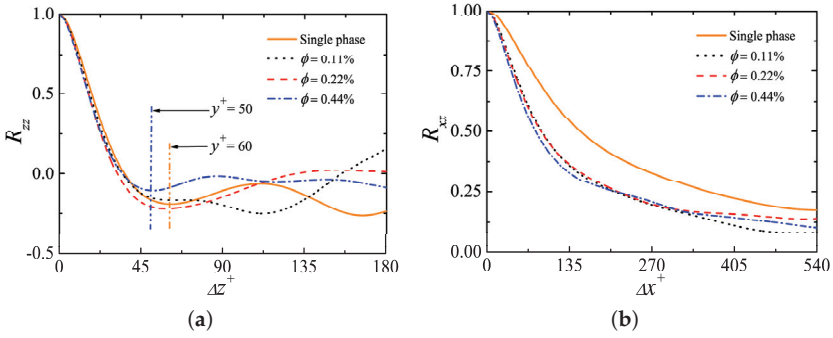

Figure 8. Autocorrelation coefficients of the streamwise velocity fluctuations versus the separations at $y^+ = 13.8$ plane: (**a**) In the spanwise direction and (**b**) in the streamwise direction.

4.3. Particle Statistics

In Figure 7a, the distributions of particle local volume fraction as function of the wall-normal locations are presented. All three profiles show a local maximum point near the wall ($y^+ = 13.8$), followed by a rapid decrease, reaching zero near the upper boundary. Note that, if a particle rests on the wall, its center will be at $y^+ = 9$. Thus the peak position is a dynamic balance between gravity, lubrication force, and turbulent transport. The observed phenomenon is consistent with the experimental measurement by Ni et al. [34] for the sediment particles. Due to the settling effect, most particles locate near the bottom wall (see Figure 9 as an example), leading to a noticeably higher concentration close to the wall. It is also found that all particle-laden curves are self-similar, exhibiting only slight discrepancies across the whole channel. This is because the particle volume fractions are small in all particle-laden cases. Based on the current parameter settings, it might be concluded that the total particle volume fraction has little effect on the normalized concentration profile.

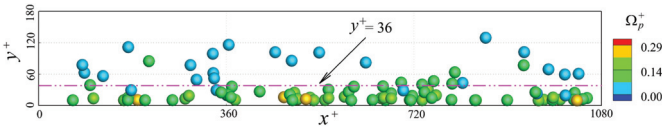

Figure 9. Side view snapshot of the particle positions taken from case $\phi = 0.44\%$, particles are colored by their angular velocities. Animations can be found in video S1 in the supplementary materials.

Figure 7b shows the particle mean streamwise velocity profiles together with their fluid counterparts for comparison. At a close proximity to the wall, particles move significantly faster than the fluid phase. This is because the particles can slip on the bottom wall whereas the fluid velocity is constrained by the no-slip condition. A similar observation is also found in the experimental results of Ebrahimian et al. [32] for particle-laden turbulent channel flows (see Figure 7a in their paper, $Re_\tau = 410$, $D^+ = 6.8$, $\phi = 0.03\%$, $\rho_p/\rho_f = 2.65$, and $\Theta = 1.49$). As shown ($y^+ < 9$), the mean slip velocity $\Delta U_{pf}^+ = U_p^+ - U_f^+$ in the present simulation is larger than that in Ref. [32]. Specifically, as $y^+ \to 0$, ΔU_{pf}^+ in case $\phi = 0.44\%$ is approximately 5.81, compared to 3.78 of Ref. [32]. The differences in ΔU_{pf}^+ between these two studies perhaps come from the different values of the particle size, friction Reynolds number Re_τ, and Shields number Θ. In the outer channel, the fluid velocity is obviously larger than the particle velocity. It can be explained by the fact that the solid particles are lifted off by ejection events, perhaps only momentarily, and then settle back down, resulting in a much smaller mean velocity in the outer region relative to the fluid velocity. It is also noted that the particle-laden curves have strong fluctuations in the outer region.

The reason is that most particles settle to the near-wall region, the statistical samples are insufficient in the upper section.

The particle and fluid RMS velocity fluctuations are compared in Figure 10a–c. The particle RMS velocity fluctuations are generally much smaller than those of the fluid phase at the same wall-normal location except for the near-wall region. This is due to the particle inertial effect, preventing fast changes in velocity. In the neighborhood of the wall, it is interesting to find that the particle wall-normal velocity fluctuations are significantly larger than the corresponding fluid components. Similar phenomenon can be also found in the study of Chan-Braun et al. [35] for Shields number $\Theta = 0.22$. In Figure 10d, the particle and fluid turbulent kinetic energy (TKE) profiles are compared. The definition of the particle TKE is an analogy to that of the fluid TKE, i.e., $TKE_P^+ = 0.5[(u_{p,rms}^+)^2 + (v_{p,rms}^+)^2 + (w_{p,rms}^+)^2]$. Besides a small region attached to the wall, the particle TKE is lower than that of the fluid phase, which is again due to the particle inertia.

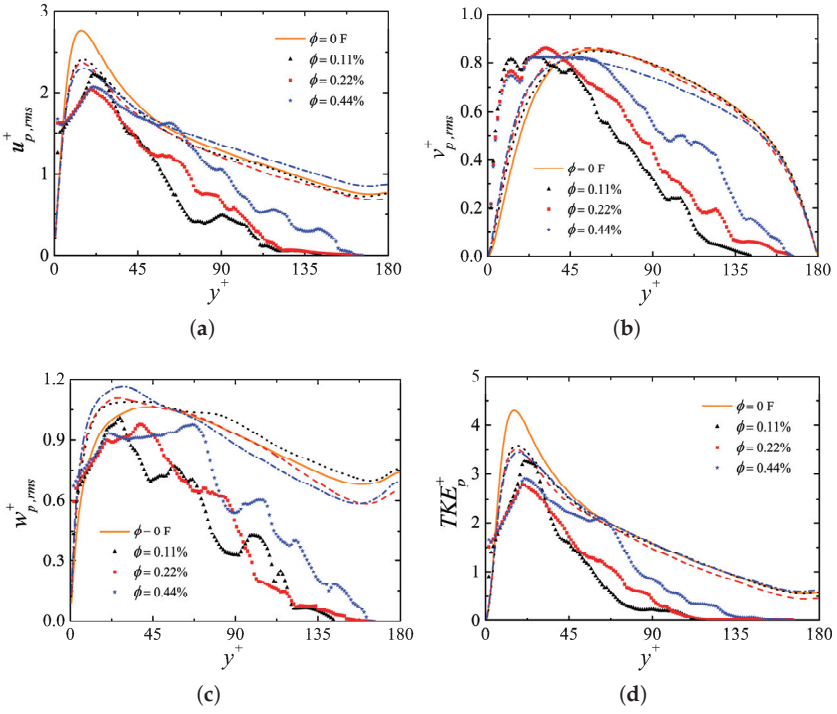

Figure 10. (**a**–**c**) Intensities of the particle RMS velocity fluctuations in the streamwise, wall-normal, and spanwise directions, respectively, and (**d**) particle turbulent kinetic energy (TKE). The corresponding profiles of the fluid phase are also shown for comparison (lines).

4.4. Particle Dynamics

Figure 9 shows the side view snapshot of particle positions from case $\phi = 0.44\%$. As observed, a large number of particles accumulate near the bottom wall whereas a few particles are suspended in the upper channel. This observation is consistent with the particle concentration profiles, as shown in Figure 7a. More specifically, approximately 70% of the particles with their normalized center positions locate in the region $y^+ \leq 36$ (twice the normalized diameter of the particles). In addition, the near-wall particles have obviously larger angular velocities than those in the outer area. One of the main reasons is because the shear stress is decreased with the wall-normal distance. Several typical transport modes of the sediment particles, such as resuspension, saltation, and rolling are

captured in the side view animation (see video S1 in the supplementary materials). It is worth mentioning that resuspension represents the sediment particles being lifted up from the bed and exhibit large jumps to eventually become suspended for a relatively long time; saltation denotes the sediments lose contact with the bed for a short while and their jump heights are within twice the particle diameter; rolling indicates the particles have angular velocities and their movements generally in contact with the bed [18].

To gain further insight into the particle motions, the wall-normal trajectories of all particles in case $\phi = 0.44\%$ are analyzed for period $0 \leq tu_\tau/H \leq 3.2$. It should be noted that $tu_\tau/H = 0$ indicates a time when the two-phase flow has reached the statistically steady state. Among them, two typical types of particle trajectories (A and B) are found, as shown in Figure 11a. As observed from Figure 11a, particle A spends all its time residing in the near-wall region and some obvious hops are identified. It could be imagined that the particle-wall collisions are frequent. Moreover, side view animation (see video S2 in the supplementary materials) visually shows that the major transport modes of this particle are saltation and rolling. It is noted that particle A remains in the lower part of the logarithmic layer and below. The saltation period is roughly $0.5H/u_\tau$. It never gains enough energy to enter the outer region.

On the contrary, particle B is occasionally lifted up and entrained by the turbulent eddies so that it resuspends and moves upward to the outer channel and then returns to the bottom wall ($0.7 \leq tu_\tau/H \leq 2.2$). Its trajectory exhibits evident rising and falling, looking like a ballistic curve. This interesting phenomenon is closely related to the combined effects of turbulent dynamics and gravitational force. The whole process of resuspension and redeposition takes more than one large eddy turnover time.

As for the wall-normal velocities (Figure 11b), particle A experiences more frequent velocity variations (negative-positive-negative) than particle B. This is because particle A almost moves near the bottom wall where the particle-wall and particle-particle interactions are intensive, while particle B is sometimes entrained to the outer region where the particle-turbulence interactions are relatively weak. On the other hand, the velocity fluctuation amplitudes of particle A are overall lower than those of particle B. At $tu_\tau/H = 0.7$, the wall-normal velocity of particle B alters from negative to positive, which means it begins to take off. This moment also indicates the particle reaches the lowest position. Later on, particle B continuously climbs up together with positive vertical velocity until the maximum wall-normal position is reached ($tu_\tau/H = 1.7$). At the early stage of this climbing, the combined effects of the upward forces (i.e., shear-induced lift force and rotation-induced lift force) overwhelm the downward gravitational force and drag force, thereby the particle rapidly accelerates and incessantly rise up. However, at the late stage, the gravitational force and drag force predominate the lift force, hence the particle decelerates till it arrives the peak point. After that, the vertical velocity changes from positive to negative and the particle quickly falls down under the effects of gravity and sweep events. When particle B settles close to the bottom wall, its vertical velocity again decelerates until a particle-wall collision takes place ($tu_\tau/H = 2.2$). This slow down process is owing to the fact that the particle encounters resistances from the turbulence and the bottom wall. The aforementioned transport processes ($0.7 \leq tu_\tau/H \leq 2.2$), i.e., resuspension and re-sedimentation, could be viewed as a free-flight stage where only the hydrodynamic force and the gravitational force affect the particle motion.

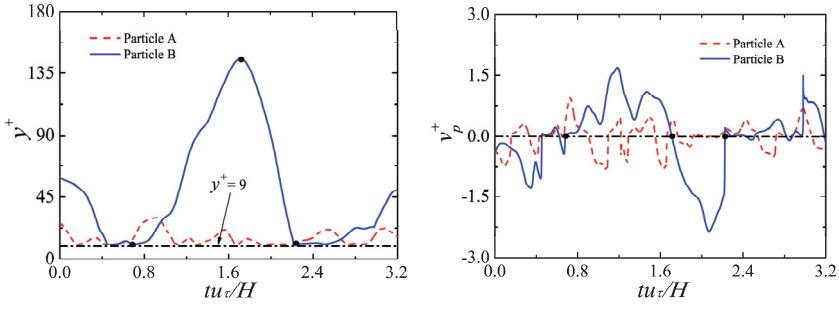

Figure 11. Time histories of two typical particle wall-normal motions extracted from case $\phi = 0.44\%$: (**a**) Center positions and (**b**) center velocities. If a particle touches the bottom wall, its normalized center position in the wall-normal direction is at $y^+ = 9$. Transport times $tu_\tau/H = 0.7$, 1.7, and 2.2 are marked with symbol "●". Side view animation can be found in video S2 in the Supplementary Materials.

4.5. Particle Clustering

Figure 12a shows the results of the particle radial distribution functions (RDFs), $\overline{g(r_i)}$. This quantity estimates the probability of finding a second particle at distance r_i away from the target particle, which is defined as $\overline{g(r_i)} = (N_i/V_i)/(N/V)$, where r_i is the distance of two particle centers, N_i is the number of particle pairs separeted with a distance $(r_i - \Delta r, r_i + \Delta r)$, Δr is set to be $0.1R$ in this simulation; $V_i = 4\pi[(r_i + \Delta r)^3 - (r_i - \Delta r)^3]/3$ is the shell volume, $N = N_p(N_p - 1)/2$ is the total number of particle pairs in the flow system, and $V = L_x \times L_y \times L_z$ is the total volume of the computational domain. The value of $\overline{g(r_i)}$ at the distance equals to the particle diameter indicates the level of two-particle clustering. As shown, all particle-laden cases display obvious peaks at the separation distance $r_i = D$, followed by a quick drop, then gradually decrease when r_i further increases. The findings concerning two-particle clustering have the highest RDFs are in line with the simulation results of Lashgari et al. [36], where turbulent channel flows laden with finite-size neutrally buoyant particles were studied.

The probability density functions (PDFs) of the two-particle clustering orientation angles θ are plotted in Figure 12b. The orientatin angle is defined as $\theta = tan^{-1}(\sqrt{(y_A - y_B)^2 - (z_A - z_B)^2}/\|x_A - x_B\|)$, where (x_A, y_A, z_A) and (x_B, y_B, z_B) are the center coordinates of two contact partilces A and B, respectively. When $0 \leq \theta \leq 45^\circ$, the particle clustering aligns towards the streamwise direction; when $\theta > 45^\circ$, it aligns along the cross-streamwise directions. It is observed that the two-particle clustering seems to uniformly orientate in all angles with the exceptions of the angles around 0 and 45°. Near zero degree, the orientation angles have the lowest probability. This is likely due to the strong particle-turbulence interactions so as to destroy the contact particles exactly align the streamwise direction. It is also interesting to note that the two-particle clustering has a slight preference to orientate close to 45°. The possible reason is closely related to the streamwise vortices who grow outward from the near-wall region with their heads inclining at 45° to the streamwise direction [37].

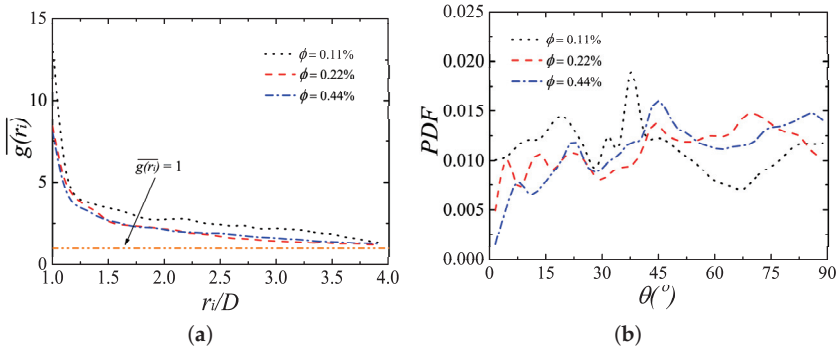

Figure 12. (**a**) The radial distribution functions (RDFs) as a function of center-to-center distance and (**b**) probability density functions (PDFs) of the particle-pair orientation angles.

4.6. Discussion on the Particle Concentration Distribution

As reported by Wang and Ni [38], there are two different kinds of patterns for the particle concentration distribution in open channels, i.e., pattern I and pattern II, as shown in Figure 13a. Pattern I displays an increasing concentration downward, with a maximum value at the bottom wall. On the other hand, pattern II exhibits the maximum concentration at some position above the bottom wall and then shows the decreasing value towards the wall. The mechanisms for the formations of these two different patterns are primarily ascribed to the lift forces acting on the particles by the surrounding fluid and the wall lubrication force [38]. In general, small heavy particles ($\rho_p/\rho_f > 1$) are usually formed the pattern I and it can be modeled by the Rouse formula [39]; while large light particles ($\rho_p/\rho_f \leq 1$) commonly form pattern II and it can be modeled by the kinetic theory of particle-fluid two-phase flows, which is given as Equation (12) [38]. Evidently, our current particle concentration distributions belong to the pattern II regime.

$$\frac{C}{C_a} = (\frac{\eta}{\eta_a})^{\zeta-1} e^{-Z_*(\eta-\eta_a)}, \tag{12}$$

where C is the vertical concentration at some position y above the bottom, $\eta = y/H$, C_a is a reference concentration at a reference location η_a (i.e., bed-layer thickness, $\eta_a = y_a/H$), and Z_* and ζ denotes the relative dynamic effects of fluid turbulent intensity and particle weight as well as the static characteristics of the fluid and particles in a given sized space. Usually, Z_* is a linear function of ω_s/u_τ, (i.e., $Z_* = a(\omega_s/u_\tau)$), where ω_s is the particle terminal settling velocity; ζ is related to the particle-fluid density ratio and the particle relative size, (i.e., $\zeta = 1 + b(D/H)/\sqrt{\rho_p/\rho_f}$). a and b are two adjustable constants.

In the current fitting, the concentration profile of case $\phi = 0.44\%$ is chosen. The reference location η_a is set to be 0.01 [40] since no apparent bed-layers are formed, which leads to $C_a = 0.12$. Based on Equation (12), the two adjustable parameters a and b are fitted as 23.35 and 56.68, respectively. Figure 13b shows the fitting results versus the actual concentration distribution from case $\phi = 0.44\%$. It is clearly observed that the fitting data and the present concentration match well in the near-wall region, while some differences are detected far away from the wall. Overall, the fitting is reasonable with the R-squared value being 0.85. The deviations might come from two reasons: (i) The different treatments of the particle collisions. In the theoretical model, the particle inter-collisions and particle-wall collisions are neglected. However, in the present simulation, the lubrication force model and the soft-sphere collision model are considered when particle-particle and particle-wall collisions occur; (ii) the theoretical model is derived under the condition of two-dimensional steady state assumption, whereas the current simulation is a three-dimensional sediment-laden flow. Similar deviations were also found in [38] who

compared their prediction results with other authors' experimental data (see Figure 3 in their paper).

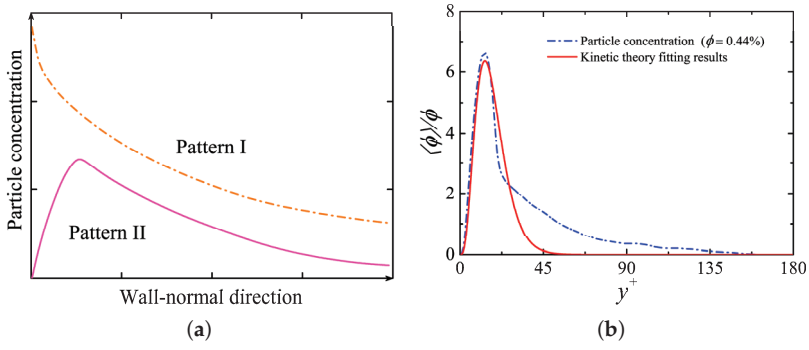

Figure 13. (**a**) Two different patterns of the particle concentration distribution and (**b**) particle concentration profile from case $\phi = 0.44\%$ versus a fitting curve based on the kinetic theory.

5. Conclusions

In this study, interface-resolved direct numerical simulations based on the lattice Boltzmann method are used to explore the sediment-turbulence interactions in the turbulent open channel flows. The effects of different particle volume fractions on the statistics of the fluid and particle phases, flow structures, and particle dynamics are numerically investigated. According to the simulation results, the following conclusions are drawn:

(i) The presence of heavy particles substantially reduces the maximum fluid streamwise velocity fluctuations, and this effect is more pronounced at a higher particle volume fraction. In the near-wall region, the fluid wall-normal and spanwise velocity fluctuations are both augmented when compared to the single-phase flow. The particles force the TKE to distribute in a more isotropic manner and also make the TKE more homogeneous in the wall-normal direction.

(ii) By visualizing the vortical structures, it is found that particles suppress the generation of the large-scale coherent vortices and simultaneously create numerous small-scale vortices in the near-wall region. Particles have a tendency to reside in the low-speed velocity regions and alter the streaky structures to a less organized state.

(iii) Third itemThe particle TKE is much smaller than the fluid TKE except in the region very close to the wall. Under the current parameter settings, the normalized vertical particle concentration profiles are self-similar. Additionally, a general match between the present concentration profile and a theoretical model is found.

(iv) Owing to the settling effect, most particles accumulate in the vicinity of the bottom wall, where the particle-wall and particle-particle collisions and the particle-turbulence interactions are strongest. By tracking the particle trajectories, different modes of the sediment transport, such as resuspension, saltation, and rolling, are captured.

Supplementary Materials: The following are available online at https://www.mdpi.com/2311-5521/6/6/217/s1. See the supplementary materials for the sediment transport animations.

Author Contributions: Conceptualization, L.H. and L.-P.W.; formal analysis, L.H.; funding acquisition, L.-P.W.; methodology, L.H. and Z.D.; project administration, L.-P.W.; resources, L.-P.W.; visualization, L.H.; writing—original draft, L.H.; writing — review and editing, L.H., C.P. and L.-P.W. All authors have read and agreed to the published version of the manuscript.

Funding: This work has been supported by the Southern Marine Science and Engineering Guangdong Laboratory (Guangzhou) (Grant No. GML2019ZD0103), the National Natural Science Foundation of China (NSFC award numbers 91852205, 91741101, and 11961131006), NSFC Basic Science Center Program (Award number 11988102), the U.S. National Science Foundation (CNS-1513031, CBET-1706130), the National Numerical Wind Tunnel program, Guangdong Provincial Key Laboratory of Turbulence Research and Applications (2019B21203001), Guangdong-Hong Kong-Macao Joint Laboratory for Data-Driven Fluid Mechanics and Engineering Applications (2020B1212030001), and Shenzhen Science and Technology Program (Grant No. KQTD20180411143441009).

Institutional Review Board Statement: Not applicable.

Informed Consent Statement: Not applicable.

Data Availability Statement: The data presented in this study are available on reasonable request from the authors.

Acknowledgments: Computing resources are provided by the Center for Computational Science and Engineering of Southern University of Science and Technology and by National Center for Atmospheric Research (CISL-UDEL0001).

Conflicts of Interest: The authors declare no conflict of interest.

References

1. Rashidi, M.; Hetsroni, G.; Banerjee, S. Particle-turbulence interaction in a boundary layer. *Int. J. Multiph. Flow* **1990**, *16*, 935–949. [CrossRef]
2. Baker, L.J.; Coletti, F. Experimental study of negatively buoyant finite-size particles in a turbulent boundary layer up to dense regimes. *J. Fluid Mech.* **2019**, *866*, 598–629. [CrossRef]
3. Righetti, M.; Romano, G.P. Particle-fluid interactions in a plane near-wall turbulent flow. *J. Fluid Mech.* **2004**, *505*, 93–121. [CrossRef]
4. Dwivedi, A.; Melville, B.W.; Shamseldin, A.Y.; Guha, T.K. Flow structures and hydrodynamic force during sediment entrainment. *Water Resour. Res.* **2011**, *47*, 499–509. [CrossRef]
5. Balachandar, S.; Eaton, J.K. Turbulent dispersed multiphase flow. *Annu. Rev. Fluid Mech.* **2010**, *42*, 111–133. [CrossRef]
6. Maxey, M. Simulation methods for particulate flows and concentrated suspensions. *Annu. Rev. Fluid Mech.* **2017**, *49*, 171–193. [CrossRef]
7. Tenneti, S.; Subramaniam, S. Particle-resolved direct numerical simulation for gas-solid flow model development. *Annu. Rev. Fluid Mech.* **2014**, *46*, 199–230. [CrossRef]
8. Pan, Y.; Banerjee, S. Numerical investigation of the effects of large particles on wall-turbulence. *Phys. Fluids* **1997**, *9*, 3786–3807. [CrossRef]
9. Kidanemariam, A.G.; Chan-Braun, C.; Doychev, T.; Uhlmann, M. DNS of horizontal open channel flow with finite-size, heavy particles at, low solid volume fraction. *New J. Phys.* **2013**, *15*, 025031. [CrossRef]
10. Ji, C.N.; Munjiza, A.; Avital, E.; Ma, J.; Williams, J.J.R. Direct numerical simulation of sediment entrainment in turbulent channel flow. *Phys. Fluids* **2013**, *25*, 056601. [CrossRef]
11. Yousefi, A.; Costa, P.; Brandt, L. Single sediment dynamics in turbulent flow over a porous bed-insights from interface-resolved simulations. *J. Fluid Mech.* **2020**, *893*. [CrossRef]
12. Derksen, J.J. Simulations of granular bed erosion due to a mildly turbulent shear flow. *J. Hydraul. Res.* **2015**, *53*, 622–632. [CrossRef]
13. Peng, C. Study of turbulence modulation by finite-size solid particles with the lattice Boltzmann method. Ph.D. Thesis, University of Delaware, Newark, DE, USA, 2018.
14. Gao, H.; Li, H.; Wang, L.-P. Lattice Boltzmann simulation of turbulent flow laden with finite-size particle. *Comput. Math. Appl.* **2013**, *65*, 194–210. [CrossRef]
15. Peng, C.; Wang, L.-P. Direct numerical simulations of turbulent pipe flow laden with finite-size neutrally buoyant particles at low flow Reynolds number. *Acta Mech.* **2019**, *230*, 517–539. [CrossRef]
16. Peng, C.; Ayala, O.M.; Wang, L.-P. Flow modulation by a few fixed spherical particles in a turbulent channel flow. *J. Fluid Mech.* **2020**, *884*. [CrossRef]
17. Tang, G.H.; Tao, W.Q.; He, Y.L. Lattice Boltzmann method for simulating gas flow in microchannels. *Int. J. Mod. Phys. C* **2004**, *15*, 335–347. [CrossRef]
18. Rowiński, P.; Banaszkiewicz, M.; Pempkowiak, J.; Lewandowski, M.; Sarna, M. *Hydrodynamics-Hydrodynamic and Sediment Transport Phenomena*, 1st ed.; Springer: London, UK, 2014.
19. Liu, X.; Ji, C.N.; Xu, X.L.; Xu, D.; Williams, J.J.R. Distribution characteristics of inertial sediment particles in the turbulent boundary layer of an open channel flow determined using Voronoï analysis. *Int. J. Sediment Res.* **2017**, *32*, 401–409. [CrossRef]

20. Shao, X.M.; Wu, T.H.; Yu, Z.S. Fully resolved numerical simulation of particle-laden turbulent flow in a horizontal channel at a low Reynolds number. *J. Fluid Mech.* **2012**, *693*, 319–344. [CrossRef]
21. Eshghinejadfard, A.; Zhao, L.H.; Thévenin, D. Lattice Boltzmann simulation of resolved oblate spheroids in wall turbulence. *J. Fluid Mech.* **2018**, *849*, 510–540. [CrossRef]
22. Peng, Y.; Luo, L.S. A comparative study of immersed-boundary and interpolated bounce-back methods in LBE. *Prog. Comput. Fluid Dyn.* **2008**, *8*, 156–167. [CrossRef]
23. Bouzidi, M.; Firdaouss, M.; Lallemand, P. Momentum transfer of a Boltzmann-lattice fluid with boundaries. *Phys. Fluids* **2001**, *13*, 3452–3459. [CrossRef]
24. Zhao, W.F.; Yong, W.A. Single-node second-order boundary schemes for the lattice Boltzmann method. *J. Comput. Phys.* **2017**, *329*, 1–15. [CrossRef]
25. Wen, B.; Zhang, C.Y.; Tu, Y.S.; Wang, C.L.; Fang, H.P. Galilean invariant fluid-solid interfacial dynamics in lattice Boltzmann simulations. *J. Comput. Phys.* **2014**, *266*, 161–170. [CrossRef]
26. Caiazzo, A.; Junk, M. Boundary forces in lattice Boltzmann: Analysis of momentum exchange algorithm. *Comput. Math. Appl.* **2008**, *55*, 1415–1423. [CrossRef]
27. Brändle de Motta, J.C.; Breugem, W.P.; Gazanion, B.; Estivalezes, J.L.; Vincent, S.; Climent, E. Numerical modelling of finite-size particle collisions in a viscous fluid. *Phys. Fluids* **2013**, *25*, 083302. [CrossRef]
28. Breugem, W.P. A combined soft-sphere collision/immersed boundary method for resolved simulations of particulate flows. In Proceedings of the ASME 2010 3rd Joint US-European Fluids Engineering Summer Meeting and 8th International Conference on Nanochannels, Microchannels, and Minichannels, Montreal, QC, Canada, 1–5 August 2010.
29. Lammers, P.; Beronov, K.N.; Volkert, R.; Brenner, G.; Durst, F. Lattice BGK direct numerical simulation of fully developed turbulence in incompressible plane channel flow. *Comput. Fluids* **2006**, *35*, 1137–1153. [CrossRef]
30. Zhou, J.; Adrian, R.J.; Balachandar, S.; Kendall, T.M. Mechanisms for generating coherent packets of hairpin vortices in channel flow. *J. Fluid Mech.* **1999**, *387*, 353–396. [CrossRef]
31. Blackwelder, R.F.; Eckelmann, H. Streamwise vortices associated with the bursting phenomenon. *J. Fluid Mech.* **1979**, *94*, 577–594. [CrossRef]
32. Ebrahimian, M.; Sanders, R.S.; Ghaemi, S. Dynamics and wall collision of inertial particles in a solid-liquid turbulent channel flow. *J. Fluid Mech.* **2019**, *881*, 872–905. [CrossRef]
33. Kim, J.; Moin, P.; Moser, R. Turbulence statistics in fully developed channel flow at low Reynolds number. *J. Fluid Mech.* **1987**, *177*, 133–166. [CrossRef]
34. Ni, J.R.; Wang, G.Q.; Borthwick, A.G.L. Kinetic theory for particles in dilute and dense solid-liquid flows. *J. Hydraul. Eng.* **2000**, *126*, 893–903. [CrossRef]
35. Chan-Braun, C.; García-Villalba, M.; Uhlmann, M. Direct numerical simulation of sediment transport in turbulent open channel flow. In *High Performance Computing in Science and Engineering*; Springer: Berlin/Heidelberg, Germany, 2010.
36. Lashgari, I.; Picano, F.; Costa, P.; Breugem, W.P.; Brandt, L. Turbulent channel flow of a dense binary mixture of rigid particles. *J. Fluid Mech.* **2017**, *818*, 623–645. [CrossRef]
37. Robinson, S.K. Coherent motions in the turbulent boundary layer. *Annu. Rev. Fluid Mech.* **1991**, *23*, 601–639. [CrossRef]
38. Wang, G.Q.; Ni, J.R. Kinetic theory for particle concentration distribution in two phase flow. *J. Eng. Mech.* **1990**, *116*, 2738–2748. [CrossRef]
39. Rouse, H. Modern conceptions of the mechanics of turbulence. *Trans. Am. Soc. Civ. Eng.* **1937**, *102*, 463–505. [CrossRef]
40. van Rijn, L.C. Sediment Transport, Part II: Suspended Load Transport. *J. Hydraul. Eng.* **1984**, *110*, 1613–1641. [CrossRef]

fluids

MDPI

Article

Exact Solutions of Navier–Stokes Equations for Quasi-Two-Dimensional Flows with Rayleigh Friction

Natalya Burmasheva [1], Sergey Ershkov [2,*], Evgeniy Prosviryakov [1] and Dmytro Leshchenko [3]

[1] Institute of Engineering Science UB RAS, Ural Federal University, 620049 Ekaterinburg, Russia
[2] Department of Scientific Researches, Plekhanov Russian University of Economics, Scopus Number 60030998, 36 Stremyanny Lane, 117997 Moscow, Russia
[3] Odessa State Academy of Civil Engineering and Architecture, 65029 Odessa, Ukraine
* Correspondence: sergej-ershkov@yandex.ru

Abstract: To solve the problems of geophysical hydrodynamics, it is necessary to integrally take into account the unevenness of the bottom and the free boundary for a large-scale flow of a viscous incompressible fluid. The unevenness of the bottom can be taken into account by setting a new force in the Navier–Stokes equations (the Rayleigh friction force). For solving problems of geophysical hydrodynamics, the velocity field is two-dimensional. In fact, a model representation of a thin (bottom) baroclinic layer is used. Analysis of such flows leads to the redefinition of the system of equations. A compatibility condition is constructed, the fulfillment of which guarantees the existence of a nontrivial solution of the overdetermined system under consideration. A non-trivial exact solution of the overdetermined system is found in the class of Lin–Sidorov–Aristov exact solutions. In this case, the flow velocities are described by linear forms from horizontal (longitudinal) coordinates. Several variants of the pressure representation that do not contradict the form of the equation system are considered. The article presents an algebraic condition for the existence of a non-trivial exact solution with functional arbitrariness for the Lin–Sidorov–Aristov class. The isobaric and gradient flows of a viscous incompressible fluid are considered in detail.

Keywords: exact solutions; Navier–Stokes equations; Rayleigh friction; Kolmogorov flow; isobaric flows; gradient flows; overdetermined system; solvability condition

Citation: Burmasheva, N.; Ershkov, S.; Prosviryakov, E.; Leshchenko, D. Exact Solutions of Navier–Stokes Equations for Quasi-Two-Dimensional Flows with Rayleigh Friction. *Fluids* **2023**, *8*, 123. https://doi.org/10.3390/fluids8040123

Academic Editors: Joseph J. Kuehl and D. Andrew S. Rees

Received: 19 February 2023
Revised: 20 March 2023
Accepted: 28 March 2023
Published: 3 April 2023

1. Introduction

The study of flows that take place in nature and technical hydrodynamic systems is often characterized by the predominance of the horizontal component of the velocity field over the vertical one [1–7]. Examples of such flows are large-scale flows both in the ocean and in atmospheres of rotating planets, the convective circulation on the Sun and other stars, the spatial evolution of gas and plasma flows in galaxies, and flows both in magnetized plasma and in thin layers of fluid [1–7]. In addition, a class of such flows can be implemented in laboratory conditions, in which direct and indirect measurements of various parameters in complex geometry and topologies of flows can be reproduced [1–7].

The suppression of the vertical velocity component can be due to various reasons. As an illustrative example, we indicate the following factors: the physical competition between regimes of a uniform rigid-body rotation and differential rotation in a fluid, the presence of a magnetic field for an electrically conductive fluid, a pronounced stratification of the force field that induces the movement of a fluid (for example, by a non-uniform density), a small thickness of the fluid layer, and a combination of the phenomena listed above [1–7]. To describe large-scale incompressible fluid flows moving in thin layers, mathematical models based on the representation of the velocity field by a quasi-two-dimensional flow

have proved themselves well [3,4,8,9]. In other words, quasi-two-dimensional flows are two-dimensional in velocity but three-dimensional in geometric coordinates [8,10–12].

$$\left(V_x(t,x,y,z), V_y(t,x,y,z), 0\right)$$

The construction of exact solutions for the Navier–Stokes equations describing quasi-two-dimensional flows is sometimes a more difficult task than finding exact solutions for three-dimensional flows. The main difficulty in finding exact solutions for the velocity field with two nonzero components depending on three coordinates is due to the fact that the reduced equations of motion for an incompressible fluid are overdetermined [8,13–17]. Overdetermination means that the number of equations of the system exceeds the number of functions found from these equations. For isobaric flows of incompressible fluids, exact solutions that take into account the horizontal inhomogeneity of the velocity field were reported in [14,16–18]. The study of gradient shear flows in the exact formulation was carried out in [19–23]. For problems of convection, thermal diffusion, and inhomogeneous flows of geophysical hydrodynamics, the exact solutions presented in [16–18] were generalized in articles [24–26] and in a review [8].

The exact solutions found in [8,13–26] for various force fields can be used to solve boundary value problems with a free boundary [27–32]. When describing ocean flows, there is the problem of taking into account the effect of bottom roughness on the structure of the velocity field. In [3], the authors proposed introducing a new force into the Navier–Stokes equations to take into account the roughness of the bottom. This force, which takes into account an external friction according to the Rayleigh law, makes it possible to more accurately describe large-scale flows that take place in natural and technical systems. Note that the Rayleigh friction coefficient depends on both the physical features of the hydrodynamic system and the edge conditions at the flow boundaries [3].

So far, exact solutions for strictly two-dimensional flows (V_x (t,x,y,z), V_y (t,x,y,z), 0) have been considered, and then their stability has been studied [3–7]. Already in pioneering articles [33–35] devoted to the study of the Kolmogorov flow with an initial sinusoidal profile, there was a lack of exact solutions for quasi-two-dimensional flows of the form (V_x (t,x,y,z), V_y (t,x,y,z), 0).

We repeat once again that the fundamental difficulty in constructing exact solutions is related to the overdetermination of the system of Navier–Stokes equations together with the incompressibility equation.

This article partially fills the gap in the finding of exact solutions for quasi-two-dimensional flows considered additionally with Rayleigh frictions for various classes of flows. Note that the study of isobaric and gradient flows does not take into account the rotation of the fluid.

Neglecting the influence of the Coriolis force on the fluid flow is due to the intention of the authors to demonstrate the main difficulties associated with the establishment of the solvability condition for the overdetermined system of hydrodynamic equations and the structure of exact solutions, in comparison with the known results obtained from the classical form of the Navier–Stokes equations. This is performed by the authors as they wanted to show the main difficulties that arise when constructing a solvability condition for the overdetermined system of equations that arises during modeling.

2. Problem Statement

Isothermal shear flows of a viscous incompressible fluid are considered here, taking into account the integral influence of the near-bottom boundary layer, which are described by the following system of nonlinear differential equations in partial derivatives [3,36]:

$$\frac{\partial V_x}{\partial t} + V_x\frac{\partial V_x}{\partial x} + V_y\frac{\partial V_x}{\partial y} = -\frac{\partial P}{\partial x} + \nu\left(\frac{\partial^2 V_x}{\partial x^2} + \frac{\partial^2 V_x}{\partial y^2} + \frac{\partial^2 V_x}{\partial z^2}\right) - \lambda V_x \quad (1)$$

$$\frac{\partial V_y}{\partial t} + V_x\frac{\partial V_y}{\partial x} + V_y\frac{\partial V_y}{\partial y} = -\frac{\partial P}{\partial y} + \nu\left(\frac{\partial^2 V_y}{\partial x^2} + \frac{\partial^2 V_y}{\partial y^2} + \frac{\partial^2 V_y}{\partial z^2}\right) - \lambda V_y \quad (2)$$

$$\frac{\partial P}{\partial z} = 0 \quad (3)$$

$$\frac{\partial V_x}{\partial x} + \frac{\partial V_y}{\partial y} = 0 \quad (4)$$

Navier–Stokes systems (1)–(4) consist of projections of the momentum equations (Equations (1)–(3)) on the axes of the orthogonal coordinate system and the continuity equation (Equation (4)) for the case of incompressible fluids. In systems (1)–(4), the standard denotation is introduced: $V_x(t,x,y,z)$ and $V_y(t,x,y,z)$ are projections of the velocity vector; $P(t,x,y,z) = p/\rho_0$ is the pressure p normalized to the fluid density ρ_0; ν is the kinematic viscosity.

A distinctive feature of Equations (1) and (2) is the consideration of the Rayleigh friction force, characterized by the value of the friction coefficient λ. An additional term on the right-hand sides of Equations (1) and (2), containing this coefficient, makes it possible to take into account the bottom roughness. The value of the parameter λ is determined by the edge conditions of the boundary value problem in the geophysical hydrodynamics [3].

Equation (3) means that the pressure does not change with depth. In fact, we are talking about a narrow baroclinic layer existing in the world's ocean and its internal (near-continental) seas, where the temperature practically does not change.

Among all the equations of the system under consideration, only Equation (3) is isolated, implying that normalized pressure P depends only on part of the spatial coordinates.

However, at the same time, generally speaking, the dependence of the pressure on the other two spatial coordinates and time remains. That is, Equation (3) does not mean the constancy of pressure, but simply narrows the range of parameters on which the pressure value depends:

$$P = P(t, x, y) \quad (5)$$

Let us remark that the consideration of shear flows (i.e., flows with a zero vertical velocity) leads to the need to investigate the system of constitutive relations (systems (1)–(4) for compatibility of solutions for separate equations of the aforementioned system). Indeed, the system under the consideration includes four scalar equations for determining three unknown functions—namely, velocities V_x and V_y and pressure P.

To conclude, regarding the solvability condition for systems (1)–(4), we apply the approach presented in [17] for the classical equations of the hydrodynamics of incompressible Newtonian fluids. We differentiate the first equation of the system with respect to x and the second with respect to y, and we sum up the results. As a result of the algebraic manipulations, due to the fact that partial derivatives on analytical functions are always commutative, we obtain the following equation:

$$\begin{aligned}
&\frac{\partial}{\partial t}\left(\frac{\partial V_x}{\partial x} + \frac{\partial V_y}{\partial y}\right) + \left(\frac{\partial V_x}{\partial x}\right)^2 + \left(\frac{\partial V_y}{\partial y}\right)^2 + V_x\frac{\partial}{\partial x}\left(\frac{\partial V_x}{\partial x} + \frac{\partial V_y}{\partial y}\right) \\
&\quad + V_y\frac{\partial}{\partial y}\left(\frac{\partial V_x}{\partial x} + \frac{\partial V_y}{\partial y}\right) + 2\frac{\partial V_y}{\partial x}\frac{\partial V_x}{\partial y} \\
&= \nu\left[\frac{\partial^2}{\partial x^2}\left(\frac{\partial V_x}{\partial x} + \frac{\partial V_y}{\partial y}\right) + \frac{\partial^2}{\partial y^2}\left(\frac{\partial V_x}{\partial x} + \frac{\partial V_y}{\partial y}\right) + \frac{\partial^2}{\partial z^2}\left(\frac{\partial V_x}{\partial x} + \frac{\partial V_y}{\partial y}\right)\right] \\
&\quad - \frac{\partial^2 P}{\partial x^2} - \frac{\partial^2 P}{\partial y^2} - \lambda\left(\frac{\partial V_x}{\partial x} + \frac{\partial V_y}{\partial y}\right). \quad (6)
\end{aligned}$$

Let us take into account during our calculations that the continuity equation (Equation (4)) in the resulting equation (Equation (6)) simplifies the latter as follows:

$$\left(\frac{\partial V_x}{\partial x}\right)^2 + \left(\frac{\partial V_y}{\partial y}\right)^2 + 2\frac{\partial V_y}{\partial x}\frac{\partial V_x}{\partial y} = -\frac{\partial^2 P}{\partial x^2} - \frac{\partial^2 P}{\partial y^2}. \tag{7}$$

The derivation of the compatibility condition for solutions of the overdetermined system of Equations (1)–(4), written in the form of (7), does not bring the result closer to constructing the solution itself. First, let us study the solvability of systems (1)–(4) in the Lin–Sidorov–Aristov class of exact solutions [4,8,37,38]. Within the specified class, the velocities V_x and V_y are linear forms of two spatial coordinates with a non-linear arbitrary dependence of the coefficients in these forms on both the third spatial coordinate and time:

$$V_x(x,y,z,t) = U(z,t) + u_1(z,t)x + u_2(z,t)y,$$

$$V_y(x,y,z,t) = V(z,t) + v_1(z,t)x + v_2(z,t)y. \tag{8}$$

The Lin class, with its external simplicity, first allows us to study the behavior of the velocity and acceleration fields. Secondly, it allows us to preserve the nonlinearity of the Navier–Stokes equations and to describe the nonlinear effects observed in real fluids.

We substitute expressions (5) and (8) into the above-considered systems (1)–(4), and we obtain as a result the following:

$$\begin{gathered}
\frac{\partial U}{\partial t} + \frac{\partial u_1}{\partial t}x + \frac{\partial u_2}{\partial t}y + (U + u_1x + u_2y)u_1 + (V + v_1x + v_2y)u_2 \\
= -\frac{\partial P}{\partial x} + \nu\left(\frac{\partial^2 U}{\partial z^2} + \frac{\partial^2 u_1}{\partial z^2}x + \frac{\partial^2 u_2}{\partial z^2}y\right) - \lambda(U + u_1x + u_2y), \\
\frac{\partial V}{\partial t} + \frac{\partial v_1}{\partial t}x + \frac{\partial v_2}{\partial t}y + (U + u_1x + u_2y)v_1 + (V + v_1x + v_2y)v_2 \\
= -\frac{\partial P}{\partial x} + \nu\left(\frac{\partial^2 V}{\partial z^2} + \frac{\partial^2 v_1}{\partial z^2}x + \frac{\partial^2 v_2}{\partial z^2}y\right) - \lambda(V + v_1x + v_2y), \\
u_1 + v_2 = 0.
\end{gathered} \tag{9}$$

Let us reduce the number of equations and unknown terms in subsystem (9) using the relation

$$v_2 = -u_1 \tag{10}$$

between spatial accelerations, which is a direct consequence of the last equation of this system. As a result, we obtain:

$$\begin{gathered}
\left(\frac{\partial U}{\partial t} + Uu_1 + Vu_2 - \nu\frac{\partial^2 U}{\partial z^2} + \lambda U\right) + \left(\frac{\partial u_1}{\partial t} + {u_1}^2 + u_2v_1 - \nu\frac{\partial^2 u_1}{\partial z^2} + \lambda u_1\right)x \\
+\left(\frac{\partial u_2}{\partial t} - \nu\frac{\partial^2 u_2}{\partial z^2} + \lambda u_2\right)y = -\frac{\partial P}{\partial x}, \\
\left(\frac{\partial V}{\partial t} + Uv_1 - Vu_1 - \nu\frac{\partial^2 V}{\partial z^2} + \lambda V\right) + \left(\frac{\partial v_1}{\partial t} - \nu\frac{\partial^2 v_1}{\partial z^2} + \lambda v_1\right)x \\
-\left(\frac{\partial u_1}{\partial t} - \left({u_1}^2 + u_2v_1\right) - \nu\frac{\partial^2 u_1}{\partial z^2} + \lambda u_1\right)y = -\frac{\partial P}{\partial y}.
\end{gathered} \tag{11}$$

Obviously, the left-hand sides of Equation (11) are linear forms in the spatial coordinates x and y. Hence, the right-hand sides of these equations (pressure derivatives with respect to x and y) must also be linear forms of the same coordinates. Therefore, the degree of the polynomial P does not exceed two.

The same conclusion also follows from the compatibility condition. By a direct substitution, one can verify that the compatibility condition for solution (7) for class (8), taking into account condition (9), takes the following form:

$$2\left({u_1}^2 + u_2 v_1\right) = -\frac{\partial^2 P}{\partial x^2} - \frac{\partial^2 P}{\partial y^2}. \tag{12}$$

Equation (12) has a function on the left-hand side that depends only on both time t and the vertical coordinate z, which means that the right-hand side of this equation can also be thought to depend only on these parameters. Thus, terms higher than the second degree cannot enter into pressure P.

3. Case 1: The Pressure P Depends Only on Time t

Let us assume that the pressure depends only on the current time t, i.e., represented in the form of

$$P = P_0(t). \tag{13}$$

The structure of pressure (13) allows us to consider it as a known function, specified at the boundaries of the fluid flow region. Therefore, what remains is to determine only the components of the velocity field (8).

In addition, due to (13), the compatibility condition (12) takes a simpler form:

$${u_1}^2 + u_2 v_1 = 0. \tag{14}$$

Note that relation (14) was obtained earlier, for example, in [9,17,39], but only steady flows were considered there. In view of the similarity of the form of condition (14) and the compatibility conditions given in [9,17,39], expression (14) is suitable for both steady and unsteady flows.

By virtue of Equations (13) and (14) and the independence of spatial coordinates on each other, the equations of system (11) are reduced to several autonomous equations in the following form:

$$\frac{\partial u_1}{\partial t} - \nu\frac{\partial^2 u_1}{\partial z^2} + \lambda u_1 = 0,\ \frac{\partial u_2}{\partial t} - \nu\frac{\partial^2 u_2}{\partial z^2} + \lambda u_2 = 0,\ \frac{\partial v_1}{\partial t} - \nu\frac{\partial^2 v_1}{\partial z^2} + \lambda v_1 = 0, \tag{15}$$

$$\frac{\partial U}{\partial t} + U u_1 + V u_2 - \nu\frac{\partial^2 U}{\partial z^2} + \lambda U = 0,\ \frac{\partial V}{\partial t} + U v_1 - V u_1 - \nu\frac{\partial^2 V}{\partial z^2} + \lambda V = 0 \tag{16}$$

Note that all equations of system (15) are isolated. These are linear partial differential equations of the heat conduction type with a source [40].

Let us further introduce into consideration the linear differential operator of a parabolic type:

$$L(\cdot) = \frac{\partial}{\partial t} - \nu\frac{\partial^2}{\partial z^2} + \lambda$$

System (15) can then be represented as a set of the following operator equations of the same type:

$$Lu_1 = 0,\ Lu_2 = 0,\ Lv_1 = 0 \tag{17}$$

After finding the proper solution to system (17), one should return to the integration of the quasi-nonlinear equation (Equation (16)).

Let us consider the special case of a steady flow. The operator L takes the following form:

$$L(\cdot) = -\nu\frac{\partial^2}{\partial z^2} + \lambda.$$

Consequently, Equation (17) turns into second-order ordinary differential equations with constant coefficients.

The general solution of the homogeneous operator equation $Lu = 0$ can be easily written out:

$$u(z) = c_1 \exp(kz) + c_2 \exp(-kz). \tag{18}$$

where c_1 and c_2 are constants of integration:

$$k = \sqrt{\frac{\lambda}{\nu}} \in R.$$

In view of compatibility condition (14) and the structure of solution (18), the appropriate solution to the system of the operator equation (Equation (17)) is determined by the set of functions:

$$u_1 = u\cos\theta\sin\theta,\ u_2 = u\cos^2\theta,\ v_1 = -u\sin^2\theta, \tag{19}$$

where u is the function in the form of (18) and θ is some number.

Note that if we put $\lambda = 0$ (ignoring the Rayleigh friction), then the characteristic equation corresponding to the differential equation will have a multiple (zero) root. In this case, the solution presented in [9,39] will be obtained. Thus, despite the external similarity of the structure of solution (19) with congruent solutions given in [9,39], we can assume that our current study has generalized the previously presented results.

Then, to completely determine the structure of the velocity field, what remains is to solve the system of two linear equations, which is a simplification of Equation (16) for the case of steady flows under consideration:

$$\lambda U + Uu_1 + Vu_2 - \nu\frac{d^2U}{dz^2} = 0,\ \lambda V + Uv_1 - Vu_1 - \nu\frac{d^2V}{dz^2} = 0. \tag{20}$$

To construct an exact solution of these linear equations with variable coefficients, let us substitute solution (19) for spatial accelerations into Equation (20):

$$\lambda U + Uu\cos\theta\sin\theta + Vu\cos^2\theta - \nu\frac{d^2U}{dz^2} = 0,$$

$$\lambda V - Uu\sin^2\theta - Vu\cos\theta\sin\theta - \nu\frac{d^2V}{dz^2} = 0. \tag{21}$$

Let us consider a special case when $\sin\theta = 0$. System (21) is then greatly simplified:

$$\lambda U + Vu - \nu\frac{d^2U}{dz^2} = 0,\ \lambda V - \nu\frac{d^2V}{dz^2} = 0. \tag{22}$$

The last equation can be written as $LV = 0$, the solution of which has form (18):

$$V = c_3 \exp(kz) + c_4 \exp(-kz).$$

Consequently, the inhomogeneity Vu in the first equation of system (22) will be equal to:

$$Vu = c_1c_3 \exp(2kz) + c_2c_4 \exp(-2kz) + c_1c_4 + c_2c_3.$$

We look for a particular solution corresponding to it in the form:

$$U_{part} = c_5 \exp(2kz) + c_6 \exp(-2kz) + c_7.$$

By substituting the expression above into the first equation of system (22), we obtain:

$$\lambda(c_5\exp(2kz)+c_6\exp(-2kz)+c_7)+c_1c_3\exp(2kz)+c_2c_4\exp(-2kz)+c_1c_4+c_2c_3$$

$$-\nu\Big(4k^2c_5\exp(2kz)+4k^2c_6\exp(-2kz)\Big)=0.$$

Taking into account the linear independence of the functions involved, we arrive at the following system of equations:

$$\lambda c_5+c_1c_3-4\nu c_5\left(\sqrt{\frac{\lambda}{\nu}}\right)^2=0,\ \lambda c_6+c_2c_4-4\nu c_6\left(\sqrt{\frac{\lambda}{\nu}}\right)^2=0,$$

$$\lambda c_7+c_1c_4+c_2c_3=0.$$

The solution of such systems as above is easy to find:

$$c_5=\frac{c_1c_3}{3\lambda},\ c_6=\frac{c_2c_4}{3\lambda},\ c_7=-\frac{c_1c_4+c_2c_3}{\lambda}.$$

Thus, the final solution to system (22) takes the form:

$$U=c_8\exp(kz)+c_9\exp(-kz)+\frac{c_1c_3}{3\lambda}\exp(2kz)+\frac{c_2c_4}{3\lambda}\exp(-2kz)-\frac{c_1c_4+c_2c_3}{\lambda}$$

$$V=c_3\exp(kz)+c_4\exp(-kz). \tag{23}$$

Let us now return to the analysis of system (21). In the general case, if we consider $\sin\theta\neq 0$, we can multiply the first equation of system (21) by $\sin\theta$ and the second one by $\cos\theta$, and then we can add them as a result. After algebraic transformations, we obtain:

$$\lambda(U\sin\theta+V\cos\theta)-\nu\frac{d^2}{dz^2}(U\sin\theta+V\cos\theta)=0$$

or

$$L(U\sin\theta+V\cos\theta)=0.$$

The solution of the last equation in view of Equation (18) has the form:

$$U\sin\theta+V\cos\theta=c_3\exp(kz)+c_4\exp(-kz). \tag{24}$$

Let us express the velocity U from the resulting relation and substitute it into any equation of system (21) that we are solving here, for example, into the second equation:

$$\lambda V-(c_3\exp(kz)+c_4\exp(-kz)-V\cos\theta)u\sin\theta-Vu\cos\theta\sin\theta-\nu\frac{d^2V}{dz^2}=0.$$

Having carried out elementary transformations, we obtain an inhomogeneous equation of the form

$$LV=\sin\theta(c_1c_3\exp(2kz)+c_2c_4\exp(-2kz)+c_1c_4+c_2c_3).$$

Relying on the actions performed in the process of searching for a solution to the inhomogeneous equation of system (22) and its final solution (23), we can easily write out the general solution of the last inhomogeneous equation:

$$V=c_5\exp(kz)+c_6\exp(-kz)$$

$$-\sin\theta\left(\frac{c_1c_3}{3\lambda}\exp(2kz)+\frac{c_2c_4}{3\lambda}\exp(-2kz)-\frac{c_1c_4+c_2c_3}{\lambda}\right). \quad (25)$$

What remains is to substitute expression (25) into relation (24) to obtain the exact solution describing the behavior of the velocity U:

$$U=\frac{1}{\sin\theta}(c_3\exp(kz)+c_4\exp(-kz)-V\cos\theta)$$

$$=\frac{c_3-c_5}{\sin\theta}\exp(kz)+\frac{c_4-c_6}{\sin\theta}\exp(-kz)$$

$$+\cos\theta\left(\frac{c_1c_3}{3\lambda}\exp(2kz)+\frac{c_2c_4}{3\lambda}\exp(-2kz)-\frac{c_1c_4+c_2c_3}{\lambda}\right). \quad (26)$$

4. Case 2: The Pressure P Is a Linear Form of the Horizontal Coordinates x and y

In this case, the pressure can be represented as the following linear form:

$$P(x,y,t)=P_0(t)+xP_1(t)+yP_2(t). \quad (27)$$

Note that despite adding more terms in the pressure representation (in comparison with form (13)), the compatibility condition in form (14) remains relevant, as the right-hand side of condition (12) for function (27) will be equal to zero.

Let us see how the change in the pressure structure P (27) will affect the form of the equations of system (11). It is easy to verify that by a direct substitution of expression (27), due to the independence of spatial coordinates, system (11) can be reduced to the following system:

$$\frac{\partial u_1}{\partial t}-\nu\frac{\partial^2u_1}{\partial z^2}+\lambda u_1=0,\ \frac{\partial u_2}{\partial t}-\nu\frac{\partial^2u_2}{\partial z^2}+\lambda u_2=0,\ \frac{\partial v_1}{\partial t}-\nu\frac{\partial^2v_1}{\partial z^2}+\lambda v_1=0, \quad (28)$$

$$\frac{\partial U}{\partial t}+Uu_1+Vu_2-\nu\frac{\partial^2U}{\partial z^2}+\lambda U=-P_1,\ \frac{\partial V}{\partial t}+Uv_1-Vu_1-\nu\frac{\partial^2V}{\partial z^2}+\lambda V=-P_2. \quad (29)$$

Comparing systems (15) and (16), and (28) and (29), we notice that the equations for determining the spatial gradients remain unchanged. Let us account for additional terms in expression (27) affecting only the equations for the U and V components. They become inhomogeneous and therefore even more difficult for the exact integration in a general form.

In the particular case of steady flows, the spatial gradients, as in the case of the uniform pressure, will be described by solution (19). So, system (29) will take the form:

$$\lambda U+Uu\cos\theta\sin\theta+Vu\cos^2\theta-\nu\frac{d^2U}{dz^2}=-P_1,$$

$$\lambda V-Uu\sin^2\theta-Vu\cos\theta\sin\theta-\nu\frac{d^2V}{dz^2}=-P_2. \quad (30)$$

In this case, the terms on the right-hand side of both equations in Equation (30) are constant. If we assume that $\sin\theta=0$, then, by analogy with the abovementioned case, we arrive to the system of inhomogeneous equations:

$$LU=-P_2-Vu,\ LV=-P_2. \quad (31)$$

If $\sin\theta \neq 0$, then, by carrying out transformations similar to those made in the case of a uniform pressure, we again come to an inhomogeneous equation as a result:

$$L(U\sin\theta + V\cos\theta) = -P_1\sin\theta - P_2\cos\theta. \tag{32}$$

Obtaining the solution to Equation (32) above is not difficult, as the inhomogeneity on the right-hand side is constant. This means that we will obtain a linear relationship connecting both homogeneous velocity components.

Expressing further the velocity U in terms of the velocity V (as it was performed above) and substituting into the second equation of system (32), we can, after integration, write out the exact solution for the velocity V. Then, afterward, using the relationship between the components U and V, we can find the exact solution for the velocity U. Calculations and transformations that should be performed according to the above-specified algorithm are not given here, due to two reasons. First, we have already described above the application of the standard technique for finding a particular solution corresponding to the inhomogeneity. Secondly, this entire algorithm has already been considered in sufficient detail using the example of the case of the uniform pressure.

5. Case 3: The Pressure P Is Determined by a Quadratic Dependence on the Coordinates x and y

In this case, the pressure is described by the following sum:

$$P(x,y,t) = P_0(t) + xP_1(t) + yP_2(t) + \frac{x^2}{2}P_{11}(t) + xyP_{12}(t) + \frac{y^2}{2}P_{22}(t).$$

The appearance of the quadratic terms in expression (25) (in comparison with form (22)) changes the structure of the compatibility condition (12) (with respect to the condition (14)):

$$P_{11} + P_{22} + 2\left({u_1}^2 + u_2v_1\right) = 0. \tag{33}$$

In addition, taking into account the terms of the second order also affects the resulting system of equations for the components of the velocity field:

$$\frac{\partial u_1}{\partial t} + {u_1}^2 + u_2v_1 - \nu\frac{\partial^2 u_1}{\partial z^2} + \lambda u_1 = -P_{11},\ \frac{\partial u_2}{\partial t} - \nu\frac{\partial^2 u_2}{\partial z^2} + \lambda u_2 = -P_{12},$$

$$\frac{\partial v_1}{\partial t} - \nu\frac{\partial^2 v_1}{\partial z^2} + \lambda v_1 = -P_{12}, -\left(\frac{\partial u_1}{\partial t} - \left({u_1}^2 + u_2v_1\right) - \nu\frac{\partial^2 u_1}{\partial z^2} + \lambda u_1\right) = -P_{22}, \tag{34}$$

$$\frac{\partial U}{\partial t} + Uu_1 + Vu_2 - \nu\frac{\partial^2 U}{\partial z^2} + \lambda U = -P_1,\ \frac{\partial V}{\partial t} + Uv_1 - Vu_1 - \nu\frac{\partial^2 V}{\partial z^2} + \lambda V = -P_2. \tag{35}$$

As of now, all equations have become obviously inhomogeneous. This means that the structure of the solution becomes more complicated and the form of some equations has also to be changed.

Let us pay attention to the first and last equations of system (34), presented in the following form:

$$\frac{\partial u_1}{\partial t} - \nu\frac{\partial^2 u_1}{\partial z^2} + \lambda u_1 = -P_{11} - \left({u_1}^2 + u_2v_1\right),\ \frac{\partial u_1}{\partial t} - \nu\frac{\partial^2 u_1}{\partial z^2} + \lambda u_1 = P_{22} + \left({u_1}^2 + u_2v_1\right).$$

Both equations are equations for determining the component u_1 of the velocity field (8). Note that the left-hand sides of these equations coincide, so the right-hand sides must also match:

$$-P_{11} - \left({u_1}^2 + u_2 v_1\right) = P_{22} + \left({u_1}^2 + u_2 v_1\right).$$

Obviously, the last equation coincides with Formula (33). Thus, if relation (33) is satisfied, the first equation in system (34) or the last one can be ignored. The choice of the "discarded" equation is determined conveniently by solving the particular boundary value problem.

Note that in the case of steady flows, the integration of systems (34) and (35) is to be reduced again to solving a set of inhomogeneous equations with linear operator L. The integration of these systems should be carried out completely in a similar way as in case of the uniform pressure, which has been analyzed above in detail.

We perform the appropriate actions to obtain a solution for steady-state flows. In this case, the solution class (8) takes the form:

$$V_x(x,y,z) = U(z) + u_1(z)x + u_2(z)y,$$

$$V_y(x,y,z) = V(z) + v_1(z)x + v_2(z)y. \tag{36}$$

The pressure P is described by a quadric of horizontal coordinates x and y with constant coefficients:

$$P(x,y) = P_0 + xP_1 + yP_2 + \frac{x^2}{2}P_{11} + xyP_{12} + \frac{y^2}{2}P_{22}.$$

We construct the solution for systems (34) and (35) for the special case of class (36):

$$V_x(x,y,z) = U(z) + u_2(z)y,\ V_y(x,y,z) = V(z). \tag{37}$$

The choice of class (37) is explained by the fact that by the invertible transformation of horizontal coordinates (a rotation in the horizontal plane around the origin of coordinates), it is possible to move from class (37) to class (36) using the following expressions:

$$x \to \cos\varphi x + \sin\varphi y\ ,\ y \to -\sin\varphi x + \cos\varphi y;$$

$$V_x \to \cos\varphi V_x + \sin\varphi V_y\ ,\ V_y \to -\sin\varphi V_x + \cos\varphi V_y \tag{38}$$

The reverse transition from class (36) to class (37) is also possible with the correct choice of the rotation angle value in expression (38).

So, the component u_2 from class (37) can be found from the corresponding equation of system (34):

$$-\nu u_2'' + \lambda u_2 = -P_{12}.$$

Here, the stroke denotes the derivative by the z coordinate. The solution of the latter equation is easily constructed using the characteristic equation:

$$u_2 = A\exp(kz) + B\exp(-kz) - \frac{P_{12}}{\lambda}, \tag{39}$$

as before $k = \sqrt{(\lambda/\nu)}$, A and B are constants of integration.

In this case, system (35) for class (37) becomes weakly related, i.e., an isolated equation is clearly distinguished in it:

$$V'' - k^2 V = \frac{P_2}{\nu},\ U'' - k^2 U = \frac{Vu_2 + P_1}{\nu}. \tag{40}$$

The solution of the first equation of system (40) is easily constructed:

$$V = C_1 \exp(kz) + D_1 \exp(-kz) - \frac{P_2}{\lambda}. \tag{41}$$

Here, C_1 and D_1 are constants of integration.

The solution of the second equation of system (40) consists of two parts—the general solution U_1 of a homogeneous equation and a particular solution U_2 of an inhomogeneous equation. Solution U_1 has a structure similar to expression (41):

$$U_1 = C_2 \exp(kz) + D_2 \exp(-kz).$$

Here, C_2 and D_2 are constants of integration.

The form of solution U_2 is determined by the structure of the heterogeneity $Vu_2 + P_1$:

$$\frac{Vu_2 + P_1}{\nu} = \frac{1}{\nu}\left(AC_1 \exp(2kz) - \frac{P_{12}C_1 + P_2 A}{\lambda} \exp(kz) - \frac{P_{12}D_1 + P_2 B}{\lambda} \exp(-kz) \right.$$

$$\left. + BD_1 \exp(-2kz) + AD_1 + BC_1 + P_1 \right). \tag{42}$$

In other words, we look for the solution U_2 in the following form:

$$U_2 = \alpha_1 \exp(2kz) + \alpha_2 \exp(kz) + \alpha_3 \exp(-kz) + \alpha_4 \exp(-2kz) + \alpha_5. \tag{43}$$

Let us substitute expression (43) into the second equation of system (40):

$$U_2'' - k^2 U_2 = 3k^2 \alpha_1 \exp(2kz) + 3k^2 \alpha_4 \exp(-2kz) - k^2 \alpha_5. \tag{44}$$

Comparing the coefficients for linearly independent functions $\exp(2kz)$, $\exp(kz)$, $\exp(-kz)$, and $\exp(-2kz)$ in expressions (42) and (44), we conclude that the solution exists only if the conditions are met:

$$P_{12}C_1 + P_2 A = P_{12}D_1 + P_2 B = 0.$$

So, as a result, we obtain the following solution for the component U:

$$U = \frac{C_1 A}{3\lambda} \exp(2kz) + C_2 \exp(kz) + D_2 \exp(-kz) + \frac{D_1 B}{3\lambda} \exp(-2kz) - \frac{AD_1 + BC_1 + P_1}{\lambda}. \tag{45}$$

Now, we can write out the solution for class (37):

$$V_x = U + u_2 y = \frac{C_1 A}{3\lambda} \exp(2kz) + (Ay + C_2) \exp(kz) + (By + D_2) \exp(-kz)$$

$$+ \frac{D_1 B_2}{3\lambda} \exp(-2kz) - \frac{AD_1 + BC_1 + P_1}{\lambda}.$$

$$V_y = V = C_1 \exp(kz) + D_1 \exp(-kz). \tag{46}$$

Finally, we apply the rotation transformation (38) to solution (46):

$$V_x = \cos\varphi \left[\frac{C_1 A}{3\lambda} \exp(2kz) + (A(-\sin\varphi x + \cos\varphi y) + C_2) \exp(kz) \right.$$

$$+(B(-\sin\varphi x+\cos\varphi y)+D_2)\exp(-kz)+\frac{D_1B_2}{3\lambda}\exp(-2kz)-\frac{AD_1+BC_1+P_1}{\lambda}$$

$$-\frac{P_2}{\lambda}(-\sin\varphi x+\cos\varphi y)\Big]+\sin\varphi[C_1\exp(kz)+D_1\exp(-kz)],$$

$$V_y=-\sin\varphi\Big[\frac{C_1A}{3\lambda}\exp(2kz)+(A(-\sin\varphi x+\cos\varphi y)+C_2)\exp(kz)$$

$$+(B(-\sin\varphi x+\cos\varphi y)+D_2)\exp(-kz)+\frac{D_1B_2}{3\lambda}\exp(-2kz)-\frac{AD_1+BC_1+P_1}{\lambda}$$

$$-\frac{P_2}{\lambda}(-\sin\varphi x+\cos\varphi y)\Big]+\cos\varphi[C_1\exp(kz)+D_1\exp(-kz)]. \quad (47)$$

Thus, the exact solution of systems (34) and (35) is obtained for steady-state flows within the framework of class (8).

Note that the coefficients before the x and y coordinates in the constructed solution (47) are linear combinations of the functions $\exp(kz)$, $\exp(-kz)$. In other words, the coefficients before x and y are expressions of the form (39) that satisfy the equations of system (34) for determining the components of the velocity field (8).

6. The Analysis of the Solution

We consider a boundary value problem for a visual illustration of the influence of the friction force on the properties of a steady flow of fluid. The velocity and pressure fields have the following structure:

$$V_x=U(z),\ V_y=V(z),\ P(x,y)=P_0+xP_1+yP_2. \quad (48)$$

Expressions in (48) are a special case of class (8) for $u_1=u_2=v_1=v_2=0$. System (28) for these values takes the form

$$\lambda U-\nu\frac{d^2U}{dz^2}=-P_1,\ \lambda V-\nu\frac{d^2V}{dz^2}=-P_2. \quad (49)$$

If friction is ignored (i.e., assuming $\lambda=0$), equations in Equation (49) describe a flow with a parabolic profile, i.e., Couette–Poiseuille-type flow:

$$U=\frac{P_1}{2\nu}z^2+s_1z+s_2,\ V=\frac{P_2}{2\nu}z^2+s_3z+s_4. \quad (50)$$

However, taking into account the drag coefficient λ fundamentally changes the structure of the solution, and it ceases to be polynomial:

$$U=s_1\exp\left(\sqrt{\frac{\lambda}{\nu}}z\right)+s_2\exp\left(-\sqrt{\frac{\lambda}{\nu}}z\right)-\frac{P_1}{\lambda},\ V=s_3\exp\left(\sqrt{\frac{\lambda}{\nu}}z\right)+s_4\exp\left(-\sqrt{\frac{\lambda}{\nu}}z\right)-\frac{P_2}{\lambda}. \quad (51)$$

To determine the integration constants s_1, s_2, s_3, and s_4, consider the following boundary conditions. We now assume that the flow occurs in an extended horizontal layer with non-deformable boundaries. At the lower boundary $z=0$, the no-slip condition is satisfied:

$$U(0)=V(0)=0. \quad (52)$$

On the upper boundary $z=h$, the distribution of velocities is given:

$$U(h)=W\cos\varphi, V(h)=W\sin\varphi. \quad (53)$$

Under conditions (52) and (53), the exact solution (51) takes the form:

$$U(Z) = \frac{\exp(a(1-Z))(-1+\exp(2aZ))}{-1+\exp(2a)} W\cos\varphi$$

$$+\frac{\exp(-aZ)(-1+\exp(aZ))(-\exp(a)+\exp(aZ))}{1+\exp(a)}\frac{P_1}{\lambda},$$

$$V(Z) = \frac{\exp(a(1-Z))(-1+\exp(2aZ))}{-1+\exp(2a)} W\sin\varphi$$

$$+\frac{\exp(-aZ)(-1+\exp(aZ))(-\exp(a)+\exp(aZ))}{1+\exp(a)}\frac{P_2}{\lambda}. \quad (54)$$

In solution (54), the substitutions are introduced:

$$a = \frac{h\sqrt{\lambda}}{\sqrt{\nu}},\ Z = \frac{z}{h} \in [0;1].$$

We normalize solution (54) to the characteristic flow velocity W, retaining the notation:

$$U = \frac{\exp(a(1-Z))(-1+\exp(2aZ))}{-1+\exp(2a)} \cos\varphi$$

$$+\frac{\exp(-aZ)(-1+\exp(aZ))(-\exp(a)+\exp(aZ))}{1+\exp(a)}\frac{\gamma_1}{\mathrm{Re}\delta a^2},$$

$$V = \frac{\exp(a(1-Z))(-1+\exp(2aZ))}{-1+\exp(2a)} \sin\varphi$$

$$+\frac{\exp(-aZ)(-1+\exp(aZ))(-\exp(a)+\exp(aZ))}{1+\exp(a)}\frac{\gamma_2}{\mathrm{Re}\delta a^2}. \quad (55)$$

Here,

$$\gamma_1 = \frac{h^3 P_1}{\nu^2}, \gamma_2 = \frac{h^3 P_2}{\nu^2},\ \mathrm{Re} = \frac{Wl}{\nu},\ \delta = \frac{h}{l},$$

l is a characteristic scale in horizontal x and y coordinates.
Note that the following passage to the limit is performed for solution (55):

$$\lim_{a=\frac{h\sqrt{\lambda}}{\sqrt{\nu}}\to 0} U = \frac{2\mathrm{Re}\delta\cos\varphi + \gamma_1(-1+Z)}{2\mathrm{Re}\delta} Z,$$

$$\lim_{a=\frac{h\sqrt{\lambda}}{\sqrt{\nu}}\to 0} V = \frac{2\mathrm{Re}\delta\sin\varphi + \gamma_2(-1+Z)}{2\mathrm{Re}\delta} Z. \quad (56)$$

Solution (56) describes the Couette–Poiseuille flow profile, and if we additionally put $\gamma_1 = 0$ and $\gamma_2 = 0$ (i.e., ignore the possible pressure drop in horizontal directions), then there will be a classic linear Couette profile:

$$U = \cos\varphi Z,\ V = \sin\varphi Z.$$

The velocity field profile (55) is determined by the interaction of two nonlinear flows, one of which is induced by the movement of the upper boundary, the other by the pressure difference (Figure 1). The hodograph of the velocity vector is shown in Figure 2.

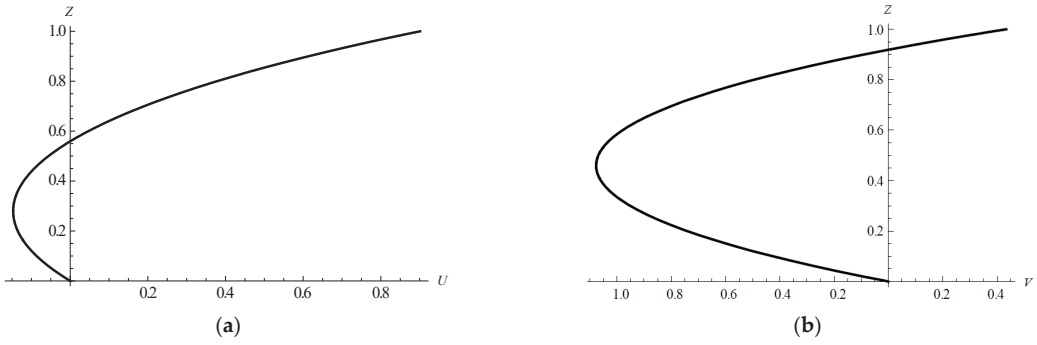

Figure 1. (**a**) Velocity profile U; (**b**) Velocity profile V.

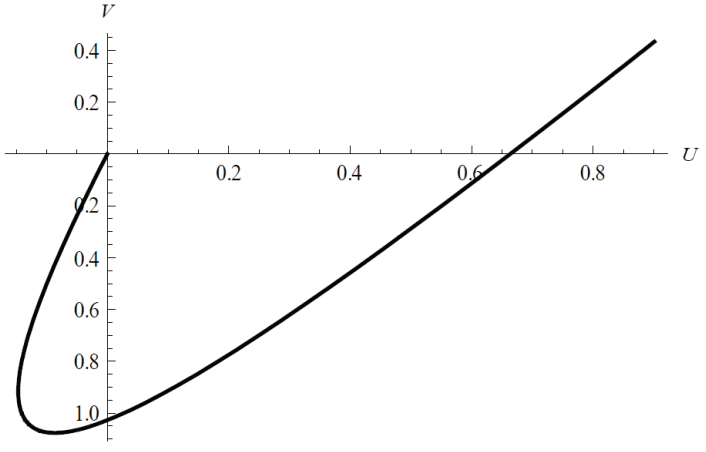

Figure 2. Velocity vector hodograph.

Note that the characteristic value a = $\sqrt{2}$ was used in the calculations. This value results from the expression $\lambda = 2\nu/h^2$ [3]. For comparison, Figure 3 shows the profiles of the velocity field determined by exact solution (50) taking into account boundary conditions (52) and (53).

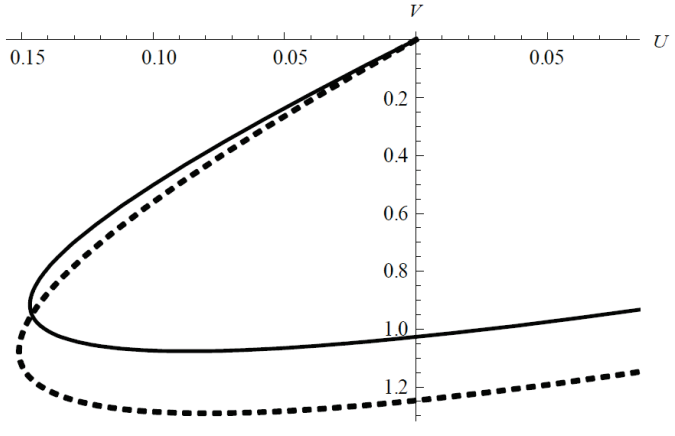

Figure 3. Velocity vector hodograph with friction (solid line) and without friction (dashed line).

As can be seen from Figure 3, there is a qualitative similarity of the hodographs: there is a return section on both curves, and both curves intersect the axes, which indicates the occurrence of countercurrents, but significant differences in quantitative estimates are visible.

7. Conclusions

In this article, the problem of the overdetermination for the system of equations used to describe shear flows of viscous fluids, additionally introducing into consideration the Rayleigh friction, is studied. The reduced systems of equations for the velocity field that is linear in the x and y coordinates are given. It is shown that the pressure should be a polynomial depending on the aforementioned coordinates, and the degree of such polynomials does not exceed two. Conditions for avoiding the abovementioned overdetermination are derived for the constructed class of solutions. It is shown that the form of the compatibility condition for solutions of such systems depends on the chosen structure of the pressure field. It is also shown that this structure affects the form of equations for determining the components of the velocity field. Among other findings, new nontrivial exact solutions (within the suggested class) that take into account the Rayleigh friction are constructed for the particular case of steady flows.

Author Contributions: Conceptualization, N.B., S.E. and E.P.; methodology, N.B., S.E., E.P. and D.L.; writing—original draft preparation, N.B., S.E. and E.P.; writing—review and editing, N.B., S.E., E.P. and D.L. All authors have read and agreed to the published version of the manuscript.

Funding: This research received no external funding.

Data Availability Statement: The data are contained within the article.

Conflicts of Interest: The authors declare no conflict of interest.

References

1. Ekman, V.W. On the influence of the Earth's rotation on ocean-currents. *Ark. Mat. Astron. Fys.* **1905**, *2*, 1874–1954.
2. Pedlosky, J. *Geophysical Fluid Dynamics*; Springer: Berlin, Germany; New York, NY, USA, 1987.
3. Dolzhansky, F.V.; Krymov, V.A.; Manin, D.Y. Stability and vortex structures of quasi-two-dimensional shear flows. *Phys. Usp.* **1990**, *33*, 495–520. [CrossRef]
4. Aristov, S.N. Eddy Currents in Thin Liquid Layers. Ph.D. Thesis, Institute of Automation and Control Processes, Vladivostok, Russia, 1990.
5. Drazin, P.G.; Reid, W.H. *Hydrodynamic Stabilityi*; Cambridge University Press: Cambridge, UK, 1981.
6. Drazin, P.G.; Riley, N. *The Navier–Stokes Equations: A Classification of Flows and Exact Solutions*; Cambridge University Press: Cambridge, UK, 2006.
7. Nezlin, M.V. Rossby solitons (Experimental investigations and laboratory model of natural vortices of the Jovian Great Red Spot type). *Sov. Phys. Usp.* **1986**, *29*, 807–842. [CrossRef]
8. Ershkov, S.V.; Prosviryakov, E.Y.; Burmasheva, N.V.; Christianto, V. Towards understanding the algorithms for solving the Navier–Stokes equations. *Fluid Dyn. Res.* **2021**, *53*, 044501. [CrossRef]
9. Burmasheva, N.V.; Prosviryakov, E.Y. A class of exact solutions for two-dimensional equations of geophysical hydrodynamicswith two Coriolis parameters. *Izv. Irkutsk. Gos. Univ. Ser. Mat.* **2020**, *32*, 33–48.
10. Ladyzhenskaya, O.A. On nonstationary Navier–Stokes equations. *Vestn. Leningr. Univ.* **1958**, *19*, 9–18.
11. Ladyzhenskaya, O.A. On some gaps in two of my papers on the Navier–Stokes equations and the way of closing them. *J. Math. Sci.* **2003**, *115*, 2789–2791. [CrossRef]
12. Pukhnachev, V.V. Symmetries in the Navier–Stokes equations. *Uspekhi Mekhaniki* **2006**, *1*, 6–76.
13. Aristov, S.N.; Knyazev, D.V.; Polyanin, A.D. Exact solutions of the Navier–Stokes equations with the linear dependence of velocity components on two space variables. *Theor. Found. Chem. Eng.* **2009**, *43*, 642–662. [CrossRef]
14. Ershkov, S.; Prosviryakov, E.; Leshchenko, D. Exact solutions for isobaric inhomogeneous Couette flows of a vertically swirling fluid. *J. Appl. Computat. Mech.* **2023**, *9*, 521–528.
15. Baranovskii, E.S.; Burmasheva, N.V.; Prosviryakov, E.Y. Exact solutions to the Navier–Stokes equations with couple stresses. *Symmetry* **2021**, *13*, 1355. [CrossRef]
16. Aristov, S.N.; Prosviryakov, E.Y. Unsteady layered vortical fluid flows. *Fluid Dyn.* **2016**, *51*, 148–154. [CrossRef]
17. Zubarev, N.M.; Prosviryakov, E.Y. Exact solutions for layered three-dimensional nonstationary isobaric flows of a viscous incompressible fluid. *J. Appl. Mech. Tech. Phys.* **2019**, *60*, 1031–1037. [CrossRef]

18. Burmasheva, N.V.; Prosviryakov, E.Y. Exact solutions to Navier–Stokes equations describing a gradient nonuniform unidirectional vertical vortex fluid flow. *Dynamics* **2022**, *2*, 175–186. [CrossRef]
19. Bogoyavlenskij, O. The new effect of oscillations of the total angular momentum vector of viscous fluid. *Phys. Fluids* **2022**, *34*, 083108. [CrossRef]
20. Bogoyavlenskij, O. The new effect of oscillations of the total kinematic momentum vector of viscous fluid. *Phys. Fluids* **2022**, *34*, 123104. [CrossRef]
21. Prosviryakov, E.Y. Layered gradient stationary flow vertically swirling viscous incompressible fluid. *CEUR Workshop Proc.* **2016**, *1825*, 164–172.
22. Ershkov, S.V.; Shamin, R.V. On a new type of solving procedure for Laplace tidal equation. *Phys. Fluids* **2018**, *30*, 127107. [CrossRef]
23. Ershkov, S.V. Non-stationary creeping flows for incompressible 3D Navier–Stokes equations. *Eur. J. Mech. B Fluids* **2017**, *61*, 154–159. [CrossRef]
24. Bashurov, V.V.; Prosviryakov, E.Y. Steady thermo-diffusive shear Couette flow of incompressible fluid. Velocity field analysis. *Vestn. SamGTU-Seriya-Fiz.-Mat. Nauk.* **2021**, *25*, 781–793. [CrossRef]
25. Burmasheva, N.V.; Prosviryakov, E.Y. Exact solutions to the Navier–Stokes equations describing stratified fluid flows. *Vestn. SamGTU-Seriya-Fiz.-Mat. Nauk.* **2021**, *25*, 491–507. [CrossRef]
26. Burmasheva, N.V.; Prosviryakov, E.Y. Exact solutions to the Oberbeck–Boussinesq equations for shear flows of a viscous binary fluid with allowance made for the Soret effect. *Bull. Irkutsk. State Univ.-Ser. Math.* **2021**, *37*, 17–30. [CrossRef]
27. Ingel, L.K.; Kalashnik, M.V. Nontrivial features in the hydrodynamics of seawater and other stratified solutions. *Phys. Usp.* **2012**, *55*, 356–381. [CrossRef]
28. Öz, Y. Rigorous investigation of the Navier–Stokes momentum equations and correlation tensors. *AIP Adv.* **2021**, *11*, 055009. [CrossRef]
29. Wang, C.Y. Exact solutions of the unsteady Navier–Stokes equations. *Appl. Mech. Rev.* **1989**, *42*, 269–282. [CrossRef]
30. Wang, C.Y. Exact solutions of the steady-state Navier–Stokes equations. *Annu. Rev. Fluid Mech.* **1991**, *23*, 159–177. [CrossRef]
31. Pukhnachev, V.V. Strip deformation problem in three models of hydrodynamics. *Theoret. Math. Phys.* **2022**, *211*, 701–711. [CrossRef]
32. Korobkov, M.V.; Pileckas, K.; Pukhnachov, V.V.; Russo, R. The flux problem for the Navier–Stokes equations. *Russ. Math. Surv.* **2014**, *69*, 1065–1122. [CrossRef]
33. Meshalkin, L.D.; Sinai, I.G. Investigation of the stability of a stationary solution of a system of equations for the plane movement of an incompressible viscous liquid. *J. Appl. Math. Mech.* **1961**, *25*, 1700–1705. [CrossRef]
34. Obukhov, A.M. Kolmogorov flow and laboratory simulation of it. *Russ. Math. Surv.* **1983**, *38*, 113–126. [CrossRef]
35. Sivashinsky, G.I. Weak turbulence in periodic flows. *Phys. D Nonlinear Phenom.* **1985**, *17*, 243–255. [CrossRef]
36. Kalashnik, M.V.; Kurgansky, M.V.; Chkhetiani, O.G. Baroclinic instability in geophysical fluid dynamics. *Phys. Usp.* **2022**, *65*, 1039–1070. [CrossRef]
37. Lin, C.C. Note on a class of exact solutions in magneto-hydrodynamics. *Arch. Ration. Mech. Anal.* **1958**, *1*, 391–395. [CrossRef]
38. Sidorov, A.F. Two classes of solutions of the fluid and gas mechanics equations and their connection to traveling wave theory. *J. Appl. Mech. Tech. Phys.* **1989**, *30*, 197–203. [CrossRef]
39. Burmasheva, N.V.; Prosviryakov, E.Y. Exact solutions for steady convective layered flows with a spatial acceleration. *Rus. Math.* **2021**, *65*, 8–16. [CrossRef]
40. Polyanin, A.D.; Zaitsev, V.F. *Handbook of Nonlinear Partial Differential Equations*; Chapman & Hall; CRC Press: Boca Raton, FL, USA, 2004.

MDPI AG
Grosspeteranlage 5
4052 Basel
Switzerland
Tel.: +41 61 683 77 34

Fluids Editorial Office
E-mail: fluids@mdpi.com
www.mdpi.com/journal/fluids

Academic Open
Access Publishing

mdpi.com

ISBN 978-3-7258-1356-8